This electronic thesis or dissertation has been downloaded from the King's Research Portal at https://kclpure.kcl.ac.uk/portal/

mRNA delivery by laser-induced poration using porous silicon nanoparticles

Spiteri, Chantelle

Awarding institution:
King's College London

The copyright of this thesis rests with the author and no quotation from it or information derived from it may be published without proper acknowledgement.

END USER LICENCE AGREEMENT

Unless another licence is stated on the immediately following page this work is licensed under a Creative Commons Attribution-NonCommercial-NoDerivatives 4.0 International licence. https://creativecommons.org/licenses/by-nc-nd/4.0/

You are free to copy, distribute and transmit the work

Under the following conditions:

- Attribution: You must attribute the work in the manner specified by the author (but not in any way that suggests that they endorse you or your use of the work).
- Non Commercial: You may not use this work for commercial purposes.
- No Derivative Works - You may not alter, transform, or build upon this work.

Any of these conditions can be waived if you receive permission from the author. Your fair dealings and other rights are in no way affected by the above.

Take down policy

If you believe that this document breaches copyright please contact librarypure@kcl.ac.uk providing details, and we will remove access to the work immediately and investigate your claim.

Download date: 13. Jan. 2025

mRNA delivery by laser-induced poration using porous silicon nanoparticles

This thesis is submitted to King's College London
for the degree of
Doctor of Philosophy

by
Chantelle Spiteri
December 2023

Acknowledgements

I would first like to thank my supervisor, Dr Ciro Chiappini, for his exceptional support, encouragement, patience and guidance throughout my PhD studies. Dr Chiappini welcomed me into his research group and provided me with the opportunity to work on an exceptional project at the interface of multiple disciplines. His insights and advice were invaluable in overcoming the numerous challenges faced during the course of this research. I am deeply grateful for the enthusiasm he showed for my work and for the stimulating scientific discussions we shared.

I would also like to thank my second supervisor, Professor Khuloud Al-Jamal, for sharing her expertise in chemistry and providing access to facilities in her lab. My appreciation extends to my thesis committee - Professors Agi Grigoriadis, Professor Karen Liu, Dr Joanna Jackow and Dr Davide Danovi - whose feedback and guidance helped refine and enhance this thesis. I also wish to acknowledge Dr. Frédérique Cunin and her research group at the University of Montpellier for welcoming me during my research visit. The opportunity to work in their lab was invaluable to my project and resulted in key data presented in Chapter 6. I am particularly thankful to Dr. Sofia Dominguez-Gil, Dr. Magali Gary-Bobo and Dr. Jean-Olivier Durand for their support during my stay.

I am grateful to all past and present members of the Chiappini Lab and the Centre for Craniofacial and Regenerative Biology, especially Dr. Salman Mustfa, Dr. Priya Vashisth, Dr. Maria Grazia Barbato, Dr. Hongki Kim, William Edwards, Chenlei Gu, Ningjia Sun, Yikai Wang, Hongting Zhu and Sam Mclennan for their assistance and collegiality. Particular thanks to Dr. Valeria Caprettini for her invaluable support with the optoporation experiments, Dr. Martti Kaasalainen for sharing his extensive nanoparticles expertise and Dr. Cong Wang and Dr. Davide Martella for SEM imaging assistance. It was a privilege to collaborate with such a talented and supportive team.

I am eternally grateful to my family for their love and support throughout this journey. In particular, I want to thank my father who has been my number one fan and chef. His unwavering belief in me and his wise counsel during our frequent phone calls kept me motivated through the ups and downs of research. I am thankful for my mother and sister who were there when I needed reassurance or a listening ear, as well as to my new family

members - Anna, Joe and Josephine - for checking in on my progress and reminding me there was a light at the end of the tunnel.

Most importantly, deepest thanks to my partner Benji for being my backbone and better half. His endless support and encouragement gave me the confidence I needed to see this project through to the end. I am forever grateful for the late night discussions we shared when experiments were not proceeding as anticipated. He helped me think through problems from new angles and design better approaches. During the most stressful and challenging times, I could always rely on you for moral and emotional support. Simply put, I could not have completed this journey without you by my side.

Abstract

Access to the inside of the cell remains one of the long-standing hurdles for therapeutics and diagnostics. A diversity of physical, biological and chemical methodologies have emerged to achieve the delivery of membrane-impermeable exogenous materials across the cell membrane. Striving for spatial-temporal control and enhanced in vitro intracellular delivery efficiencies, optoporation has emerged as a promising technique. This physical method involves using a high-intensity laser pulse to induce transient pores within the cell membrane. Specifically, the high selectivity of optical transfection enables precise cellular manipulation for a deeper understanding of biomolecular mechanisms and opens new avenues, for example, in in vitro studies on stem cell differentiation and reprogramming dynamics. To improve the optoporation efficiency, nanomaterials such as gold and carbon-based nanoparticles are often coupled with the laser, however, these are not biodegradable and can be genotoxic, limiting their applicability in advanced therapies and modelling.

This work presents an alternative photothermal nanomaterial to the conventional, frequently used nanoparticles. Herein, I fabricated and characterised biodegradable porous silicon nanoparticles through metal-assisted chemical etching and electrochemical etching to produce rod-like and discoid-like particles, respectively. Viability assays have shown that a 24-hour interaction between the nanoparticles and the cells had no significant influence on cell death or proliferation. The two different geometries, both approximately 300 nm in size, were coupled with a femtosecond laser in the near-infrared region (800 nm). The coupling excited the porous silicon nanoparticles and achieved spatial-selective control over the delivery of propidium iodide only in the individually laser-scanned MCF-7 breast cancer cells. Maintaining cell viability after delivery is crucial, therefore, the short-term cell viability (30 minutes) post-optoporation was confirmed in 2D cell culture through calcein-AM retention as a sign of reversible membrane permeability. Through further optimisations of this nano-sensitised optoporation technique, propidium iodide was also delivered in selected areas within the 3D MCF-7 cancerous spheroid model. Furthermore, this optoporation system led to the spatial-selective transfection of the cells with eGFP mRNA and expression of the fluorescent GFP protein for both the 2D and the 3D systems. Thus, confirming selective cellular manipulation of target cells. These data demonstrate efficacy of porous

silicon nanoparticles combined with a femtosecond laser in the near-infrared region for the delivery and expression of genetic material. The successful outcome observed in both the 2D and 3D models establishes the groundwork for spatial-temporal nucleic acid delivery, enabling applications in cell engineering and advancing our understanding of cellular biological mechanisms.

COVID-19 Impact Statement

The onset of the COVID-19 pandemic in early 2020 significantly disrupted my PhD research, altering the original timeline and scope of my project. When the pandemic hit in March 2020, I was just beginning my first year of studies. For 6 months from March to September 2020, I was unable to access the lab facilities due to university lockdowns. During this time, I focused my efforts on an extensive literature review which resulted in a published review paper. However, without access to the lab, I could not make progress on experiments or data collection critical for my research objectives.

When restricted lab access resumed in September 2020, I could only use selected equipment like the SEM on designated days with limited time slots available. This severely constrained my ability to characterise nanoparticles and perform my optoporation studies. I also lost access to confocal microscope during the lockdown. When labs reopened, there were long queues to get retrained on the confocal and as a result, I went months without being able to utilise confocal microscopy to analyse my samples. Such limitations on equipment access remained in place until mid-2021.

Additional delays accumulated when key lab systems like the pulsed laser system broke down in early 2021. Repairs were delayed by 2-3 months due to both COVID-19 and newly introduced customs checks for imported parts between the European Union and the UK. Additionally, the responsible engineer contracted COVID which caused further delays. Moreover, the optical microscope attached to the femtosecond laser setup suffered a major malfunction, which took an additional 3 months to get fixed. Consequently, by the time the laser and microscope were repaired and aligned, I had lost almost half a year of research time. As such, I was only able to collect the bulk of my optoporation data in the last 2 years as lab access gradually normalised. Despite these constraints, I made every effort to optimise the available time by leading the development of my project, presenting at numerous international conferences, and supporting my peers. However, the pandemic significantly hindered my ability to achieve the original research goals proposed at the start of my studies. As such, this statement is meant to provide context on the extraordinary conditions under which this research was conducted.

Author’s Declaration

Declaration of Authenticity

I hereby certify that this thesis represents my own original work, except where explicit attribution is made to collaborative efforts or previously published material. All research was carried out independently by me between 2019 and 2023 while studying at King's College London. No substantial portion of this work has previously been submitted to fulfil requirements for any degree at this or any other institution. All external sources are properly acknowledged and cited.

Copyright Declaration

Table of Contents

Acknowledgements 2

Abstract 4

COVID-19 Impact Statement 6

Author's Declaration 7

Table of Contents 8

Table of Figures 12

Table of Tables 15

Table of Acronyms 16

Chapter 1 – Introduction 18

- 1.1 Single-cell Targeting 18
- 1.2 Gene Delivery Techniques 20
  - 1.2.1 Viral Vectors 21
  - 1.2.2 Carrier Mediated Delivery 22
  - 1.2.3 Microinjection 24
  - 1.2.4 Nanoneedles 26
  - 1.2.5 Electroporation 27
  - 1.2.6 Sonoporation 32
  - 1.2.7 Optoporation 34
- 1.3 Cell Membrane Repair 35
- 1.4 Summary 38
- 1.5 Introduction to Optoporation 41
- 1.6 Mechanisms of Transient Pore Formation by Optoporation 43
  - 1.6.1 Photothermal Pore Formation 43
  - 1.6.2 Photomechanical Pore Formation 43
  - 1.6.3 Photochemical Pore Formation 45
- 1.7 Direct Optoporation 45
- 1.8 Indirect Optoporation 50
  - 1.8.1 Gold Nanoparticles 50
  - 1.8.2 Carbon Based Nanoparticles 53
  - 1.8.3 Other Nanomaterials 55
- 1.9 Porous Silicon Nanoparticles 61
  - 1.9.1 Fabrication of Mesoporous Silicon Nanoparticles 61
  - 1.9.2 Electrochemical Etching 61
  - 1.9.3 Metal Assisted Chemical Etching 62

1.9.4 Surface Modification of pSi Nanoparticles 63
1.9.5 Biodegradability 63
1.9.6 Porous Silicon Nanoparticles as Drug Delivery Carriers 64
1.9.7 Porous Silicon Based Biosensors 66
1.9.8 Photophysical Mechanism in Photodynamic and Photothermal Therapy 68
1.10 Summary 70
Chapter 2 - Project Aim and Objectives 72
Chapter 3 - Materials and Methods 75
3.1 Nanoparticles Fabrication and Characterisation 75
3.1.1 Nanoparticles Fabrication through Electrochemical Etching 75
3.1.2 Nanoparticle Fabrication through Metal-Assisted Chemical Etching (MACE) 76
3.1.3 Amine Group, FITC and Ocean Blue Functionalisation of pSi Nanoparticles 78
3.1.4 Particle Size and Surface Charge Measurements 78
3.1.5 Estimation of Specific Surface Area, Pore Size and Pore Volume with N_2 sorption 79
3.1.6 Loading EC Nanoparticles with mRNA 79
3.2 Cell culture 79
3.2.1 Cryopreservation and Thawing 80
3.3 Investigating the Interaction between the Nanoparticles and MCF-7 cells 80
3.3.1 Cell Preparation for SEM and EDX 80
3.3.2 CellTiter-Glo® Viability Assay in the 2D System 81
3.4 MCF-7 Spheroid Preparation 82
3.4.1 Methocel Preparation 82
3.4.2 Hanging Drop Method 82
3.4.3 Addition of Nanoparticles to the Spheroids 82
3.4.4 Collagenase Treatment for Nanoparticle Diffusion to the Core of the Spheroids .. 83
3.4.5 Spheroids Cryosections 83
3.5 Bright Field and Immunofluorescence Imaging 84
3.6 CellTiter -Glo® Viability Assay in the 3D System 84
3.7 Multiphoton Femtosecond Laser Set-up 84
3.8 Optoporation Experiments 85
3.8.1 Determining the Effect of pSi Nanoparticles Incubation Time on the Loading Density 85
3.8.2 MCF-7 Monolayer Cellular Construct 85
3.8.3 Cellular Optoporation Efficiency in 2D cell cultures 85
3.8.4 Short-Term Viability Post-Optoporation 86
3.8.5 Imaging for ROS 86
3.8.6 Imaging for Caspase 3/7 87

3.8.7 In Vitro mRNA Transfection with Optoporation 87
3.8.8 In vitro mRNA Transfection with Lipofectamine (Control) 87
3.8.9 Cellular Optoporation Efficiency in 3D Spheroids 88
3.9 Grafting Electrochemically Etched Nanoparticles with Isocyanopropyltriethyoxysilane (ICPES)-azobenzene@Lys 88
3.9.1 Synthesis of Azobenzene@Lys(diBoc) 88
3.9.2 The Silanisation Step 89
3.9.3 Grafting to the Nanoparticles forming pSiNPs-ICPES-azobenzene@Lys(diBoc) ... 89
3.9.4 Deprotection from the Boc Moiety 89
3.9.5 mRNA Loading and Gel Electrophoresis 90
3.9.6 Cellular Optoporation Efficiency in 3D Spheroids 90
3.10 Statistical Analysis 90
Chapter 4 - pSi Nanoparticles Fabrication and their Interactions with MCF-7 cells 91
4.1 Introduction 91
4.2 Electrochemically Etched Nanoparticle Fabrication 95
4.2.1 Characterisation of the Electrochemically Etched Nanoparticles 97
4.3 Metal Assisted Chemical Etched Nanoparticle Fabrication 100
4.3.1 Centrifuge Speed Impact on Nanoparticle Size and Storage-Solvent Stability 101
4.3.2 Optimising the Sonication 102
4.3.3 MACE Nanoparticle Characterisation 103
4.4 Surface Functionalisation of pSi Nanoparticles 106
4.5 The Interaction of MCF-7 Cells with pSi Nanoparticles 112
4.5.1 Toxicity of the Nanoparticles 114
4.6 3D Cell Culture System and Nanoparticles Interactions 117
4.6.1 Spheroid Formation 118
4.6.2 Nanoparticles Interaction with 3D MCF-7 Spheroids 119
4.6.3 Nanoparticle Diffusion to the MCF-7 Spheroid Core 122
4.7 Concluding Remarks 126
Chapter 5 - Spatially selective delivery 128
5.1 Introduction 128
5.2 Optical Setup 132
5.2.1 Customisable Laser Control Software Interface 133
5.2.2 ‘Multi Scan Bleach’ Command Box 135
5.2.3 ‘Laser Setup’ Command Box 136
5.3 Investigating the Poration efficiency of pSi Nanoparticles 137
5.4 Short-Term Cell Viability Assessment with EC Nanoparticles 140
5.5 Optimisation of Laser–Induced mRNA Transfection 142
5.5.1 eGFP mRNA Concentration Titration 143

5.5.2 Imaging and Laser Impact on eGFP mRNA Expression 145
5.5.3 Loading of pSi Nanoparticles with eGFP mRNA 146
5.6 Optimisations for Nucleic Acid Delivery and Protein Expression 148
5.6.1 Laser Scanning Area 149
5.6.2 The effect of pSi Nanoparticles Incubation Time on the Loading Density 150
5.6.3 Laser Power and EC–Nanoparticle Concentrations Impact 152
5.6.4 Scanning Speed Impact on Uptake Efficiency 154
5.6.5 Short–term Cell Viability 156
5.6.6 Reactive Oxygen Species and Apoptosis 158
5.7 Altering the Functionalisation of the EC Nanoparticles 162
5.8 GFP mRNA transfection via optoporation 163
5.9 Optoporation of 3D MCF–7 Spheroids 167
5.10 Concluding Remarks 172
Chapter 6 – Photo-switchable Molecule for Controllable mRNA Release 174
6.1 Introduction 174
6.2 Synthesis of ICPES–azobenzene–lys pSi Nanoparticles 177
6.2.1 Synthesis of ICPES–azobenzene–lys–diBoc 177
6.2.2 Grafting of ICPES-azobenzene-lys and Characterisation 181
6.3 Toxicity of the Nanoparticles 183
6.4 Reactive Oxygen Species and Apoptosis 184
6.5 Complexation with mRNA 187
6.6 Delivery of eGFP mRNA in 2D Cell Culture System 188
6.7 Delivery of eGFP mRNA in 3D Tumour Models 190
6.8 Concluding Remarks 193
Chapter 7 - Conclusion 194
Chapter 8 - Future Work 198
Chapter 9 – References 201

Table of Figures

Figure 1: A schematic of the microfluidic system with a jet injector. 25
Figure 2: An overview of the different electroporation devices discussed. 32
Figure 3: Membrane pore formation through direct and indirect optoporation. 35
Figure 4: A selection of the various proposed intracellular delivery methods. 39
Figure 5: Schematic of the laser cavity. 41
Figure 6: Excited-state energy diagram showing one-photon and two-photon excitation. 42
Figure 7: Change in photoluminescence of the biosensor upon DNA binding. 67
Figure 8: Jablonski diagram showing characteristic photophysical processes on laser excitation of pSi nanoparticles. 69
Figure 9: Summary of the setup used for electrochemical etching. 76
Figure 10: Arrangement of the hanging drops containing cells as placed on the lid of the petri dish. 82
Figure 11: Characterisation of the electrochemically etched silicon wafer. 97
Figure 12: Optimisation of the nanoparticle concentration for DLS measurements. 98
Figure 13: The relative percentage frequency of EC nanoparticles with a given aspect ratio. 99
Figure 14: Pore size analysis of EC nanoparticles. 100
Figure 15: Nanowires fabrication through MACE. 101
Figure 16: Centrifuge speed impact on nanoparticle size and storage-solvent stability. 102
Figure 17: The effect of sonication time on nanoparticle size. 103
Figure 18: The relative percentage frequency of MACE nanoparticles with a given aspect ratio. 104
Figure 19: Overlay of the aspect ratio relative frequency distribution for EC and MACE nanoparticles. 105
Figure 20: Pore size analysis of EC nanoparticles. 106
Figure 21: An illustration of the APTES-tagged nanoparticle reaction. 107
Figure 22: The effect of nanoparticle concentration on the zeta potential measurements. 108
Figure 23: The effect of incubation time and APTES concentration on the zeta potential measurement. 109
Figure 24: Fluorescence images of tagged nanoparticles. 110
Figure 25: An illustration of the chemical reactions involved in the formation of FITC and ocean blue-tagged nanoparticles. 111
Figure 26: Surface charge measurements of EC and MACE nanoparticles after surface functionalisation. 112
Figure 27: SEM images of the MCF-7 without and with 1 hour of nanoparticle incubation. 113

Figure 28: EDX analysis of EC and MACE nanoparticles on MCF-7 cells. 114
Figure 29: An illustration of the CellTiter-Glo assay principle. 115
Figure 30: Cell viability assay for both EC and MACE nanoparticles. 116
Figure 31: Co-incubation of EC nanoparticles with MCF-7 cells. 117
Figure 32: MCF-7 spheroids formed by the hanging drop method. 119
Figure 33: MCF-7 spheroids formed when adding EC nanoparticles to the floating cells pre-spheroid formation. 120
Figure 34: Roundness and solidity of spheroids. 120
Figure 35: 3D Cell viability assay for both EC and MACE nanoparticles. 121
Figure 36: Confocal images of 10 μm thick spheroids' cryosections. 122
Figure 37: The resulting spheroids after 6 hours of incubation with different concentrations of collagenase. 124
Figure 38: Nanoparticle penetration within collagenase-treated spheroids. 125
Figure 39: Schematic of the experimental setup. 133
Figure 40: MATLAB user interface. 134
Figure 41: A summary of the optoporation experiment workflow. 135
Figure 42: Representation of scanned areas by the laser. 136
Figure 43: Delivery of propidium iodide to laser–targeted cells. 138
Figure 44: pSi nanoparticles enhance the cell poration efficiency. 139
Figure 45: Short term viability assay at 30 μg/mL EC–nanoparticles and 65 mW. 141
Figure 46: Short term viability at different scanning speed with 65mW laser power. 142
Figure 47: A schematic of eGFP mRNA structure. 143
Figure 48: Influence of increasing eGFP mRNA concentration on transfection efficiency. 144
Figure 49: GFP expression in lipofectamine treated cells after 24 hours. 146
Figure 50: Loading of the mRNA into the pSi nanoparticles. 147
Figure 51: Visualisation of Cy5–tagged eGFP mRNA delivery in MCF–7 cells. 148
Figure 52: Optimisation of laser scanning area. 149
Figure 53: Impact of incubation time on nanoparticles' loading density. 151
Figure 54: Cell viability assay for EC–nanoparticles after different incubation times. 151
Figure 55: The effect of different incubation times on cell poration efficiency. 152
Figure 56: The effect of EC–nanoparticle concentration on cell poration efficiency. 154
Figure 57: The effect of scanning speed on the poration efficiency at 29 mW. 155
Figure 58: The effect of scanning speed on the poration efficiency at 65 mW. 156
Figure 59: Short term viability assay at 29 mW with 100 μg/mL EC–nanoparticles. 157
Figure 60: Short term viability at different scanning speed at 29 mW with 100 μg/mL. 158
Figure 61: ROS detection using DCFH–DA. 160
Figure 62: Caspase 3/7 detection. 161

Figure 63: GFP mRNA transfection using lipofectamine. 163
Figure 64: GFP mRNA transfection via optoporation at 35 mW and 100 µg/mL of EC nanoparticles. 164
Figure 65: GFP mRNA transfection via optoporation at 35 mW and 150 µg/mL of EC–nanoparticles. 165
Figure 66: GFP mRNA transfection via optoporation. 167
Figure 67: Interaction of EC–nanoparticles with spheroids. 168
Figure 68: Optoporation on spheroids with uniformly mixed EC–nanoparticles. 169
Figure 69: Optoporation on spheroids with EC nanoparticles at its periphery. 170
Figure 70: Optoporation on spheroids with EC nanoparticles at its periphery. 170
Figure 71: A schematic representation of reversible trans-cis isomerisation of azobenzene 176
Figure 72: A schematic representation of ICPES–azobenzene–lys pSi nanoparticle synthesis. 179
Figure 73: ^{1}H NMR of azobenzene-lys-diBoc (1). 180
Figure 74: ^{1}H NMR of ICPES–azobenzene–lys–diBoc (2). 180
Figure 75: FTIR spectra for pSi and ICPES-azobenzene-lys pSi. 182
Figure 76: SEM images of ICPES–azobenzene–lys pSi nanoparticles. 183
Figure 77: Cell viability assay for ICPES–azobenzene–lys pSi nanoparticles. 184
Figure 78: ROS detection using DCFH–DA. 185
Figure 79: Caspase 3/7 assay. 186
Figure 80: Gel retardation assay for eGFP mRNA complexation with ICPES-azobenzene-lys pSi nanoparticles. 187
Figure 81: GFP mRNA transfection via optoporation. 189
Figure 82: Controls for optoporation-mediated GFP mRNA delivery into MCF-7 spheroids. 191
Figure 83: GFP mRNA transfection via optoporation in MCF-7 spheroids. 192

Table of Tables

Table 1: Summary of the various delivery and transfection methods. 40
Table 2: Summary of direct optoporation. 48
Table 3: Summary of nanomaterial mediated optoporation 58
Table 4: Main peaks of interest from the ICPES–azobenzene–lys pSi nanoparticles FTIR. 182

Table of Acronyms

APTES	3-aminopropyltriethoxysilane
BET	Brunauer-Emmett-Teller
BJH	Barrett-Joyner-Halenda
Calcein-AM	Calcein- acetoxymethyl ester
DAPI	4',6-diamidino-2-phenylindole
DCFH-DA	2’7’–dichlorodihydrofluorescein diacetate
DLS	Dynamic light scattering
DMEM	Dulbecco's modified eagle medium
DMF	Dimethylformamide
DMSO	Dimethylsulfoxide
EC	Electrochemical etching
EDX	Energy-dispersive X-ray spectrometer
ELS	Electrophoretic light scattering
FITC	Fluorescein isothiocyanate
FTIR	Fourier transform infrared spectroscopy
HF	Hydrofluoric acid
HMDS	Hexamethyldisilazane
IAP	Inhibitory apoptotic protein
ICPES	Isocyanatopropyltriethoxysilane
IPA	Isopropanol
MACE	Metal assisted chemical etching
MCF-7	Michigan cancer foundation-7
Methocel	Methylcellulose
NIR	Near infrared
OB	Ocean blue
$^1O_2$	Singlet oxygen
PBS	Phosphate buffer saline
PDI	Polydispersity index
PDT	Photodynamic therapy
PFA	Paraformaldehyde
PS	Phosphatidylserines

pSi	Porous silicon
PTT	Photothermal therapy
ROS	Reactive oxygen species
TFA	Trifluoroacetic acid
SEM	Scanning electron microscope
VNBs	Vapour nanobubbles
WGA	Wheat germ agglutinin

Chapter 1 – Introduction

1.1 Single-cell Targeting

Cells perform intricate biochemical reactions that are precisely coordinated by the location of the cell and the timing of gene expression (Seo & Lee, 2022). For example, animal models have demonstrated that early embryonic development relies on signalling centres consisting of localised groups of cells that secrete or inhibit morphogens. The action of the morphogens is under spatiotemporal control to provide organisational cues and break the axial symmetry of the embryo. Current human pluripotent stem cell culture systems do not recreate such localised morphogen signalling. Instead, researchers typically supplement entire cultures with a set morphogen which has been seen to produce reproducible patterning of human embryonic stem cell colonies into radial zones expressing markers characteristic of the three germ layers (Warmflash et al., 2014). However, this approach leads to poor control over cell organisation. Alternatively, microfluidic approaches have provided morphogen gradients and achieved an in vivo-like axial arrangement of the germ layers (Manfrin et al., 2019). Despite the achievements of such a system, the cell culture models have been limited to 2D systems, yet 3D systems are essential to recapitulate the events occurring in vivo. In fact, a more recent study showed asymmetric differentiation of a human epiblast in a 3D Matrigel model (Simunovic et al., 2019). However, the poorly defined chemical composition of Matrigel presents complexity in defining the specific signals governing differentiation (Kozlowski et al., 2021). An opportunity exists to better mimic embryonic conditions through specific single-cell transfection within a cluster to induce an asymmetric expression of the selected morphogens.

Single-cell transfection techniques could offer a new approach to tightly regulate and understand the mechanisms driving mammalian development. The generation of such embryonic model systems would enable small molecule screening and also loss and gain-of-function studies to learn about the mechanisms driving mammalian development (Boroviak, 2022; Chow et al., 2016). In addition, transfection techniques enable specific suppression or expression of a gene which is useful in functional studies aimed at understanding the regulatory mechanisms occurring during a particular cellular process (Fus-Kujawa et al., 2021; Kim & Eberwine, 2010). For example, delivering the nucleic acid Malat1 siRNA suppressed the expression of Malat1 and accelerated the rate of myogenic differentiation, thus shedding light on myogenesis occurring at postnatal growth and on the muscle regeneration mechanisms after an injury (Chen et al., 2017). Similarly, nucleic acid delivery has also proven valuable in revealing new cancer biology insights into tumour heterogeneity dynamics (Zhao et al., 2018). A key approach for these studies involves engineering bottom-up cancer models that recreate cancer-linked events to determine gene function in tumour development. For instance, delivery of *Anln* siRNA demonstrated that inhibiting the expression of the cytoskeletal scaffolding protein anillin, suppressed cytokinesis. In turn, this reduced tumour initiation and growth without compromising the function of healthy liver tissues (Zhang et al., 2018). This suggests that inhibition of this protein could be an effective strategy to prevent hepatocellular carcinoma in patients suffering from liver damage (Zhang et al., 2018).

These studies rely on the introduction of foreign genetic material into the cells and though conceptually straightforward, efficient intracellular delivery faces multiple challenges. Among which, access to the cytosol requires overcoming the cell membrane which poses as a barrier to large hydrophilic molecules like nucleic acids (Nicolson, 2014). Additionally, there is interest at studying cells at the single-cell level because this provides detailed cellular characterisation which would otherwise be overlooked by bulk cellular analysis. Unlike the bulk, single-cell delivery techniques enable targeted genetic modification of individual cells while they are cultured within a population of untreated control cells. As a result, spatiotemporal nucleic acid delivery is needed to allow cargo delivery specifically to the cells of interest within heterogeneous and homogenous cell culture systems at the desired time point. Therefore, numerous techniques have been developed to surpass the cell membrane and deliver nucleic acids into a single-cell. However, most methods struggle to balance high throughput and selectivity. There is often a trade-off between high-throughput techniques that target large cell populations simultaneously but lack selectivity, versus low-throughput techniques with spatial and temporal control over the single-cell cargo delivery but reduced overall efficacy (Brooks et al., 2020, Shinde et al., 2021).

Broadly speaking, precisely manipulating cellular functions provides critical insights into disease mechanisms and enables progress in cell therapy and gene editing for regenerative medicine and fundamental biology research. The ideal delivery platform would facilitate spatiotemporal control over intracellular delivery at the single-cell level and possess the ability to target specific cells within a heterogeneous cellular environment. In addition, a technique would be beneficial if it possesses access to the cells that are both in a 2D culture environment or in a 3D organoid model to unravel complex tissue interactions in areas like tumourigenesis and early embryonic development. Such intricate control would allow the generation of enhanced genetic disease models that could accelerate diagnoses and therapeutic development (Katti et al., 2022).

1.2 Gene Delivery Techniques

Gene delivery strategies can be broadly grouped into viral (biological) or non-viral methods – including both chemical and physical strategies. In brief, viral mediated transduction utilises viruses such as retrovirus, adenovirus and adeno-associated virus as vectors to deliver the foreign biomolecules into cells. Similarly, a diverse range of non-viral chemical vectors loaded with the desired cargo can be internalised by the cell to ultimately release their cargo within the cytosol.

Several physical techniques have been developed to facilitate the delivery of cargo molecules into cells by creating transient pores in the cell membrane. Approaches such as electroporation, sonoporation, and optoporation utilise electric fields, ultrasound waves, and lasers respectively to induce pores that enable diffusion of extracellular cargo into the cell cytosol. Other physical approaches puncture the cell membrane through needles such as in the microinjection approach where a microneedle directly injects the cargo into a specific location within the cell. Similarly, in nanoneedles, the cells settle on the nanostructure that can penetrate the membrane to release their content into the cell cytosol. Alternatively, the tight interaction between the nanoneedles and the cell membrane promotes cargo uptake via endocytosis. Given that the cells tolerate micron-sized membrane disruptions, the delivery of virtually any large cargo dispersed in solution becomes feasible to be delivered into the cell through these physical techniques (McNeil & Kirchhausen, 2005).

As described in more detail below, each of these techniques has its strengths and limitations in their role in gene delivery. In the discussion, importance is given to the application of the technique in single-cell targeting and in providing spatiotemporal control over intracellular delivery.

1.2.1 Viral Vectors

Viruses have been used as vectors to efficiently transduce cells by exploiting viral infection pathways for cellular entry and nucleic acid delivery. The viral coding regions such as E1A genes in adenoviruses are removed to prevent uncontrolled viral replication inside the host cell that could lead to pathogenicity (Bulcha et al., 2021). This removed region can be replaced with the desired DNA sequence that needs to be delivered (Thomas et al., 2003). Once internalised, the delivered nucleic acid can integrate into the host genome or remain as an episomal vector (Stewart et al., 2018).

In vitro viral vector applications commonly aim to modulate the cell function by altering the expression of a specific gene product. This approach holds great interest in neuroscience for mapping neuronal circuits and investigating treatments for neurological diseases (Haggerty et al., 2020). For example, protein misfolding and aggregation are linked to neurodegenerative diseases such as amyotrophic lateral sclerosis (ALS). In fact, genetic screening revealed that serine-rich chaperone protein1 (SRCP1) could play a role in reducing protein aggregation. Therefore, lentivirus expressing SRCP1 infected cell cultures and mouse models to monitor its impact on insoluble protein levels and identify its potential as a therapeutic option for ALS (Luecke et al., 2023). This example demonstrates the utility of viral vectors to determine gene and protein function in disease models.

Viral vectors have typically shown high transduction efficiencies with high specificity by altering the receptor on the surface of the viral vector. Yet, their broader application is limited by several weaknesses. One of their major downfalls is the safety concerns arising from potential insertional mutagenesis by randomly integrating the nucleic acid into the host genome, potentially activating oncogenes or disrupting essential genes (Wang et al., 2021). In addition, the nucleotide packaging capacity of viral vectors is limited, for instance, adeno-associated viruses can typically accommodate only up to 5 - 7.5 kb, thus restricting the cargo that can be delivered (Puhl et al., 2019). In order to overcome this size limitation, delivery of the encoding components of the CRISPR/Cas system ranging from 9-19 kb involves a dual viral delivery method however this approach requires a high viral dose, raising safety concerns (Søndergaard et al., 2020). Adenovirus vectors on the other hand can carry much larger CRISPR cargo but are also limited by their immunogenicity (Mengstie, 2022). Additionally, viral vector production can be labour-intensive and technically challenging. Such substantial limitations with viral vectors continue to drive forward the development of non-viral carriers alternatives.

Viral vectors are unsuitable for the scope of this project because internalisation depends on virus-receptor interactions (Maginnis, 2018). Consequently, viral delivery only enables transduction of the bulk and lacks single-cell specificity within a heterogenous cellular population.

1.2.2 Carrier Mediated Delivery

Carrier-mediated strategies involve encapsulating the desired cargo within a nanocarrier that can interact with the cell membrane, gain entry into cells through endocytosis pathways and then release the cargo inside the cytoplasm (Durymanov & Reineke, 2018; Houthaeve et al., 2022). The specific endocytic pathway exploited depends on both the cell type as well as the size, shape, surface chemistry and other physical properties of the nanocarrier (Lai & Wong, 2018). In general, cationic polymers and liposomes have been extensively developed from the other carrier-mediated vesicles for gene delivery (Pack et al., 2005). These cationic vesicles possess numerous positively charged functional groups on their surface allowing for electrostatic attraction of the negatively charged nucleic acids (Pack et al., 2005). Additionally, the positive surface charge facilitates interaction with the negatively charged cellular membrane to initiate endocytosis (Park et al., 2014). The ionisable nature of the lipid excipients is key, as they become protonated in the acidic endosomal environment triggering destabilisation of the endosomal membrane and facilitating the cytoplasmic release of the mRNA cargo (He et al., 2022).

Liposomes in particular, have emerged as nanocarriers for anti-tumour applications, offering improved therapeutic efficacy, reduced toxicity with the ability to selectively target tumours (Wang, et al., 2021). Researchers have developed "actively-targeted" liposomes by decorating the surface with monoclonal or engineered antibodies. These targeting antibodies are designed to bind to specific antigens overexpressed on the surface of cancer cells, enabling the selective delivery of the liposomal cargo (Sawant & Torchilin, 2012). An example of this is the targeting of the human epidermal growth factor receptor (HER2), which is overexpressed in 20-30% of breast cancers and associated with a poorer prognosis. Conjugating liposomes with anti-HER2 antibodies can facilitate the specific accumulation of the drug payload within HER2-positive breast tumour cells leading to 69% of cell death (Myat et al., 2024).

Apart from anti-tumour purposes, liposomes and lipid technologies have demonstrated significant advantages in the delivery of biological drugs such as proteins, peptides, and nucleic acids. These carrier systems can enhance the stability, cellular uptake, and bioavailability of these sensitive molecules (Fang & Chen, 2022). Some examples of recently marketed liposomal and LNP-based biological drugs include the mRNA-based COVID-19 vaccines developed by Moderna and Pfizer-BioNTech. These vaccines utilize lipid nanoparticle delivery platforms to encapsulate the mRNA encoding the SARS-CoV-2 spike protein. After injection, the mRNA is efficiently delivered into the host cell cytoplasm, where the cationic lipid component plays a critical role in promoting endosomal escape (Buschmann et al., 2021; Pascolo, 2021). This allows the mRNA to be translated, producing the viral antigen and stimulating the desired immune response. Beyond these two approved mRNA vaccines, other lipid-formulated mRNA vaccine candidates are currently undergoing clinical trials (He et al., 2022).

The application of carrier-mediated delivery systems in 3D cellular models has recently emerged but with limited success thus far. For example, cationic polymers failed to transfect GFP into A549 multicellular tumour spheroid (Paris et al., 2020). This is likely attributed to inadequate penetration in the 3D structure. Similarly, cationic liposomes were shown to only permeate approximately 60 μm deep from the spheroid surface (Koloskova et al., 2018). Meanwhile, another study obtained transfection efficacy in HEK293 spheroids using an alternative cationic nanocarrier that appeared to mediate delivery deep into the 3D structure. However, the expression and penetration depth was not quantitatively characterised (Lv et al., 2015).

Ultimately, while showing initial promise for 3D applications, current carrier-mediated delivery has been predominantly limited to bulk 2D cell populations which has mostly been developed for in vivo delivery (Brooks et al., 2020). Furthermore, this technique is not suitable for the scope of this project because any delivery facilitated by carrier-mediated technique lacks spatiotemporal control.

1.2.3 Microinjection

Microinjection was the first intracellular delivery technique with the capability to introduce virtually any cargo directly into the individual cells and is therefore a powerful tool for single-cell studies. Simply put, a needle with less than 5 µm in diameter can penetrate the cellular barriers, namely the cell surface membrane and nuclear membrane to precisely inject the foreign cargo into the cell. The cargo is delivered in controlled quantities to a wide range of cell types and can also be delivered at specific timing thus offering spatial and temporal control (Duckert et al., 2021; Taverna et al., 2012).

Significant strengths of microinjection include precise quantitative control of the genetic modification substance into the single-cell. This principle was demonstrated through a proof of concept by the delivery of synthetic modified mRNA and a plasmid cocktail to human foreskin fibroblast (Chow et al., 2016). The results not only showed that multiple substances can be microinjected into single-cells but also that the amount of substance delivered could affect the quantity of protein synthesised in the cell. Such a technique can be applied to study cell responses to different dosages of exogenous DNA or RNA (Chow et al., 2016). This feature is particularly important in nuclease-based therapeutic strategies because delivering a high concentration of nucleases can lead to high cell death due to cytotoxicity, but an insufficient amount would not lead to knock-in mutations. Indeed, knock-in efficiencies in mouse zygotes to generate genetically modified mice were dependent on the injection of CRISPR/Cas9 mRNA concentration (Raveux et al., 2017).

Like any other technique, microinjection has certain limitations. One of the greatest limitations of microinjection is its low throughput because cells are transfected individually rendering the technique as very time consuming. In addition a highly skilled operator is needed to carry out the transfection which makes this technique labour intensive. As a result the transfection rate of microinjection is low, with only a few hundreds of cells that can be injected among thousands of cells. To increase the rate of microinjection, microfluidic devices, semiautomated and fully automated systems have been introduced with the scope of increasing the efficiency and transfecting more cells in a shorter period. In a semi-automated system, the microneedle is calibrated once for penetration into adherent cells that exist in a monolayer. A technician uses a joystick to move the microneedle to an non-transfected cell and lowers the microneedle to inject the cargo (Viigipuu & Pasi, 2004; Wang et al., 2008). Recent developments have also provided a fully automated robotic system, where the coordinates of the well are defined and then the system identifies the location of the cells followed by microinjection. These systems have increased the transfection rate, however, constant monitoring is still required to maintain the same focal plane and identify any clogging of the needle (Muthaiyan, 2016; Shull et al., 2019).

Furthermore, a microfluidic system was based on the microinjection approach, creating a high-throughput single-cell injection system. Cells in suspension moving through the channels were drawn onto a 0.5 µm diameter hollow-tip glass needle embedded in PDMS. A picolitre-jet carrying the macromolecules of interest then penetrated the immobilised cell (**Figure 1**). After injection, flow reversal dislodged the cell from the needle and the cell were collected. By leveraging microfluidic technology, this system enabled a rapid approach that automatically injected 3600 cells per hour (Adamo & Jensen, 2008). However, the limitation lies in the frequent cell clogging from biological debris which hinders consistency in the delivery technique (Adamo et al., 2013). In addition, these higher throughput techniques have mostly been explored in 2D cell culture systems both for adherent and suspension cells. Selecting cells within the 3D system remains mainly a manual approach with the limitations described above.

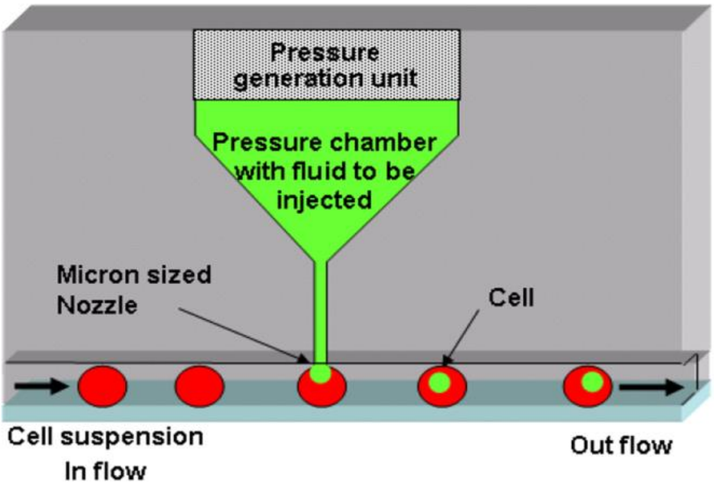

Figure 1: A schematic of the microfluidic system with a jet injector. Cells in suspension flow through the channels, are drawn up through the nozzle and a miniaturised jet is fired to inject the cells. Figure reproduced from Adamo et al., Copyright © 2013, with permission from the IOP (Adamo et al., 2013).

1.2.4 Nanoneedles

Nanoneedles are an arrangement of vertical high-aspect ratio nanostructures that protrude from a surface to form a tight junction with the cell membrane enabling access to the cell cytosol for intracellular delivery (Chiappini et al., 2015). The platform has the capacity to interact with a large number of cells at a time, enabling for high throughput intracellular delivery. Nanoneedles have also been used to deliver a wide range of cargo to a diverse range of cell types, including adherent, non-adherent and hard-to-transfect cells (Elnathan et al., 2022).

One type of the nanoneedle is the solid nanowire that spontaneously penetrate the cell membrane to grant direct access to the cytosol when cells are placed on top of the nanowires. Using silicon nanowires, Shalek et al. demonstrated over 95% delivery of DNA, RNA, peptides, proteins and other small molecules to primary cell types and immortalised cell line (Shalek et al., 2010). Diamond nanoneedles array of 5 μm in height and a diameter of ~300 nm reprogrammed pluripotent stem cells with 1.17% efficiency. Despite the low efficiency of the diamond nanoneedles, this is still 2 orders of magnitude higher than the transfection efficiency achieved with electroporation (Yuan et al., 2020). Another type of nanoneedles are the biodegradable porous silicon nanoneedles that disintegrate over time providing a temporary interface with the cells. These nanoneedles also achieved a high transfection efficiency of DNA plasmid and siRNA of over 90% in HeLa cells (Chiappini, et al., 2015).

Alternatively, cells have been cultured on hollow nanostraw arrays containing a lumen through which cargo molecules flow via fluid transport to transfect the overlaid cells. The Melosh group used alumina nanostraws with direct fluidic access to the cytosol and successfully delivered GFP plasmids. However transfection efficiency in both HeLa and CHO cells was low, only reaching up to 10% (Vandersarl et al., 2012). Similarly, carbon nanotubes arrays integrated with a microfluidic device reported plasmid DNA delivery with 84% efficiency in the HEK293 cell line (Golshadi et al., 2016).

Despite the high efficiency, nanoneedle fabrication is a complex and labour-intensive multi-step process. Additionally, transfection efficiency is heavily dependent on the fine tuning of the nanoneedle height, diameters and densities with varying effects on different cell types (Elnathan et al., 2015). More importantly, nanoneedles lack the capacity to target single-cells or enable precise spatiotemporal control over intracellular delivery unless integrated with the electroporation or optoporation techniques. These techniques are described in more detail in section 1.2.5 Electroporation and 1.2.7 Optoporation respectively. Lastly, the flat surface restricts the application to 2D cell culture system or tissues and thus far there is no evidence on its suitability in delivering nucleic acid to 3D multicellular spheroid models.

1.2.5 Electroporation

Electroporation is a delivery technique that leverages pulsed applied potentials to permeate cellular membranes for the delivery of exogenous substances (Tsong, 1991). The application of a trans-membrane potential causes strong polarisation of the cell surface membrane, which induces an enhanced membrane permeability by the creation of temporary hydrophilic nanopores (Dong & Chang, 2021). Consequently, biomolecules are able to transit across the membrane via diffusion (along a concentration gradient) or electrophoretic (along a potential gradient) transport (Stewart et al., 2018). The delivery of molecules can be targeted towards cellular structures in the bulk, as well as hybridised with additional techniques to offer delivery at the single-cell level.

Bulk Electroporation

In conventional bulk electroporation, cells are suspended in a conductive buffer solution containing the desired cargo and are then placed between two electrodes (Chang et al., 2016) (**Figure 2a**). While this simple technique can deliver various cargo to many cell types (Liu et al., 2022) including hard-to-transfect cells (Hashemi et al., 2012), it is limited by the low cellular viability.

A key challenge for electroporation is balancing the parameters needed to permeabilise cell membrane while minimising damage and death to the cells. Conditions that induce cell and nuclear membrane permeabilisation require pulse strengths of around 1 kV/cm and micro- to milli-second pulse lengths (Liu et al., 2022). However, the high voltages needed to generate such strong electric fields across millimetre-scale electrode gaps result in increased cell death (Caprettini et al., 2017). Moreover, the applied voltage also generates a high electric current that trigger a temperature increase of the solution (referred to as Joule heating) that can reach up to 20 °C (Kar et al., 2018). This increase in temperature is not only harmful to the cells (Weaver et al., 2012) but could also damage the cargo of interest (Shokouhi et al., 2020). The distance between the two electrodes causes nonuniform distribution of the electric field between the two electrodes. As a result, those cells in close proximity to the electrode experience excessive electric field causing irreversible damage and eventually leading to cell death. To the contrary those cells further away from the electrodes have insufficient transmembrane potential and will not be permeabilised (Dong & Chang, 2021). In addition, the random cell distribution between the two electrodes leads to heterogenous cargo delivery with cells facing the positive electrode undergoing more stress and pore formation due to the negative resting potential of the cell (Shi et al., 2018).

Single-cell Electroporation

The miniaturisation of the electroporation device is based on the same principles as the bulk electroporation but scaled down to allow for permeation at the single-cell level (Kar et al., 2018). These electroporation devices are created by integrating nanotechnology and microfluidic fabrication which reduce the distance between the electrodes for electroporation to occur at lower voltages and improve the viability of the cells (Geng et al., 2010). In addition, the smaller electrodes only electroporate specific regions within the cells, preventing excessive damage to the membrane (Duckert et al., 2021).

The three single-cell miniaturised electroporation devices discussed here are selected based on their throughput, selectivity and application. These being nanostraw-based, nanochannel-based and microfluidic-flow electroporation devices.

Nanochannel-based Devices

In an attempt to address the shortcomings of microscale electroporation, Lee’s group pioneered the introduction of a nanochannel electroporation (NEP) approach aimed at achieving intracellular delivery at the single-cell level (Boukany et al., 2011). The device comprised of two microchannels connected by a nanochannel with ~90 nm aperture. One microchannel contained the cell to be transfected and the other microchannel contained the transfection agent (**Figure 2b**). An intense electric field was created at the nanochannel causing a localised disruption on a very small region within the cell surface membrane, minimising damage to the cell. In fact, as a proof of principle propidium iodide, mRNA and plasmid expressing GFP were all delivered to single-cells (Boukany et al., 2011).

A major limitation of this method is the slow and low throughput of individually placing the cells into one of the microchannels by using optical tweezers (Zhao et al., 2015). For this shortcoming, the same group designed a micro-cap array for the microchannel to trap the cells when this is dipped in solution, therefore eliminating the use of optical tweezers. As a result, numerous cells were trapped in the platform meaning that multiple individual cells could be electroporated at the same time (Chang et al., 2016). Additionally, modifications in the number of pulses and duration provided dosage control of the transfection agent (Dong & Chang, 2021). Through this design, a titration study was also possible to investigate the dose effect of microRNAs in cardiomyocytes and identify a threshold-dose that cause the disorder of the mitochondrial homeostasis in miR-29 based gene therapy (Chang et al., 2016).

Overall, this method enables high throughput, single-cell gene analysis designed to target individual isolated cells but lacks spatial control for delivery to single-cells within a cluster.

Microfluidic flow-through Electroporation

Microfluidic flow-through electroporation utilises microchannels embedded with electrodes to electroporate cells in suspension as they continuously flow through the microchannels in the solution containing the cargo. The cells are then permeabilised as they pass through an applied electric potential within the channels (Wang & Lu, 2006), (**Figure 2c**).

This approach offers greater viability over the bulk poration while maintaining a high throughput, mostly because of the continuous flowing solution which helps mitigate the negative effect of Joule heating. For example, Geng et al. reported a microfluidic design with a high continuous flow rate of up to 20 mL/min, transfecting 10^4 – 10^8 cells per minute. Using CHO cells, they achieved ~75% plasmid transfection efficiency with ~60% cell viability (Geng et al., 2010). A similar set-up demonstrated comparable transfection efficiencies and viabilities across several cell lines (Bhattacharjee et al., 2016). An added benefit of this design is the reduction in cost by replacing a pulse generator with a constant voltage. The design involved passing cells through a series of wide and narrow microchannels where the cells only experience a strong electrical field when passing through the narrow constriction. Therefore constant voltage can be applied while creating a pulse-like electrical field effect at a lower cost (Geng et al., 2010).

The high throughput of inflow electrophoresis makes it a promising tool for manufacturing CAR-T cell therapies by delivering consistent mRNA into primary human T cells with minimum impact on cell viability (Lissandrello et al., 2020). In fact, this approach is currently being explored in clinical trials for mRNA engineered CAR-T cells (NCT03608618). However, the application of this approach is limited in some other in vitro areas. Particularly the microfluidic-flow through electroporation relies on cells in suspension, making it an unsuitable application for sensitive adherent cell lines. Additionally, microfluidic approaches like this also suffer from potential clogging of the microchannels, leading to inconsistent delivery (Brooks et al., 2020).

Nanostraw-based Electroporation

Nanostraws for electroporation are wide hollow nanostructures with a high aspect ratio, typically made of alumina or otherwise coated with a conductive material such as gold (Caprettini et al., 2017) (**Figure 2di-iii**). The electric field applied acts as a valve that transiently opens the membrane at the nanostraw tip allowing for biomolecules to flow from the microfluidic channel into the target cell through the lumen of the nanostraw structure (Schmiderer et al., 2020).

The integration of nanostraw with electroporation provide precise spatial and temporal control over cargo delivery and also allows for repeated delivery to the same cell. Cao et al. provided intricate control over the delivered dosage by adjusting the applied voltage, the reagent concentration and the delivery duration. In this manner, biomolecule cargo such as mRNA, DNA and proteins have been efficiently delivered into hard-to-transfect primary cell types like neurons, stem cells and cardiomyocytes (Cao et al., 2018). In addition, the cells remain adhered to the nanostructure for days permitting for the delivery of plasmids to the same cell at different time intervals (Xie et al., 2013). In fact 74% of the CHO cells expressed the two plasmids delivered a day apart. Such sequential control is important for experiments requiring periodic transfection or knocking down previously expressed genes before subsequent transfection.

A combination of the nanostraw with electroporation achieved results which were previously unattainable when using the two standalone systems. In fact, nanostraws on their own did not access the cytosol of non-adherent primary cells while bulk electroporation impacted the differential expression of more than 2,000 genes (Schmiderer et al., 2020) leaving a negative impact on the cellular viability. On the other hand, nanostraw-based electroporation showed >70% delivery of nucleic acids in human primary stem cells (Tay & Melosh, 2019). Similarly direct comparison between viral, bulk electroporation and nanostraw-based electroporation revealed that nanostraw electroporation had minimal disruption to cellular division. Furthermore, nanostraw electroporation exhibited the lowest calcium ion concentration, which is associated with cellular stress (Tay & Melosh, 2019).

In summary, the nanostraw electroporation system provides excellent spatiotemporal control over delivery, dose control and high transfection yields. However there are some limitations. This platform is only suitable for the delivery of cargo in a 2D layer of cells as its application is limited for delivery into 3D cell systems. Moreover, nanostraw fabrication involves atomic layer deposition which is an expensive and time consuming technique limiting the scalability of this approach (Wen et al., 2019). Additionally, the nanostructure-based devices face manufacturing and fragility challenges which is made more complex when compounded with the electroporation system. Lastly, while biocompatibility is demonstrated, the voltages used still approach water electrolysis potentials (~1.23 V) that can generate harmful reactive oxygen species (Chen et al., 2020).

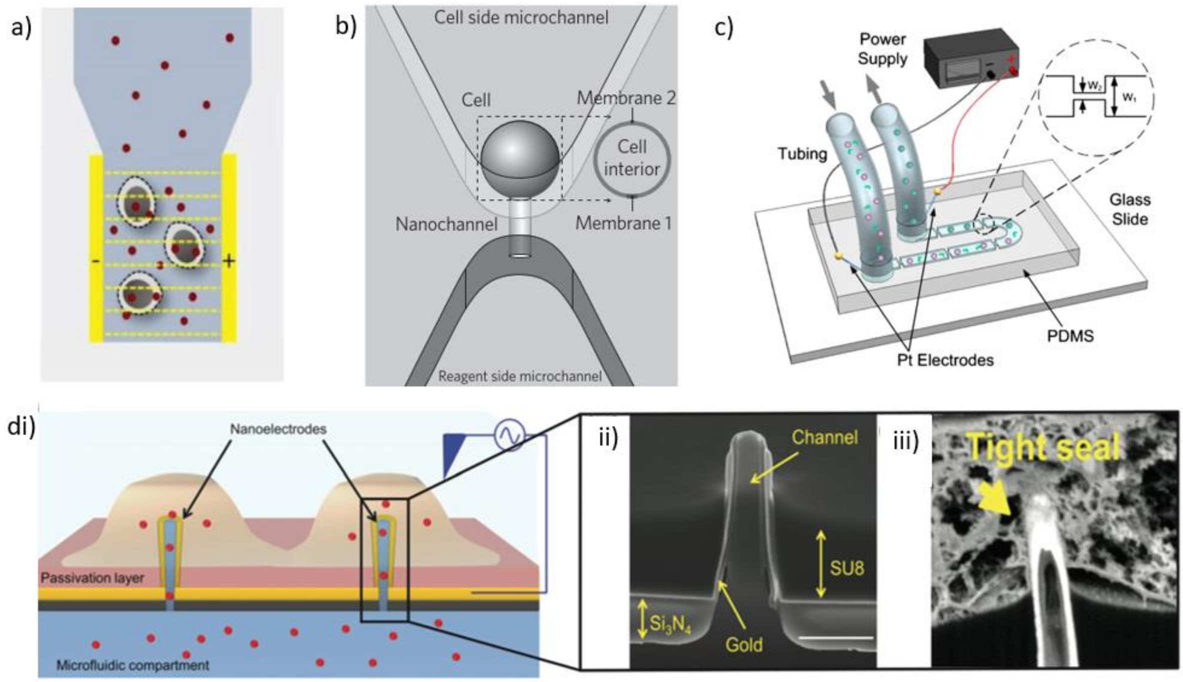

Figure 2: An overview of the different electroporation devices discussed. A schematics of electroporation in the bulk population. Figure reproduced from Hur et al., Copyright © 2021, with permission form Wiley-VCH (Hur & Chung, 2021). b) A schematic of the nanochannel-based device consisting of two microchannels connect with a nanochannel. The cell is on one side of the microchannel next to the nanochannel and the solution containing the cargo is contained in the other microchannel. Figure reproduced from Boukany et al., Copyright © 2011, with permission form Springer Nature (Boukany et al., 2011). c) A schematic of the microfluidic flow-through device highlighting the narrow channels where electroporation occur as the cells flow through the chip. Figure reproduced from Geng et al., Copyright © 2010, with permission form Springer Nature (Geng et al., 2010). di) A schematic of the protruding hollow nanotubes into the cells, ii) SEM image of a cross section of a single hollow nanotube coated with a gold layer for conductivity and iii) SEM image of interface between the nanotubes and the cell membrane forming a tight seal. Figure reproduced from Shokouhi et al., Copyright © 2020, with permission from RSC Publication (Shokouhi et al., 2020).

1.2.6 Sonoporation

Sonoporation is a physical technique that utilises ultrasound waves to produce microbubbles which subsequently collapse to permeabilise the cell membrane. The burst bubble creates a void in which the surrounding medium rushes to fill, forming a jet and shockwaves that punctures the membrane (Delalande et al., 2013; Lentacker et al., 2014). Careful control of ultrasound acoustic pressure, pulse duration and number of pulses modulates the size of the bubbles and hence regulates the degree of permeabilisation (Fan et al., 2013). In fact, applying long pulse of 10 ms resulted in cell death due to bubble coalescing and creating large pores within the cell membrane while shorter 8 μs pulses achieved viable GFP plasmid delivery of ~7%. This result was on par with transfection efficiency obtained with lipofection (Fan et al., 2013).

Various cargo have been delivered into the cells using sonoporation, however this technique suffers from low cell viability. A meta-analysis study has shown that molecular delivery efficiency and post-sonoporation viability in vitro frequently remain below 50% (Liu et al., 2012). Recent examples have shown only marginal improvements in cell viability. For instance, dextran and GFP plasmid delivery via microbubbles had a cardiac cell viability of ~60% post-sonoporation (Bhutto et al., 2018). Similarly delivery of siRNA in vitro to murine and human T cells successfully achieved ~60% transfection efficiency with a viability of ~60% (Karki et al., 2019). This drop in cell viability when compared to the controls stems from the heterogenous and uncontrolled membrane disruption inherent in microbubble cavitation dynamics. As a result, some cells experience violent cavitation leading to excessive damage while others remain unaffected (Liu et al., 2016).

While traditionally sonoporation is a bulk delivery technique, efforts have emerged to study sonoporation dynamics and pore kinetics formation at the single-cell level (Rich et al., 2022). For example, one strategy utilises femtosecond laser pulses to generate isolated microbubbles that were guided with ultrasound pulses to a desired distance from the membrane of a Xenopus oocyte (Zhou et al., 2012). The results demonstrate that membrane disruption only occurred when the bubbles collapsed near the cell membrane. However, even at the same impact distance, longer ultrasound pulses led to a variation in the pore sizes, suggesting that bubble behaviour is altered under these conditions (Zhou et al., 2012). Recently, systems integrating arrays of transducers have enabled trapping and generation of single microbubbles which collapse to induce sonoporation of targeted cells. Using this platform, propidium iodide delivery exceeding 80% efficiency was obtained while maintaining cell viability above 90% (Meng et al., 2014). This highlights that controlling the position of the microbubble with respect to the cell membrane can result in higher delivery efficiency and viability compared to what is currently achieved with bulk sonoporation methods.

In conclusion, although research has demonstrated the possibility of single-cell manipulation, the intricate coordination of the cavitation control with precise bubble guidance is a complex and a challenging process. Consequently, these spatiotemporal approaches are useful to enhance our understanding of the sonication process, aiming to optimise delivery efficiency and viability. However, bulk sonoporation remains the approach employed for intracellular delivery investigation for cellular function studies.

1.2.7 Optoporation

In optoporation (also referred to as photoporation) the cell membrane is disrupted by a focused high-intensity monochromatic light pulse (Tsampoula et al., 2007). As a result, transient pores are generated through which the impermeable exogenous molecules in the surrounding cell medium can diffuse to access the cell (Kim & Eberwine, 2010).

Optoporation techniques can be broadly categorised as either 'direct optoporation' where the laser is focused on the membrane or 'indirect optoporation' which utilises laser-sensitive nanomaterials to enhance throughput and efficiency (**Figure 3**) (Xiong et al., 2016). Both the direct and indirect optoporation provide intracellular delivery under temporal and spatial control (Mashel et al., 2020; Stevenson et al., 2010). For example, considering the indirect method, gold plasmonic nanotubes connected with a microfluidic channel could control the delivery of cargo into the selected cells once irradiated with the laser. The laser pulses directed at specific nanotubes resulted in transient openings of the cell membrane enabling molecule to flow through from the microfluidic channel through the nanotube into the cell (Messina et al., 2015). The spatiotemporal control for both the direct and indirect set-ups is discussed in more detail in section 1.7 Direct Optoporation and 1.8 Indirect Optoporation.

The optoporation technique offers advantages such as compatibility with most microscopy setups and adaptability for both adherent and suspended cells. For example, HeLa adherent cells transfected with GFP plasmid in the presence of nanoparticles achieved a transfection efficiency and viability of more than 90% (Vanzha et al., 2017). Raes et al. show that the same optoporation set-up was suitable for transfection in both adherent and non-adherent cells. In this example, mRNA was successfully transfected into HeLa cells with 38% transfection efficiency and with 45% in Jurkat T cells (Raes et al., 2020).

A significant challenge for optoporation lies in the absence of standardised methodology and researchers often rely on published data as a guide for initiating optimisation procedures based on the specific equipment and setup in place (Antkowiak et al., 2013; Soman et al., 2011). Therefore to ensure optimal transfection efficiency, multiple parameters need to be fine-tuned for the different cell lines. In fact, a meta-analysis (Hosseinpour & Walsh, 2021) demonstrated that the reported transfection efficiency rates for a titanium-sapphire 800 nm laser ranged from 0.3% (Tsukakoshi et al., 1984) to 182% (counting the proliferation of transfected cells) (Praveen et al., 2011). Such a wide-ranging disparity underscores the necessity for optimising the optical setup and also to standardise the way in which transfection efficiency is reported (Hosseinpour & Walsh, 2021).

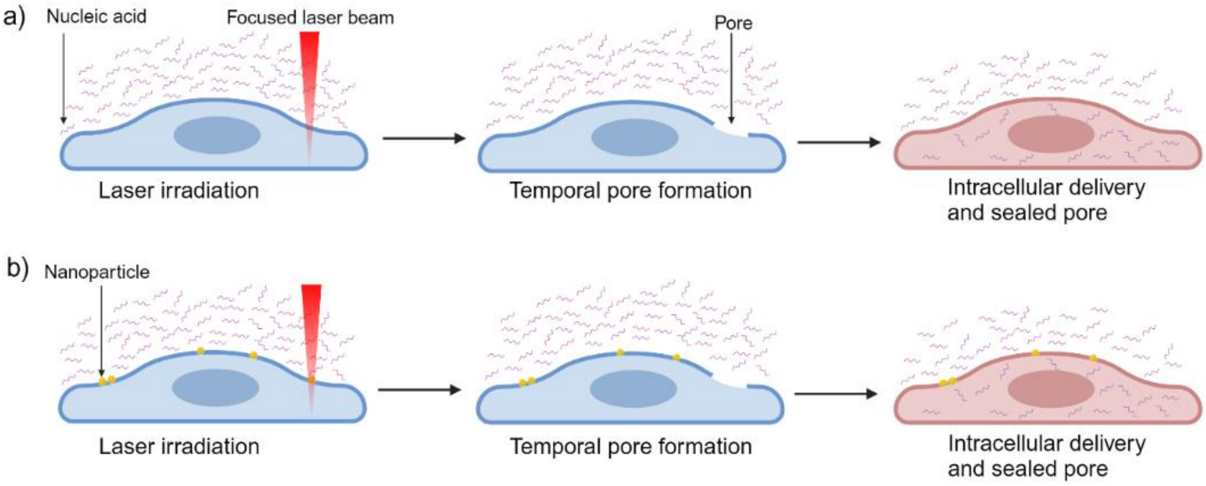

Figure 3: Membrane pore formation through direct and indirect optoporation.Direct laser-induced optoporation involves focusing the laser beam precisely on the cell membrane. b) Indirect (nanoparticles mediated) optoporation involves focusing the laser beam either directly on the nanoparticle or using a broad laser beam to interact with the nanoparticles in solution leading to membrane pore formation. Created with BioRender.com

1.3 Cell Membrane Repair

The success of physical delivery techniques that disrupt the cell membrane, relies on the cell's ability to rapidly detect and repair transient membrane porations. However, the mechanical tension created by the plasma membrane's adhesion to the cytoskeleton and extracellular matrix can impede the membrane's ability to self-seal after disruption (Blazek et al., 2015). Consequently, cellular repair pathways that reduce this membrane tension tend to promote more effective resealing. One such mechanism involves the targeted reorganization of the actin cytoskeleton, facilitated by actin-depolymerising enzymes. This dynamic disassembly of the actin network has been shown to significantly enhance the capacity of the cell for effective membrane repair (Abreu-Blanco et al., 2014; Miyake et al., 2001). Cells could also employ a vesicle fusion based mechanism including key proteins like synaptotagmins and SNARE receptors (Barisch et al., 2023). This triggers the targeted fusion of intracellular vesicles with the damaged membrane, allowing the incorporation of additional membrane material to fill the gap and relieve tension in the surrounding area (Blazek et al., 2015). Upon completing membrane repair a process that may extend over a few minutes to hours (Moe et al., 2015), the cell seeks to retain homeostasis of its intracellular component. This is a crucial phase that determines whether the cell will return to its original state before disruption, will perform the induced alterations or whether it will follow programmed cell death (Stewart et al., 2018).

Disruption of the cell membrane results in an instantaneous uncontrolled exchange of molecules between the inside of the cell and its surrounding environment (Bischofberger et al., 2012). One of the most critical molecules involved in the cellular response to plasma membrane is the influx of calcium ions (Cooper & Mcneil, 2015; McNeil & Kirchhausen, 2005). As an integral secondary messenger, calcium ions regulate numerous signalling pathways and depending on the fluctuations of calcium levels in the cell, calcium can facilitate membrane repair processes or trigger cell death (He et al., 2022). In fact, research has shown that in laser permeabilised cells devoid of calcium ions, necrosis was enhanced to 80% in HeLa cells (Jimenez et al., 2014). Similarly, in the presence of chelating agents capturing calcium ions, the damaged membrane failed to reseal. This was visualised using an impermeable dye (FM1-43) which continued entering the cytosol through the breached membrane (Bouter et al., 2011). To the contrary, in the presence of calcium ions, cytosolic proteins like annexin bind to the negatively charged phospholipid head groups of the membrane in a calcium-mediated process. The rapid accumulation of annexins at the site of membrane damage forms a 2D plug along the membrane ridge and prevents rupture expansion (Bouter et al., 2011). Additionally, the calcium-activated protease calpain has also been identified as a critical component in membrane repair, as disruption of calpain function prevented successful membrane resealing following laser-induced damage (Mellgren 2007). However, exceeding a calcium concentration threshold of 10 μM had a deleterious effect that impeded cellular repair (Babiychuk et al., 2009; Draeger et al., 2014). Such high concentrations hampered mitochondrial function (Braun et al., 2007) and activated proteases such as calpains that degraded intracellular components and activated apoptotic pathways (Bischofberger et al., 2012). Therefore, calcium acts like a double-edged sword. At moderate levels it initiates membrane repair pathways but in excess triggers cell death. Reflecting this, calcium concentration is often titrated down from 1 mM to ~5 – 20 μM in buffer solutions (Draeger et al., 2011; Potez et al., 2011).

Electroporation (Ruzgys et al., 2019) and optoporation (Minai et al., 2013) techniques can induce oxidative stress that hinders plasma membrane repairing process by causing lipid peroxidation (De La Haba et al., 2013). A study utilising femtosecond laser permeabilisation showed that reactive oxygen species (ROS) significantly prolonged the resealing time to 300 s compared to 100 seconds for the non-ROS exposed controls (Duan et al., 2015). Supplementing cells with antioxidants has shown promise in facilitating recovery of the membrane disruption under oxidative conditions. For example, myocytes exposed to oxidative stress displayed enhance membrane repair when supplemented with vitamin E or with vitamin C (Howard et al., 2011). Without the vitamins, these cells failed to repair the membrane in oxidatively-stressed environments (Howard et al., 2011). Therefore, antioxidant treatment may help mitigate in optoporation processes to inhibit the negative impact of ROS on membrane resealing processes.

Successfully restoring structural membrane integrity does not guarantee functional rescue as the initial permeabilisation events can also trigger secondary stress pathways in the cell. If a critical threshold is exceeded, regulated cell death programs like apoptosis and necrosis may be activated, even after fully structural restoration of membrane integrity. Therefore, despite successful early membrane restoration, the irreversible disturbance of cellular homeostasis can still elicit delayed cell death. In fact, it was demonstrated that while 50% of the dead cells post-electroporation was attributed to immediate necrosis, the other half stemmed from apoptosis detected as early as 3 hours after the electroporation process (Piñero et al., 1997).

The specific mechanisms employed for cell repair can vary considerably based on the nature of the damage (Barisch et al., 2023). Therefore, understanding perforation response pathways and the endogenous molecular participants in cellular membrane resealing process is key to preserve cellular viability and improve outcomes. This knowledge allows modification of environmental conditions to mitigate immediate damage as well as the secondary effects, thereby increasing the chances of successful delivery. Acute viability post permeabilisation can be quickly assessed via ROS and apoptosis assays. However, longer-term functional assessments after allowing cells a suitable recovery period are equally crucial for evaluating cellular survival and preserved functionality, thereby evaluating the efficacy of the delivery techniques.

1.4 Summary

A desired technique for the scope of this project is one that achieves intracellular delivery under precise spatiotemporal control into individual cells within a population, without impacting the surrounding cells. Viral vectors, carrier-mediated, nanoneedle and sonoporation techniques have all demonstrated their suitability for bulk intracellular delivery but their application for single-cell studies remain limited. Those techniques that show single-cell delivery such as electroporation does not provide delivery to specific cells within the bulk while microinjection is labour-intensive resulting into low throughput.

In contrast, optoporation is a non-contact approach that combines high-precision spatiotemporal control, with high throughput by utilising laser-sensitive nanoparticles. This enables efficient delivery while maintaining high cell viability. Optoporation is detailed further below to better understand the current capabilities and limitation of this technique for targeted intracellular delivery.

The discussed transduction and transfection methods are summarised in **Figure 4** and **Table 1**.

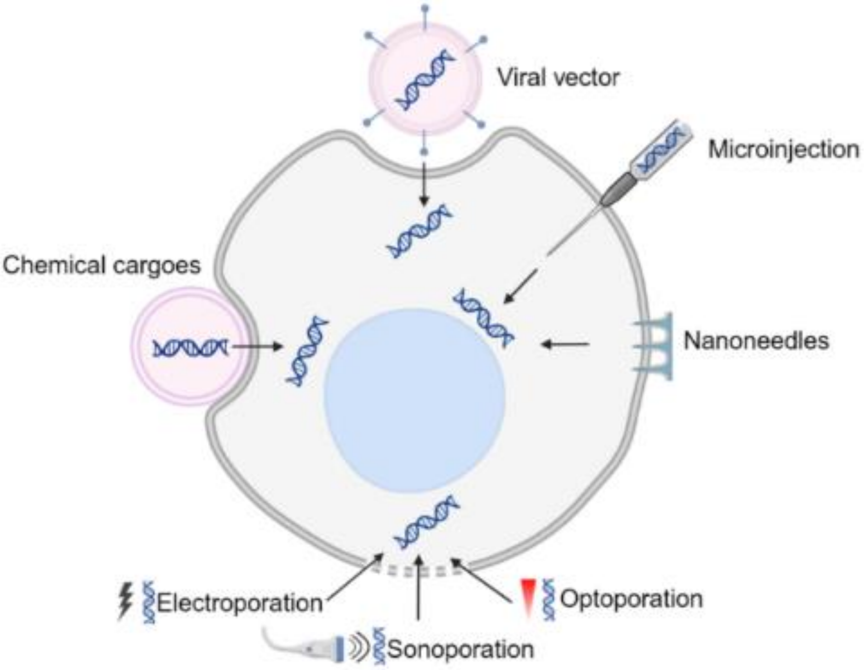

Figure 4: A selection of the various proposed intracellular delivery methods. Created with BioRender.com

Table 1: Summary of the various delivery and transfection methods. Reproduced and adapted from (Dong & Chang, 2021; Kim & Eberwine, 2010). SCT = Single-cell targeting possible.

Method	Description	Strengths	Challenges	SCT
Viral vectors	Engineered viruses	– High efficiency and viability	– Biosafety issues – Insertional mutagenesis – Limited package size	No
Chemical cargo	Cationic polymers	– High efficiency – No package size limit	– Chemical toxicity – Variable efficiency	No
Nanoneedles/ nanowires	Penetrating pillars	– Delivery of diverse materials	– Restricted to adherent cells – Complex design and fabrication	No
Sonoporation	Acoustic pressure waves	– High throughput	– Low cell viability	No
Microinjection	Microneedle	– High efficiency – Low cytotoxicity	– Labour intensive – Low throughput	Yes
Bulk Electroporation	Applied voltage	– High throughput	– Low cell viability – Low uniformity	No
Nanochannel-based electroporation		– High throughput – High cell viability – High delivery efficiency	– Complex device fabrication	Yes
Nanostraw-based electroporation		– High cell viability – High delivery efficiency	– Complex device fabrication	Yes
Flow-through microfluidic electroporation		– High throughput – High delivery efficiency	– Low cell viability	Yes
Optoporation	Focused laser beam	– Transfect single-cells within a population	– Variable efficiency	Yes

1.5 Introduction to Optoporation

Optoporation uses a high-power tightly focused laser beam that can be precisely targeted to individual cells for the localised temporary permeation of their membranes without affecting neighbouring cells. The laser generation process begins by exciting electrons into unstable high-energy states. When the excited electrons return to their ground state, they release photons. These photons can interact with other high-energy electrons, stimulating their return to the ground state and emission of more photons. As photons bounce between two mirrors, they stimulate further excitation and emission events in a cascading amplification process. Eventually, a coherent laser beam of monochromatic wavelength forms and escapes through a semi-reflective mirror to reach the target cell culture sample (**Figure 5**).

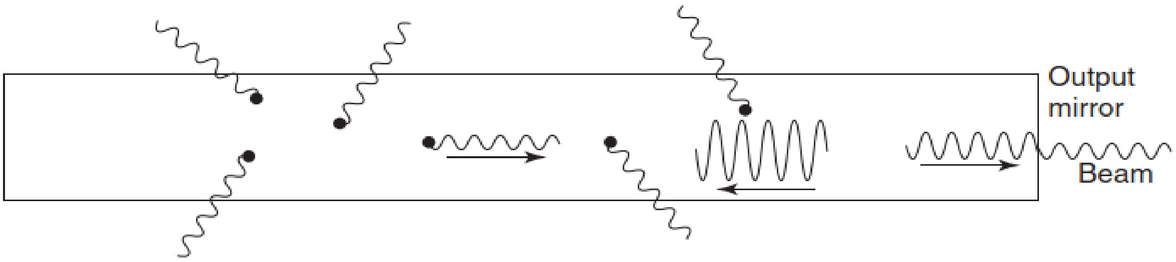

Figure 5: Schematic of the laser cavity. Spontaneous emission starts in all directions. The photons oscillate back and forth between two mirrors and are amplified to become the laser beam that escapes through a semi-reflective mirror. Figure reproduced from Hecht, Copyright © 2019, with permission from Wiley (Hecht, 2019).

Depending on the duration of the laser emission, lasers can be categorised into two basic types: those emitting a continuous beam of light with constant energy delivery and those emitting a series of pulses. Research has demonstrated that a continuous wave violet diode laser source transfected approximately 40% of mammalian cells, marking the first instance of successful siRNA transfection using a continuous wave source (Torres et al., 2010). While continuous UV diode lasers are relatively inexpensive and yield an efficient transfection rate, operating in the UV spectrum risks damaging DNA by highly absorbing intracellular components at this light spectrum (Mohanty et al., 2003; Palumbo et al., 1996). Instead, the near-infrared spectrum (700 – 1000 nm) is preferred as it induces less phototoxicity than UV radiation, making it a safer option for potential therapeutic use in living organisms. Additionally, compared to UV wavelengths, NIR experiences significantly less absorption and scattering, allowing it to penetrate more deeply through tissue (Mohanty et al., 2003).

However, the lower photon energies at these wavelengths are insufficient to induce optoporation through one-photon excitation (as discussed in section 1.6 Mechanisms of Transient Pore Formation by Optoporation). Using femtosecond or picosecond pulsed lasers enables multiphoton absorption to overcome this barrier. Though each pulse is ultrashort, the high repetition rate concentrates a high number of photons per second into the focal point (Wang et al., 2010). The sum of the energy absorbed is similar to that absorbed through a single high-energy photon and thus sufficient to excite an electron (**Figure 6**). In addition, multiphoton irradiation is limited to the pulsed laser's focal point contrary to one-photon excitation where irradiation occurs through the entire beam path (Li & Fourkas, 2007). This is because the photon density is high at the focal point and it drops off sharply outside the focal point. As a result, multiphoton femtosecond pulsed lasers can selectively porate target cells while avoiding widespread irradiation to the surrounding cells. For example, this precision was demonstrated by using a multiphoton femtosecond laser to perform nanosurgery on cortical neurons, where individual dendritic spines could be selectively dissected without causing any collateral damage to the surrounding neuronal structure (Sacconi et al., 2007).

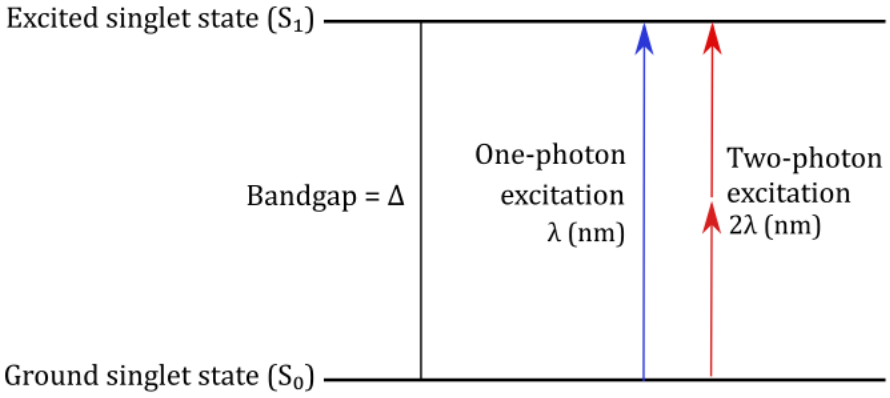

Figure 6: Excited-state energy diagram showing one-photon and two-photon excitation. Ionisation energy requires absorption of one photon from a relatively shorter wavelength (λ) with higher photon energy or two photons of longer wavelengths (2λ) and comparably lower photon energy.

1.6 Mechanisms of Transient Pore Formation by Optoporation

The formation of the transient pores in the cell membrane during optoporation can occur through various mechanisms, mainly categorised as photothermal, photomechanical and photochemical effects. The contribution of each mechanism depends on the laser pulse frequency and the laser fluence (energy per unit area) (Xiong et al., 2016). These mechanisms can occur individually or in combination regardless of whether the laser is specifically focused on the cell membrane or indirectly activates sensitising nanoparticles to enhance throughput. In the latter approach, photothermal nanoparticles concentrate and transduce light energy to amplify optoporation efficiency.

1.6.1 Photothermal Pore Formation

The photothermal mechanism is induced as the medium and the cellular content absorb photons within the UV and visible range, which increases the temperature of a localised area within the sample. This typically happens when using continuous wave irradiation or low-intensity pulsed laser light.

Localised heating increases membrane permeability by denaturing transmembrane proteins or causing local transition in the lipid bilayer (Delcea et al., 2012). In certain cases, photoabsorbent dye like phenol red with absorption at 488 nm can improve light absorption and enhance this photothermal effect (Palumbo et al., 1996). The changes in the cell membrane induced by this process are generally reversible below a certain light dosage. For example, irradiating CHO cells with continuous wave argon laser at 488 nm and a light dose of 2.5 MJ/cm^2 resulted in tiny black spots that disappeared within five minutes. However, higher light dosages of ≥ 5 MJ/cm^2 caused permanent changes in cell morphology and also cell death (Schneckenburger et al., 2002). Similarly, in indirect optoporation, the sensitisers absorb the irradiation, convert it to thermal energy and direct the heat to the cell membrane to disrupt it (Hatef et al., 2015).

1.6.2 Photomechanical Pore Formation

Irradiating cells with high-energy, short laser pulses (<10 ns) induces localised rapid heating and evaporation resulting in thermal-mediated vapour nanobubbles (VNBs) (Xiong et al., 2014). The VNBs continue to expand until eventually collapse to generate high-pressure shockwaves capable of creating membrane perforations between 200 nm – 2 µm (Sankin et al., 2010).

By tuning the laser intensity, the size of the resulting VNBs can be controlled which impacts not only the perforation size on cell membranes but also their resealing time (Lapotko, 2009). In fact, Yamane et al. found that irradiating cells with 90 µJ pulses to induce VNBs caused irreparable damage in HeLa cells, evidenced by the inability to restore electrical impedance to pre-optoporation levels. However, when the pulses were reduced to 28 µJ, the impedance level immediately recovered to its initial state within 2 minutes as the pores could reseal rapidly after VNB permeation (Yamane et al., 2014). This suggests that careful modulation of the laser energy input is crucial to create pores with dimensions that facilitate membrane integrity restoration and prevent cellular death.

A key limitation of VNB mediated optoporation is the difficulty in restricting permeabilisation to single cells. While cells need to be within 30 µm of the collapsing cavitation bubble for membrane poration to occur (Gac et al., 2007; Li et al., 2013), the shockwaves lack selectivity. On the other hand, this mechanism provides high throughput with improved cellular viability possibly because the VNBs insulate the surrounding environment preventing thermal diffusion beyond the optoporation site. For instance, Xiong et al demonstrated that laser intensities exceeding the VNB formation threshold (>1.02 J/cm^2) enabled >90% eGFP siRNA knockdown. In comparison, ~40% knockdown was achieved with sub-threshold conditions relying only on photothermal permeation (Xiong et al., 2014).

Alternatively, the ultrafast pulses in the femto- and picosecond range can deliver a high amount of energy in a short period, inducing multiphoton ionisation. In this process electrons are promoted into the conduction band, here referred to as 'quasi-free' electrons for simplicity (Rau et al., 2006). These quasi-free electrons transfer energy to the surrounding medium and form plasma-mediated cavitation bubbles that expand and generate shockwaves once they break (Boulais et al., 2012; Lachaine et al., 2014; Quinto-Su & Venugopalan, 2007). The generation of the quasi-free electrons depends on the input irradiance thus it is possible to fine-tune the plasma density for single-cell manipulation without eliciting damaging effects (Vogel et al., 2005).

1.6.3 Photochemical Pore Formation

A short pulsed laser with a high repetition rate (>1 MHz) and laser fluence below that of plasma-mediated bubble formation threshold are likely to contribute towards photochemical interactions. This process generates free electrons through ionisation (Vogel et al., 2005) resulting in highly reactive oxygen species which can increase the permeability of the cell membrane (Xiong et al., 2023). The permeabilisation occurs as the ROS and free radicals initiate a chain reaction of lipid peroxidation resulting in a localised destruction of the lipids forming the cell membrane (Delcea et al., 2012). Such a process was demonstrated by Eversole et al. at 80 MHz repetition rate and a 270 fs laser pulse at laser fluence below the threshold for the formation of VNBs or heat-induced poration-triggered photochemical mechanisms. The addition of the antioxidant ascorbic acid quenched the ROS resulting in a decreased optoporation efficiency. Hence this suggests that membrane permeation via this approach relied on ROS generation (Eversole et al., 2020).

In summary, a comprehensive understanding of the processes involved in inducing pore formation through optoporation allows for improved control over delivery efficiency and cytotoxicity.

1.7 Direct Optoporation

Direct optoporation involves precisely focusing the laser on the cell membrane. Modulating the scanning area of the laser beam over the cells allows for single-cell targeting while providing spatial and temporal control of intracellular delivery (Stewart et al., 2018). Optical transfection dates back to 1984 when Tsukakoshi et al. pioneered the use of nanosecond pulsed laser technology (Tsukakoshi et al., 1984). They employed a 355 nm wavelength and a 5 ns pulse duration with an Nd: YAG UV-emitting laser to introduce DNA plasmids coding for an enzyme that provided antibiotic resistance into rat kidney cells. A following landmark report in 2002 demonstrated the feasibility of DNA transfection to individual cells with no apparent cell death using femtosecond, high-intensity, near-infrared laser pulses at 800 nm wavelength (Tirlapur & König, 2002).

Direct femtosecond lasers have emerged as tools for transfecting hard-to-transfect cells such as stem cells and primary neurons. Transfecting stem cells is a major research objective for tissue regeneration and biotechnology. Early attempts reported the successful DNA plasmid pEGFP-N1 transfection of individual human salivary gland stem cells under 5-7 mW mean power. Interestingly, tracking the cells for 8 days revealed that the cells were still able to successfully biosynthesise the fluorescent protein (Uchugonova et al., 2008). Advancing this line of research, introducing physiologically relevant genes such as Gata-6 in mouse stem cells induced morphological changes characteristic of differentiation. Molecular analysis of the germ layer markers through rt-PCR confirmed the upregulation of Gata-4 and the downregulation of Oct-4 and NANOG marking significant process in understanding stem cell behaviour (Mthunzi et al., 2010).

Moreover, femtosecond laser technology has been applied to transfect individual stem cells within embryos. This groundbreaking achievement involved injecting fluorescent markers deep within well-developed annelid embryos, demonstrating the precision and depth of femtosecond laser-based cell manipulation (Torres-Mapa et al., 2011). Similarly, low repetition rate and high pulse energy successfully introduced mRNA and resulted in the manipulation of gene expression in individual cells of vertebrate embryos including chicks and zebrafish (Hosokawa et al., 2011). In vivo direct optoporation for delivery is limited, however a particular study did demonstrate gene delivery of naked DNA in rat muscle in vivo without causing muscle damage (Zeira et al., 2003).

Optoporation allows for spatial control over the introduction of genetic material even on a sub-cellular level. This intricate control enabled the assessment of the biological functions of small molecules in specific regions of living cells, offering valuable insights into cellular processes. For instance, introducing and translating Elk1 mRNA in primary rat dendrites, a transcription factor involved in differentiation, proliferation, tumorigenesis and apoptosis resulted in cell death. However, introducing the same mRNA in the cell bodies did not induce cell death, highlighting the importance of sub-cellular localisation on protein function (Barrett et al., 2006). Similarly, the use of a focused femtosecond laser beam allowed the entry of nanomolar concentrations of impermeable rhodamine phalloidin into HEK and primary cortical neurons with spatial selectivity (Dhakal et al., 2014).

One of the bottlenecks of direct optoporation is the low throughput, mainly because the setup requires precise cell-by-cell focusing of a Gaussian laser beam through a microscope objective (Xiong et al., 2016). Hence, this process is notoriously challenging and labour intensive, rendering the single-cell optoporation process to be very time consuming. In fact, mismatching the vertical alignment between the laser beam and the cell membrane by just 3 μm could reduce the transfection efficiency of the laser pulse by 50% (Tsampoula et al., 2007)**.** To overcome the stringent requirements for focusing, a non-diffracting Bessel laser beam that does not require precise axial positioning was used to transfect CHO cells with plasmids. The set-up achieved 20 times the axial distance when using a Bessel beam in comparison to the Gaussian beam, allowing cells to be transfected over a 100 μm axial range (Tsampoula et al., 2007). However, it is worth noting that the high laser intensity delivery through a non-diffracting Bassel beam carries a greater risk of damaging the cells potentially leading to apoptotic cell death (Tirlapur et al., 2001; Vogel et al., 2005). Higher throughput can be achieved by combining the laser set-up with a microfluidic approach facilitating a constant fast flow of cells through the laser focal region for optoporation. However, the reported transfection efficiencies for this approach were lower than those observed in single-cell experiments because the laser light was not focused on the individual cells and only a fraction of the cells were directly hit by the laser (Breunig et al., 2014; Marchington et al., 2010). The same research group designed a software aided automated system designed to assess the position of cells within the field of view through image contrast analysis. This is followed by laser illumination and control of the relevant microscope hardware to position the cells under the laser beam (Breunig et al., 2015).

The various research are summarised in **Table 2.**

Table 2: Summary of direct optoporation. Reproduced and adapted from (Hosseinpour & Walsh, 2021).

Mode of irradiation	Wavelength (nm)	Cell/animal	Cargoes	Efficiency	Cellular viability	Reference
Pulsed (5 ns)	355	Normal rat kidney cell	Eco-gpt gene	0.60%	/	(Tsukakoshi et al., 1984)
Pulsed (90 fs), 80 MHz	800	Chinese hamster ovary (CHO-K1), Rat kangaroo kidney epithelial (PtK2)	Plasmid DNA encoding GFP	GFP expression occurred after laser treatment	/	(Tirlapur & König, 2002)
Pulsed (200 fs), 76 MHz	780	BALB/c mice	Plasmid DNA encoding luciferase	Gene expression occurred after laser treatment	/	(Zeira et al., 2003)
Pulsed (12 fs)	792	Human salivary gland stem cells, Human pancreatic stem cells	Plasmid DNA encoding GFP	hPSC 70%, Hsgsc 80%	/	(Uchugonova et al., 2008)
Pulsed (200 fs), 80 MHz	790	Ovary hamster cells (CHO- K1), Kidney human cells (HEK- 293), Brain mouse/rat cells (NG108-15), Brain human cells (SK-N- SH), Embryo mouse cells (E14g2a)	Plasmid DNA encoding mito DsRed	Transfection rates: CHO-K1: 63%. HEK-293: 52%, NG108-15: 40%, SK-N-SH: 45%, E14g2a: 25%	/	(Mthunzi et al., 2010)
Pulsed (180 fs), 80MHz	800	*P. lamarckii* embryos	Dextran	55%	/	(Torres-Mapa et al., 2011)

Pulsed (120 fs)	800	Single cells of zebrafish, chick, shark, and mouse embryo	DNA plasmids encoding GFP	50%	/	(Hosokawa et al., 2011)
Pulsed (100 fs), 80MHz	800	Human embryonic kidney (HEK293)	Propidium iodide	42%	67%	(Marchington et al., 2010)
Pulsed (100 fs), 80MHz	840	Primary rat neurons	Elk1 mRNA	Cells transfected with Elk1 mRNA	/	(Barrett et al., 2016)
Pulsed (100 fs), 80MHz	800 - 850	Human embryonic kidney (HEK), primary cortical neurons	Rhodamine phalloidin	Cells stained with rhodamine phalloidin	/	(Dhakal et al., 2014)
Pulsed (15 fs), 85MHz	800	Chinese hamster ovary (CHO-K1)	Plasmid DNA encoding GFP	~2%	~100%	(Breunig et al., 2014)
Pulsed (15 fs), 85MHz	800	Chinese hamster ovary (CHO-K1)	Plasmid DNA encoding GFP	60-70%	~80%	(Breunig et al., 2015)
Pulsed (100 fs), 80MHz	800	Human embryonic kidney (HEK-29H)	Plasmid DNA encoding GFP	HEK cells transfected plasmid DNA and expressed GFP	/	(Soman et al., 2011)
Pulsed (200 fs), 80MHz	800	Chinese hamster ovary (CHO-K1)	Plasmid DNA encoding mito DsRed	56%	/	(Praveen et al., 2011)
Pulsed (140 fs), 90MHz	715 - 955	Canine mammary cells (MTH53a)	Plasmid DNA encoding GFP	70%	90%	(Baumgart et al., 2008)
Pulsed (120 fs), 80MHz	800	Chinese hamster ovary (CHO-K1)	Plasmid DNA encoding GFP	80%	70%	(Stevenson et al., 2006)
Pulsed (200 fs), 80MHz	800	Chinese hamster ovary (CHO-K1)	Plasmid DNA encoding mito DsRed	72%	>70%	(Antkowiak et al., 2010)

1.8 Indirect Optoporation

Indirect optoporation is a nanomaterial-mediated technique whereby nanomaterials serve as sensitisers to enhance the intracellular delivery throughput while lowering the laser intensities required to induce the transient pores, thus preserving viability (Xiong et al., 2014).

The incorporation of nanoparticles with the cells for optoporation typically involves the following steps:

1) The first step involves the addition of nanoparticles to the adherent cells or to cells in suspension, followed by a pre-determined incubation period. Alternatively, if using a nanomaterial platform such as nanostraws, the cells can be directly incubated on the platform itself.
2) Laser irradiation is performed to permeabilise the cell membrane and allow the effector molecule in the surrounding solution to enter the cytosol. Typically the effector molecule is a fluorescent molecule to allow easy readout or nucleic acids for gene editing and regulation.
3) After irradiation, the washing of the cells is followed by the addition of a fresh culture medium to facilitate continued cell growth.
4) The last steps involved monitoring and imaging the cells to subsequently calculate the delivery efficiency.

1.8.1 Gold Nanoparticles

Gold nanoparticles have a surface plasmon which induces oscillations of electrons upon light absorption within specific wavelengths, allowing the nanoparticles to efficiently convert light energy into heat. The heat generated by the gold nanoparticles is transferred from the nanoparticles to the surrounding environment, resulting in the formation of VNBs that permeabilise cell membranes (Xie & Zhao, 2017). Therefore, gold nanoparticles are well-suited as photothermal agents for optoporation.

The photothermal effect of gold nanoparticles has been shown to permeabilise cell membranes for the delivery of various compounds including relatively large proteins, mRNA and plasmids. For example, monoclonal antibodies were delivered into OCVAR-3 cells using gold nanorods irradiated at 532 nm and at the NIR region of 730 nm to enable deeper tissue penetration. This resulted in delivery efficiencies of 80% and 60% respectively, with the antibodies binding to the Ki-67 proliferation marker, while maintaining cell death below 20% (Yao et al., 2020). Similarly, optoporation with gold nanorods was used to deliver mixed-lineage domain like protein (MLKL) and caspase proteins into B16 melanoma tumour cells to induce regulated cell death (Van Hoecke et al., 2019). MLKL protein delivery rapidly induced necrosis within one hour with a cell viability drop to 62%, while mRNA transfection coding for MLKL triggered cell death within 16 hours after transfection (Van Hoecke et al., 2018). Caspase 3 and 8 delivery triggered apoptosis with associated cellular changes like membrane blebbing and a drop in cell viability to 64% and 71% respectively (Van Hoecke et al., 2019). In another recent study, successful delivery and expression of GFP mRNA was achieved in both adherent HeLa and non-adherent Jurkat T cells through VNBs optoporation in the presence of gold nanoparticles. In addition, this process proved to be gentler with a fivefold increase in cell transfection efficiency (~20%) as compared to electroporation (Raes et al., 2019, 2020). Furthermore, the same research team achieved the delivery of Cas9 ribonucleoprotein in hard-to-transfect stem cells and T cells, achieving knock-out levels exceeding 80% in H1299-eGFP cells that could be used in spatially controlled ex-vivo stem cell engineering (Raes et al., 2021). These studies demonstrated the ability of optoporation to deliver functional proteins and nucleic acids into the cell. Yet, most of this research executed bulk delivery as a means to improve optoporation throughput.

Lukianova-Hleb et al. demonstrated targeted gene delivery at the single cell level by transfecting individual cells with GFP cDNA plasmids. Delivery was mediated by clusters of densely-packed gold nanoparticles composed of 4 – 20 nanoparticles. The individual cells were exposed to a single short laser pulse of 0.5 ns duration at 532 nm with low fluence and formed nanobubbles next to the target cells. The size of the nanobubbles was precisely controlled through the laser pulse energy applied and achieved a delivery efficiency of 74% in J32 cells and a 9% transfection efficiency in stem CD34 cells after 48 hours of incubation (Lukianova-Hleb et al., 2011). Despite reporting single cell delivery, the plasmid was not delivered under spatiotemporal control and did not distinguish between specific cells within a population. On the other hand, Xiong et al. developed an automated spatially resolved nanoparticle-enhanced photoporation (SNAP) platform offering spatially-targeted single cell delivery with high throughput. In fact, this platform can process up to 200 cells per second by programming a motorised microscope stage to move the sample in a pre-defined pattern with respect to the laser beam. Alternatively, the software has an image recognition feature to recognise individual cells based on distinct cellular characteristics like fluorescent biomarkers. The specific cells are then exposed to a porating laser pulse with a beam diameter slightly less than a typical cell size. Thus, the SNAP platform enables automated delivery to individual cells at spatially distinct locations with high throughput and selectivity (Xiong et al., 2017). Such a system aligns closely with the laser scanning setup employed in this research project, where individual cells can be selectively targeted by automatically move the laser beam.

By altering the geometry of gold nanoparticles, their optical properties can be precisely regulated to tune the peak resonance to minimise damage to cells while maintaining potent photothermal effects for optoporation. For this reason, various nanoparticle structures, such as rod-shaped particles, gold nanostars and silica-gold core-shell nanoshells, have been engineered to shift the absorption peak away from visible wavelengths into the near-infrared region (Hasanzadeh et al., 2021; MacKey et al., 2014). For instance, nano-corrugated mushroom-shaped gold-coated polystyrene nanoparticles absorbed in the near-infrared region and yielded a 94% intracellular propidium iodide delivery and ~100% cell viability (Santra et al., 2020). Similarly, off-resonance NIR femtosecond laser excitation at 800 nm of 100 nm citrate-capped gold nanoparticles enabled high membrane perforation and subsequent transfection of DNA plasmids into human cancer cells (Baumgart et al., 2012). The same group also decorated these citrate-capped gold nanoparticles with monoclonal antibodies that targeted and subsequently perforated cancer cells overexpressing CD44 receptors when exposed to NIR femtosecond laser (Bergeron et al., 2015). Thus these studies demonstrate a non-invasive tool for gold-mediated optoporation.

Despite the potential for biomedical applications, a key limitation of gold nanoparticles is their tendency to fracture into small fragments when subjected to high-intensity laser pulses (Rudiuk et al., 2011). These fragmented nanoparticles can intercalate with cellular DNA, preventing protein expression and causing genotoxic effects (Liu, et al., 2020; Pan et al., 2007; Tsoli et al., 2005). In fact, Pan et al. demonstrated that 20 nm gold nanoparticles incubated with fibroblasts induced oxidative DNA damage and downregulated cell cycle genes that inhibited proliferation 3 days post-nanoparticle exposure (Li et al., 2008). Furthermore, another study reported that 2 nm sized gold nanoparticles caused irreparable DNA damage, cellular morphological changes and also resulted in mitochondrial stress at concentrations of <25 μg/mL (Schaeublin et al., 2011). Another limitation linked to nanoparticle fragmentation was that this led to the destruction of proteins bound to the nanoparticle surface (Rahmanzadeh et al., 2019). Lastly, the non-biodegradable nature of gold nanoparticles results in the accumulation of high concentrations inside cells, posing safety and regulatory concerns for therapeutic applications (Berdecka et al., 2023). Overcoming these biocompatibility issues around genotoxicity, cytotoxicity, and intracellular fate is critical to enable broader clinical implementation of gold nanoparticle-mediated optoporation platforms.

1.8.2 Carbon Based Nanoparticles

Carbon-based nanomaterials, particularly carbon nanotubes and graphene exhibit the remarkable ability to easily traverse cell membranes, rendering them highly effective cargo carriers and delivery vehicles for drug and nucleic acids (Hong et al., 2015). Going back to the 1990s, it was reported that carbon nanoparticles have the capacity to absorb optical energy when exposed to NIR irradiation. This absorption leads to significant heating (photothermal effect) which activates the decomposition of carbon black via a carbon-steam reaction (Chen et al., 1997; Löwen & Madden, 1992). As a result, VNBs are formed, eventually bursting and generating shockwaves.

Inspired by the controlled generation of shockwaves, researchers have explored the potential of carbon nanomaterials as photosensitisers for photothermal therapy (Kumar et al., 2021). In photothermal therapy cells are selectively targeted for elimination through the application of NIR light, harnessing the heat generated by these carbon-based materials. For example, selective destruction of cancer cells can be achieved by functionalising carbon nanotubes with a folate moiety allowing for selective internalisation inside cells with the complementary receptor tumour marker (Kam et al., 2005). Upon exposure to NIR irradiation, these nanotubes induced endosomal rupture, leading to the release of the cargo into the cytosol. This process has shown great promise in vitro, as it resulted in cancer cell death while leaving normal cells unharmed (Kam et al., 2005).

The interaction between the carbon nanostructures and the NIR pulses can also induce localised heating suitable for intracellular delivery applications. Specifically, irradiating carbon black nanoparticles with a 200 nm average diameter resulted in the permeabilisation of cell membranes. This enabled the delivery of small molecules, proteins, and DNA into DU145 human prostate carcinoma and GC-9L cells, all while maintaining high cell viability (Chakravarty et al., 2010). Subsequently, the research group transitioned to a cheaper nanosecond laser system and meticulously optimised various laser exposure parameters, such as pulse fluence, number of pulses, pulse repetition rate and carbon black nanoparticle concentration. As a results, the optimised system achieved intracellular delivery of dextran molecules of varying molecular weights ranging between 10 – 500 kDa, with >88% delivery efficiency and cell viability close to 100%. (Sengupta et al., 2014).

Comparing the cellular bioeffects between three different forms of carbon during nanosecond-pulsed NIR laser irradiation demonstrated that single-wall carbon nanotubes displayed limited reversible permeabilisation. The single-wall carbon nanotubes could only facilitate calcein uptake into cells when subjected to high laser intensity. However, this approach led to irreversible permeabilisation, resulting in cell fragmentation or non-viability. In contrast, multi-walled carbon nanotubes exhibited higher uptake levels compared to carbon black nanoparticles (Holguin et al., 2018). Interestingly, research on multi-walled carbon nanotubes is not commonly explored in this context of intracellular delivery via optoporation.

Graphene quantum dots (GQDs) can also serve as photothermal sensitisers and have been used as a platform for live cell labelling in microscopy. Compared to gold nanoparticles, GQDs have greater resistance against fragmentation when exposed to pulsed laser irradiation. This resilience allows for repeated optoporation of cells using the same set of GQDs, enabling precise control over the quantity of fluorescent labels delivered into cells for desired contrast (Liu et al., 2018). However, an issue arose where GQDs tended to aggregate in the cell culture medium, causing excessively large vapor bubbles upon irradiation which led to significant cell damage. To address this, GQDs were functionalised with a polyethylene glycol coating to improve colloidal stability. This modification significantly improved the system and facilitated the delivery of dextran molecules of varying molecular weights into cells while improving cell viability (Liu et al., 2020).

The use of carbon-based nanomaterials has been limited due to concerns about cytotoxicity including ROS generation, DNA damage and lysosomal membrane dysfunction that eventually lead to cell death via apoptosis or necrosis (Yuan et al., 2019). For instance, multiwalled carbon nanotubes and single wall carbon nanotubes have induced oxidative stress leading to apoptosis in certain cell types as early as 6 hours after exposure (Sohaebuddin et al., 2010). A comparative study revealed that carbon nanotubes, carbon nanofibers, and carbon nanoparticles inhibited cell proliferation and caused cell death across several tested cell lines. Interestingly, the detrimental impact was more pronounced as the aspect ratio decreased, with carbon nanoparticles showing the strongest negative effects (Magrez et al., 2006). Consequently, carbon nanotubes were added to the Substitute It Now (SIN) list as a material to avoid (Hansen & Lennquist, 2020). This highlights the importance of thoroughly evaluating the biocompatibility and safety of carbon nanomaterials before considering them for biomedical applications. Overcoming the cytotoxic profile of these platforms remains a key challenge limiting their clinical translation for optoporation and other delivery approaches.

1.8.3 Other Nanomaterials

Numerous other nanomaterials have been explored to a minor extent as promising candidates for optoporation including iron oxide, black phosphorus, polydopamine and titanium nanoparticles.

Iron oxide nanoparticles (IONPs) can absorb light in the near-infrared (NIR) region and have been investigated for use in photothermal therapy (Chu et al., 2013; Estelrich & Busquets, 2018). A comparison of spherical, wire-like, and hexagonal IONP structures did not reveal differences in their photothermal effect, as at a concentration of 0.5 mg/mL, all three structures reduced cellular viability by approximately 50%. However, this concentration may be too high to avoid side effects (Chu et al., 2013). Furthermore, clusters of IONPs were more effective for photothermal therapy than individual nanoparticles at equal iron concentrations. The IONP clusters transduced more heat, inducing greater temperature increases that led to cell death (Shen et al., 2015). Moreover, the porous hollow structure of IONPs enables loading with doxorubicin (DOX). When exposed to NIR lasers, the loaded DOX is released, accelerating apoptosis in targeted cells (Hu et al., 2018).

Magnetic IONPs have also shown potential in delivering macromolecules, such as plasmid DNA, without compromising the cell viability. Magnetic attraction is used to guide the nanoparticles to the bottom of the culture plate before cell seeding to ensure efficient heat transfer between cells and the nanoparticles upon NIR irradiation. In fact, this technique achieved a GFP plasmid transfection efficiency of 67% in HeLa cells and 30% in a hard-to-transfect primary cell line (Wang et al., 2018). Recently, magnetic iron oxide nanoparticles of 500 nm were compared to gold nanoparticles for delivering compounds into hard-to-transfect macrophages (Harizaj, Van Hauwermeiren, et al., 2021). The results show that iron oxide nanoparticles outperformed the gold nanoparticles, achieving 51% delivery efficiency in delivering 150 kDa dextran compared to only 37% efficiency for the gold nanoparticles. Therefore, iron oxide nanoparticles offer a promising alternative to gold nanoparticles for macromolecule delivery (Harizaj, Van Hauwermeiren, et al., 2021). Yet, concerns related to cytotoxicity and low solubility in aqueous solution remain which are currently limiting the clinical application of iron oxide nanoparticles (Manshian et al., 2017).

Titanium-based nanostructures are also photothermal candidates for optoporation. Titanium-oxide nanotubes, nanofibres, microflowers and microspike structures have all delivered propidium iodide or dextran while maintaining cellular viability (Mohan et al., 2021; Mohan et al., 2021; Nalluri et al., 2011; Xiong et al., 2021). Laser-irradiation of a nanoblade consisting of 100 nm thick titanium film coating a glass micropipette with a 2 μm tip diameter facilitated the delivery of large cargo including DNA, RNA, polystyrene beads and bacteria (Wu et al., 2011). A slightly different high throughput approach involved a two-dimensional array of a titanium microdish chip device. Upon irradiation with a wavelength of 1050 nm, the titanium microdish device generated photothermal cavitation bubbles that disrupted the cells resting on top of the dish (Shinde et al., 2020). Once again the limitation lies in the wavelength needed to activate the nanoparticles. Overall, titanium oxide nanoparticles need to be irradiated by a 532 nm laser pulse which restricts tissue penetration depth compared to NIR.

In back-to-back publications, the same research group demonstrated black phosphorus quantum dots and polydopamine nanoparticles as promising new photothermal agents for optoporation. Using functionalised black phosphorus quantum dots of ~20 nm achieved ~80% siRNA and ~40% GFP mRNA delivery in adherent and suspended cells upon irradiation with either visible light (532 nm) or NIR (800 nm) pulsed laser (Wang et al., 2021). This approach also attained 10 kDa dextran delivery in 2 mm phantom gel simulating the presence of thick tissue to obtain ~80% delivery efficiency. Thus highlighting its potential suitability for transfection in thick tissues (Wang et al., 2021). Furthermore, the same research group explored for the first time the application of 500 nm polydopamine nanoparticles as sensitisers enabling GFP mRNA transfection efficiency of ~45% for HeLa and Jurkat cells (Harizaj et al., 2021). Similar to other nanomaterials described, the efficiency depended on the concentration of the nanoparticles, the laser energy and the size of the nanoparticles. Small nanoparticles of 150 or 250 nm exhibited higher optoporation efficiency than larger nanoparticles, with minimal resultant impact on T-cell functionality (Berdecka et al., 2023). In contrast, larger 400 nm nanoparticles led to a substantial drop in viability to ~55% along with the lowest delivery efficiency achieved. This poorer performance is possibly attributed to the larger pores formed in the T-cell membranes which proved difficult for the small cells to repair, therefore, underscoring the need to finely tune nanoparticle size as a means to optimise optoporation delivery efficiency.

The various research is summarised in **Table 3**.

Table 3: Summary of nanomaterial mediated optoporation . Reproduced and adapted from (Hosseinpour & Walsh, 2021; Stevenson et al., 2010; Wang et al., 2023).

Type of material	Mode of irradiation	Wavelength (nm)	Cell/animal	Cargoes	Efficiency	Cellular viability	Reference
Gold	Pulsed (7 ns)	561	HeLa cells, Jurkat E6-1 cells	GFP mRNA	38% HeLa, 45% Jurkat T	>80%	(Raes et al., 2020)
	Pulsed (7 ns) 20 Hz	561	Jurkat T cells, CD4+ T cells	Dextran 10 kDa	>60% Jurkat, >40% CD4+ T	>70%	(Raes et al., 2019)
	Pulsed (3 ns)	532	H1299-EGFP cells, Mesenchymal stem cells (MSC), Primary T cells	Dextran 10 kDa, Cas9 RNP	Knock out of >80% H1299, 60% MSC, 34% T cells	>70%	(Raes et al., 2021)
	Pulsed (7 ns) 20 Hz	561	HeLa cells, Normal human embryonic kidney cells (NHEK)	Dextran 10 kDa	~90%	>80%	(Xiong et al., 2017)
	Pulsed (45 fs) 1 kHz	800	Human melanoma cells (WM278)	Lucifer Yellow, YFP-SMAD2 DNA plasmids	70% Lucifer yellow, 23% DNA plasmids	>80%	(Baumgart et al., 2012)
	Pulsed (850 ps) 20.25kHz	532	Canine pleomorphic mammary adenoma cells (ZMTH3)	GFP protein (27 kDa)	43%	>80%	(Heinemann et al., 2014)
	Pulsed (850 ps) 20.25kHz	532	Canine pleomorphic mammary adenoma cells (ZMTH3)	anti GFP siRNA (14 kDa)	88%	>90%	(Heinemann et al., 2013)
	Pulsed (850 ps) 20.25kHz	532	Canine pleomorphic mammary adenoma cells (ZMTH3), Chinese hamster ovarian (CHO)	Dextrans 10 - 2000 kDa	Varies - highest at 10 kDa with 88%	>73%	(Kalies et al., 2014)

	Pulsed (4 ns) 10 Hz	532, 730	Ovarian adenocarcinoma (OVCAR-3)	Dextran, FITC labelled antibody TuBB-9	~80% at 532 nm ~60% at 730 nm	>80%	(Yao et al., 2020)
	Pulsed (5 ns) 10 Hz	945	HeLa cells, Human colorectal carcinoma cells (HCT-8)	Propidium iodide	94%	100%	(Santra et al., 2020)
	Pulsed (100 fs) 80 MHz	800	Retinal ganglion cells (RGC)	siRNA	siRNA delivered to the cells	/	(Wilson et al., 2018)
	Pulsed (0.5 ns)	532	Jurkat T cells, human CD34+ CD117+ stem cells	Plasmid DNA encoding GFP	71%	83%	(Lukianova-Hleb et al., 2011)
Carbon	Pulsed (100 fs)	800	Human prostate cancer cells (DU145), rat gliosarcome cell (GS-9L)	Small molecules, proteins, plasmid DNA encoding for luciferase	For both cell lines: >90% calcein positive, >35% BSA positive, 22% DNA	>90%	(Chakravarty et al., 2010)
	Pulsed (5-9 ns)	1064	Prostate cancer cells (DU145), Rat cardiomyoblast cells (H9c2)	Calcein and FITC-dextran	~88%	~100%	(Sengupta et al., 2014)
	Pulsed (7 ns)	561	HeLa cells	Fluorescent probes	51%	>80%	(Liu et al., 2018)
	Pulsed (7 ns) 20 Hz	561	HeLa cells, Jurkat cells	Dextran (70, 500 kDa)	~80%	~80%	(Liu et al., 2020)
Iron	continuous for 30s	808	HeLa cells	Plasmid DNA encoding GFP	67%	~100%	(Wang et al., 2018)
	Pulsed (7 ns)	647	HeLa cells, H1299 cells, Jurkat cells, Human CD3+ T cells	Cas9 RNP, anti GFP siRNA	>60%	>80%	(Xiong et al., 2021)

	Pulsed (7 ns) 20 Hz	561	Mice primary macrophages	Dextran 150 kDa	51%	~80%	(Harizaj et al., 2021)
Black phosphorus	Pulsed (5 ns and 2 ns)	532, 800	HeLa, Lung carcinoma cells (H1299-eGFP)	eGFP siRNA, GFP mRNA	>80% eGFP siRNA, >40% GFP mRNA	>80%	(Wang et al., 2021)
Polydopamine	Pulsed (3 ns)	532	Jurkat cells	Dextran 500 kDa	>70%	>70%	(Berdecka et al., 2023)
	Pulsed (7 ns) 20 Hz	561	Jurkat cells	eGFP mRNA	~45%	~50%	(Harizaj et al., 2021)
Titanium	Pulsed (5 ns) 10 Hz	1050	Human carcinoma of uterus cells (SiHa), Mouse neural crest-derived cells(N2a)	Propidium iodide	98%	92%	(Shinde et al., 2020)
	Pulsed (6 ns)	532	Human embryonic kidney cells (HEK293)	eGFP mRNA, DNA encoding DsRed	46%	>90%	(Wu et al., 2011)
	Pulsed (5 ns) 10 Hz	680	Human colorectal carcinoma cells (HCT)	Propidium iodide	93%	98%	(Mohan et al., 2021)
	Pulsed (5 ns) 10 Hz	680	HeLa cells	Propidium iodide	93%	98%	(Mohan et al., 2021)

1.9 Porous Silicon Nanoparticles

Porous silicon (pSi) has attracted significant attention in the biomedical field due to its remarkable physical and chemical properties. These include biocompatibility, biodegradability, high loading capacity, easily functionalised surface properties and also have photothermal characteristics (Li et al., 2018). As a result, porous silicon nanoparticles have been investigated for their use in drug delivery systems, biosensing, and their potential in photodynamic and photothermal tumour therapy.

1.9.1 Fabrication of Mesoporous Silicon Nanoparticles

The process of fabricating nanoparticles provides flexibility in obtaining nanoparticles with the desired structure, pore size and porosity. In the vast majority of the studies discussed depended on the fabrication of discoidal-like porous silicon nanoparticles produced through a top-down approach by etching a solid silicon wafer. The fabrication process offers control over the pore sizes of the structure typically within the 2 – 50 nm range which is classified as mesoporous structures (Lee et al., 2007; Secret et al., 2013; Xia et al., 2016). Herein, I also explain the fabrication of metal-assisted chemical etching to produce rod-like nanoparticles with a higher aspect ratio than the electrochemically etched nanoparticles.

1.9.2 Electrochemical Etching

In electrochemical etching, the wafer is immersed in an aqueous electrolyte containing fluoride, typically hydrofluoric acid (HF), and an alcohol followed by the application of a current. The alcohol is typically ethanol and it serves as a surfactant to prevent hydrogen bubbles from accumulating on the porous silicon surface during the etching process (Loni, 2014). In addition, the dilution of the alcohol affects the porosity as increasing the alcohol content relative to HF enlarges the average pore diameter (Burham et al., 2014). For instance, reducing ethanol from a 3:7 to 9:1 HF: ethanol ratio decreased pore sizes from 60 – 200 nm down to 5 – 10 nm after a 20 minute etch. The pore size can also be tuned by the applied current density and etch duration. Increasing either parameter enlarges the pore diameters (Loni, 2014). For example, a lower 33 mA/cm^2 current density generated 10 nm pores which required 90 minutes etch time. However, applying 99 mA/cm^2 current density shortened the 10 nm pore etch time to 30 minutes. Similarly, doubling the etch duration from 30 to 60 minutes under constant current density widened pore sizes from 10 nm to 18 nm (Loni, 2014).

After the electrochemical etching process generates the desired porous silicon layer morphology, an electropolishing pulse detaches it from the bulk silicon wafer (Tieu et al., 2019). The anodised wafer then undergoes an ethanol rinse step to remove residual fluoride toxic etching waste like HF, along with by-products such as silicon tetrafluoride (SiF_4) and hexafluorosilicic acid (H_2SiF_6) (Koynov et al., 2011). The formation of these by-products is explained in the equation (1) and (2) where the h^+ are supplied by the etching current.

$\mathrm{Si} + 4\ \mathrm{HF} + 4\ \mathrm{h}^+ \quad \rightarrow \quad \mathrm{SiF}_4 + 4\ \mathrm{H}^+$ Equation 1

$\mathrm{SiF}_4 + 2\ \mathrm{HF} \quad \leftrightarrow \quad \mathrm{H}_2\mathrm{SiF}_6$ Equation 2

1.9.3 Metal Assisted Chemical Etching

Metal assisted chemical etching (MACE) generates porous silicon nanowires as another top-down approach, requiring an aqueous etching solution composed of HF, an oxidising agent and a catalytic metal. Typically, silver is deposited as the catalytic metal onto the surface of the silicon wafer to promote the charge transfer between the oxidising agent, which is usually hydrogen peroxide (H_2O_2), and the silicon. Consequently, the silicon undergoes oxidation and dissolves in HF, forming H_2SiF_6 (Levy-Clement, 2014) as summarised through the following reactions:

$\mathrm{Si} + 6\ \mathrm{HF} + 4\ \mathrm{h}^+ \quad \rightarrow \quad \mathrm{H}_2\mathrm{SiF}_6 + 4\ \mathrm{H}^+$ Equation 3

$\mathrm{H}_2\mathrm{O}_2 + 2\ \mathrm{H}^+ \quad \rightarrow \quad 2\ \mathrm{H}_2\mathrm{O} + 2\ \mathrm{h}^+$ Equation 4

In MACE, the dissolved metal catalysts induce anisotropic etching primarily underneath the catalytic metal deposits. This accelerated vertical etching caused the metal particles to sink into the forming porous silicon layer, resulting in an organised array of high aspect ratio porous structures commonly referred to as silicon nanowires (Chattopadhyay et al., 2002). Similar to electrochemical etching, the pore morphology can be tuned by the etching solution parameters. For example, increasing the oxidant concentration enlarges the pore diameter and the porosity of the silicon nanowires (Bai et al., 2013; Chiappini et al., 2010). The resulting nanowires are then fragmented through sonication to obtain rod-like nanoparticle structures.

1.9.4 Surface Modification of pSi Nanoparticles

Chemical modification of the porous silicon surface can provide a means to adjust the chemical stability of the material, control biodegradability and enable biomolecule immobilisation**.** The high reactivity of the silicon surface arises from readily oxidised silicon-silicon (Si-Si) and silicon-hydrogen bonds (Si-H_x) in the presence of air or water (Sailor, 2014).

Thermal oxidation is the most prevalent stabilisation approach. The specific surface species formed depend on factors like temperature and oxidation duration. Since Si-Si bonds are weaker than Si-H bonds, low temperature oxidation primarily targets Si-Si-bonds by incorporating a single oxygen atom, resulting in SiO_y-Si-H_x while retaining Si-H bonds (Pap et al., 2004). However, oxidising at temperatures exceeding 60 °C causes the Si-H bond to undergo oxidation forming of Si-O and Si-OH bonds (Ogata et al., 1995). Alternatively, porous silicon can be oxidised by water through a nucleophilic attack by the hydroxide ion (OH^-) inducing the breaking of Si-Si bonds and the formation of Si-O bonds instead (Sailor, 2014).

Oxidised porous silicon surfaces readily undergo silanisation reactions that introduce a variety of chemical functionalities. A popular approach uses 3-aminopropyltriethoxysilane (APTES) to couple primary amine (-NH_2) groups to the oxidised porous silicon surface. This enables subsequent conjugation to amine-reactive molecules and provides positive charges that attract negatively charged nucleic acids through electrostatic interactions, enabling nucleic acid loading onto the nanoparticles (Tinsley-Bown et al., 2000). For example, histidine or lysine amino acids can be reacted with the primary amine of APTES via a peptide bond. The amine groups present on the imidazole ring of histidine and on the lysine side chain allow electrostatic interactions for complexing with plasmid DNA and delivering it to the cells. In fact, unmodified porous silicon nanoparticles hardly transfected the cells with the plasmid while APTES, histidine and lysine functionalised nanoparticles enabled successful transfection and expression (Chaix et al., 2019), thus demonstrating that porous silicon cationic surface are very promising for nucleic acid delivery.

1.9.5 Biodegradability

In contrast to solid crystalline silicon, mesoporous silicon exhibits a significantly larger surface area which enhances its water solubility and degradability. Oxidative hydrolysis enables dissolution of unoxidised silicon in the presence of water. The proposed mechanism involves the Si-H bonds undergoing hydrolytic attack to form Si-OH bonds and release hydrogen gas. These Si-OH bonds weaken the Si-Si back bond, making them susceptible to additional water attack. This generates $HSi(OH)_3$ which rapidly converts in solution to $Si(OH)_4$, forming soluble orthosilicic acid.

This biodegradable matrix offers a dual advantage: it enables sustained release at targeted sites within the body and gradually undergoes biological elimination after interaction with the cells (Ahuja & Pathak, 2009). The degradation process transforms porous silicon into non-toxic orthosilicic acid as verified through molybdate blue assays (Anglin et al., 2008) and ICP analysis (Chiappini et al., 2010). In fact, a high concentration of 0.2 mg/mL of electrochemically etched nanoparticles exhibited no substantial impact on cellular viability and 50 µg/mL completely degraded within 4 hours (Mayne et al., 2000). Orthosilicic acid is a weak acid that can potentially acidify the cellular environment at high concentrations (Belton et al., 2012). However, large amounts of orthosilicic acid would be needed to overcome the buffering capacity of both cell culture media and the cell's natural buffers. Therefore, minor fluctuations in pH may occur but are usually well tolerated, so orthosilicic acid is generally regarded as relatively non-toxic at typical exposure levels.

It is important to note that the degradation rate of porous silicon is influenced by factors such as the degree of porosity, pore size distribution and surface chemistry. Consequently, the degradation rate of porous silicon can be adjusted, spanning from minutes to months (Godin et al., 2010).

1.9.6 Porous Silicon Nanoparticles as Drug Delivery Carriers

An extensively explored characteristic is the nanoparticle's ability to serve as a delivery vehicle for various substances, including small molecules, peptides and genetic materials making it an ideal therapeutic carrier. For instance, pSi nanoparticles were loaded with liposomal siRNA that targeted EphA2 oncoprotein in ovarian tumour cells associated with high-metastatic potential. The results showed a sustained gene silencing effect lasting for at least three weeks, without any observed toxicity (Tanaka et al., 2010).

During transfection experiments, a well explored approach is loading the nanoparticles with nucleic acids to effectively deliver the nucleic acids to the targeted cells. For example, loading MRP1 (multidrug resistant protein 1) siRNA into functionalised pSi nanoparticles achieved a 60% knockdown of MRP1 expression in glioblastoma cells, in contrast to the 10% reduction observed in the negative control. This induced apoptosis in 30% of the tumour cells. (Wan et al., 2014). The issue remained in releasing the nucleic material payload once inside the cell. External stimuli such as light and heat have been regularly used to facilitate the release of nucleic acid from silicon nanoparticles–based delivery systems (Chang et al., 2012, Kamegawa et al., 2018). Endosomal compartments form upon the internalisation of siRNA–loaded pSi nanoparticles and the amine group from the APTES functionalised nanoparticles served as a buffer by protonating amines, countering the pH decrease in the endosome (Behr, 1997). In turn, this triggered an influx of counter ions, induced osmotic swelling and eventual rupture of the endosomal membrane thus facilitating siRNA release from the endosome (Ping, 2022). However, degradation of the nanoparticles could inadvertently release the nucleic acid within the endosome, leading to the destruction of the nucleic acid (Wan et al., 2014).

Apart from siRNA, larger nucleic acids like mRNA and plasmid DNA have been delivered. For example, endothelial factor-1-eGFP plasmid was electrostatically coupled with APTES functionalised pSi nanoparticles of ~420 nm in size at a mass ratio of 100: 1 and transfected HEK 293 cells with a transfection efficiency of 15.6 % (Wareing et al., 2017). Similarly, uptake of fluorescein-labelled pDNA encoding luciferase reporter gene through amino–acid functionalised pSi nanoparticles has been monitored through the mean fluorescent intensity measured. Thus, providing promising results for plasmid delivery, though its expression outcome remains unreported (Chaix et al., 2019). Hence, these studies suggest that using porous silicon nanoparticles to deliver targeted siRNA and silence the genes typically overexpressed in cancer cells could present a means to overcome chemotherapeutic drug resistance and reduced tumour metastasis.

A few silicon-based delivery systems have advanced to clinical trials, demonstrating their potential in the field of medicine. One such system involves the use of partially porosified silicon nanoparticles loaded with the medical isotope ^{32}P for brachytherapy. In this approach, the device is injected under local anaesthesia directly into the tumour, enabling targeted irradiation within a maximum tissue range of approximately 8 mm (Kumeria et al., 2017; Tieu et al., 2019).

1.9.7 Porous Silicon Based Biosensors

Porous silicon provides an ideal platform for biosensing application because of its highly tuneable surface facilitating the immobilisation of a wide range of bioreceptors (Moretta et al., 2021). In addition, the high surface area to volume ratio allows for densely packing the surface with receptors to enhance sensitivity (Chhasatia et al., 2017). When a target analyte binds to its specific bioreceptor on the porous silicon surface, it forms a complex that generates a measurable optical or electrical signal rendering porous silicon a suitable label-free biosensor (Sailor & Wu, 2009).

DNA hybridisation biosensors utilise porous silicon by immobilising a short single stranded DNA probe on the surface. Then, the target analyte in solution binds as the complementary DNA strand to the probe, forming a double stranded structure (Tieu et al., 2019). The hybridisation of the analyte replaces the air in the porous matrix, causing an increase in the refractive index. This increase quenches the photoluminescence of the porous silicon, resulting in a red-shift (Mariani et al., 2016) For example, Chan et al. functionalised the surface of porous silicon layers with a DNA probe sequence which upon hybridisation with the bacteriophage lambda cDNA resulted in an increase of photoluminescence. In fact, a spectral red-shift of 12 nm was reported (**Figure 7**) while no spectral shift was observed when the sensor was exposed to a non-complementary DNA. Thus, highlighting the selectivity of the biosensor towards detecting the specific virus (Chan et al., 2001). Similarly, immobilising a specific DNA strand and exposing it to 10 µM complementary DNA in solution resulted in a 12% variation in photoluminescence (Di Francia et al., 2005). Photoluminescence-based biosensors have received less research interest than other sensing techniques likely because photoluminescence measurements can suffer interference from various factors (Bonanno & Segal, 2011; Sailor & Wu, 2009). Instead tracking the refractive index changes enables label-free detection an provide information of whether the target analyte has bound to the pSi structure. The common limit of detection of these sensors is typically within the µM - nM range although recent applications have managed to lower this to pM concentrations (Leonardi et al., 2021). For example using layer-by-layer electrostatic nano-assembly of oppositely charged polyelectrolytes resulted in high sensitivity in streptavidin detection with a detection limit of 600 fM. This method seems to obtain superior performance compared to silane-based covalent chemistry (Mariani et al., 2018).

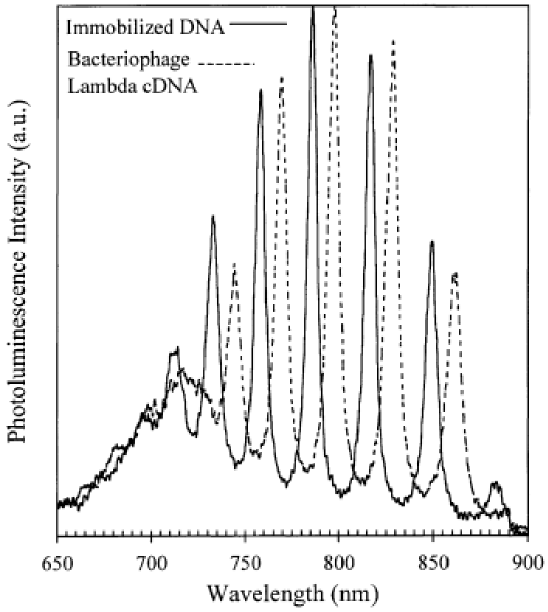

Figure 7: Change in photoluminescence of the biosensor upon DNA binding. A 12 nm red-shift is observed when the bacteriophage lambda DNA binds to a complementary DNA sequence immobilised on the porous silicon sensor surface. Figure reproduced from Chan et al., Copyright © 2001, with permission from Elsevier (Chan et al., 2001).

Porous silicon biosensors can detect antibody-antigen interactions through interferometric measurements. The detection and quantification of immunoglobulin levels like IgG, can provide information about the function of the immune system or the level of immunity. Szili et al. developed a technique analogous to the ELISA test by using HRP enzymes-conjugated antibodies specific for IgG in the presence of tetramethylbenzidine as a chromogenic compound. Once the antibody-antigen complex formed, the HRP enzyme catalysed the oxidation of TMB producing a colour product which caused a change in the effective optical thickness measurement. The oxidation of the chromagen amplified the signal enabling detection of IgG as low as 0.2 µg/mL (Szili et al., 2011). In another approach, pSi immunosensor detected binding of antigen (goat anti-human IgG) to surface immobilised human IgG by monitoring resistance changes using cyclic voltammetry. The resulting antigen-antibody complex inhibited the electron transfer causing a decrease in anodic current (Prabhakar et al., 2012). While antibodies are commonly used in immunosensors, they have downsides like high cost, large size and instability that can lead to a reduction in biological performance (Tieu et al., 2019).

Aptamers offer an alternative to antibodies as their short single stranded DNA or RNA oligonucleotides fold into 3D conformations that can selectively bind with targeted analytes such as proteins while providing higher selectivity than antibodies. For example, Chhasatia et al. compared an aptamer-based and antibody-based porous silicon platform for their detection of insulin. The binding of the insulin caused a refractive index change measured through a red-shifted interferometry signal with the aptasensor reporting higher response and lower limit of detection than the antibody sensor (Chhasatia et al., 2017). Similarly, an aptamer specific to the blood coagulating factor α-thrombin was detected with an aptasensor, reaching a 1.5 nM detection limit with high selectivity (Terracciano et al., 2016). This sensor also demonstrated reversibility as upon heating, the affinity with the thrombin was lost enabling the device to be reused (Terracciano et al., 2016).

1.9.8 Photophysical Mechanism in Photodynamic and Photothermal Therapy

Porous silicon is a promising nanomaterial for optoporation because of its ability to be excited by two-photon infrared light (Park et al., 2009). This feature has proven to be particularly advantageous in photodynamic therapy and photothermal therapy, offering a minimally invasive strategy for treating solid tumours in cancer therapy.

The photodynamic process relies on photosensitisers such as porous silicon, capable of absorbing light to generate ROS responsible for cancer cell destruction (Kovalev & Fujii, 2005). Upon laser irradiation, these nanoparticles absorb light and transition from their ground singlet state (S_0) to one of the vibronic energy levels of the short-lived excited singlet state (e.g. S_1, S_2). The excited electron can subsequently revert to its ground state through radiative and non-radiative pathways (**Figure 8**). Radiative decay pathways are collectively termed photoluminescence and includes the fluorescence and phosphorescence emissions. In fluorescence, a radiative transition occurs between two states of the same multiplicity (e.g. S_1 and S_0), whilst in phosphorescence, the radiative transition occurs between different multiplicities (e.g. T_1 and S_0). Phosphorescence is typically facilitated by intersystem crossing (ISC), in which an isoenergetic transfer of the excited electron occurs between a singlet and triplet excited state. The triplet excited state is characterised by a long lifespan of 10 – 100 μs (Gross et al., 2003; Grumezescu, 2016).

Beyond radiative pathways, there are two prominent oxygen quenching pathways, referred to as type 1 and type 2 mechanisms (**Figure 8 inset**). In type 1 reactions, an electron transfer from the excited silicon molecule in the triplet state to molecular oxygen forming radicals. These radicals can subsequently interact with oxygen, yielding superoxide (O_2^-) and hydroxyl radicals (·OH) which can initiate a chain reaction of lipid peroxidation, ultimately leading to cell death via necrosis (Grumezescu, 2016). Alternatively in type 2 reactions, the energy from the excited triplet state of pSi is transferred to molecular oxygen, producing highly reactive singlet oxygen ($^1O_2$) (Fujii et al., 2005). Singlet oxygen is a highly cytotoxic ROS that culminated in cell death, either through necrosis or apoptosis (Shen et al., 2016).

In addition, to enhance the interaction of pSi nanoparticles with the laser, the nanoparticles were conjugated with a porphyrin ring. When irradiated at 650 nm, these conjugated nanoparticles induced 42% cell death compared to only 19% cell death in the absence of the laser (Secret et al., 2013). Continuing on the same line of research, two-photon excitation yielded an increased production of ROS leading to 75% cell death (Secret et al., 2014).

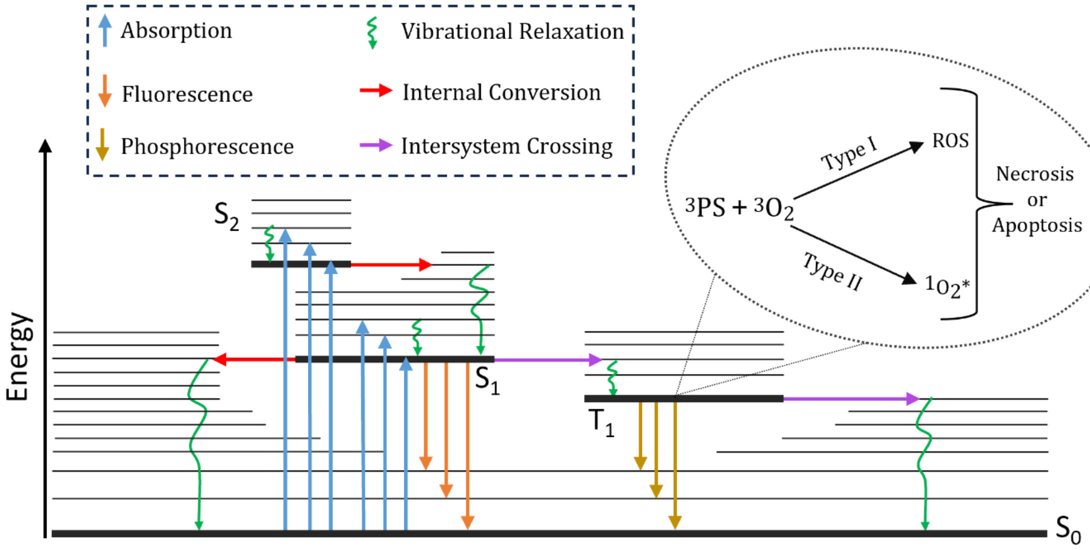

Figure 8: Jablonski diagram showing characteristic photophysical processes on laser excitation of pSi nanoparticles. Photophysical processes are initiated by the absorption of photons, initiating a transition of an electron from the ground state to an excited state S_n (e.g. S_1 or S_2). Photophysical pathways for the electron from the excited state to another electronic state can either be radiative (fluorescence or phosphorescence) or non-radiative (internal conversion or intersystem crossing). Transition from higher energy vibronic energy levels to the lowest energy vibronic energy level of a given electronic state is facilitated by vibrational relaxation. **Inset**: Reaction of the excited pSi nanoparticles (referred to here as a photosensitiser, or PS in short) with oxygen, results in Type I (ROS) and Type II (singlet oxygen) quenching pathways.

Similarly, extensive research has been conducted on the concept of generating sufficient localised heat for cancer treatment (Hong et al., 2011; Jaque et al., 2014; Xia et al., 2016).

In fact, because of the wider energy band gap than crystalline silicon, porous silicon nanoparticles could elevate the temperature to 55 °C after 3 minutes of NIR exposure at 300 mW cm^{-2} leading to significant cell damage (Lee et al., 2008). For instance, Hong et al. identified that in vitro cells treated with both pSi and near-infrared (NIR) irradiation generated heat that attained a low cell viability of 6.7%, as compared to untreated cells or cells treated with only one type of treatment (either pSi or NIR irradiation) (Hong et al., 2012). In another study, the photothermal property and the drug-carrying ability of porous silicon nanoparticles were synergistically used in chemo-photothermal therapy. In this instance, NIR irradiated cells containing pSi nanoparticles loaded with anti-cancer doxorubicin (DOX) triggered the release of DOX inside cancer cells and exhibited significantly improved inhibition of the proliferation of cancer cells in vitro (Xia et al., 2016).

1.10 Summary

Optoporation offers intricate spatial control over the introduction of various cargo molecules into the cytosol by disrupting the cell membrane. As a results, this technique has demonstrated potential for gene therapy and genetic engineering by enabling the delivery of DNA plasmids, mRNA and CRISPR/Cas components for gene editing, regulation and expression. In addition, the precise spatial delivery of nucleic acids, proteins and small compounds has facilitated the study of stem cell differentiation providing valuable insights into stem cell behaviour. In addition, the introduction and translation of specific mRNA molecules into distinct cell regions has also revealed the impact of localisation on protein function and processes such as differentiation, proliferation, and apoptosis. Beyond stem cell research, optoporation holds promise for applications in areas like CAR-T cell therapy, where it could enable the efficient delivery of gene-editing components like CRISPR/Cas into hard-to-transfect T cells for ex vivo engineering. Clinically, optoporation could facilitate targeted drug delivery by functionalising nanoparticles with targeting moieties for specific cell types like cancer cells. Moreover, optoporation facilitates the intracellular delivery of macromolecules, probes, and imaging agents for applications like live-cell microscopy.

The optoporation approach can either entail direct laser use, which is labour intensive or can employ sensitisers to increase the throughput. However, these sensitisers are generally non-biodegradable and may cause cytotoxicity highlighting the need for alternative optoporation agents. Porous silicon nanoparticles emerge as a promising nanomaterial for exploring reversible cell permeation and biomolecule delivery because of their biodegradable and biocompatible nature. Moreover, porous silicon nanoparticles are easy to fabricate, can be readily functionalised to tune optoporation efficiency, and have shown to interact with femtosecond laser irradiation at the NIR region. Collectively, these properties underscore the potential suitability of porous silicon nanoparticles for use as optoporation agents.

Chapter 2 - Project Aim and Objectives

This project aims to develop an optoporation platform for selectively delivering biomolecules into chosen cells within a cell population, both in a 2D cell culture and in a 3D model system.

Cellular function depends heavily on the precise timing and location of the gene expression. Therefore, single-cell gene delivery tools that enable precise spatial and temporal control are essential for dissecting complex gene regulatory pathways underlying cellular function. However, current intracellular delivery technologies possess limitations in efficiency, biocompatibility, single-cell selectivity and spatiotemporal control over nucleic acid delivery. Optoporation in the presence of nanomaterials has shown promise as a highly selective transfection approach for introducing nucleic acids into the desired cells without impacting neighbouring cells. Nevertheless, in vitro, optoporation research has thus far predominantly been explored in 2D cultures and is restricted by the degradability and cytotoxicity of some of the nanomaterials used. This project aims to address these gaps by engineering porous silicon nanoparticles as a biodegradable nanomaterial that can couple with near-infrared irradiation to induce transient membrane permeability. Porous silicon nanoparticles have previously been used in photothermal and photodynamic therapy, both of which rely on disruptive nanoparticle-laser interaction to compromise cell membrane integrity. Building on these foundations, I hypothesised that fine-tuning the laser parameters and nanoparticle features, such as concentration and surface chemistry, can allow the restoration of membrane integrity post-optoporation

The use of porous silicon nanoparticles in conjunction with near-infrared radiation for spatial-temporal biomolecule delivery offers several advantages. Firstly, the absorption characteristics of these nanoparticles through a two-photon excitation system in the near-infrared region enables penetration into tissues, allowing for the optoporation of cells embedded deep within the 3D cellular environments. Secondly, in contrast to flat substrates, porous silicon nanoparticles exhibit uniform distribution within 3D systems, affording greater flexibility over the targeted delivery areas. Additionally, the surface of porous silicon nanoparticles can be readily functionalised, thereby improving light absorption and enhancing the efficiency of optoporation for intracellular delivery.

To achieve the prescribed aim, three primary objectives were defined as follows:

Objective 1: Optimising mesoporous silicon nanoparticles for efficient optoporation (Chapter 4).

Research suggests nanoparticle geometry may influence optoporation efficiency. To investigate this relationship, the first aim centred on developing and optimising porous silicon nanoparticles of varying geometries. This involved fabricating discoidal-like nanoparticles via the electrochemical etching method and optimising metal-assisted chemical etching techniques to generate porous silicon rod-like structures. By exposing 2D and 3D cell cultures to a range of nanoparticle concentrations, I determined the seeding density window that maintained viability, and that needed to be explored for optoporation purposes.

Objective 2: Optoporation-mediated intracellular delivery in 2D and 3D cell cultures (Chapter 5).

Laser-triggered cargo delivery relies on nanoparticles that can interact with light to induce transient and localised membrane permeability. As geometry may modulate the optoporation outcome, the second aim sought to quantitatively compare discoidal and rod-like nanoparticles for light-triggered membrane poration capacity using propidium iodide uptake as a marker. After identifying the optimal nanoparticle structure, I systematically optimised the laser parameters to strike the right balance between maximising optoporation efficiency and minimising cytotoxic impacts as measured through cell viability assays. Having optimised the formulation for nanoparticle delivery, and the laser excitation settings, I evaluated the nucleic acid transfection and downstream expression in a 2D cell culture system. Finally, I also investigated the feasibility of optoporation in 3D cancer spheroid models by delivering propidium iodide into 3D cell cultures.

Objective 3: Enhancing optoporation efficiency using mesoporous silicon nanoparticles functionalised with photo-switchable organic ligands (Chapter 6).

Coordinated application of light-controlled nucleic acid release and optoporation presents a potential strategy to amplify the yield of nucleic acid delivery. This coordinated strategy formed the basis of the third aim, which focused on developing and implementing a photo-switchable porous silicon nanoparticle system for amplified nucleic acid transfection. Initial efforts centred on synthesising and characterising a photo-switchable molecule with nucleic acid binding capacity and grafting this compound onto the nanoparticles' surface. I tested the improved transfection approach in the 2D and 3D cell culture environments.

Chapter 3 - Materials and Methods

3.1 Nanoparticles Fabrication and Characterisation

3.1.1 Nanoparticles Fabrication through Electrochemical Etching

The electrochemically etched nanoparticles were obtained by the following steps:

A. Mesoporous silicon was anodised from boron doped p+ type Si (100) oriented wafers (University Wafers Inc, USA) with a resistivity of 0.01 - 0.02 Ω cm. The electrolyte solution consisted of hydrofluoric acid (HF, 50%, VLSI Selectipur®, 7664-39-3) and absolute ethanol (99%, Sigma-Aldrich, 32221) in a 1: 2 volumetric ratio. Electrochemical etching of porous multilayers was carried out in a Teflon etch cell that exposed 8.2 cm in diameter of the polished silicon wafer surface (anode), using a platinum mesh counter electrode (cathode). The backside of the silicon wafer was contacted with a sheet of aluminium foil so that only the front side of the wafer was exposed to anodise electrolyte (**Figure 9a, b**).

B. Two current densities were applied successively in which a lower current density of 42 mA/cm^2 was applied for 3 s, followed by an upper value of current density of 168 mA/cm^2 for 0.35 s. These two currents were repeated for 360 times taking approximately 20 minutes of etching time. After cycle completion, the etched layers were lifted off from the crystalline silicon substrate via a high current density of 246 mA/cm^2 for 1 s.

C. The hydrogen-terminated surface of the anodised pSi was stabilised via thermal oxidation by heating the etched wafer in the air at 300 ˚C for 2 hours.

D. The almost freestanding pSi films were then easily scrapped from the wafer (**Figure 9c**), and fractured by probe sonication (Sonics & Materials™ Ultrasonic Processor model VCX130) in isopropanol (IPA, Sigma-Aldrich, 59300) for 6 hours, 70% power with 4 s on and 4 s off.

E. The resulting dispersion of pSi nanoparticles was then centrifuged at 20,000 rcf for 5 minutes to remove the fine particles in the supernatant solution while keeping the pellet.

F. The pellet was redispersed in IPA via sonication for a few seconds. The solution was then centrifuged at 1300 rcf for 5 minutes and the brown supernatant solution containing the particles of the desired size was collected.

G. Step F was repeated five times until the supernatant was almost clear. The supernatant solutions collected through the 1300 rcf were combined and centrifuged at 20,000 rcf, to remove the supernatant and redistribute the pellet in a known volume of IPA. This step produced a concentrated solution of nanoparticles.

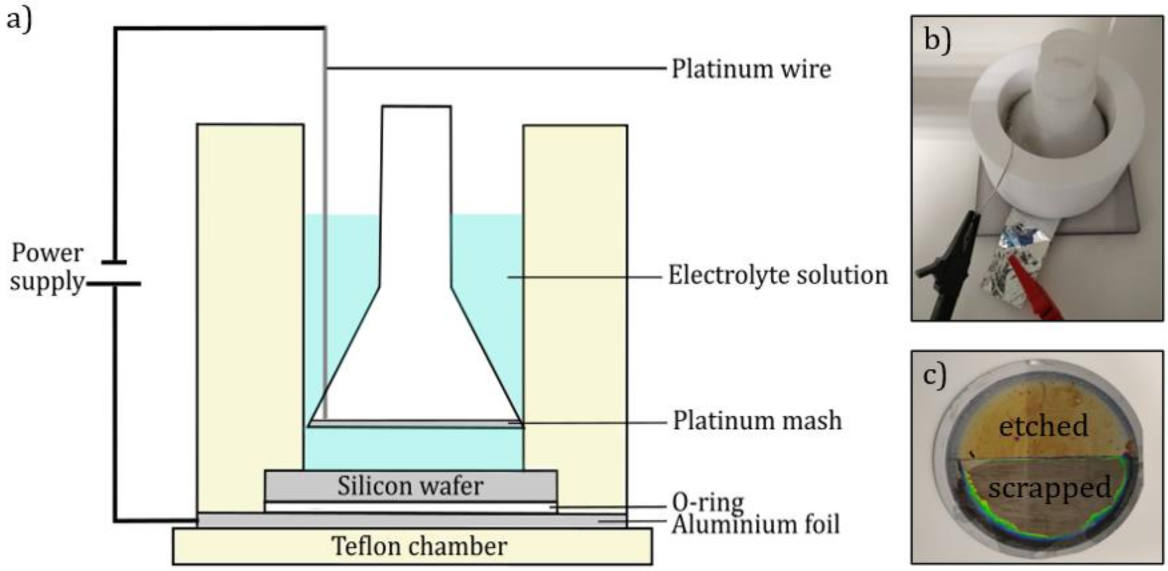

Figure 9: Summary of the setup used for electrochemical etching. a) schematic of the electrochemical etching chamber, b) the electrochemical chamber set up for the etching process, c) half scrapped wafer to remove the etched films form the solid silicon wafer.

3.1.2 Nanoparticle Fabrication through Metal-Assisted Chemical Etching (MACE)

A. MACE nanowires fabrication consisted of dipping the wafer in a solution of 5 mL 0.4 silver nitrate ($AgNO_3$, Sigma-Aldrich, 31630), 20 mL HF and 75 mL of distilled water for 2 minutes with continuous mixing. The wafer was then washed with water and ethanol and left to dry.

B. Next, the wafer was dipped in 400 mL of etching solution H_2O_2: HF (1.5% v/v) for 20 minutes. The etching solution was prepared by mixing 80 mL of 49% v/v HF, 6 mL 30% wt hydrogen peroxide (H_2O_2, Acros Organics, AC411885000) and topped up with distilled water in a polypropylene beaker.

C. To stop the etching, the wafer was removed from the etching solution, then rinsed with distilled water and ethanol, and dried with compressed air.

D. The silver was removed by dipping the etched wafer in 100 mL of gold etchant (Sigma-Aldrich, 651818) solution for 10 minutes. The wafer was then washed with water and ethanol and left to dry.

E. The hydrogen-terminated surface of the pSi was stabilised via thermal oxidation by heating the etched wafer in the air at 300 °C for 2 hours.

F. The etched silicon layer was scrapped off from the wafer and fractured by ultrasonication (Elma, model Elmasonic S) in water for 8 hours. This was an optimised step that was determined by comparing the hydrodynamic diameter of the nanoparticles obtained when sonicating in water versus IPA. The preferred solution was selected.

G. The resulting dispersion of pSi nanoparticles was then centrifuged at 20,000 rcf for 5 minutes to remove the fine particles in the supernatant solution while keeping the pellet.

H. The pellet was redispersed in ethanol via sonication for a few seconds. The solution was then centrifuged at 3000 rcf for 5 minutes and the brown supernatant solution containing the nanoparticles of the desired size was collected. This was an optimised step that was determined by comparing the hydrodynamic diameter of the nanoparticles obtained when centrifugating at 1000, 2000 and 3000 rcf for 5 minutes.

I. The supernatant solutions collected were combined and centrifuged at 20,000 rcf, to remove the supernatant and redistribute the pellet in a known volume of ethanol. This step produced a concentrated solution of nanoparticles.

3.1.3 Measuring Nanoparticles Roundness using ImageJ

Roundness was measured by processing the images on ImageJ. Each image was loaded onto ImageJ and a suitable upper and lower threshold were identified in order to pick the pixels that clearly make up the nanoparticles. Once the threshold is set, the particle roundness was measured by using the analyse particles function. Due to the presence of small pores and image noise, a criterion of identified particles being > 100 nm was applied. The mean and standard deviation of the roundness was reported.

3.1.4 Amine Group, FITC and Ocean Blue Functionalisation of pSi Nanoparticles

The mesoporous silicon nanoparticles prepared by both the EC anodisation and the MACE method were functionalised with 3-aminopropyltriethoxysilane (APTES, Thermo Scientific, 430941000). The APTES functionalisation was carried out by mixing the 1 mg/mL of nanoparticles and 2% APTES in a thermoshaker (Eppendorf Thermomixer® C Model 5382) at 800 rpm at room temperature for 2 hours. The resulting functionalised particles were washed twice with IPA, once with ethanol and redispersed in 4 mL of ethanol. The 2% APTES concentration was optimised by investigating different APTES concentrations ranging from 0.5 – 5%. To directly measure APTES functionalisation saturation, aliquots were withdrawn after 1, 2, 5 and 24 hours at each APTES concentration tested. The surface charge of the nanoparticles in these aliquots was then quantified as an indication of amine density on the particles.

To the APTES tagged nanoparticles in IPA, fluorescein isothiocyanate (FITC, Sigma-Aldrich, F7250) was added in the ratio of 3 mg: 0.0213 mmoles respectively and left mixing in a thermoshaker at 800 rpm for 2 hours at room temperature. To stop the functionalisation reaction, the particles were washed three times with ethanol and redispersed in a known volume of ethanol and stored at 4 °C for later use. Same process of FITC applied for functionalising Ocean Blue (OB, Tocris, 6489) to EC nanoparticles.

3.1.5 Particle Size and Surface Charge Measurements

Particle size was characterised by dynamic light scattering (DLS) measurements (Zetasizer Nano ZS, Malvern Instruments, Malvern, U.K), based on the intensity fluctuation of back-scattering laser light. Readings of the hydrodynamic diameter and polydispersity index (PDI) were done at 25°C with 1.5 mg/mL nanoparticle concentration in ethanol with viscosity set to 1.07 cP and refractive index to 1.36. Measurements were taken three times and average values reported.

Surface charge was characterised by ζ-potential measurements (Zetasizer Nano ZS, Malvern Instruments, Malvern, U.K). The electrophoretic mobility of pSi nanoparticles was measured via the electrophoretic light scattering (ELS) technique using the Schmolukowski equation. A 10 – 80 μg/mL range of nanoparticles concentrations were tested to determine its influence on the reading. The measurements were performed by dispersing the nanoparticles in a 5 mM potassium phosphate buffer, pH 6.0. The buffer solution was prepared from a stock solution of 100 mM as 13.2 μL potassium phosphate dibasic (K_2HPO_4, Sigma, P-3786) and 86.8 µL potassium phosphate monobasic (KH_2PO_4, Sigma, P-0662) were added to 19.9 mL of water. An average from three consecutive measurements was taken for each run.

3.1.6 Estimation of Specific Surface Area, Pore Size and Pore Volume with N_2 sorption

The specific surface area, the pore size and the pore volume of pSi for EC and MACE nanoparticles were characterised by Dr Frédérique Cunin and her group at the Institute Charles Gerhardt Montpellier (ICGM). The suspension of pSi nanoparticles was dried at 60 °C to obtain 50 mg powdered nanoparticles. The surface area calculations were done using N_2-sorption isotherms at 77 K (TriStar 3000 Micromeritics Inc.), specific surface areas were calculated using the Brunauer-Emmett-Teller (BET) method and the pore size and pore volume were calculated with the Barrett-Joyner-Halenda (BJH) method.

3.1.7 Loading EC Nanoparticles with mRNA

The protocol was taken from Wan et al., 2014 and Wang et al., 2018 with modifications. A 100 µL of 25 µM of Cy5-tagged eGFP mRNA was prepared in ethanol from a stock of 3 mM. A volume of 40 µL from the 25 µM mRNA was mixed with 500 µg of amine-functionalised pSi nanoparticles to final volume of 500 µL in ethanol. The resulting solution was mixed in a thermomixer at 25 °C for 1 hour for the mRNA to adsorb onto the surface and pores of pSi nanoparticles. Then, to separate the unbound mRNA in solution from the mRNA bound to the nanoparticles, the mixture was centrifuged at 6000 rpm at 4 °C for 10 minutes. The collected supernatant solution was quantified using the NanoDrop 2000 (Thermo Fisher Scientific) at a wavelength of 260 nm. The loaded mRNA onto the nanoparticles was calculated by subtracting the amount of mRNA left in the supernatant after incubation from the initial mRNA in solution. Visualisation of the nanoparticles loaded with mRNA was carried out through fluorescent images at the Cy5 channel to visualise the Cy5 tagged mRNA together with the nanoparticles.

3.2 Cell culture

The cell type used in this study is Michigan Cancer Foundation-7 (MCF-7) epithelial breast cancer cell line. All cell cultures were supplemented with 5% carbon dioxide in humidified incubators at 37 °C and all aspects of tissue culture were handled under sterile conditions in safety cabinets and practising strict aseptic techniques. Prior to culturing, the cells tested negative for mycoplasma contamination. The MCF-7 cells were cultured with Dulbecco's Modified Eagle Medium (DMEM), high glucose, GlutaMAX™ (Gibco™, 10569010) supplemented with 10% fetal bovine serum (FBS) (Gibco™, 10270106) and 1% Penicillin Streptomycin (P/S, Gibco™, 15070063) and trypsinised (Gibco™, 25300054) once confluence was observed.

3.2.1 Cryopreservation and Thawing

To freeze MCF-7 cells, the cells were trypsinised and resuspended 1 x 10^6 cells in 1 mL of the freezing medium made up of 10% dimethyl sulfoxide (DMSO, ChemCruz®, sc-358801) and 90% FBS. The cell suspension was transferred to a cryovial (Greiner Cryos™, 122263) and stored in a cell freezing vial container (Corning™ CoolCell™ LX, 432003) at -80 °C overnight with IPA to achieve an approximate -1 °C per minute of cooling. The cryovial was transferred to a -196 °C liquid nitrogen tank the next day for long-term storage.

To thaw the cells, the cryovial was retrieved from the liquid nitrogen tank and thawed in a water bath at 37 °C for 1 minute. The solution of the cryovial was transferred to 10 mL of DMEM in a falcon tube and centrifuged at 1000 rpm for 3 minutes to pellet the cells and remove the DMSO from the supernatant. The cell pellet was resuspended in 5 mL of DMEM and transferred to a T-25 flask (Greiner CELLSTAR®, 690175) treated with polystyrene to increase hydrophobicity for cell adherence. The medium was changed the next day and the cells were left to grow for a few days prior to reaching 80% confluency leading to splitting.

3.3 Investigating the Interaction between the Nanoparticles and MCF-7 cells

3.3.1 Cell Preparation for SEM and EDX

On a 13 mm glass coverslip (VWR, 631-0148) 60,000 MCF-7 cells were seeded and incubated for 24 hours. After 24 hours, the desired concentration of pSi nanoparticles in OptiMEM was added and left incubating for a further hour. The cells were fixed with 4% wt/vol paraformaldehyde (PFA) for 15 minutes and then washed three times in phosphate buffer saline (PBS, Sigma-Aldrich, D8537) at 5 minutes intervals. Subsequently the cells were dehydrated through a graded ethanol series starting with

50% ethanol in distilled water for 10 minutes, then increasing the ethanol concentration to 75, 90, 95 and 100%, each time leaving the solution for 5 minutes. The 100% ethanol step was repeated twice, the second time left for 10 minutes. The cells were submerged in a solution of hexamethyldisilazane (HMDS, Sigma-Aldrich, 440191) and ethanol in the ratio of 1: 2 respectively which was then changed to 2: 1 respectively and finally to 100% HMDS, each step for 10 minutes. The HDMS formed a hydrophobic surface that preserved the external surface features (Katsen-Globa et al., 2016; Nation, 1983). The HMDS was left to evaporate slowly in the fume hood overnight resulting in a dried sample for the next day. The sample underwent gold sputter coating to cover the cells with an approximately 10 nm thick layer of gold to avoid signal saturation due to the accumulation of electrons on the biological components.

In addition to imaging the sample surface structure, elemental analysis was conducted with an energy-dispersive X-ray spectrometer (EDX) detector. The same sample preparation process was followed as above with the difference that the cells were seeded on polystyrene surfaces instead of the glass slides.

3.3.2 CellTiter-Glo® Viability Assay in the 2D System

The viability of MCF-7 was assessed for 24 hours after the interaction of the cells with the nanoparticles. In a 96-well plate, 10,000 cells were added per well in 100 µL DMEM and incubated for 24 hours. The desired nanoparticle concentrations ranging from 30 – 200 µg/mL were prepared in OptiMEM reduced serum media (Gibco™, 11058021). The DMEM was removed from the cells, replaced with 100 µL of the nanoparticle solution, and incubated for a further one hour. After one hour, the pSi nanoparticles were gently washed away with 100 µL DMEM and cells were further incubated for 24 hours. MCF-7 cells were supplemented with an equal volume of CellTitre-Glo® 2.0 luminescent cell viability assay reagent (Promega, G924B) and was covered with aluminium foil to protect from light. The plate was mixed vigorously for 2 minutes using an orbital shaker (180 rpm) and then was left on the bench for 10 minutes for the signal to equilibrate. The solution of each well was transferred to a 96 black F-bottomed well plate (Corning®, 3991) with three wells containing only DMEM and another three containing only CellTitre-Glo reagent thus serving as the blanks. The luminescent signal of each well was measured using CLARIOstar® Plus plate reader (BGM labtech) with 3600 gain.

3.4 MCF-7 Spheroid Preparation

3.4.1 Methocel Preparation

To prepare 1.2% w/v of Methocel™,1.5 grams of Methocel™ A4M (3000-5000 mPa.s - medium viscosity, Sigma-Aldrich, 94378) were transferred to a 250 mL Duran® glass bottle together with a magnetic stirrer and autoclaved for 45 minutes. Once the autoclaving process was finished, 250 mL of the DMEM media was added to the Methocel™ under septic conditions and placed on a hot plate at 70 °C for 30 minutes, with stirring set on a high. The temperature was lowered to 30°C for one hour then the heating was turned off and left to reach room temperature. The glass bottle was left stirring at 4 °C overnight and then stored for up to 6 months at 4 °C for later use.

3.4.2 Hanging Drop Method

Once confluency was reached, the cells were trypsinised and 120,000 cells were suspended in 1 mL of Methocel: DMEM with a final concentration of 1:4 (v: v) to form the seeding solution. Repeatedly, 25 µL containing 3000 cells were withdrawn from the seeding solution and transferred to the lid of the petri dish forming individual drops. The bottom of the petri dish was covered with 5 mL of PBS to serve as a hydration chamber. The lid was inverted and placed on the top of the petri dish for the drop to hang – a method known as the hanging drop method (**Figure 10**). The cells were incubated for 24 hours to form a spheroid.

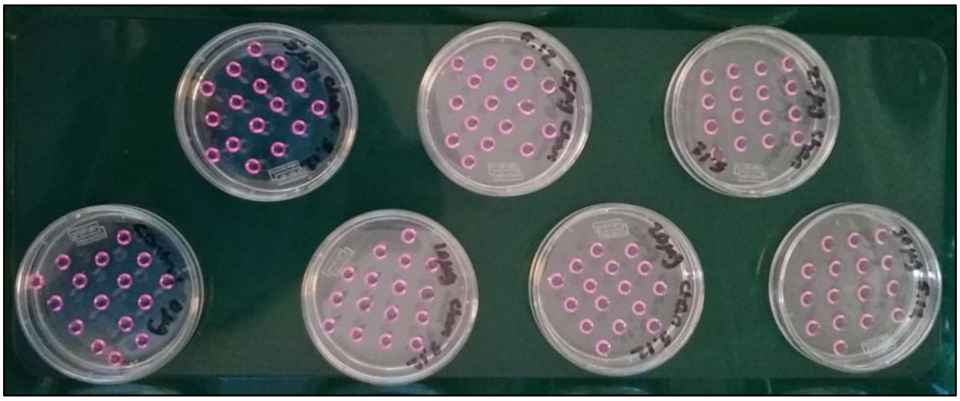

Figure 10: Arrangement of the hanging drops containing cells as placed on the lid of the petri dish.

3.4.3 Addition of Nanoparticles to the Spheroids

To add pSi nanoparticles to the cell suspension, the same protocol as above (3.4.3 Addition of Nanoparticles to the Spheroids) was applied with a slight variation. The desired concentration of the nanoparticles was withdrawn into an Eppendorf tube, centrifuged to form a pellet and the supernatant removed. The pellet was resuspended by sonicating with 100 μL of DMEM. To the nanoparticle suspension, cells, DMEM and methocel were added to form a seeding solution with a final concentration of 1: 4 (v: v) Methocel: DMEM. The resulting solution was used to form the individual drops.

Alternatively, nanoparticles were added only after incubating the cells through the hanging drop method for 24 hours. Therefore, the nanoparticle solutions were only added once the spheroids have already formed. In such a case, the desired concentration of the nanoparticles was withdrawn into an Eppendorf tube, centrifuged to form a pellet and remove the supernatant to redisperse in a small volume of OptiMEM. The nanoparticle solution was added to the drop holding the spheroids followed by an hour-long incubation.

3.4.4 Collagenase Treatment for Nanoparticle Diffusion to the Core of the Spheroids

The collagenase treatment protocol was adapted from Goodman et al., 2007. Spheroids were obtained after 24 hours of growth and checked for their spherical uniformity. For each experiment, 5 spheroids were handpicked with a pipette tip and transferred to a 1.5 mL Eppendorf tube. The appropriate concentration of collagenase (from *Clostridium histolyticum*, 0.44 U/mg, Sigma-Aldrich, C0130) was dissolved in OptiMEM ranging from 0.17 – 1.68 mg/mL. Collagenase was added to the spheroid together with 30 μg/mL of EC nanoparticles that was also dissolved in OptiMEM. Further OptiMEM was added to have a final volume of 500 μL per Eppendorf tube. The tubes were rotated at minimum speed for 3 hours in an incubator at 37 °C. The spheroids were removed and washed with PBS before further processing.

3.4.5 Spheroids Cryosections

The spheroids were fixed with 4% wt/vol PFA for 30 minutes and then washed three times in PBS at 5 minutes intervals. A 15% sucrose solution (Sigma-Aldrich, S9378) was added to the spheroids and left for 3 hours at 4 °C which was exchanged for 30% sucrose solution and left overnight at 4 °C. The spheroids were embedded in O.C.T (CellPath, KMA-0100-00A) and the sections were collected with a cryotome (Bright, OTF5000). The chamber and specimen temperature was set at -20 °C and the 10 μm thick sections were collected onto glass slides, superfrost® plus slides (Fisher Scientific, 12625336).

3.5 Bright Field and Immunofluorescence Imaging

The cryosectioned spheroids were stained with 1:1000 wheat germ agglutinin, Alexa Fluor™ 594 Conjugate (WGA, 1 µg/mL, Invitrogen, W11262) for 10 minutes to stain the cell membrane red followed by washing twice with PBS. The sections were further stained with 1:1000 4',6-diamidino-2-phenylindole (DAPI, 1 µg/mL, Sigma-Aldrich, D9542) for 5 minutes to stain the nucleus of the cells blue. The sections were then washed twice with PBS and were mounted with fluorescent mounting medium (Sera Care, 55700005).

Bright-field microscopy was performed on a Leica DMi8 inverted microscope (Leica-Microsystems). Immunofluorescent images were obtained using an inverted microscope (Nikon Eclipse Ti-E)

3.6 CellTiter -Glo® Viability Assay in the 3D System

The viability of MCF-7 spheroids interacting with the nanoparticles for 24 hours was assessed. A cell suspension with the respective nanoparticle concentration were grown via the hanging drop method. After 24 hours, the spheroids were transferred with a pipette tip to a 96-well plate where each well contained 4 spheroids to reduce variability per well. Each well was supplemented with and equal volume of CellTiter-Glo® 3D luminescent cell viability assay (Promega, G968A) as that of DMEM and was covered with aluminium foil to protect from light. The plate was mixed vigorously for 5 minutes using an orbital shaker (180 rpm) and then was left on the bench for 25 minutes for the signal to equilibrate. The solution of each well was transferred to a 96 black F-bottomed well plate with three wells containing only DMEM and another three containing only CellTitre-Glo reagent thus serving as the blanks. The luminescent signal of each well was measured using CLARIOstar® Plus plate reader with 3600 gain.

3.7 Multiphoton Femtosecond Laser Set-up

Optoporation and imaging of the cells was performed via a homemade setup. A 200 fs pulsed laser with tuneable wavelengths (700 – 1068 nm) pumped via a Verdi laser through an optical path reaching the inverted epifluorescent microscope (Nikon). All optoporation experiments were carried out at 800 nm and calibrated at the start of every experiment. The size and location of the areas targeted for optoporation, the scanning speed and the laser power were controlled via a custom-made micromanager controller system. Samples were illuminated through a 20x objective, 0.75 numerical aperture and the camera captured images automatically before and after optoporation.

3.8 Optoporation Experiments

3.8.1 Determining the Effect of pSi Nanoparticles Incubation Time on the Loading Density

MCF-7 cells were incubated at a seeding density of 10,000 in a 96 well plate for 24 hours to achieve approximately 60% confluency. After 24 hours, the DMEM was removed from the cells and replaced with an OptiMEM solution containing 30 µg/mL of FITC tagged EC-nanoparticles. The nanoparticles were left incubating for 30 minutes, one hour, two hours or four hours before washing with OptiMEM to remove the unbound nanoparticles. The cells at the four time points were imaged for FITC and the fluorescence was related to the relative concentration of nanoparticles that settled on the cells. Images were processed through ImageJ to reduce background signal by background subtraction, thresholding and single pixel removal.

3.8.2 MCF-7 Monolayer Cellular Construct

MCF-7 cells were incubated at a seeding density of 40,000 in an ibidi-glass bottom 8 well plates (Ibidi, 80807) for 24 hours to achieve approximately 60% confluency. After 24 hours, the DMEM was removed and replaced with an OptiMEM solution containing nanoparticles at a particular concentration and incubated for a further hour. After one hour, unbound pSi nanoparticles were washed away with OptiMEM.

3.8.3 Cellular Optoporation Efficiency in 2D cell cultures

Cells were prepared as described in section 3.8.2 MCF-7 Monolayer Cellular Construct. The OptiMEM was replaced with a solution of OptiMEM containing 7.5 µM of propidium iodide (Sigma-Aldrich, P4864). Cells were optoporated at a range of laser powers and scanning speeds. A new field of view was obtained for each different laser power or scanning speed tested. The cells were imaged with Cy3 filter, both before the optoporation treatment and post-optoporation and images were imported to ImageJ. The success of propidium iodide delivery was calculated by subtracting the signal of the pre-optoporation from the post-optoporation image and checking whether the propidium iodide inside the cells correlated with the same cells that were targeted with the laser. A percentage of poration efficiency was obtained. Overall, each experiment has 3 replicas all with three fields of view per replica for every different condition tested.

3.8.4 Short-Term Viability Post-Optoporation

Cells were prepared as described in section 3.8.2 MCF-7 Monolayer Cellular Construct. Cells were optoporated at a range of laser powers and scanning speeds. A new field of view was obtained for each different laser power or scanning speed tested. The cells were imaged with Cy3 filter, both before the optoporation treatment and post-optoporation. Immediately post-optoporation, cell viability was probed with calcein-acetomethoxy (AM) (2.5 µM, BD Bioscience, 564061). After 10 minutes the cells were washed with OptiMEM and viability imaging was performed using a DMi8 Microscope. The success of propidium iodide delivery together with the cells' ability to cleave the 'AM' moiety from calcein by cellular esterase was a measure of the cells' viability 30 minutes post-optoporation. A percentage of the short-term viability post-optoporation was obtained. Overall, each experiment had 3 replicas, with three fields of view per replica for every different condition tested.

3.8.5 Imaging for ROS

Cells were incubated at a seeding density of 40,000 in an ibidi-glass bottom 8 well plates (Ibidi, 80807) for 24 hours to achieve approximately 60% confluency. After 24 hours, two negative controls were prepared for detecting the presence of ROS. One of the controls involved the addition of 1 µM of fluorescent 2',7'–dichlorofluorescein diacetate (DCFH-DA, abcam, ab113851) and one control was without DCFH-DA to measure for any background fluorescence. The positive control involved the addition of 200 µM of H_2O_2 with the cells and the sample was incubated for 1 hour. Then the cells were washed with OptiMEM and DCFH-DA was incubated with the cells for 10 minutes prior to imaging.

Cells were prepared as described in section 3.8.2 MCF-7 Monolayer Cellular Construct. DCFH-DA was added to the cells and the cells were targeted with the laser to determine whether optoporation lead to ROS generation. Imaging for ROS was done 10 minutes after optoporation.

3.8.6 Imaging for Caspase 3/7

Cells were prepared as described in section 3.8.2 MCF-7 Monolayer Cellular Construct. After 24 hours the cells were optoporated in the presence of 5 µM caspase 3/7 (Invitrogen™, C10723) and returned back to the incubator. Imaging for caspase 3/7 detection was carried out one hour after optoporation with a 488 nm excitation wavelength.

3.8.7 In Vitro mRNA Transfection with Optoporation

Cells were prepared as described in section 3.8.2 MCF-7 Monolayer Cellular Construct. After one hour, unbound pSi nanoparticles were washed away and cells were incubated with OptiMEM for 10 minutes to minimise mRNA degradation (Raes et al., 2020). The OptiMEM wash was removed from the cells and replaced by 100 µL of OptiMEM containing 0.5 µg of eGFP mRNA (EZ Cap™, R1016) and 0.5 µg of eGFP Cy5 tagged mRNA (EZ Cap™, R1011).

Cells were immediately optoporated at a range of laser powers and at a pre-determined scanning speed. A new field of view was obtained for each different laser power used and this was carefully mapped to retrieve the same exact area the next day. After laser treatment of multiple field of views within a single well, which took approximately 30 - 45 minutes, the cells were supplemented with fresh DMEM and returned to the incubator for 24 hours prior to analysing the mRNA expression.

3.8.8 In vitro mRNA Transfection with Lipofectamine (Control)

Cells were prepared as described in section 3.8.2 MCF-7 Monolayer Cellular Construct. After one hour, unbound pSi nanoparticles were washed away and cells were incubated with OptiMEM for 10 minutes. A 1 µL of lipofectamine™ MessengerMax™ (Invitrogen, LMRNA001) was added to 25 µL of OptiMEM and incubated at room temperature for 10 minutes. A 0.5 µg of eGFP mRNA and 0.5 µg of eGFP Cy5 tagged mRNA were diluted in 25 µL of OptiMEM, were mixed well via pipetting, were added to the lipofectamine™ dilution and the resulting 50 µL were incubated for 5 minutes at room temperature. The OptiMEM was replaced by fresh 350 µL of OptiMEM together with the 50 µL of lipofectamine-mRNA solution. Cells were then incubated for a further 24 hours prior to analysing the mRNA expression.

For the experiment involving a titration of the eGFP mRNA concentration, the same protocol described here was carried out where a total of 0.125, 0.25, 1.0 and 2.0 µg of eGFP mRNA and eGFP Cy5 tagged mRNA were added in a 1: 1 proportion. The resulting mRNA was mixed with 0.125, 0.25, 1.0 and 2.0 µL of lipofectamine respectively.

3.8.9 Cellular Optoporation Efficiency in 3D Spheroids

Spheroids were prepared as described in section 3.4.3 Addition of Nanoparticles to the Spheroids. Both types of spheroids, those with uniformly mixed EC-nanoparticles and those with EC-nanoparticles at its periphery were transferred to an ibidi-glass bottom 8 well plates. A solution of OptiMEM with 7.5 µM of propidium iodide was added and optoporation was performed at multiple areas within the spheroid. Images were taken at z-steps of 10 µm both before and after optoporation to determine the optoporation delivery depth within the spheroid.

3.9 Grafting Electrochemically Etched Nanoparticles with Isocyanopropyltriethyoxysilane (ICPES)-azobenzene@Lys

This work was done in collaboration with Dr Frédérique Cunin and her group at the Institute Charles Gerhardt Montpellier (ICGM). The protocols described below were first carried out at ICGM under the supervision of Dr Sofia Dominguez-Gil and replicated at the King's College London facility.

3.9.1 Synthesis of Azobenzene@Lys(diBoc)

Azobenzene@Lys(diBoc) was supplied in the dry state by the technicians at ICGM. The protocol for its synthesis was adapted from Rahim et al., 2011. Hydroxybenzotriazole (306 mg, 2.26 mmol) and N,N'-dicyclohexylcarbodiimide (600 mg, 2.91 mmol) were added under an Argon atmosphere to a solution of Boc-Lys(Boc)-OH (dicyclohexylammonium) salt (682 mg, 1.96 mmol) in dry/anhydrous dimethylformamide (DMF) (10 mL) at room temperature. After one hour 4,4'-diaminoazobenzene (600 mg, 2.83 mmol) was added and the mixture was stirred at room temperature overnight. The mixture was then diluted with brine and extracted with ethyl acetate. The combined extracts were dried ($MgSO_4$) and the solvent was removed under reduced pressure. The residue was purified through column chromatography, dichloromethane: ethyl acetate and dried to form an orange solid. The resulting compound was characterised by ^{1}H NMR and FTIR.

3.9.2 The Silanisation Step

Azobenzene@Lys(diBoc) (69.2 mg) was added to a 50 mL 3-neck round-bottomed flask, attached to a reflux system and flushed with an inert gas, nitrogen. Anhydrous tetrahydrofuran (THF, Thermo scientific, 457071000, 4 mL) and isocyanopropyltriethoxysilane (ICPES, Sigma-Aldrich, 413364, 34.82 µL) were added and the mixture was stirred at 65 °C in an oil bath (silicon oil, Sigma-Aldrich, 85409) for 24 hours. For purification, n-Pentane (Fisher, P/1020/08, 5 mL) was added and an orange precipitate formed. The excess pentane was decanted and left to evaporate via a nitrogen trap and an orange solid, ICPES-azobenzene@Lys(diBoc) was obtained. The resulting compound was characterised by ^{1}H NMR and FTIR.

3.9.3 Grafting to the Nanoparticles forming pSiNPs-ICPES-azobenzene@Lys(diBoc)

The nanoparticles (14 mg) were sonicated for 15 minutes prior to the reaction ensuring a homogenous solution. The solvent of the nanoparticles was removed via centrifugation at 20,000 rcf and redispersed in toluene (Fisher, T/2300/15, 4 mL) by sonicating for 15 minutes. ICPES-azobenzene@Lys(diBoc) (5.6 mg) was dissolved in toluene (2 mL) to have a mass ratio of 2.5: 1 between the nanoparticles and ICPES-azobenzene@Lys(diBoc) respectively. The two solutions were combined in a 50 mL Schlenk tube, three drops of water were added to promote hydrolysis and the solutions was stirred at 50 °C in an oil bath for 18 hours under inert conditions. After 18 hours, the reaction was stopped by removing the toluene via centrifugation at 20,000 rcf and the resulting nanoparticles were washed four times with ethanol. The resulting nanoparticles was characterised by FTIR, DLS and ζ-potential measurements.

3.9.4 Deprotection from the Boc Moiety

pSiNPs-ICPES-azobenzene@Lys(diBoc) was centrifuged at 20,000 rcf to remove the solvent, replace it with dichloromethane (Honeywell, 32222, 3 mL) and sonicate for 15 minutes. Trifluoroacetic acid (TFA, Fisher, T/3256/PB05, 6 mL) was added causing the solution to turn pink. The reaction was stirred at room temperature for 30 minutes, stopped by centrifugation at 20,000 rcf and washed four times with ethanol. The resulting nanoparticles was characterised by FTIR, DLS and ζ-potential measurements.

3.9.5 mRNA Loading and RNA Gel

mRNA and EC-nanoparticles were prepared in the mass ratio of 1: 10, 1: 25 and 1: 50 respectively to a final volume of 22 µL per sample. The mRNA and nanoparticle mixture was left incubating at 37 °C for one hour for complexation. After complexation, the samples were mixed with a DNA loading dye and were loaded on a 2% agarose gel stained with 1 µL of ethidium bromide. Gel electrophoresis was performed with 100 V for 30 minutes. For visualisation of the mRNA integrity, a UV lamp was used.

3.9.6 Cellular Optoporation Efficiency in 3D Spheroids

Spheroids were prepared as described in section 3.4.3 2Addition of Nanoparticles to the Spheroids. Spheroids with uniformly mixed grafted nanoparticles were transferred to an ibidi-glass bottom 8 well plates. A solution 0.5 µg of eGFP mRNA and 0.5 µg of eGFP Cy5 tagged mRNA were diluted in 100 µL of OptiMEM and added with the spheroids. Optoporation was performed at multiple areas within the spheroid. After laser treatment, which took approximately 30 - 45 minutes, the cells were supplemented with fresh DMEM and returned to the incubator for 24 hours prior to analysing the mRNA expression. After 24 hours, the spheroids were prepared as described in section 3.4.5 Spheroids Cryosections. The 10 µm thick sections were stained as described in section 3.5 Bright Field and Immunofluorescence Imaging and imaged for GFP expression using Leica DMi8 inverted microscope.

3.10 Statistical Analysis

All data were presented as mean with standard deviation and were analysed using the GraphPad Prism 9.4.1 software (La Jolla, CA, USA). The statistical tests used in each figure are mentioned in the figure caption. A p-value <0.05 was set as the level of statistical significance.

Chapter 4 - pSi Nanoparticles Fabrication and their Interactions with MCF-7 Cells

4.1 Introduction

The primary objective of this chapter is to fabricate and characterise two types of porous silicon (pSi) nanoparticles. Initially, the interaction of the nanoparticles will be examined using a 2D monolayer cell culture system. An initial screening of the biocompatibility of the nanoparticles with cells provides insights on the concentration ranges of the nanoparticles that can be incubated with cells while minimising negative impacts on cell health and viability. Moreover, the distribution of the nanoparticles among the cells will be investigated both in 2D and in 3D cellular environment. 3D cancer spheroids mimic complex 3D microenvironments, making them a suitable model to study biological mechanisms like tumorigenesis. By utilising distinct 2D and 3D culture systems, the interactions of nanoparticles can be analysed across different levels of cell organisational complexity.

Studies have already demonstrated that pSi nanoparticles can generate reactive oxygen species and heat once irradiated in the NIR region (Stojanovic et al., 2016). As a result, pSi nanoparticles have been tested for their potential as therapeutic agents in photodynamic therapy (PDT) and photothermal therapy (PTT), respectively (Jaque et al., 2014; Lee et al., 2007; Lee et al., 2012). However, whereas PDT and PTT utilise pSi nanoparticles to destroy cancer cells, optoporation has the opposite goal – it uses pSi nanoparticles along with light pulses to temporarily open pores in cell membranes for delivery of cargo into cells while leaving the cells alive.

While pSi nanoparticles remain understudied for optoporation-based delivery systems, plasmonic gold nanoparticles have been extensively examined for use in laser-induced poration. However, optoporation systems utilising gold nanoparticles face certain limitations, like poor biodegradability and potential cytotoxicity (Gupta & Malviya, 2021; Soenen et al., 2012), which biocompatible pSi nanoparticles may circumvent. The extensive prior research into optimising gold nanoparticle-mediated optoporation and analysing pSi nanoparticle parameters in PDT and PTT has provided a foundational understanding of how nanoparticle traits like shape and size influence optoporation efficiency (Bucharskaya et al., 2016).

The shape of nanoparticles can influence their absorption spectra. Specifically, different shaped nanoparticles will absorb light differently across the electromagnetic spectrum. This differential absorption of light can modulate interactions with cells and ultimately impact the efficiency of optoporation (Chen et al., 2007). This relationship between nanoparticle shape and optoporation efficiency is well explored with gold nanoparticles. A range of gold nanoparticles structures have been investigated, including but not limited to sphere- (Bergeron et al., 2015; Wilson et al., 2018), rod- (Yao et al., 2020) and star- (Bibikova et al., 2017; Hasanzadeh et al., 2021; Vanzha et al., 2017) shaped-nanoparticles. For example, gold nanostars have shown an 80% cell penetration with propidium iodide delivery in contrast to the 5% achieved with nanorods when illuminated with a wavelength of 1064 nm (Bibikova et al., 2017). On the other hand, gold nanorods have shown better interaction with 800 nm wavelength (MacKey et al., 2014; Von Maltzahn et al., 2009). While most prior work has focused on gold nanoparticles, the principles of shape-dependent optoporation may extend to other nanomaterials. As such, in this study I synthesised two different shaped pSi nanoparticles - rod-like and discoidal -like to compare their performance as mediators of optoporation.

The interplay between nanoparticle shape and size governs cellular uptake kinetics and efficiency. Ideally, nanoparticles should have slow internalisation into the cell enabling sufficient residency time on the cell surface membrane. This would position the nanoparticles in a manner that makes them easily accessible for their interaction with the laser, in contrast to having the nanoparticles endocytosed deep within the cell. For example, non-spherical nanoparticles demonstrated enhanced uptake rates and quantities compared to spherical nanoparticles (Gratton et al., 2008; Huang et al., 2010; Shahbazi et al., 2012). Additionally, size-dependent internalisation patterns exist with small nanoparticles of 50 nm exhibiting optimal cellular uptake (Jaque et al., 2014), whereas generally internalisation efficiency decreased for larger nanoparticles. In fact, the nanoparticles developed for clinical applications typically range from 2 – 200 nm as large particle sizes are more vulnerable to macrophage phagocytosis (Portney & Ozkan, 2006). However, in vitro studies have demonstrated that nanoparticle sizes of ~300 nm exhibit the lowest cellular uptake among the tested ranges (Gessner et al., 2020; Lu et al., 2009). Integrating these size considerations with shape effects, I aimed to fabricate 200-300 nm spherical and non-spherical nanoparticles. This tailored size range and morphology is expected to minimise internalisation kinetics and thus enabling greater interactions between nanoparticles and laser irradiation.

The surface chemistry of nanoparticles influences their interaction with cell membranes. One method to improve membrane interaction is silanisation with 3-aminopropyltriethoxysilane (APTES), which produces a positive surface charge to better adhere to the negatively charged cell membrane (Sanità et al., 2020). Silanisation is enabled by the etching process of nanoparticle production, which leaves reactive Si-H bonds on the surface. These bonds convert into negatively charged siloxane bridges (Si-O-Si) and silanol (Si-OH) groups during thermal oxidation and sonication. The now exposed silanol groups provide sites for cross-linking to the bifunctional APTES organosilane, which presents amine ($-NH_2$) groups on the nanoparticle surface (Jung et al., 2012; Kamegawa et al., 2018; Lee et al., 2018; Sypabekova et al., 2023). The primary amine groups on the APTES functionalised nanoparticles can readily form amide bonds with N-hydroxysuccinimide esters or carboxylic acids. This allows for the attachment of fluorescent dyes like fluorescein isothiocyanate (FITC) and ocean blue (OB) to improve nanoparticle visualisation. Additionally, the positively charged APTES surface enables the loading of negatively charged nucleic acids onto the nanoparticles through physical adsorption (Kamegawa et al., 2018).

Within this context, this chapter focuses on the fabrication, functionalisation, and cytotoxic assessment of two pSi nanoparticle morphologies – rod-like and discoid-like structures. The varying aspect ratios of the nanoparticle would present the pores in different orientations which is likely to have an impact on the nanoparticles' ability to absorb light. This variation in light absorption may translate to differences in the optoporation efficiency between the rod-like and discoid-like nanoparticles. The nanoparticles undergo a series of reactions to attach APTES followed by a FITC or ocean blue dye to track the distribution of the nanoparticles with the cells. Comprehensive physicochemical characterisation of the nanoparticles performed included dynamic light scattering (DLS), zeta potential analysis, Brunauer–Emmett–Teller (BET) surface area analysis, and scanning electron microscopy (SEM) imaging. Interaction of the nanoparticles with MCF-7 breast cancer cell membranes is initially explored qualitatively through SEM. Cytotoxic effects are then assessed via cell viability assays under increasing nanoparticle concentrations in both 2D and 3D cell culture systems..

4.2 Electrochemically Etched Nanoparticle Fabrication

Porous silicon nanoparticles can be formed by electrochemically etching a silicon wafer under an applied current, which generates porous silicon layers. The porous layers are then detached from the wafer by applying a high current and collected as a liquid suspension for ultrasonic fracturing (Heinrich et al., 1992). Sonication breaks down the layers into micron- and nanometre-sized fragments (Mason & Peters, 2002), which are then subjected to centrifugation for size fractionation.

However, sonicating a thick porous silicon layer does not provide precise control over where the layer fractures. This lack of control leads to a broad range of fragment sizes being produced, resulting in a lower yield of nanoparticles (Link & Sailor, 2003). To address this challenge, Qin et al. introduced a phased pulse method for creating pSi nanoparticles. The approach alternated between two current densities, referred to as 'low' and 'high' creating a sequence of porous silicon multilayers (Qin et al., 2014). Two current densities were needed because the current density affects the porosity and the pore size of the layers (Herino et al., 1987, Ohji et al., 2000). The 'low' current density generated a primary layer, characterised by small pores and porosity which later broke down to form the nanoparticles during sonication. The 'high' current density generated a perforation layer with bigger pores and higher porosity, acting as the preferred site for breaking the multilayers during sonication. Hence, these layers directed the fracturing process during sonication resulting in a more uniform particle distribution.

To determine an appropriate 'low' current density from which to form the nanoparticle, I tested three current densities of 10.4, 21.0, and 42.0 mA/cm^2 for 60 s. It was evident that increasing the current density resulted in a faster etching rate, causing the layer thickness to increase from ~670 nm to ~1140 nm to ~1845 nm (**Figure 11a**). Additionally, an increase in current density led to an increase in pore size. The diameter of the pores was measured from the cross-section of the layer (**Figure 11a**) using ImageJ which provided a preliminary estimation of the pore size. This initial assessment will be further confirmed through BET analysis once the desired nanoparticles have been obtained. The diameter at 10.4 mA/cm^2 was too small to be measured using ImageJ, at 21.0 mA/cm^2 the diameter was ~6 nm, and at 42.0 mA/cm^2 the diameter was ~13 nm. Xiao's study found the pore size range of 9.2 ± 1.8 – 11.8 nm ± 3.8 nm to be optimal for generating singlet oxygen ($^1O_2$) and disturbing the cell membrane (Xiao et al., 2011).

Therefore, I selected a current density of 42.0 mA/cm^2 to create nanoparticles with pore sizes within this optimal range.

The thickness of the perforation layer needed to strike a delicate balance. If the layer was too thin, cleavage will not be efficient. On the other hand, if the layer was too thick, the perforated layers themselves may fragment, generating very small porous silicon fragments. Previous research (Qin et al., 2014) has indicated that a thickness of 55 nm resulted in the highest level of homogeneity. Hence, I modified the current density to achieve a perforation layer with such a thickness and also with an increased pore size and higher porosity than the primary layer. These characteristics aimed to enhance the fracturing process of the perforation layer. Initially, a current density of 84 mA/cm^2 for 0.35 s was used, but the perforation layer was much thinner than the targeted 55 nm thickness (**Figure 11a**) and could not be measured with ImageJ. Instead, the current density was doubled to 168 mA/cm^2 for 0.35 s (**Figure 11b**), resulting in a layer with an average thickness of 52 nm ± 9 nm. This was in line with that deemed acceptable to improve the monodispersion of the particles (Qin et al., 2014).

I applied 360 cycles, each consisting of a low then a high current density etch to generate a multilayer structure of alternating thick and thin layers (**Figure 11b**). A higher current detached the etched layers from the solid silicon wafer and I subsequently sonicated the detached layers for 6-hours in IPA to fragment the multilayer structure into nanoparticles. Lastly I centrifuged the resulting solution at a speed of 1300 rcf and collected the supernatant containing the desired electrochemically etched nanoparticles (EC nanoparticles).

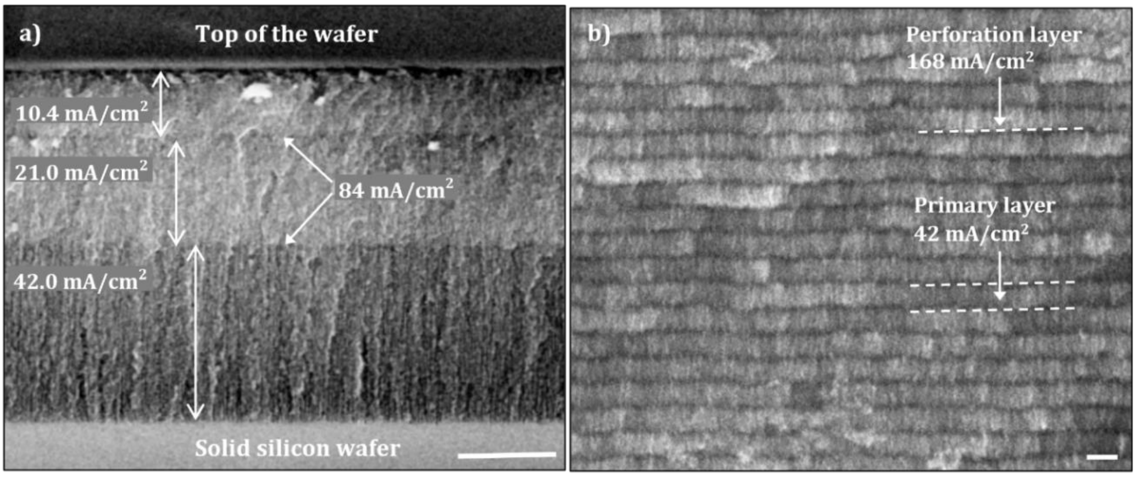

Figure 11: Characterisation of the electrochemically etched silicon wafer. The pores are growing perpendicular to the wafer surface. a) Cross-sectional SEM image of the electrochemically etched layers when 10.4, 21.0, and 42.0 mA/cm^2 were applied for 60 s. Scale bar 1 µm. b) Cross-sectional SEM image of the multilayered structure consisting of relatively thick primary layers separated by thinner perforation layers. Scale bar 200 nm.

4.2.1 Characterisation of the Electrochemically Etched Nanoparticles

DLS measurements determined the size and dispersity of the EC nanoparticle fraction that was collected after 6 hours of sonication followed by centrifuging at 1300 rcf. DLS is a commonly used method to characterise the size of the nanoparticles because it is inexpensive, well-established and easy to perform (Panchal et al., 2014). However, nanoparticle concentration affected DLS repeatability. Concentrated nanoparticle solutions produce artificially smaller sizes due to multi-scattering, where scattered light from one particle interacts with others before reaching the detector, thus losing its intensity (Bhattacharjee, 2016b; Panchal et al., 2014). On the contrary, dilute samples may not produce adequate scattering to be captured by the detector (Panchal et al., 2014). Therefore, I briefly investigated the optimal concentration for reliable determination of the nanoparticles size through DLS.

Increasing the dilution below 1.50 mg/mL increased variability among the replicates and created an instability in the polydispersity index (PDI) values (**Figure 12**). Both the hydrodynamic diameter and the PDI values appeared to stabilise when using a concentration of 1.50 mg/mL, and the standard deviation in the PDI values started to increase again slowly with higher concentrations. Therefore, 1.50 mg/mL concentration was selected for all the DLS measurements.

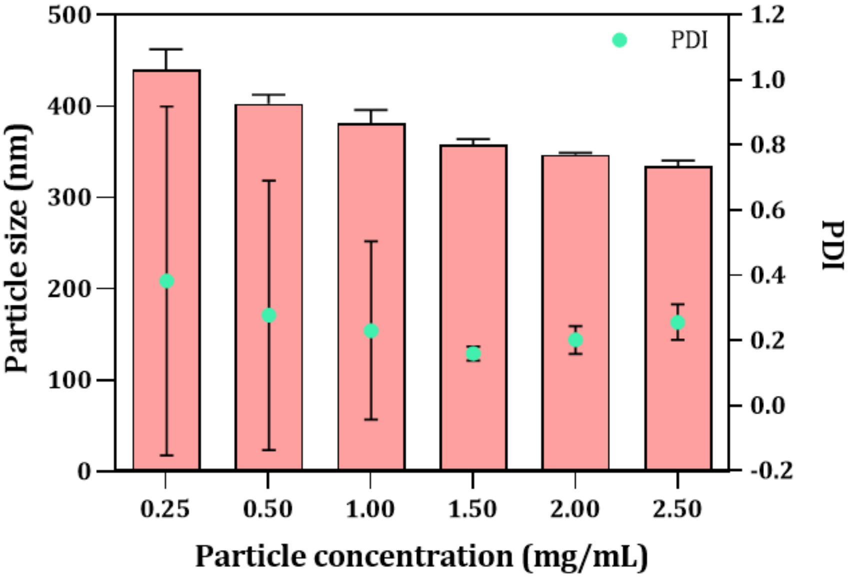

Figure 12: Optimisation of the nanoparticle concentration for DLS measurements. Particle size and PDI measurements obtained through DLS against the EC nanoparticle concentration. The PDI measurements are plotted as a secondary Y-axis.

The DLS measurements of the nanoparticles obtained through the electrochemical etching process was 282 ± 2.5 nm, with a PDI of 0.2 ± 0.02. The PDI is a parameter that describes the degree of non-uniformity of the nanoparticles' size distribution in a sample. The PDI value from DLS is derived by the following equation:

$$\mathrm{PDI} = \left(\frac{\text{standard deviation from the mean size}}{\text{mean size}}\right)^2$$

A PDI value close to 0 indicates a uniform sample with respect to the particle size. In contrast, a PDI value close to 1 indicates a high polydisperse sample with a broad size distribution. The range is divided into 3 classes with PDI of 0.0 - 0.1 described as 'monodispersed', 0.1 - 0.4 a 'moderate polydispersity' and >0.4 'broad polydispersity' (Malvern Panalytical, 2017). Therefore the EC nanoparticles fabricated here belonged to the lower range of moderate polydispersity suggesting that the nanoparticles had similar sizes.

The SEM images of the EC nanoparticles (**Figure 13**) showed the irregular discoidal structured nanoparticles of varying sizes. Using ImageJ, I calculated the aspect ratio from the SEM images by measuring the width and height of >450 nanoparticles. The aspect ratio distribution was best described by a log-normal distribution to account better for outliers in the data (Limpert et al., 2001). The majority of the nanoparticles had an aspect ratio falling between 1 and 1.5 with a median of 1.26 and a mean of 1.32 showing that the structure was roughly discoidal. The average diameter of the nanoparticles as calculated from the SEM image was of 323 nm ± 60 nm. To estimate how closely the particles resemble the shape of a circle or sphere, the roundness for the nanoparticles were measured on 208 nanoparticles by utilising the following expression,

$$roundness = \frac{4 \times area}{\pi \times x_{major}^2}$$

where area is the projected 2D area of the nanoparticle as measured using SEM and x_{major} is the length of the longest (i.e. major) axis along the nanoparticle. The roundness values indicate that the nanoparticles have an irregular shape with a mean roundness value of 0.61 ±0.16.

Nitrogen sorption isotherms were used to investigate the surface area using the Brunauer-Emmet-Teller (BET) model and the porosity using the Barrett-Joyner-Halenda (BJH) model (**Figure 14a**). These calculations revealed that the nanoparticles had a relatively large porous volume of 1.1 mL/g and a cumulative surface area of pores of 344.5 m^2/g. The nanoparticles had a porosity of 65% and an average pore diameter of 12.0 nm. This measurement closely aligned with the pore size observed in SEM images (**Figure 14b**) and was consistent with the size range deemed optimal for generating $^1O_2$.

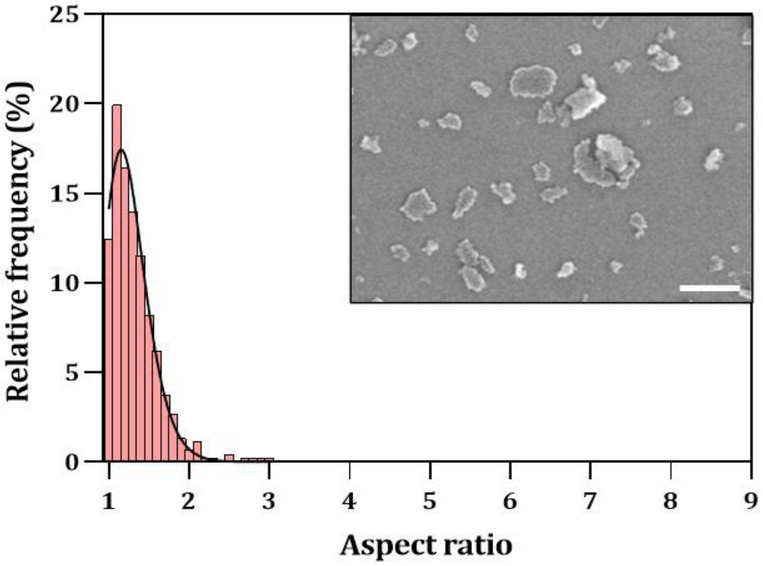

Figure 13: The relative percentage frequency of EC nanoparticles with a given aspect ratio. The aspect ratio as a measure of height vs width of the nanoparticles modelled by the lognormal distribution shows the positive skewness. Inset showing the structure of the EC nanoparticles via SEM. Scale bar 1 µm.

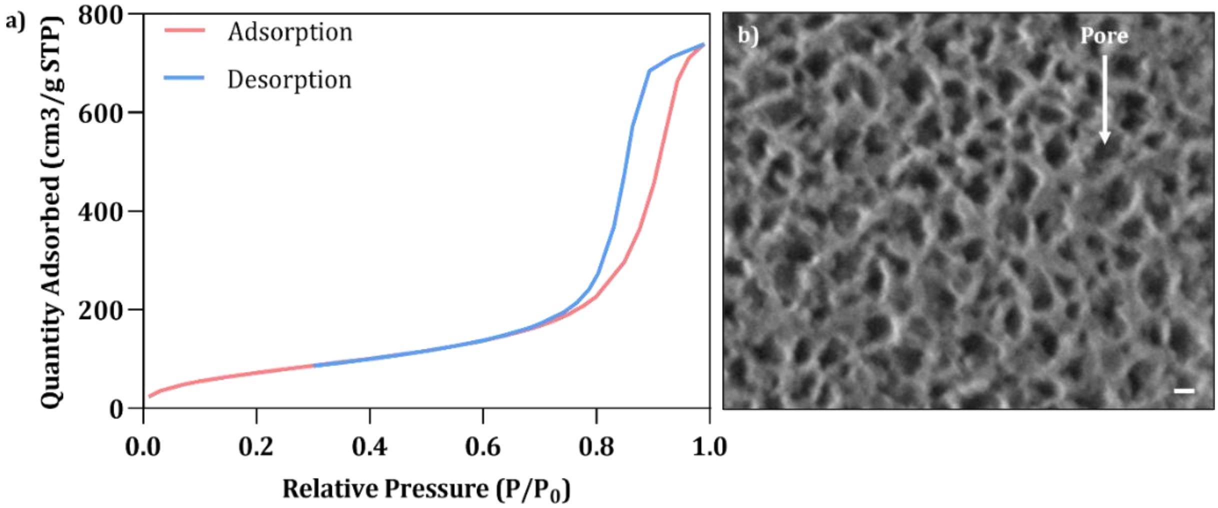

Figure 14: Pore size analysis of EC nanoparticles. a) Isotherm linear plot for the adsorption and desorption of EC nanoparticles. b) A magnified SEM image of a single EC nanoparticle's side showing the pores of ~12 nm in diameter. Scale bar 20 nm.

4.3 Metal Assisted Chemical Etched Nanoparticle Fabrication

To compare the impact of nanoparticle shape on optoporation efficiency, I fabricated rod-like nanoparticles in addition to the discoidal nanoparticles. The rod-like nanoparticles were produced through the metal assisted chemical etching (MACE) approach which initially generates porous nanowires as a layer on top of the solid silicon wafer. The layer of nanowires could be easily detached by scraping and was then transferred as a solution for sonication to break them into fragments and then collected the desired fragment through centrifugation.

The MACE fabrication process yielded 12 μm thick layer of tightly packed vertical porous silicon nanowires (**Figure 15a**) which I detached from the solid wafer by scraping (**Figure 15b**). The sonication and centrifugation parameters used to produce EC nanoparticles proved unsuitable as the resulting MACE nanoparticles were large and aggregated together. To address this, I investigated the appropriate sonicating solvents, sonication time and centrifugation speed required to better fragment the nanowires and promoting stable MACE nanoparticles of similar size but of different aspect ratio to that of the EC nanoparticles.

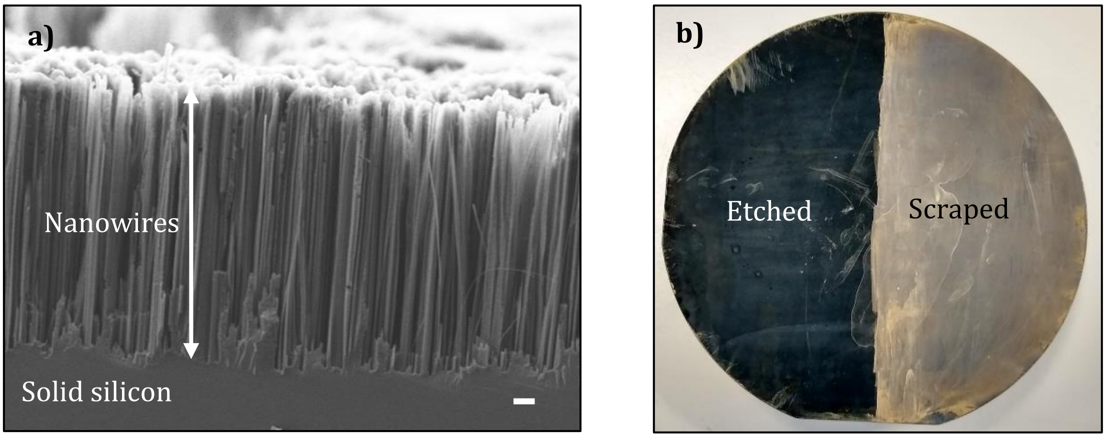

Figure 15: Nanowires fabrication through MACE. a) Densely packed nanowires are produced after the MACE of the silicon wafer. Scale bar 1 µm. b) A photograph of the silicon wafer after etching is represented by the dark surface of the wafer, which is easily scrapped to break the nanowires from the silicon surface.

4.3.1 Centrifuge Speed Impact on Nanoparticle Size and Storage-Solvent Stability

The stability of nanoparticles in suspension is affected by centrifugation speed and the storage solvent. The centrifugation speed generates fractions that affect the size collection of the nanoparticles. Additionally, the interaction of the storage solvent with the surface of the nanoparticles alters interparticle forces and impacts the aggregation of the nanoparticles. Herein, I explored the influence of ethanol and IPA to determine a suitable storage solvent that promoted stability. The greatest stability was determined by the minimal change in hydrodynamic size between two-time points: immediately after sample sonication (referred to as 'sonicated') and then again two minutes later (referred to as 'rest'). In parallel, I investigated various centrifugation speeds to achieve stable nanoparticles within the 200–300 nm range, making them comparable in size to the discoidal nanoparticles.

I sonicated the samples in a water bath sonicator with a frequency of 50 Hz in IPA for 24 hours, and centrifuged it at 1000, 2000, or 3000 rcf. Subsequently, I collected and stored the fractions in either IPA or ethanol and then analysed them by DLS. Through DLS measurements I investigated how variations in centrifugation speed and the storage solvent influenced the stability and size of the nanoparticles. When comparing the 'sonicated' and 'rest' samples (**Figure 16**) it was evident that as the centrifuge speed increased, the difference in size between the 'rest' and 'sonicated' samples decreased. In fact, at 1000 rcf in ethanol, the average difference between 'rest' and 'sonicated' was 1048 nm. However, at 3000 rcf this difference reduced to only 51 nm, with the average hydrodynamic radius of 402 nm ± 59 nm in the 'sonicated' sample. The smaller nanoparticle size obtained was likely due to larger nanoparticles preferentially settling out of suspension under high centrifugal forces. This resulted in supernatant fractions enriched in smaller nanoparticles that were less prone to aggregation. Consequently, the difference in size between 'rest' and 'sonicated' samples decreased at the same high centrifugation speed, as the supernatant contained mostly small, non-aggregating nanoparticles. This trend was observed for both ethanol and IPA, with the decrease in difference being more noticeable in ethanol. In fact, in ethanol the average variation between 'rest' and 'sonicated' at 3000 rcf was 51 nm whereas in IPA it was 369 nm.

In summary, to obtain nanoparticles less prone to aggregation, I selected a centrifugation speed of 3000 rcf and ethanol as the storage solvent.

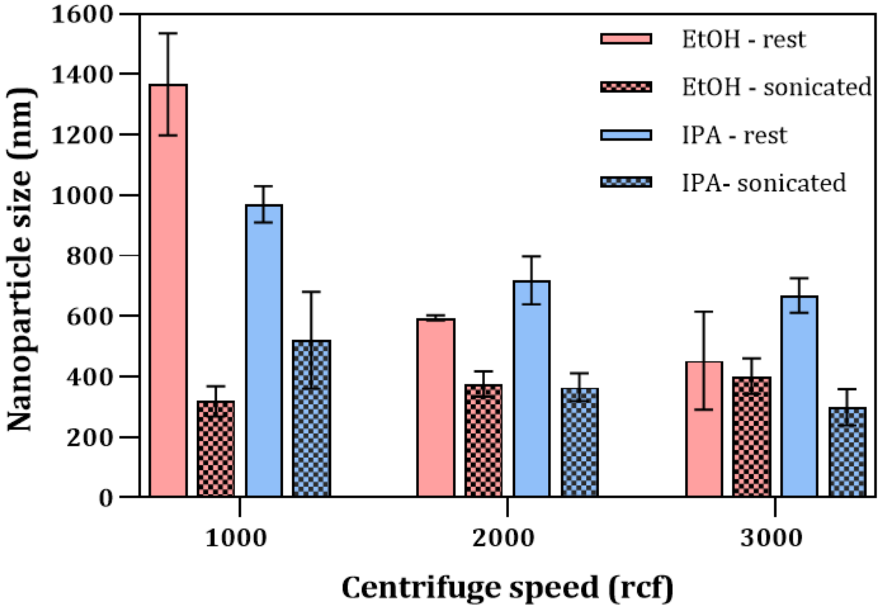

Figure 16: Centrifuge speed impact on nanoparticle size and storage-solvent stability. Nanoparticle collection at varying centrifuge speeds after 8 hour sonication in IPA with nanoparticles suspended in ethanol or IPA. Size measured at 'rest' and at 'sonicated'.

4.3.2 Optimising the Sonication

The choice of sonication solvent is a critical factor that greatly affects the efficiency of the sonication process. Viscosity and surface tension of the solvent are key properties in the cavitation process where more viscous liquids produce cavitation bubbles less readily (Ali et al., 2014). Hence, selecting an appropriate solvent for sonication allows for greater efficiency in obtaining the desired size of the nanoparticles. The sonicating solvent was changed from IPA which has a viscosity of 2.4 cP to water with a viscosity of 0.89 cP (Sheikh et al., 2019). Samples were collected at 0, 2, 8, 24, and 48 hours after sonication to monitor changes in particle size (**Figure 17**). Over time, the particle sizes decreased, going from 560 nm ± 159 nm after 2 hours of sonication to 247 nm ± 12 nm with a PDI of 0.215 ± 0.03 after 8 hours of sonication. This size obtained with water as the sonication solvent is nearly half of that obtained with IPA as the sonication solvent. The size reduction became less significant when sonication exceeded 8 hours. Given that the nanoparticle size fell within the desired range, I selected an 8 hour sonication time in water.

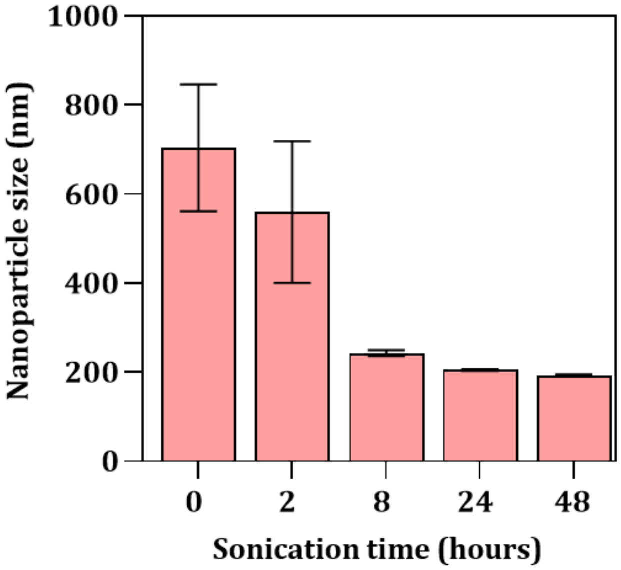

Figure 17: The effect of sonication time on nanoparticle size. The nanoparticle size drastically decreases with a longer sonication time of up to 8 hours, then the nanoparticle size is relatively stable.

4.3.3 MACE Nanoparticle Characterisation

DLS measurements are more appropriate for spherical objects, so SEM was used to further characterise the size and aspect ratio of these rod-like nanoparticles. Using ImageJ, I measured the dimensions of over 450 rod-shaped nanoparticles. The long axis of each nanoparticle corresponded to the length, and the thickness perpendicular to the axis represented the width. Overall, the rod-like nanoparticles had an average length of 404 nm ± 179 nm and an average width of 171 nm ± 58 nm. Similar to the EC particles, the distribution of the aspect ratio of the nanoparticles is represented in the frequency distribution histogram (**Figure 18**). The histogram highlights that approximately 65% of the nanoparticles had an aspect ratio ranging between 1-2.5, while less than 10% had an aspect ratio of 5 or greater. The median aspect ratio was 2.2 and the mean aspect ratio was 2.6.

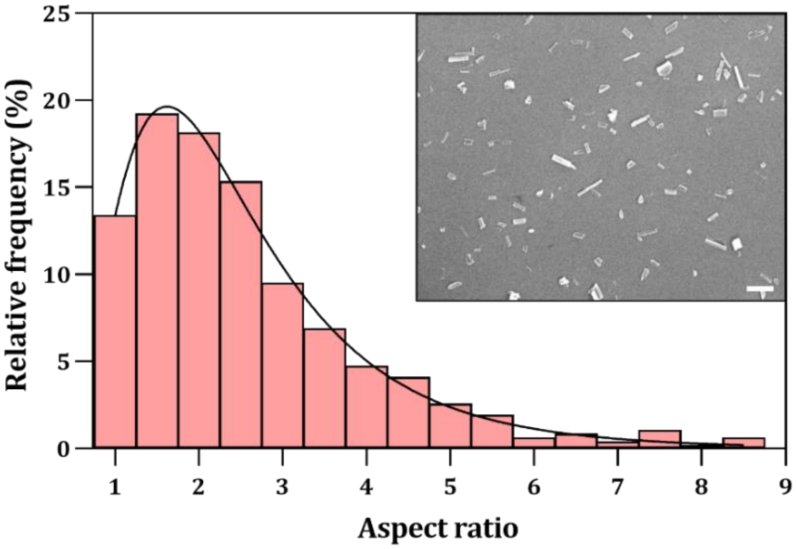

Figure 18: The relative percentage frequency of MACE nanoparticles with a given aspect ratio. The aspect ratio as a measure of height vs width of the nanoparticles modelled by the lognormal distribution shows the positive skewness. Inset showing the structure of the MACE nanoparticles via SEM. Scale bar 1 µm.

The two nanoparticle fabrication processes yielded nanoparticles with different aspect ratio. As expected, MACE fabricated nanoparticles had a larger aspect ratio, given their rod-like structure, in contrast to the discoidal-like shape of the EC nanoparticles (**Figure 19**). Additionally, the EC nanoparticles displayed a narrower aspect ratio range than then MACE nanoparticles indicating a higher structural homogeneity in the EC nanoparticles. The roundness of the MACE nanoparticles was measured using the same methodology as reported for the EC nanoparticles. Based on measurements conducted on 133 MACE nanoparticles, a lower mean roundness of 0.38 ± 0.19 was observed, consistent with the rod-like shape of the nanoparticles observed using SEM.

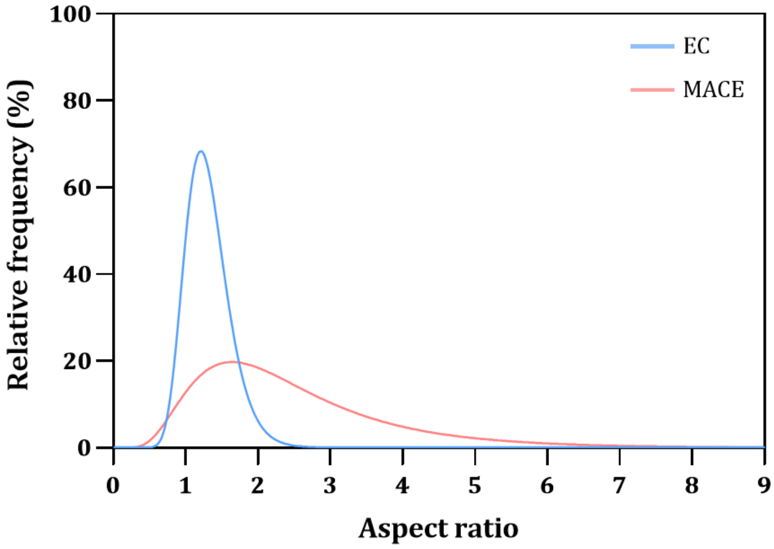

Figure 19: Overlay of the aspect ratio relative frequency distribution for EC and MACE nanoparticles.

Nitrogen sorption isotherms were used to investigate the surface area using the BET model and the porosity using the BJH model (**Figure 20a**). These calculations revealed that the nanoparticles had a relatively small porous volume of 0.11 mL/g and a cumulative surface area of pores of 77.2 m^2/g. The porosity of the nanoparticles was 50% with an average pore diameter of ~7.9 nm which closely matched the pore size observed through SEM imaging (**Figure 20b**). The porosity and the pore diameter was quite different from that obtained with the EC nanoparticles. The pore size of the MACE nanoparticles was a smaller compared to the EC nanoparticles, with a smaller surface area of the pores and pore volume. Hence, the dissimilarity between the two types of nanoparticles extended beyond the aspect ratio as the porous nature of the nanoparticles was also different. Both characteristics could potentially impact the efficiency of optoporation.

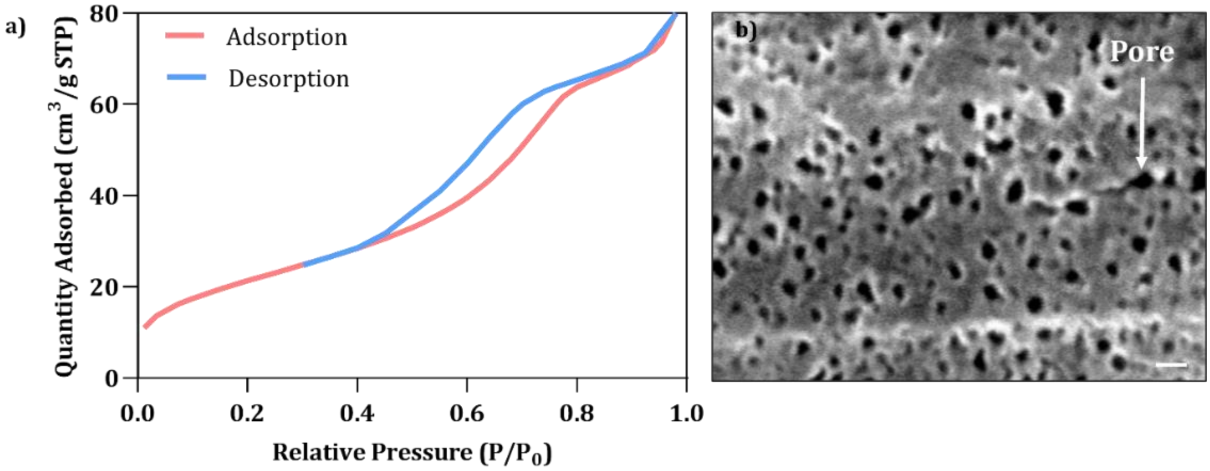

Figure 20: Pore size analysis of EC nanoparticles. a) Isotherm linear plot for the adsorption and desorption of MACE nanoparticles. b) A magnified SEM image of a single MACE nanoparticle's side showing the pores of ~7.9 nm in diameter. Scale bar 20 nm.

In summary, the optimised conditions for producing rod-like nanoparticles involved sonication in a water bath for 8 hours using water as the solvent, followed by centrifugation at 3000 rcf. This resulted in the formation of rod-like nanoparticles with an average length and width of 404 and 171 nm respectively with a median aspect ratio of 2.2 and an average pore size of ~7.9 nm.

4.4 Surface Functionalisation of pSi Nanoparticles

Fluorescently tagged nanoparticles were used to enhance the visualisation of nanoparticle distribution within the cells. This was achieved through surface modifications of the pSi nanoparticles enabling the conjugation of various compounds including fluorescent dyes and nucleic acids. The surface modification process selected was a two-step process. First, a molecule containing a free amine group was conjugated to the surface of the pSi nanoparticles and served as a linker. The second step involved a reaction between the amine group and the functional group of the fluorescent dye to produce the fluorescently tagged nanoparticles.

I selected APTES as the linker because it possesses the necessary amine group for the subsequent conjugation of the fluorescent dye. Furthermore, the process of functionalising the nanoparticles with APTES was accomplished in a single-step silanisation reaction (**Figure 21**). During this step, the nanoparticles were mixed with

APTES for 2 hours, after which the excess and unbound APTES was removed by washing the nanoparticles multiple times. As a result, the nanoparticles acquired the amine group and were primed for reacting with a fluorescent dye in the subsequent reactions.

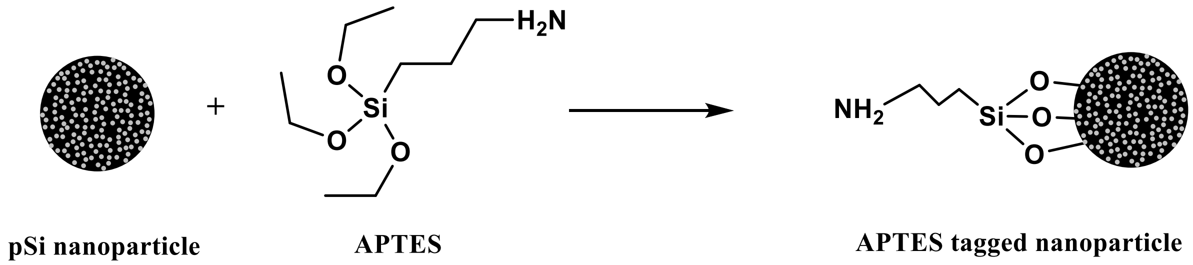

Figure 21: An illustration of the APTES-tagged nanoparticle reaction.

The success of the surface functionalisation was based on changes observed in zeta potential measurements because zeta potential is influenced by the surface-attached functional groups. In addition, previous studies have noted that zeta potential values depend on the concentration of the nanoparticles (Medrzycka, 1991; Tantra et al., 2010). Therefore, a range of nanoparticle concentrations were prepared to investigate how changes in the concentration influenced the reproducibility of the zeta potential mean and standard deviation. The results (**Figure 22**) reveal that the zeta potential remained constant within the concentration range of 10 - 40 µg/mL. However, increasing the concentration to 80 µg/mL resulted in a shift towards less negative zeta potential values accompanied by a higher standard deviation. Mechanistically, nanoparticles at higher concentrations are more likely to interact with each other. These interactions can distort the electric double layer surrounding each nanoparticle leading to a decrease in the measured zeta potential value (Bhattacharjee, 2016). In contrast, the similar zeta potential values measured at 10, 20, and 40 µg/mL suggest that these zeta potential measurements were independent of the concentration within this range. Of these the concentration 40 µg/mL was selected for further experiments because it ensures a high degree of nanoparticle functionalisation while still maintaining the zeta potential within the expected range.

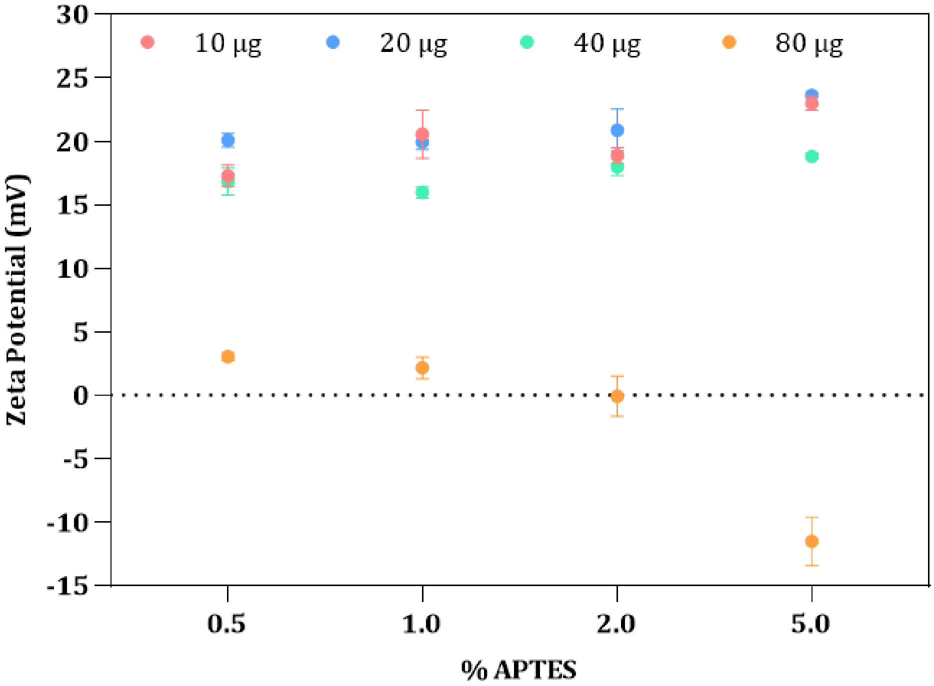

Figure 22: The effect of nanoparticle concentration on the zeta potential measurements.

Titration experiments were conducted to determine the most effective conditions for optimal APTES functionalisation and ensure saturation of the amine groups that are needed for the subsequent modifications. The experiment involved testing various APTES concentrations and different incubation times with the nanoparticles. APTES concentrations of 0.5%, 1.0%, 2.0%, and 5.0% were incubated for the duration of 1 hour, 2 hours, 5 hours and 24 hours. The 5% APTES concentration exhibited the greatest variability in positive zeta potential over time compared to the other three APTES concentrations (**Figure 23**). This variability could be attributed to self-condensed side products. Organotrialkoxysilanes like APTES can undergo undesirable self-condensation reactions, even under basic conditions, to form small oligomeric byproducts. The presence of these unpredictable self-condensed species on the nanoparticle surface could lead to the observed fluctuations in zeta potential measurements seen for the 5% APTES sample. This highlights the challenge in achieving reproducible and reliable surface functionalisation when dealing with the potential formation of such self-condensed byproducts (Jung et al., 2012). The other three concentrations yielded a narrower range of readings, with positive zeta potentials ranging from +18.2 to +27.3 mV. These results indicated successful grafting of APTES as the positive charge reflected the protonation of the amine groups ($-^{+}NH_3$) on the surface of the nanoparticles.

Comparing the 0.5% and the 1.0% with the 2.0% showed that the 2.0% had a more positive zeta potential across all the time points. Generally across the different APTES concentrations, the 1-hour incubation time yielded a lower zeta potential compared to the 2-hour and 24 hours incubation time. At 0.5% the 24 hours resulted in the highest positive zeta potential. However, when the concentration increased to 1% and 2%, the zeta potential after 2 hours of incubation was similar to the zeta potential after 24 hours. This suggests that at higher concentrations, the nanoparticle surface became saturated within the first 2 hours of incubation. The zeta potential results obtained at 5 hours of incubation were less positive across the 0.5 - 2.0% APTES concentrations compared to the 2-hour incubation results. Although this was not expected, the surface charge varied by a maximum of ±7 mV at the different time points within the 0.5 - 2.0% APTES concentration range. This indicates that zeta potential measurements were still relatively similar, marking the saturation point of APTES conjugation.

Overall, it is suggested that APTES concentration had a more pronounced effect on surface charge rather than the incubation time. The combination of 2.0% APTES and 2 hours of incubation achieved the highest positive zeta potential value of +27.3 mV ± 0.6 mV. Therefore, I selected these conditions for optimal functionalisation of the nanoparticles with APTES.

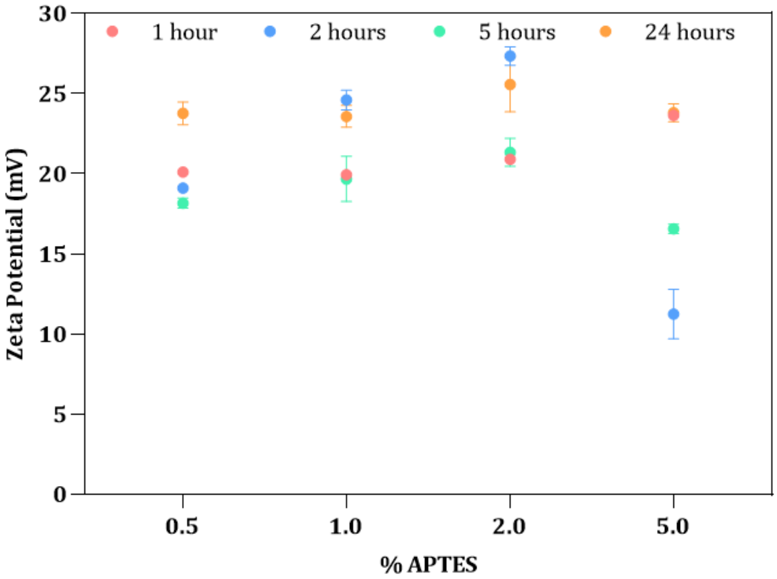

Figure 23: The effect of incubation time and APTES concentration on the zeta potential measurement.

Once the surface of the nanoparticles was functionalised with APTES, the terminal amine groups allowed for further conjugation of the fluorescent dye to the nanoparticles. This one-step reaction involved the N=C=S group of the fluorescent dye FITC forming an amide bond with the amine group of the APTES (**Figure 25**) (Baumgärtel & von Borczyskowski, 2013; Wang et al., 2021). The resulting nanoparticles fluoresced at 488 nm, providing a clear visualisation for the distribution of both EC and MACE nanoparticles onto the cells (**Figure 24a, c**). In instances where the green channel was required to observe the GFP expression, the nanoparticles were alternatively labelled with the blue fluorescent dye, carboxy-6,8-difluoro-7-hydroxycoumaryl succinimidyl ester (ocean blue fluorescent dye). The N-hydroxysuccinimide-ester (NHS-ester) of the ocean blue formed an amide bond with the amine from the conjugated APTES (**Figure 25**) and fluorescent microscopy confirmed the successful functionalisation of the particles with the dyes (**Figure 24b**).

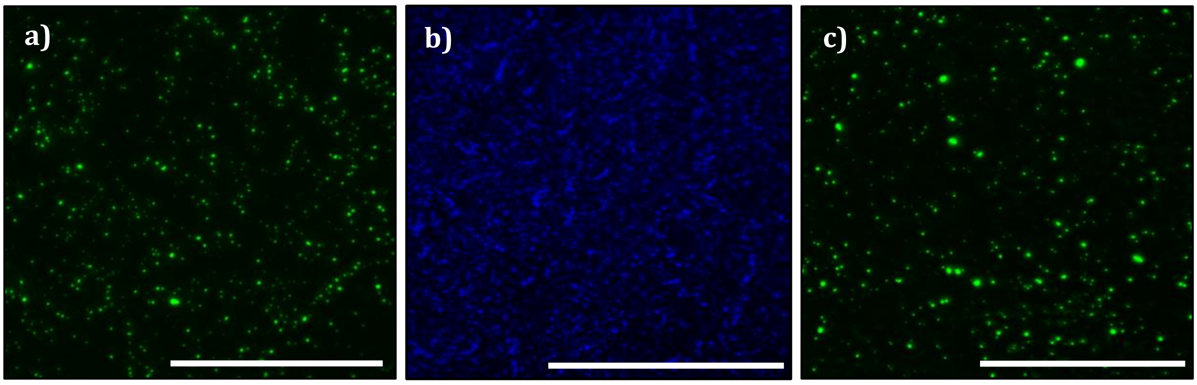

Figure 24: Fluorescence images of tagged nanoparticles. a) EC nanoparticles tagged with FITC, b) EC nanoparticles tagged with ocean blue, and c) MACE nanoparticles tagged with FITC. Scale bar 100 μm.

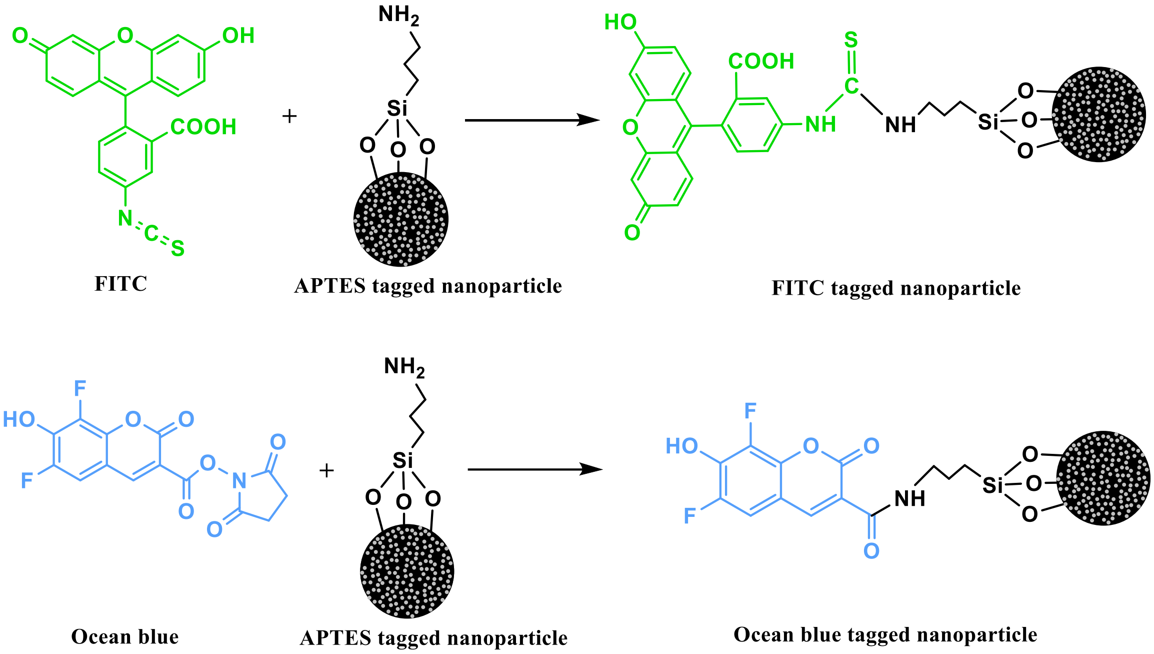

Figure 25: An illustration of the chemical reactions involved in the formation of FITC and ocean blue-tagged nanoparticles.

The surface charge measurements for both EC and MACE particles at the various functionalisation stages are summarised in **Figure 26**. The surface charge of the nanoparticles after fabrication was negative at −12.8 mV ± 0.7 mV for EC and − 25.3 mV ± 0.4 mV for MACE nanoparticles due to the siloxane bridges (Si-O-Si) and silanol (Si-OH) groups. MACE nanoparticle likely have a more negative zeta potential because oxidation occurred to a greater extent during the 8 hours water sonication process. Upon thermal oxidation, the OH groups on the surface of the particles increased, resulting in a more negative surface charge of −16.7 mV ± 0.2 mV, and −29.4 mV ± 0.3 mV for EC and MACE nanoparticles respectively. The two-step process for conjugating the fluorescent dye resulted in a positive surface charge of +13.8 mV ± 0.3 mV in EC nanoparticles and +18.9 mV ± 0.2 mV in MACE nanoparticles. Ocean blue conjugation was only performed on EC nanoparticles resulting in a surface charge of +9.6 mV ± 0.7 mV. In conclusion, monitoring changes in the surface charge of the nanoparticles served as an indication of the success of the step-by-step grafting. This process generated fluorescently tagged nanoparticles with a positive surface charge that were visible through fluorescent microscopy..

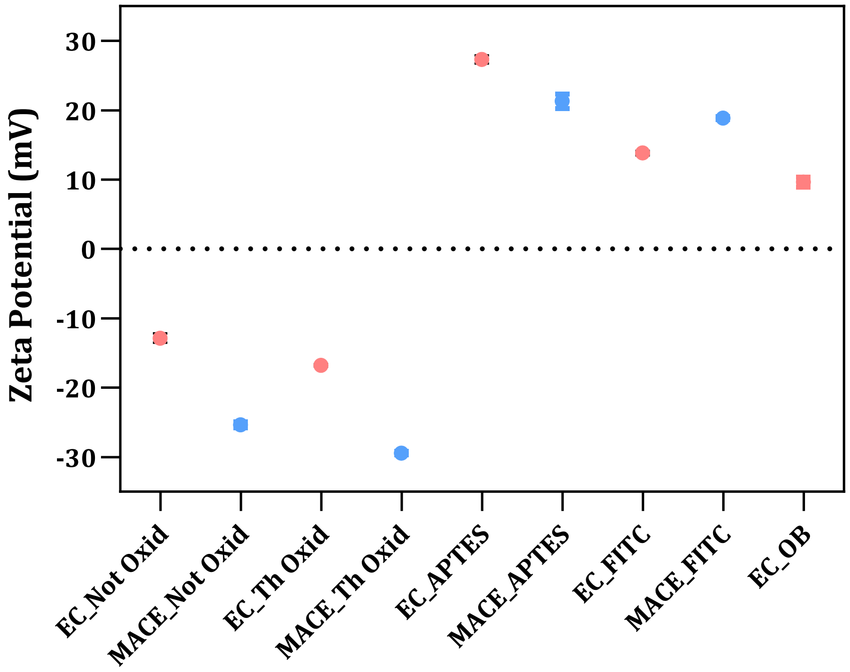

Figure 26: Surface charge measurements of EC and MACE nanoparticles after surface functionalisation.

4.5 The Interaction of MCF-7 Cells with pSi Nanoparticles

Indirect cell membrane perforation is typically achieved by interacting the laser radiation with the nanoparticles adsorbed to the cell surface membrane. To confirm nanoparticle attachment, I examined whether the EC and MACE nanoparticles remained bound to the cell membrane after the 1-hour incubation period and subsequent washing steps. The SEM images confirmed that nanoparticles were attached to the surface of the membrane

Figure **27b, c**). Furthermore, energy dispersive X-ray (EDX) elemental mapping showed that cellular environment had a predominant carbon signature (**Figure 28**) agreeing with literature (Pirozzi et al., 2018). The regions with attached pSi nanoparticles were distinguished from the cellular surface by sharp increases in silicon and oxygen intensities between 1.1 - 2.6 µm (**Figure 28a-b**) and 0.9 - 2.8 µm (**Figure 28c-d**). Overall, these results demonstrate the 1-hour incubation enables sufficient nanoparticle binding to the cell membrane surface for both nanoparticle types.

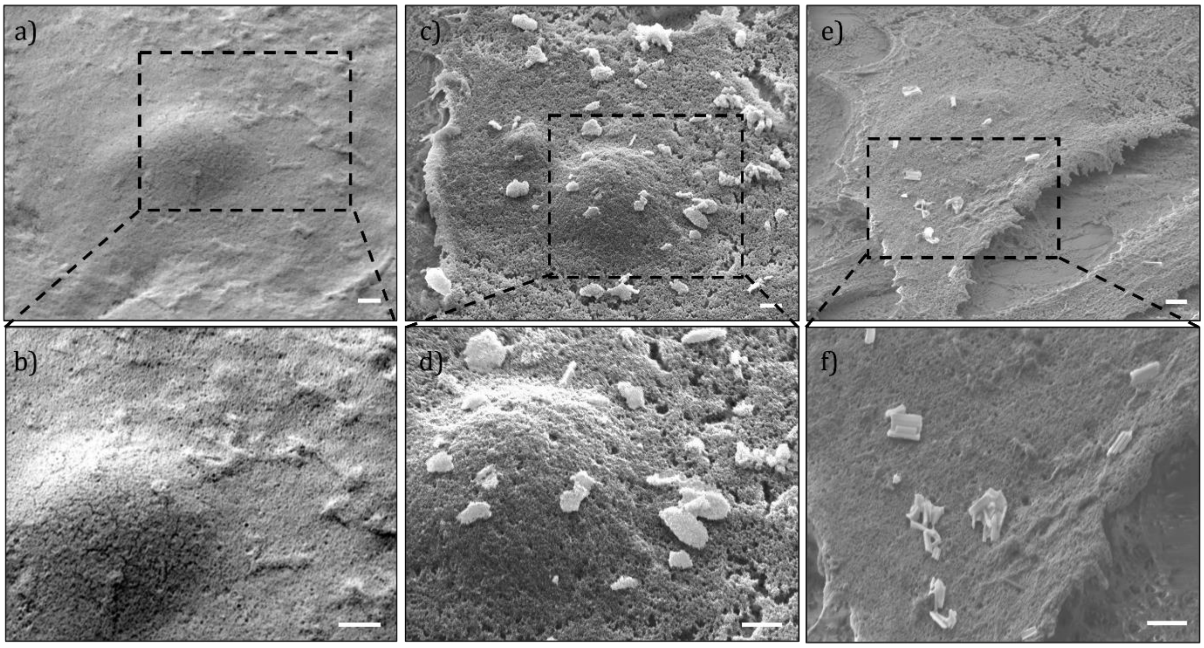

Figure 27: SEM images of the MCF-7 without and with 1 hour of nanoparticle incubation. SEM images of a, b) Control - without nanoparticles incubation, c, d) with 30 µg/mL of EC nanoparticles, e, f) with 30 µg/mL of MACE nanoparticles incubation. Images a, c, e) display an entire cell and b, d, f) display zoomed in section of the cell. These images have been processed with Adobe Photoshop to increase the contrast between the nanoparticles and the cells. Scale bar 1 µm.

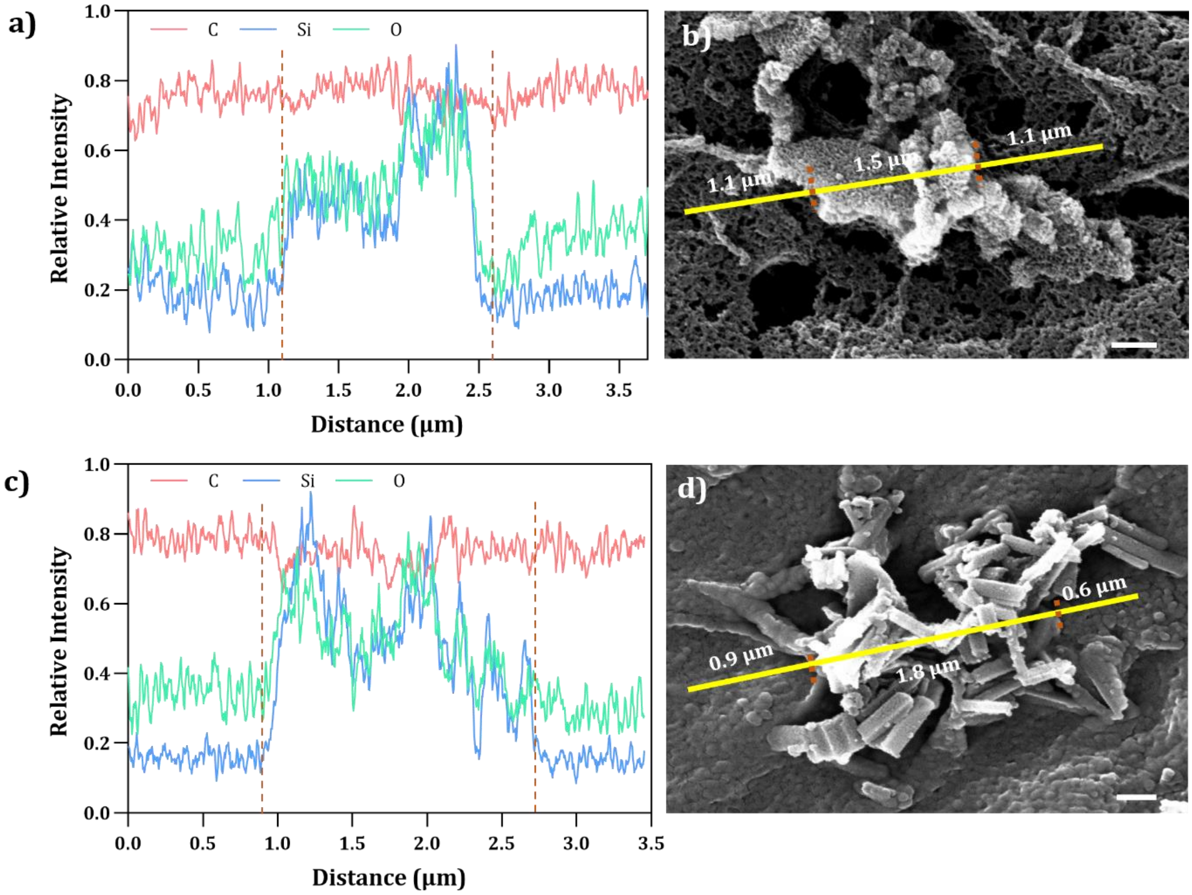

Figure 28: EDX analysis and SEM imaging of EC and MACE nanoparticles on MCF-7 cells. The left panels (a and c) show elemental peak mapping of carbon (red), silicon (blue) and oxygen (green) and the right panels (b and d) show the region of the EDX line scan. Scale bar 300 nm.

4.5.1 Toxicity of the Nanoparticles

The physical and biological interactions between nanoparticles and cells can impact cytotoxicity. Studies on pSi nanoparticles have demonstrated that cellular toxicity depends on nanoparticle concentration (Korhonen et al., 2016; Santos et al., 2010). Herein, I investigated the relationship between nanoparticle concentration and cell viability via an ATP assay, to identify concentration ranges that did not impact cell viability.

A traditional method of measuring cellular toxicity is through the MTT assay, which relies on reducing yellow tetrazole to purple formazan in living cells (Lotze & Thomson, 2005). However, pSi nanoparticles can also reduce the tetrazole to formazan due to the Si-H groups on the nanoparticles surface (Laaksonen et al., 2007). This may lead to undesired redox reactions, resulting in a false positive signal and an underestimation of the cytotoxicity of the nanoparticles. Laaksonen et al., 2007 identified that even thermally carbonised and thermally oxidised nanoparticles produced undesired redox reactions, possibly due to the remaining Si-H groups inside the pore wall. To overcome this limitation, I used the bioluminescent ATP assay, CellTiter-Glo, as a more appropriate assay. The ATP assay measures the amount of released ATP in the solution after cell lysis, serving as an indication of metabolically active cells. Importantly, the measured signal is not affected by the presence of pSi nanoparticles because instead of reduction, the signal is dependent on the luciferase reaction. Luciferase is activated in the presence of ATP and magnesium ions (Mg^{2+}) to catalyse the oxidation of D-luciferin and form an excited state of oxyluciferin (Promega, 2023; Stanley, 1989) (summarised in **Figure 29**). Light is released as the oxyluciferin returns to the ground state. The light emitted covers a broad range of wavelengths, and since the cells and medium have low background interference, light can be collected from the entire visible spectrum.

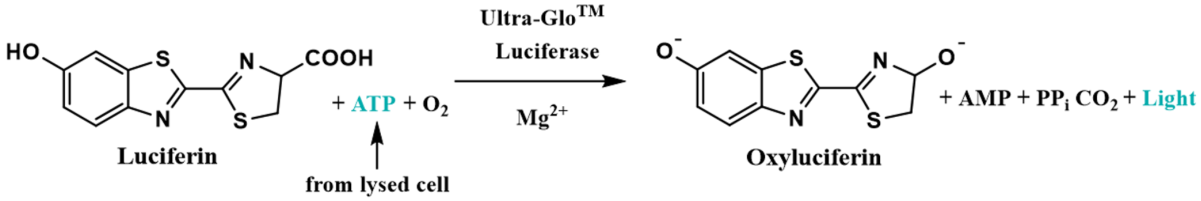

Figure 29: An illustration of the CellTiter-Glo assay principle. Luciferin is oxygenated to oxyluciferase in the presence of ATP from the lysed cells, Mg^{2+} and luciferase enzyme to produce light.

The thermally oxidised nanoparticles have a hydrophilic nature, allowing for the formation of an aqueous layer around them. This aqueous layer reduced cytotoxicity compared to non-oxidised nanoparticles by promoting protein adsorption and cell adhesion without disrupting the conformation of the cell's surface proteins (Santos et al., 2010). In this study, both EC and MACE nanoparticles were evaluated for cytotoxicity. Untreated cells represented the negative control with 100% viability (**Figure 30**). Consistent with existing literature, cytotoxicity for EC nanoparticles showed a concentration-dependent relationship (Korhonen et al., 2016; Santos et al., 2010). The cellular viability showed a slight decline upon an increase in the EC nanoparticle concentration, however, cytotoxicity levels remained below 20% for concentrations up to 200 µg/mL (**Figure 30**). Similarly, it has been reported that a high concentration of 0.2 mg/mL of electrochemically etched nanoparticles exhibited no substantial impact on cellular viability (Park et al., 2009). The viability of the cells treated with MACE nanoparticles remained unaffected throughout the range of nanoparticle concentrations tested.

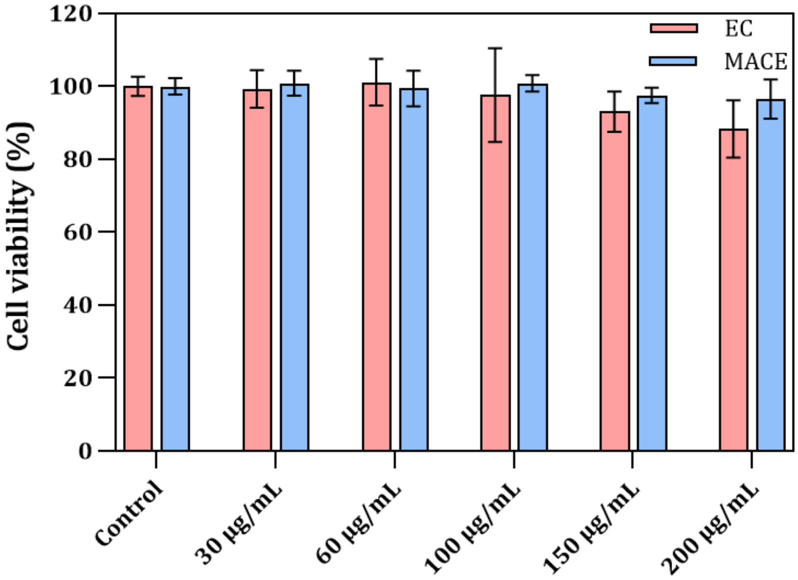

Figure 30: Cell viability assay for both EC and MACE nanoparticles. Determined with the CellTiter-Glo assay and expressed relative to the untreated control group.

Overall, the cell-viability assay results indicated that I could add at least up to 200 µg/mL of nanoparticles without significantly impacting the viability of the cells. However, using a concentration of 200 µg/mL posed a limitation as it was challenging to distinguish the cells from the surrounding high concentration of nanoparticles (**Figure 31**). Therefore, as is discussed in Chapter 5, a maximum of 150 µg/mL of nanoparticles concentrations were used during the optoporation process.

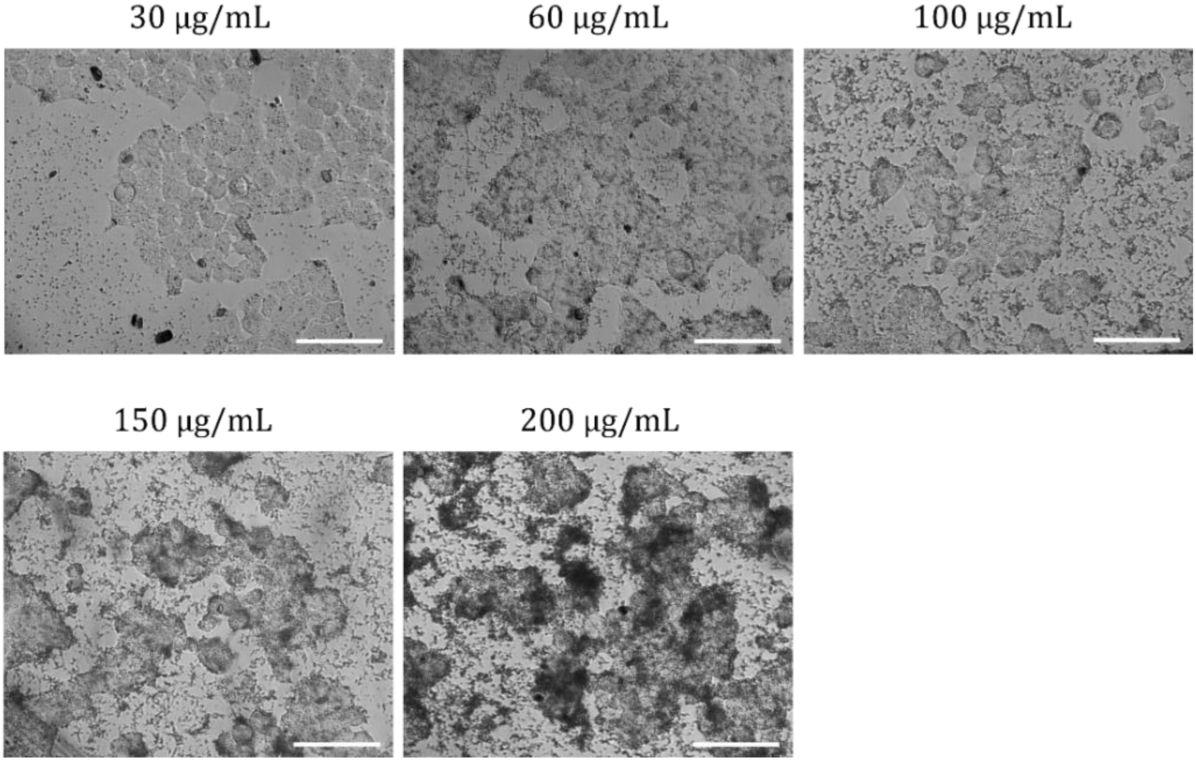

Figure 31: Co-incubation of EC nanoparticles with MCF-7 cells. Bright-field images after the addition of different EC nanoparticles with the MCF-7 cells followed by washing of the unbound nanoparticles after 1 hour of incubation.

4.6 3D Cell Culture System and Nanoparticles Interactions

Optoporation-based techniques for biomolecule delivery have predominantly focused on cell cultures as two-dimensional monolayers. Yet, the development of spatio-temporal delivery in 3D models is crucial for understanding the regulation of cell function and behaviour within a larger tissue mass. To investigate targeted delivery in a 3D cell culture system, I generated multicellular spheroids through the hanging drop method to represent the 3D models. Indeed, the choice of MCF-7 breast cancer cell line depended on the ability of the cells to readily generate 3D tumour spheroids. To maintain diffusion of nutrients, oxygen and catabolites through the multicellular layer without forming a necrotic core, spheroids should have a diameter not greater than ~500 μm (Hirschhaeuser et al., 2010; Merck, 2023a; Vinci et al., 2012). The spheroids size is tuneable by changing the initial seeding density (Leung et al., 2015).

4.6.1 Spheroid Formation

Various studies have dedicated efforts to developing systems that standardise spheroid compactness and roundness. The 'hanging drop' technique is one of the most common methods for producing spheroids, where cells are suspended in a single drop and then inverted to form a hanging drop (Timmins & Nielsen, 2007). Due to gravity, cells aggregate and generate a spheroid culture. Despite being user-heavy and low-throughput, this approach is advantageous because it is easy to handle and inexpensive. However, some cell types cannot form spheroids and instead result in loose aggregates or floating cells. To overcome this inability to coalesce, additives are added to the 3-D cultures for improved spheroid formation (Leung et al., 2015). The additives can be cross-linking agents such as collagen and fibronectin which serve as scaffolding proteins that promote cell-to-cell interactions. Alternatively, methylcellulose (MethoCel) is used which helps the cells to aggregate by increasing the viscosity of the medium (Djomehri et al., 2019; Longati et al., 2013; Urich et al., 2013). A comparison of the cross-linking agents revealed that spheroids' size and compactness were more uniform in the presence of MethoCel than in collagen (Leung et al., 2015). Therefore, to increase reproducibility, I selected MethoCel to be added to the hanging drop cultures.

The MCF-7 spheroids were produced from an already established protocol (Froehlich et al., 2016)with slight modifications in the seeding density and the MethoCel concentration applied. A 24-hour incubation period was necessary to allow the spheroids to grow ~500 μm in diameter and maintain their structure. In fact, attempting to withdraw the spheroid at earlier time points resulted in the collapse of the spheroids due to insufficient compactness. When comparing equivalent seeding densities, it was observed that a drop volume of 20 μL with 2400 cells only resulted in 35% of the spheroids to be compact and with a round structure (**Figure 32a**). Yet, using the same seeding density but increasing the volume to 25 μL with 3000 cells produced over 90% of spheroids with the desired characteristics (**Figure 32b**).

In parallel, I also attempted the liquid overlay technique as an alternative approach to produce uniform spheroids. The technique involved coating the V-shaped wells with 5% pluronic acid F-127 creating a hydrophilic layer that reduced protein adsorption and thus prevented cell adhesion to the well wall (Azizipour et al., 2022). Cells were subsequently added at the same seeding density as that of the hanging drop method and the results obtained were comparable to the hanging drop method. Given that the liquid overlay technique was more time-consuming, the hanging drop method was instead chosen for generating the ~500 µm spheroids.

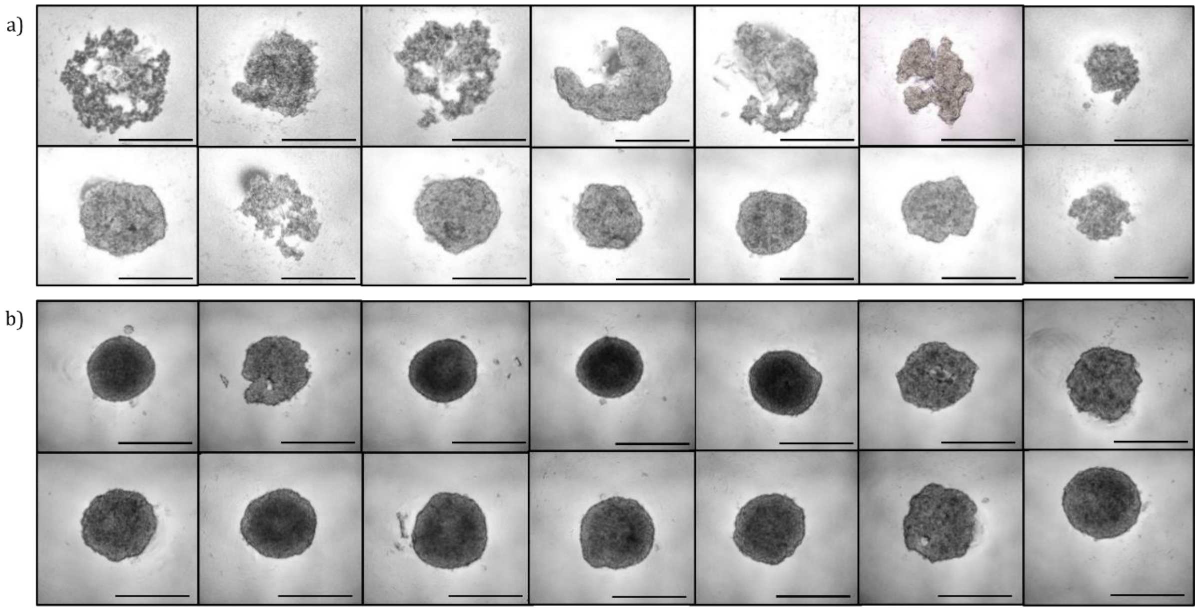

Figure 32: MCF-7 spheroids formed by the hanging drop method. The spheroids formed by a) seeding 2,400 cells in 25 µL drop volume and b) seeding 3,000 cells in 25 µL drop volume after incubating both for 24 hours. Scale bar 500 µm

4.6.2 Nanoparticles Interaction with 3D MCF-7 Spheroids

After developing a method for generating uniform MCF-7 spheroids, I investigated the effect of adding nanoparticles to the floating cells prior to the spheroid formation. Visual observation showed that spheroids created with 30 µg/mL nanoparticles had a structure similar to that of the control. Increasing the nanoparticle concentration from 30 to 100 µg/mL (**Figure 33**) resulted in less compact and more irregular spheroids.

This was confirmed by ImageJ measurements of roundness and solidity. Roundness determined how closely the shape of the spheroid resembled a perfect circle, often expressed as an aspect ratio. Solidity measures the density of an object where a value less than one indicates that the spheroid has an irregular boundary or contains holes making the spheroid less compact. Increasing nanoparticles concentration of the nanoparticles from 30 to 100 µg/mL resulted in reduced roundness and solidity (**Figure 34**), likely because the nanoparticles interfered with the cell-to-cell interactions. In fact, there was a statistical difference when comparing the roundness and solidity of the control with 100 µg/mL of EC nanoparticles. The results therefore, indicated that there was a limit on the amount of nanoparticles that could be loaded within the floating cells without affecting the spheroid formation.

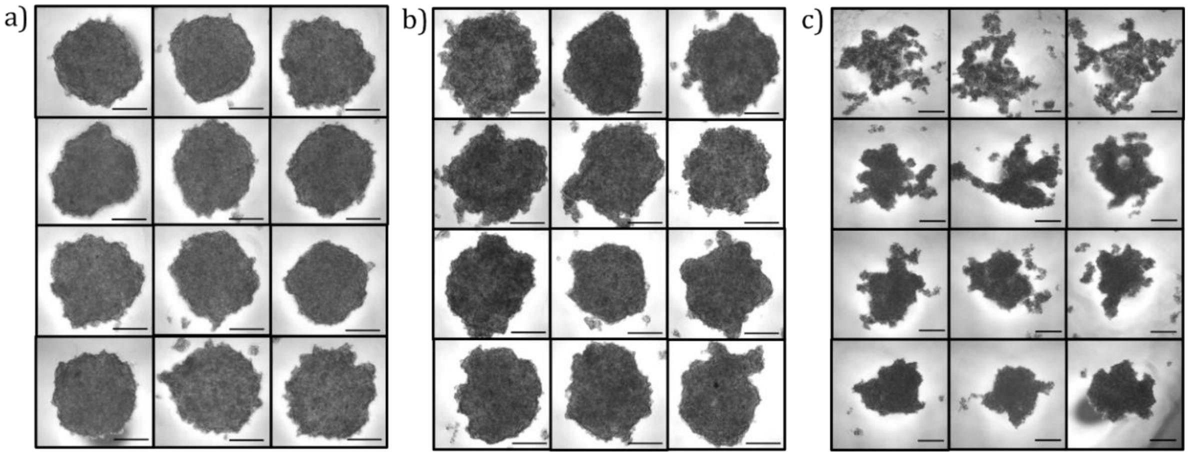

Figure 33: MCF-7 spheroids formed when adding EC nanoparticles to the floating cells pre-spheroid formation. The spheroids formed when a) 30 µg/mL, b) 60 µg/mL and c) 100 µg/mL of EC FITC tagged nanoparticles and left incubating for 24 hours with the cell in a hanging drop. Scale bar 200 nm.

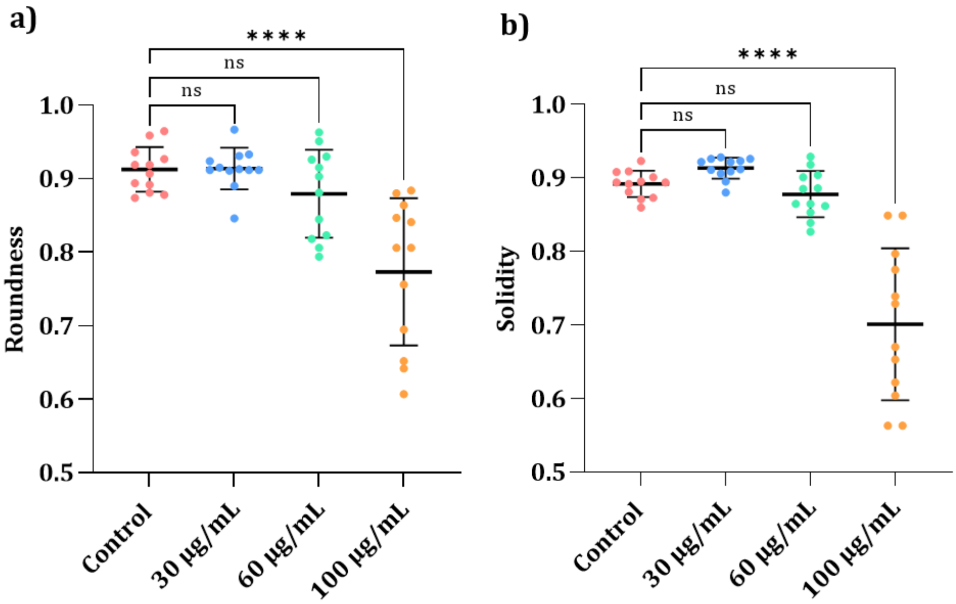

Figure 34: Roundness and solidity of spheroids. a) Roundess b) Solidity of the spheroids treated with EC nanoparticles. The control represents the absense of nanoparticles with the spheroids. The ordinary one–way ANOVA test determined a significant difference between the control and 100 µg/mL for both the roundness and solidity, ****$p<0.0001$.

The cell viability for spheroids with 30 and 60 µg/mL of EC and MACE nanoparticles was assessed after 24 hours through the CellTiter-Glo 3D assay. EC nanoparticles exhibited higher cell viability at both concentrations tested (**Figure 35**). At 60 µg/mL, EC nanoparticles led to a decline of cell viability to 81% ± 9.8, while MACE caused a decrease to 67% ± 11.6. The negative effect of the nanoparticles on viability was higher on the spheroids than in the 2D system. This could be because the presence of the nanoparticles interfered with the cells extracellular matrix adhesion leading to programmed cell death (Meredith et al., 1993). Additionally, while in the 2D system the unbound particles were washed away after 1 hour, this step was absent for the 3D spheroid formation leading to a higher effective concentration of nanoparticles. Adding the nanoparticles with floating cells (before spheroid formation) enhanced the uniform distribution of EC FITC-tagged nanoparticles. This, in turn enabled efficient optoporation and delivery to the core of the spheroid, which was a critical aspect to be further explored in Chapter 5. The uniform distribution of the EC and MACE nanoparticles within the spheroid was observed through the confocal analysis of stained cryosections from the spheroid (**Figure 36**).

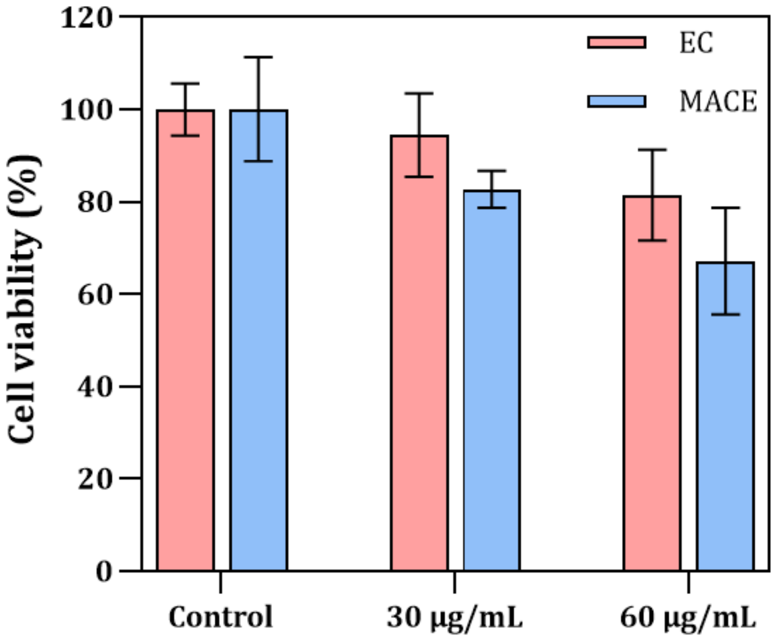

Figure 35: 3D Cell viability assay for both EC and MACE nanoparticles. Determined with the CellTiter-Glo 3D assay and expressed relatively to the untreated control group.

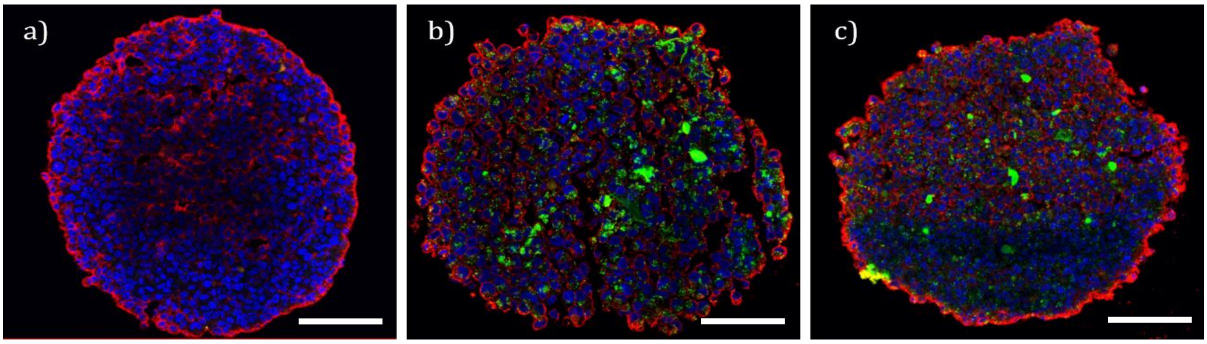

Figure 36: Confocal images of 10 µm thick spheroids' cryosections. Spheroids a) without nanoparticles (control), b) with 30 µg/mL of EC FITC nanoparticles, and c) with 30 µg/mL of MACE FITC nanoparticles. FITC-tagged nanoparticles are shown in green, DAPI in blue and WGA in red. Scale bar 100 µm.

4.6.3 Nanoparticle Diffusion to the MCF-7 Spheroid Core

An alternative approach to introducing the nanoparticles to floating cells (as described above) is to first form the 3D spheroids and subsequently add the nanoparticles to the hanging drop (Tieu et al., 2021; Zhang et al., 2022). This method allows adding a higher nanoparticle concentration to the spheroid while preserving the structure of the pre-formed spheroids. It is important to note that nanoparticles larger than 100 nm may not penetrate the densely packed spheroid. These large nanoparticles are primarily restricted to interacting with cells located in the periphery of the spheroid (Tchoryk et al., 2019, Ahmed-Cox et al., 2022). This limitation can restrict optoporation flexibility and the effective delivery of biomolecules to the spheroid core. Therefore, the objective here was to loosen the interaction between the densely packed spheroid and improve the diffusion of the nanoparticles from the periphery to the core of the spheroid. Overcoming the barriers posed by the extracellular matrix, such as hyaluronic acid and Collagen I, is crucial for facilitating nanoparticles penetration through the spheroid (Ding et al., 2019). Previous studies have demonstrated that using protease enzymes, such as collagenase, degraded the matrix and significantly improved the depth of macromolecule penetration (Goodman et al., 2007). Collagenase derived from *Clostridium histolyticum* broke down the peptide bonds of the extracellular collagen types I, II, and III (Rest et al., 1977) which are major structural components of the spheroid's matrix. Therefore, cleaving these dense collagen networks that hold the cells together resulted in loosening the cell-to-cell interaction within the spheroids.

The effect of collagenase enzyme concentration on spheroid integrity was assessed using a previously established protocol with slight modifications (Goodman et al., 2007). Incubating the spheroids for 6 hours with collagenase resulted in substantial structural damage to the spheroid at all the enzyme concentrations tested (**Figure 37**). At the lowest concentrations tested (0.17 mg/mL and 0.34 mg/mL), the spheroids disintegrated upon pipetting and transferring to the well plate. Meanwhile, concentrations of 0.84 mg/mL and higher resulted in the near-complete breakdown of the spheroids into floating cells. To optimise this protocol, the incubation time was reduced to 3 hours and the lowest concentration of collagenase of 0.17 mg/mL was used retaining the intactness of the spheroids at the end of the process (**Figure 38i**). Cryosections of 10 µm in thickness were obtained from the spheroids to investigate the impact of collagen degradation nanoparticle penetration. In the control, no green fluorescence was observed due to the absence of FITC-tagged nanoparticles (**Figure 38a-c**)**.** In the untreated collagenase spheroid, the distribution of nanoparticles was concentrated at the periphery of the spheroid, with limited penetration into the spheroid, spanning only a few microns. (**Figure 38d-f**)**.** Conversely, fluorescence was detected throughout the diameter of the treated spheroid section, with fewer particles concentrated at the periphery (**Figure 38g-i**)**.** Additionally, a slight change in the diameter of the spheroids was noted. The control, without the particles and without the collagenase, exhibited a diameter of 578 µm ± 22 nm, while the spheroids treated only with nanoparticles showed a similar diameter of 559 µm ± 15 nm. However, spheroids treated with collagenase displayed the largest diameter, measuring 687 µm ± 23 nm, approximately one-sixth larger than the control due to the reduced cell attachment.

This approach showed promise for introducing nanoparticles to the spheroid core while preserving the integrity of the spheroid. Having nanoparticles distributed throughout the z-axis of the spheroid offers flexibility for optoporation and molecule delivery to both peripheral and core cells.

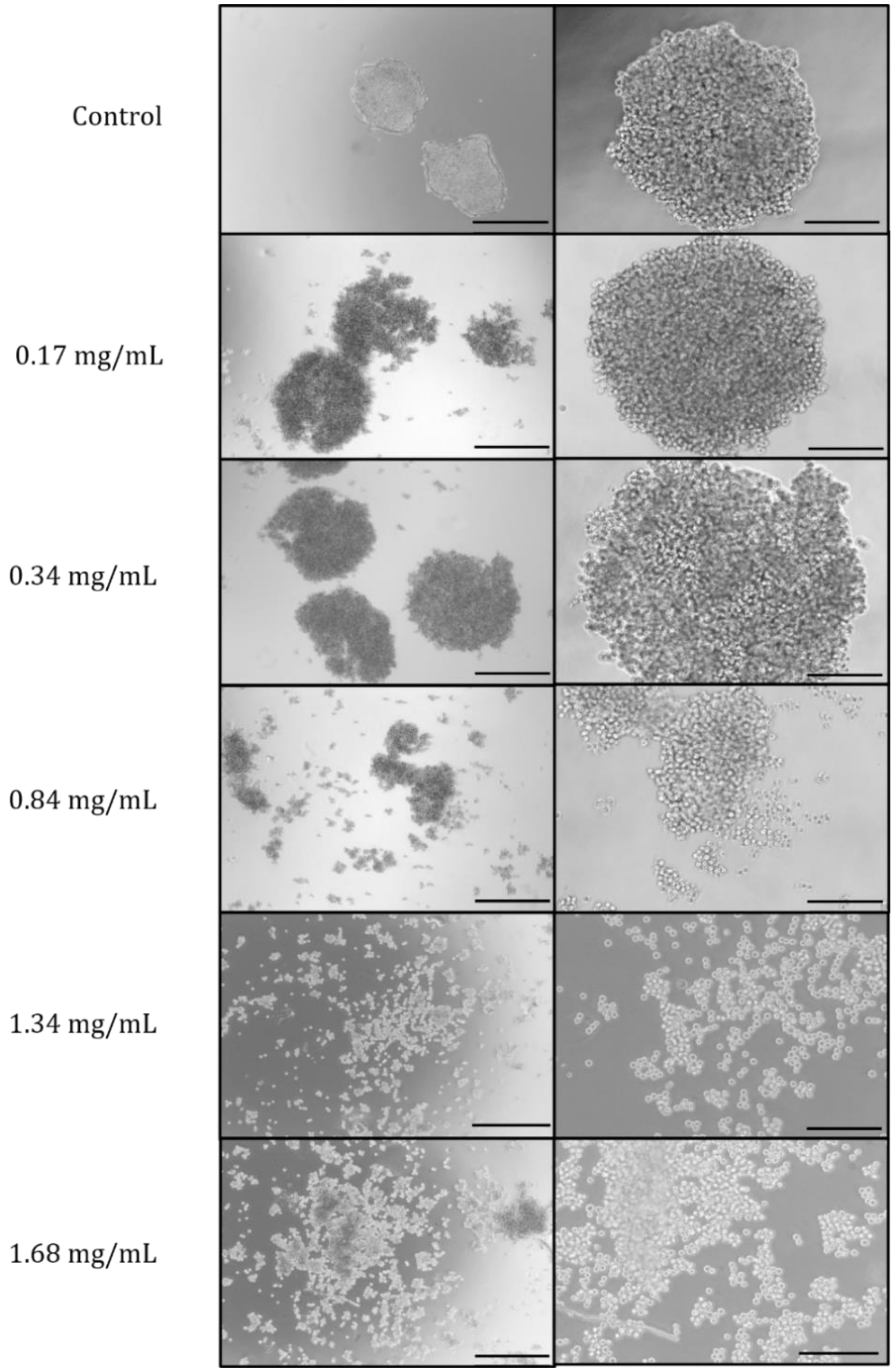

Figure 37: The resulting spheroids after 6 hours of incubation with different concentrations of collagenase. The scale bar for the left column is 500 µm, and the scale bar for the right column is 200 µm.

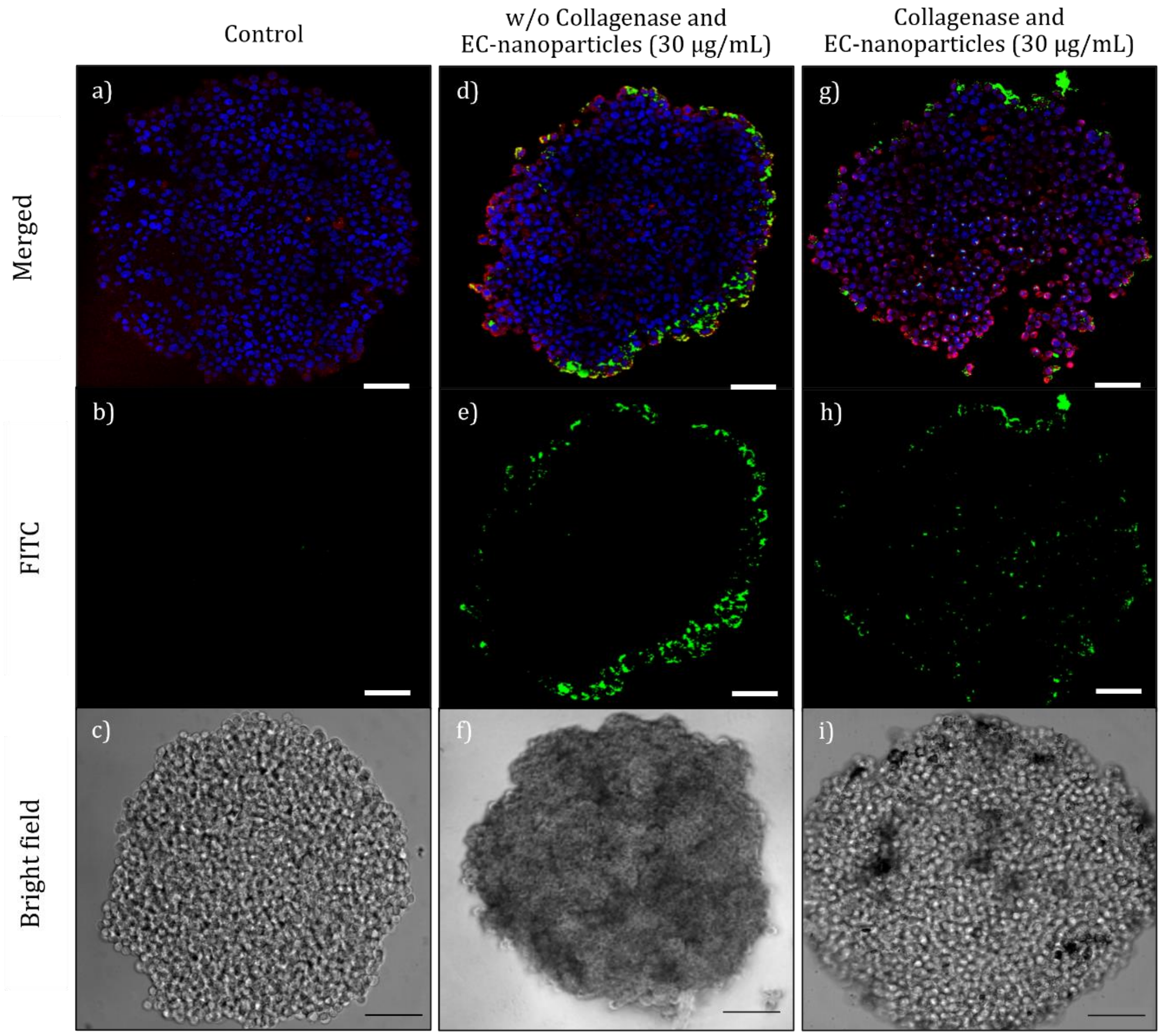

Figure 38: Nanoparticle penetration within collagenase-treated spheroids. a) – c) represent the control sample not treated with collagenase nor with nanoparticles, d) - f) spheroids treated with 30 µg/mL EC FITC nanoparticles and left incubating together for 3 hours, g) -i) spheroids treated with 30 µg/mL EC FITC nanoparticles and left incubating together with 0.17 mg/mL of collagenase for 3 hours. Scale bar 100 µm.

4.7 Concluding Remarks

In this chapter, EC and MACE nanoparticles were successfully fabricated, optimised and characterised. Characterisations included DLS measurements for size assessment, zeta potential evaluation for surface charge analysis, SEM and N_2 adsorption-desorption techniques for assessing pore size and porosity. An optimal nanoparticle concentration was determined and utilised for all readings to ensure consistency in DLS measurements and zeta potential analysis.

Two different etching approaches were employed to produce nanoparticles with varying aspect ratios. Electrochemical etching produced 323 nm-sized nanoparticles with a median aspect ratio of 1.26, while metal-assisted chemical etching yielded nanoparticles with 404 nm in length of 171 nm in width with a median aspect ratio was of 2.2. SEM images confirmed that within an hour of incubation with cells, the nanoparticles remained adhered to the cell membrane, potentially allowing for efficient interaction with the laser.

By identifying optimal APTES incubation time and concentration, positively charged nanoparticles were obtained, capable of reacting with FITC and other dyes for tracking purposes. The effect of these nanoparticles on cell viability and proliferation were assessed using the ATP assay. Remarkably, the results indicated minimal to no compromise in cell viability within the 2D system, even at concentrations up to 200 µg/mL, for both EC and MACE nanoparticles.

In the context of developing 3D models to represent larger tissue mass, spheroids of ~500 µm in size with a roundness of 0.91 were formed through the hanging drop method with MethoCel. This provided the required model for optoporation in a 3D system. To assess the toxicity of the nanoparticles on the spheroids, an ATP assay demonstrated that concentrations above 30 µg/mL negatively impacted the viability of the spheroids. This limited the nanoparticle that could be loaded with the floating cells in the hanging drop. Although higher concentrations were loaded post-spheroid formation, nanoparticle penetration was confined to the spheroid periphery. To facilitate deeper nanoparticle penetration to the core of the spheroids, nanoparticles were introduced post-spheroid formation. To address the core penetration issue, collagenase effectively loosened the cell-to-cell attachments and allowed the nanoparticles entry into the spheroid core while preserving its structural integrity.

In summary, a concentration of 30 µg/mL served as a starting point for optoporation experiments and investigation of particle differences with laser interactions. This concentration can be increased to 200 µg/mL without adversely affecting cellular viability in 2D. In 3D systems, a concentration of 30 µg/mL was optimal to maintain the integrity of the spheroids. Yet, if nanoparticles were added post-spheroid formation rather than with the floating cells pre-spheroid formation, higher concentrations can be considered.

Chapter 5 - Spatially selective delivery

5.1 Introduction

Femtosecond–pulsed lasers operating in the NIR region have been used to create localised transient poration with single–cell precision, facilitating the introduction of impermeable molecules into cellular cytoplasm. Commonly, Ti: Sapphire femtosecond lasers, operating at a high repetition rate of ~80MHz with a 100 fs pulse duration in the NIR spectral range, achieve permeabilisation by tightly focusing on the cell membrane (Antkowiak et al., 2013; Davis et al., 2013). However, this tight focusing can be low throughput while the addition of nanomaterials serve as sensitisers and amplify optical absorption. This allows cell membrane optoporation to occur at lower laser energies, reducing the invasiveness of the process and eliminates the necessity for tight focusing laser on individual cell membrane.

Effective implementation of optoporation while maintaining cell viability necessitates careful attention to sample preparation and laser parameters. Various factors influence the success of transfection, including the choice of transfection medium, cell culture conditions, cell line and confluency level (Antkowiak et al., 2013). For instance, studies on CHO–K1 cells revealed that repeated subculturing resulted in reduced cell metabolic activity and decreased cell division rates, subsequently negatively impacting optical transfection efficiency (Mthunzi et al., 2010). A similar trend applied to cultures at 100% confluence, as cells were slower to recover after subculturing which also affected the transfection efficiency (Brunner et al., 2000; Lechardeur et al., 1999). To address this issue, adherent cells should be seeded at a density that promotes cell proliferation, ensuring higher transfection efficiency in subcultures. In consideration of these factors, MCF–7 cells cultivation in this study lasted up to P30 with the well plates reaching ~60% confluency before the optoporation experiments.

The interaction between the nanoparticles and the culture medium resulted in changes to the physiochemical properties of the nanoparticles. The protein adsorption or association from the serum, led to the formation of a ‘nanoparticle–protein corona’ (Mahmoudi et al., 2011) which can potentially modify the surface charge and properties influencing biological, biochemical and cellular behaviour (Lynch et al., 2009; Walczyk et al., 2010; Zhang et al., 2012). In optical transfection experiments, Opti-MEM is a commonly used serum-free medium because it reduces protein interference and minimises the presence of heat-resistant nucleases from the serum, which could degrade RNA (von Kockritz–Blickwede et al., 2009). In fact in a comparative analysis, Opti-MEM significantly improved transfection (Young et al., 2004). Additionally, to prevent cytotoxic extracellular substances from entering the cells after rendering the membrane more permeable, the cell culture medium should be devoid of antibiotics and phenol red (Zhu et al., 2012).

The irradiation of high–intensity focused femtosecond laser generates low–density electron plasma, which in turn can lead to a substantial increase in intracellular reactive oxygen species (ROS). This phenomenon is often harnessed in various therapeutic applications including radiation therapy and chemotherapy (Minai et al., 2013). While ROS function as signalling molecules for cellular pathways and play a vital role in cell cycle progression and proliferation, their excessive accumulation can trigger oxidative stress, resulting in cellular damage (Baumgart et al., 2009). Therefore, it is important to image for the presence of ROS as this is an initial indication that the cells are not in a suitable environment. These ROS are generated as the laser ionises water, resulting in the production of H_2O^+, hydrogen ions and hydroxyl radicals (Baumgart et al., 2009).

$$H_2O \rightarrow H_2O^+ + e^-$$

$$H_2O^+ + H_2O \rightarrow H_3O^+ + OH^\cdot$$

Furthermore, ROS are pivotal in initiating apoptosis i.e. programmed cell death (Yoon et al., 2015), involving caspases' activity. These proteases are involved in several common apoptotic pathways and are frequently probed as indicators of apoptosis for imaging studies (Tang et al., 2019). Typically, executioner caspases including caspase-3 and -7 are involved in breaking down the cytoskeleton and inactivating repair enzymes, therefore, by the time cells produce these caspases, they are often beyond the point of no return (Riss et al., 2021). As a result caspase-3 and -7 are used as hallmark markers to determine if a particular treatment induced irreversible commitment to cell death (McIlwain et al., 2013; Shim et al., 2017). Alternative methods to detect apoptosis include FITC–conjugated Annexin V, a protein that binds to phosphatidylserines (PS) exposed on the cell surface during early apoptosis (Shim et al., 2017). However, Annexin V may give positive signals from membrane resealing after damage rather than true apoptosis (Bouter et al., 2011) as a result the caspase 3/7 assay is better suited to monitor apoptosis post-optoporation.

While monolayer cell cultures are great systems to optimise optoporation conditions due to the accessibility of various analytical methods, they do have limitations. The simplicity of 2D cell cultures fails to capture the complexities and physiological interplay arising from cell–cell and cell–extracellular matrix interactions, which can be offered by 3D cell models (Duval et al., 2017). Spatiotemporal drug delivery in spheroids has mainly focused on light (mostly UV light) responsive biomaterials (Jia et al., 2018) and photothermally boosted endosomal escape to release drugs in the spheroids (Lee et al., 2023).

Spheroids have been irradiated with NIR laser for photodynamic therapy where the scope was to kill the tumour cells within the spheroid. Femtosecond pulsed NIR laser focusing on the membrane of the target single cell within a 3D tissue model led to the uptake of an impermeable fluorescent dye without harming surrounding cells (Stracke et al., 2005). In another study, a 680 nm nanosecond pulsed laser in combination with gold–coated polystyrene nanoparticle nanosensitisers was used for high throughput delivery of propidium iodide to SiHa human cervical cancer spheroids. This system achieved a high delivery efficiency of 89.6 ±2.8% while maintaining high cellular viability of 97.4 ±0.4% (Gupta et al., 2021). Lastly, femtosecond laser pulses have also been used to knock out single stem cells within 3D tissue–like microenvironment to avoid undesired cell differentiation without affecting neighbouring cells (Uchugonova et al., 2008). So far, none of the research on optoporation in 3D models has successfully achieved the delivery and expression of nucleic acids in these models.

This chapter explores the spatially selective delivery of propidium iodide and nucleic acids in MCF-7 cells. To accomplish this, I initially focused on optimising the nanoparticle–laser system for optoporation within a 2D cell culture environment, utilising propidium iodide as a positive marker. I compared the poration efficiency of EC and MACE nanoparticles at different laser powers and selected the nanoparticle type that offered the highest poration efficiency. EC nanoparticles at 65 mW were chosen and further assessed for short-term cellular viability by evaluating calcein-AM retention. I then aimed to deliver larger eGFP mRNA molecules to laser-targeted cells and monitor the subsequent GFP expression. The 65 mW exposure caused cell death, hence demanding meticulous adjustments of the imaging process and laser parameters to promote cell survival and translation capability. Assessment of cell viability involved evaluating calcein–AM retention, ROS generation and caspase 3/7 activity, collectively indicating maintenance of cell viability. Building upon the success of these viability assays, the delivery and expression of eGFP mRNA in the laser-targeted cells confirmed retention of the cellular processes necessary for translation post-optoporation. Once the optimised system demonstrated effective GFP mRNA delivery and expression while preserving cell viability in a 2D model, the investigation extended towards adapting biomolecule delivery to a 3D cell environment. Spatially selective delivery of propidium iodide in MCF-7 spheroids showcased the feasibility of optoporation in more complex cellular environments.

5.2 Optical Setup

The optical pathway designed to direct the laser to the sample for optoporation included an optical isolator, a polariser and a galvanometer (**Figure 39**). The polarised laser beam passed through an optical isolator, which permitted light transmission in one direction and prevented back-reflected light that could potentially damage optical components. Next, the beam is deflected towards a shutter where the shutter then controlled whether the light source would reach the cells or be blocked during an optoporation experiment. The rotating polariser managed light intensity. Aligning the polariser's transmission axis with the polarisation direction of the incident light achieved maximum intensity but as the polariser rotated away from this alignment, the transmitted light's intensity gradually decreased to extinction. This precise control was essential for regulating the laser power directed to the sample. The laser beam then proceeded to the galvanometer scanner, an electromechanical device that played a pivotal role in converting electrical input signals into precise mechanical motions by rotating mirrors. The galvanometer's rapid mirror movement allowed for the swift and accurate deflection of a laser beam across the field of view granting exact control over the laser's position. The galvanometer's versatility laid in its ability to alter the current, enabling the mirrors to position the laser beam with alternating scanning speed along the x-axis. This scanning speed could be controlled by the software as described in section 5.2.2 'Multi Scan Bleach' Command Box. Subsequently, the laser passed through the objective lens of the microscope and focused on a specific point within the field of view. In addition, the microscope system automatically captures a fluorescent and a bright field image immediately pre- and post-optoporation. By automatically switching the light sources and filters, the software controls the capture of these sequential images (**Figure 40**a).

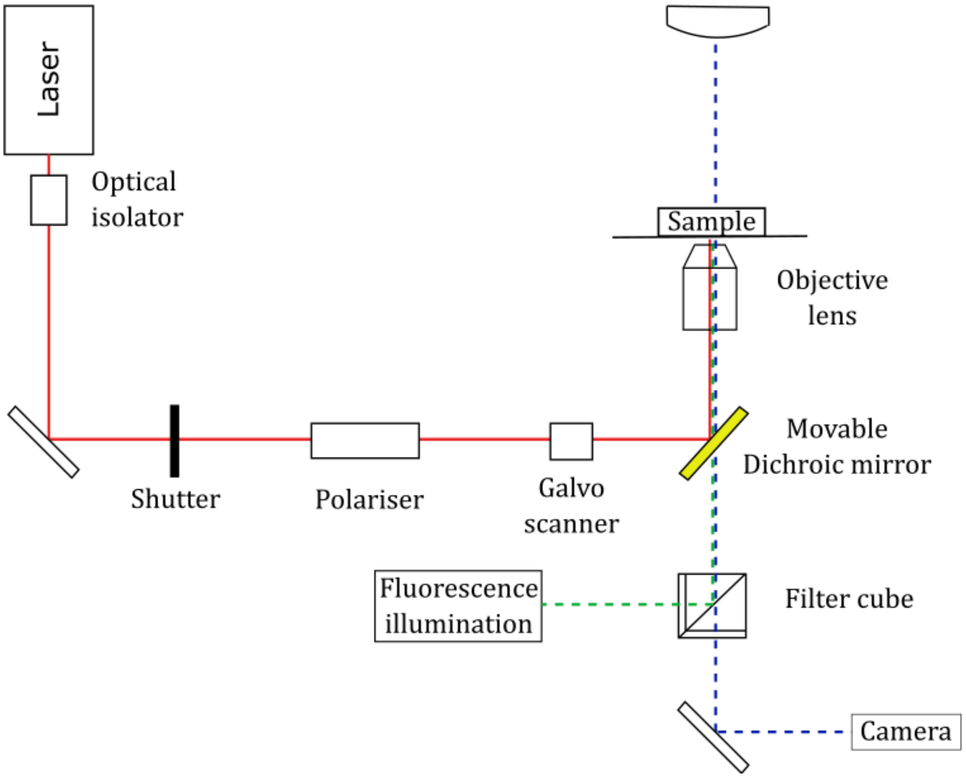

Figure 39: Schematic of the experimental setup. The laser beam passes through the optical isolator, shutter, polariser and galvanometer where it then passes through the objective lens and reaches the sample.

5.2.1 Customisable Laser Control Software Interface

An in-house MATLAB program controlled the parameters of the laser setup, including laser wavelength, laser intensity and scanning speed. It also allowed for the selection of specific areas within the field of view for the cells to be scanned by the laser.

The user interface (**Figure 40**) encompassed the following sections:

- **Imaging:** Controls the selection of the fluorescent channels, the exposure time (Exp s) and the light intensity during the imaging.
- **Multi Scan bleach:** Controls scanning speed and scanning area of the laser.
- **Laser Setup:** Controls the laser wavelength, calibrates the laser at the beginning of each experiment and rotates the polariser to manage the laser power.
- **Calibrate Laser Spot:** A calibration ensuring that the laser is in focus with the image.
- **Galvo Calibration:** A calibration ensuring that the laser scans the desired specific area within the field of view.

Of particular interest are the Laser Setup box (**Figure 40b**) and the MultiScan Bleach box (**Figure 40c**) as discussed in more detail below.

Channel	Acq	Exp (s)	
DAPI	☐	0.1	●
FITC	☐	0.1	○
CY3	☐	0.1	○
CY5	☐	0.1	○
[illegible]	☐	0.1	○
BF	☐	0.01	○

Power % 100

X rate (px/s) 10
Y step (px) 10
Repeats 1
Areas 1
Consistent Area Switch: ● No ○ Yes
Rec_W 50
Rec_H 100

laser wavelength (nm) 800
Laser power (%) 100
Laser power (mW) NA

Z-min -4
Z-max 4
Z-step 0.4
Z offset (um) 0

Max deflection (V) 4
Step deflection (V) 2

Figure 40: MATLAB user interface. Numerous parameters controlled via the in–house developed programme. The main parameters were a) the Imaging section, that controlled the selection of the fluorescent light, the exposure time and light intensity for image acquisition, b) the Multi Scan bleach, that controlled the laser wavelength and pulse energy and c) the Laser Setup, that controlled the horizontal scanning speed (x–rate), the vertical scanning step (y–step) and the number and size of the areas to scan.

The optoporation experiment workflow (**Figure 41**) started by calibrating the laser from the 'Laser Setup' box to determine the maximum laser power reaching the power meter at 800 nm after which the desired optoporation laser power could be set. Subsequently, I input the scanning speed, the scanning area size and the number of regions to scans in the 'Multi Scan Bleach' box followed by selecting the imaging channel and exposure time. Once this was set, the cells in the well plate had their medium exchanged with a solution containing the desired cargo and then selected areas within the field of view (FOV) to be targeted by the laser. Upon selecting 'select scan area' in the 'Multi Scan Bleach' box the software captured a pre-optoporation image, then optoporated the cells and captured a post-optoporation image.

The experimental workflow is summarised as follows:

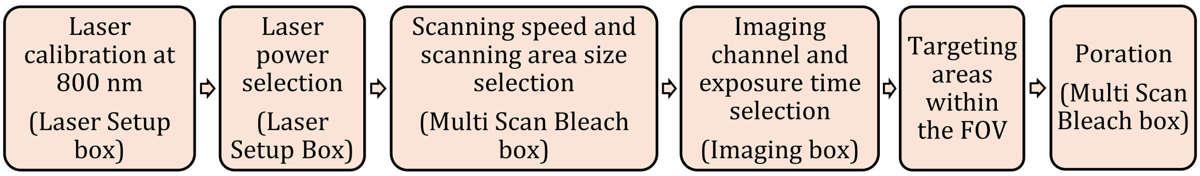

Figure 41: A summary of the optoporation experiment workflow.

5.2.2 'Multi Scan Bleach' Command Box

The laser scanning speed determined the time taken by the laser to traverse a specific area in the x direction. A higher 'x rate' corresponded to a swifter scanning speed, resulting in reduced laser exposure to the cells. The software quantified the speed in pixels per second (px/s), with a maximum achievable speed of 2000 px/s. The conversion of pixels to micrometres becomes straightforward once the field of view's scale is set. At a magnification of ×20, 1 pixel corresponded to 0.17 µm and a scanning speed of 2000 pixels/s equated to 340 µm/s. The 'y step' parameter controlled the gap between successive horizontal laser scans within the same area. For example, a 'y step' of 20 meant a 20-pixel separation between one horizontal scan and the next one within the same scanning area.

Clicking on the cells visible in the field of view caused the software to create red boxes that represented the areas to be scanned by the laser. Inputting values in the 'Rec_W' and 'Rec_H' determined the distance travelled by the laser in the x-axis and y-axis respectively. Lastly to improve the system throughput, the '#Areas' command allowed for multiple isolated areas to be scanned by the laser per acquisition.

As a proof of concept, the laser scanned a glass slide covered with a fluorescent dye that resulted in grids of photobleached areas on the fluorescently highlighted slide (with cells absent) (**Figure 42**). Seven red boxes of various sizes represented the different scanned regions in a single acquisition. Finally, photobleaching exclusively occurred within the designated red box, demonstrating the system's precision in targeting specific areas. In the presence of cells, optoporation can occur and the molecules in solution would enter into the cell.

Figure 42: Representation of scanned areas by the laser. A glass slide covered with a fluorescent dye with seven red boxes of various sizes representing the different photobleached areas with the laser in a single acquisition. The pulse energy used is 100% for exaggerated and visualisation purposes.

5.2.3 'Laser Setup' Command Box

The Ti: Sapphire femtosecond laser allowed for tuneability of the wavelength which could be controlled through the software in the 'Laser Setup' section. The wavelength was always at 800 nm for all the experiments carried out in this study. The laser calibration process performed at the start of each experiment recoded the maximum laser power reaching the sample (100%) through a power meter which was ~150 mW. However, to induce cellular poration, a fraction of this laser power was sufficient. Through the software, I controlled the amount of energy reaching the sample by calculating the percentage from the maximum power needed and inputting the value into the 'Laser Power' in the prompt. As a result, the polariser rotated to an angle and achieved the desired laser intensity, and the new value for the laser intensity displayed in the 'Laser Power mW' prompt.

5.3 Investigating the Poration Efficiency of pSi Nanoparticles

Comparing the delivery efficiency between the fabricated discoidal and rod-shaped pSi nanoparticles can help determine which nanoparticle structure performs better for optoporation applications. The impact of the interaction between nanoparticles and NIR two-photon laser pulses on cell membrane permeability can be validated by delivering impermeable fluorescent dye into a cell (Stojanovic et al., 2016).

As discussed earlier in Chapter 4, suitable conditions included a concentration of 30 μg/mL of pSi nanoparticles incubated with MCF-7 cells for one hour in a 2D system. On the other hand, control experiments consisted of cells that did not come in contact with nanoparticles. At this stage, laser scanning involved an x-step of 60 pixels and a y-step of 50 pixels, equivalent to 10 μm by 8.4 μm. The y-axis gap between one scanned line in the x-axis and the next was 10 pixels, resulting in multiple scans of the same cell in a grid-like pattern and treating a large portion of each cell with the laser. To test the optoporation efficiency, I introduced the impermeable propidium iodide in solution with the cells prior to cellular manipulation. I then laser-targeted the cells with various pulse energy levels ranging between 39 – 91 mW. If the laser-targeted cell took up the propidium iodide post-optoporation, then poration was successful. The small size of propidium iodide (668.4 Da) allowed the dye to rapidly diffuse across the poration site of the cell membrane in the cytosol. The propidium iodide bound to nucleic acids and emitted a red fluorescence signal enabling swift temporal and spatial examination of the optoporation process (Patskovsky et al., 2020).

Acquiring fluorescent pre-optoporation and post-optoporation images for cells bathed in the propidium iodide solution was necessary to calculate the poration efficiency. The efficiency of cellular poration could be determined by subtracting the fluorescent pre–optoporation image (**Figure 43a**) from the post–optoporation image (**Figure 43b**). Analysing the overlayed resultant image with marked laser-targeted areas (**Figure 43c**) determined the number of cells that had taken up propidium iodide after optoporation. Dividing this count by the total number of all the laser-targeted cells provided the poration efficiency.

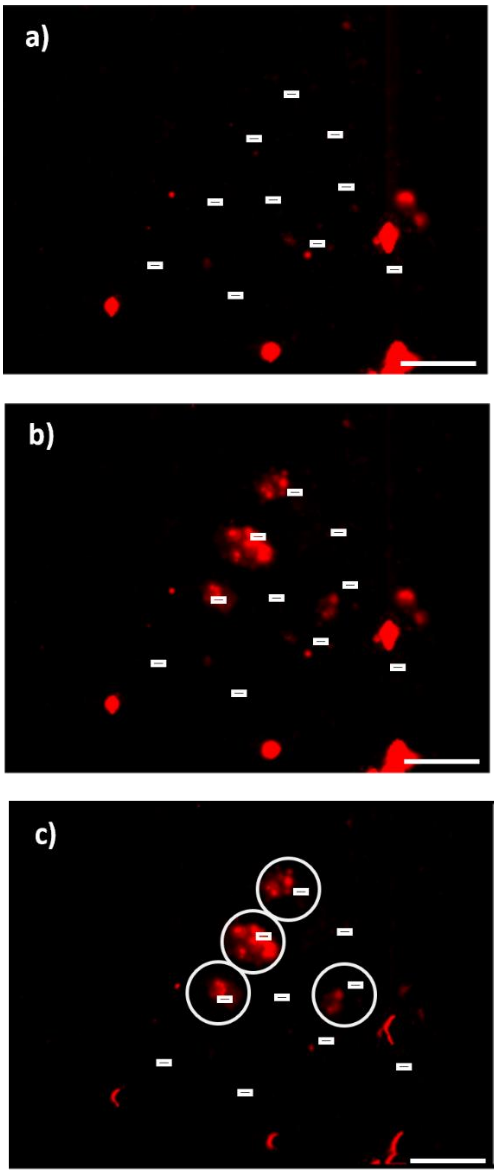

Figure 43: Delivery of propidium iodide to laser–targeted cells. a) pre–optoporation Cy3 image showing the uptake of propidium iodide by dead cells. b) post–optoporation Cy3 image showing further uptake of the propidium iodide by the laser–targeted cells. c) The resulting image after subtracting the pre-optoporation from the post-optoporation image. The white boxes represented the area scanned by the laser and the white circles represented the areas that resulted in propidium iodide uptake. Scale bar: 100 µm.

The optoporation efficiency without the presence of the nanoparticles (control) reached 2% at 78mW (**Figure 44**) marking the threshold of pulse energy needed to permeate the cell membrane. Indeed, in literature 50–100 mW of pulse energy were commonly used for membrane permeabilisation under non–sensitised conditions (Antkowiak et al., 2013). Below the 78 mW threshold, the cells in the control conditions remained unaffected with no recorded propidium iodide uptake post–optoporation.

In comparison, the addition of 30 μg/mL of EC and MACE nanoparticles led to enhanced coupling of the laser reaching optoporation efficiencies of 78% and 53%, respectively at 78 mW. These results suggested that the pulse energy should be kept at 65 mW or lower to avoid the range where poration occurred without nanoparticles. However, lowering the pulse energy also reduced the efficiency of cellular optoporation, reaching just 5% efficiency at 39 mW for both EC and MACE sensitised cells. Although EC nanoparticles appeared to perform slightly better, with MACE efficiency plateauing at ~55% and EC nanoparticles at ~80%, the difference between the two types of nanoparticles was not statistically significant (**Figure 44**).

Moving forward, I selected EC discoidal-like structured nanoparticles as the optimal nanoparticle type due to their higher optoporation efficiency and ease of fabrication compared to MACE nanoparticles. I chose a laser power of 65 mW for subsequent experiments as it provided the highest poration efficiency while avoiding the range where poration occurred in the absence of nanoparticles.

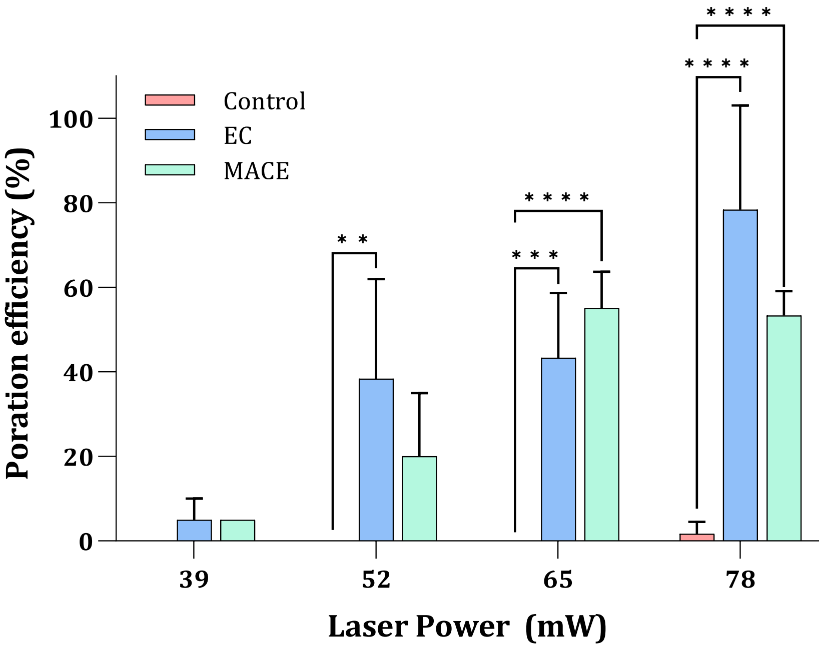

Figure 44: pSi nanoparticles enhance the cell poration efficiency. The poration efficiency measured when incubating the cells for one hour with 30 μg/mL of EC and MACE nanoparticles followed by irradiating at different laser powers. Statistical analysis using the ordinary two–way ANOVA with Tukey's post–hoc test determined there is a significant difference between the control and the use of nanoparticle on the cell poration efficiency. *p<0.05, **p<0.01, ***p<0.001, ****p<0.0001

5.4 Short-Term Cell Viability Assessment with EC Nanoparticles

Successful delivery of propidium iodide in the targeted cells was a significant achievement representing the spatially selective access to the cells. Yet, the true challenge lied in ensuring cell survival after optoporation. To evaluate short-term viability after optoporation, I assessed cellular retention of the fluorescent dye calcein-AM (acetoxymethyl ester), a cell-permeable dye after exposing the cells to a laser power of 65 mW. Calcein–AM undergoes rapid hydrolysis by intracellular esterase in viable cells, resulting in the impermeable green fluorescent calcein (Santra et al., 2014). Thus retention of the fluorescence signal indicates viable cells that were able to seal the induced transient pores suggesting recovery of the disrupted membrane(Fan et al., 2012). Conversely, non–viable cells display weak green fluorescence along the membrane or show no fluorescence at all (Eversole et al., 2020).

Cells successfully porated with restored plasma membrane integrity met two criteria, a) exhibited red fluorescence indicating propidium iodide uptake and b) retained the green fluorescent calcein dye. It is worth noting that post-optoporation, propidium iodide uptake only occurred in the targeted cells leaving the surrounding cells unaffected. The results (**Figure 45**) indicated that 30 minutes were sufficient for sealing the temporal pores created via optoporation. The experiment had to be limited to 30 minutes due to potential propidium iodide toxicity (Jones & Senft, 1985). Prolonged exposure to propidium iodide inside the cells can lead to cell death and thus give a false positive for the deaths caused by optoporation. Nevertheless, HeLa cells maintained viability after 2 hours of propidium iodide delivery (Mohan et al., 2021).

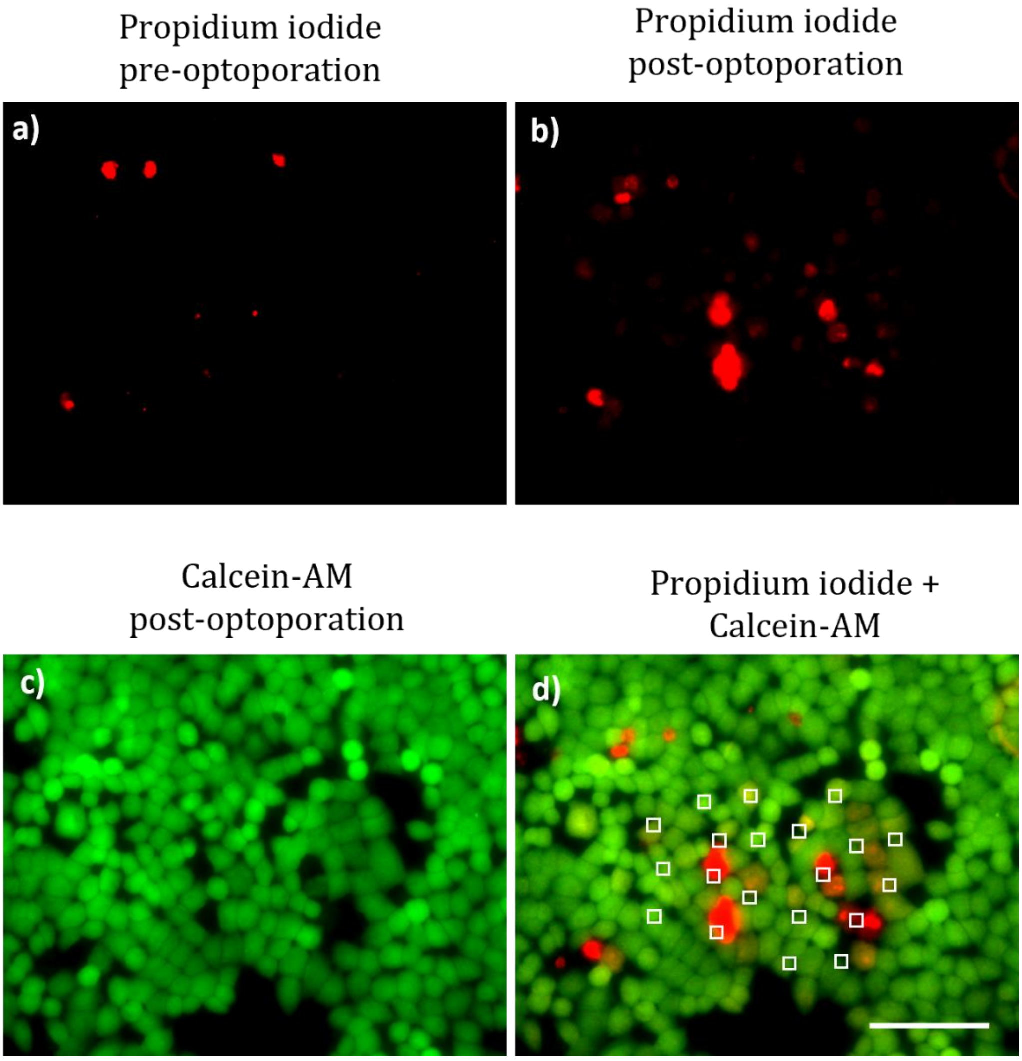

Figure 45: Short term viability assay at 30 µg/mL EC–nanoparticles and 65 mW. a) Pre–optoporation and b) post–optoporation imaging for propidium iodide to compare and avoid false–positive results. c) The retention of calcein and d) merge of the propidium iodide with calcein showing cells that have taken up propidium iodide after poration and retained the green fluorescence. Scale bar: 100 µm.

I calculated the delivery efficiency and the percentage of live cells when exposed to 65 mW of laser power by dividing the number of porated cells displaying both propidium iodide uptake and calcein retention by the total cells exposed to the laser (Saklayen et al., 2017). Similarly, dead cell efficiency involved dividing the number of porated cells displaying propidium iodide uptake and lacking green fluorescence by the total cells exposed to the laser. To examine how laser exposure time impacted delivery efficiency and short-term viability, I tested four different scanning speeds, where slower speeds corresponded to longer exposure times per cell. Repeating the optoporation process at

65 mW with 30 µg/mL at the different scanning speeds did not produce a significant difference in poration efficiency and obtained an average of ~65% efficiency. More importantly ~40% of the cells remain viable 30 minutes post-optoporation (**Figure 46**).

The percentage of cells exhibiting reversible membrane permeability through optoporation were in line with those discussed in literature, suggesting that these parameters could enable successful and comparable transfection efficiency.

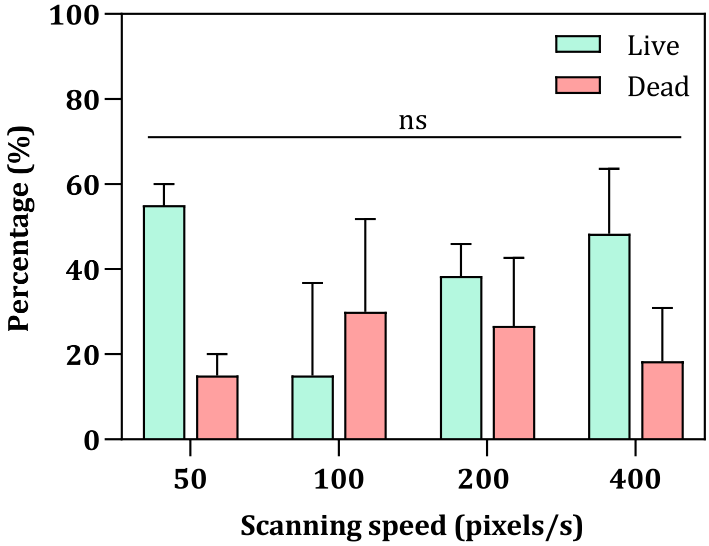

Figure 46: Short term viability at different scanning speed with 65mW laser power. Dead cells refer to porated cells with propidium iodide delivered without calcein retention, while live cells denote porated cells with propidium iodide delivered and calcein retention. The calculated percentage is derived from the total number of targeted cells, regardless of whether they are porated or not.

5.5 Optimisation of Laser–Induced mRNA Transfection

Delivering macromolecules like nucleic acids into specific target cells enables precise control over gene expression to investigate its function or model genetic diseases. It also allows characterisation of the long-term impacts of optoporation on cellular function. Herein, transfection involved delivering mRNA due to its cell cycle–independent transfection efficiency, rapid expression, and adjustable structure (Kim & Eberwine, 2010).

The nucleic acid delivered was eGFP mRNA sequence containing 996 nucleotides. The mature mRNA structure consisted of five significant parts (**Figure 47**). The mRNA had a

5'cap (m^7GpppN) followed by a 5'untranslated region (5'UTR). The coding region was the open reading frame (ORF) followed by a 3'untranslated region (3'UTR). Finally, a poly-A tail of 100–200A residues at its 3'end to enhance mRNA stability and translation (Elango et al., 2005; Mignone et al., 2002; Oh & Kessler, 2018). The mRNA possessed Cap 1 structure and chemical modifications of mRNA with 5–methoxyuridine that increased stability and protein expression compared to unmodified eGFP mRNA (Li et al., 2016).

In these experiments, I used two forms of eGFP mRNA, one tagged with Cy5 and one untagged eGFP mRNA. The Cy5 tagging allowed visual confirmation of mRNA delivery into cells through fluorescence, independent of translation. The tagged mRNA has an inverse relationship between translation efficiency and Cy5-UTP substitution (Stratech, 2023). To maximise visualisation and expression, I transfected the cells with a mixture of the tagged mRNA together with untagged mRNA in a 1:1 ratio.

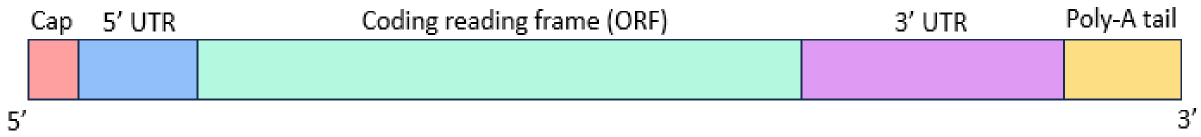

Figure 47: A schematic of eGFP mRNA structure. The five significant structures making up the mRNA including the cap, 5'UTR, coding reading frame, 3'UTR and Poly-A tail.

Initial experiments found that sample exposure to fluorescent light during optoporation decreased GFP translation 24 hours later. This led to a hypothesis that laser pulses and imaging processes may degrade GFP mRNA before translation. To address this, both imaging parameters and mRNA concentrations were optimised incrementally to minimise light-induced damage to mRNA and identify an optimal mRNA concentration for GFP expression.

5.5.1 eGFP mRNA Concentration Titration

The mRNA quantity has an impact on the transfection and expression levels, as higher mRNA concentrations are likely to increase the eGFP mRNA transfection efficiency. (Raes et al., 2020). To determine the impact of mRNA concentration in the optoporation system, I assessed the transfection of four concentrations including 0.125, 0.25, 1.0, and 2.0 μg of eGFP mRNA.

The lipofectamine controls (**Figure 48**) clearly showed that the lower concentrations of 0.125 μg and 0.25 μg of the eGFP mRNA led to a lower GFP expression compared to the higher concentrations of 1 and 2 μg. The optoporation performed at the four mRNA concentrations to investigate the influence of concentration on transfection efficiency, did not yield a positive result as none of the tested concentrations produced GFP expression. Therefore it could be concluded that the optoporation process for the transfection of cells with GFP in the presence of 30 μg/mL of EC–nanoparticles using 65 mW of laser energy proved unsuccessful. This lack of expression implied additional factors were impeding successful eGFP mRNA delivery and translation.

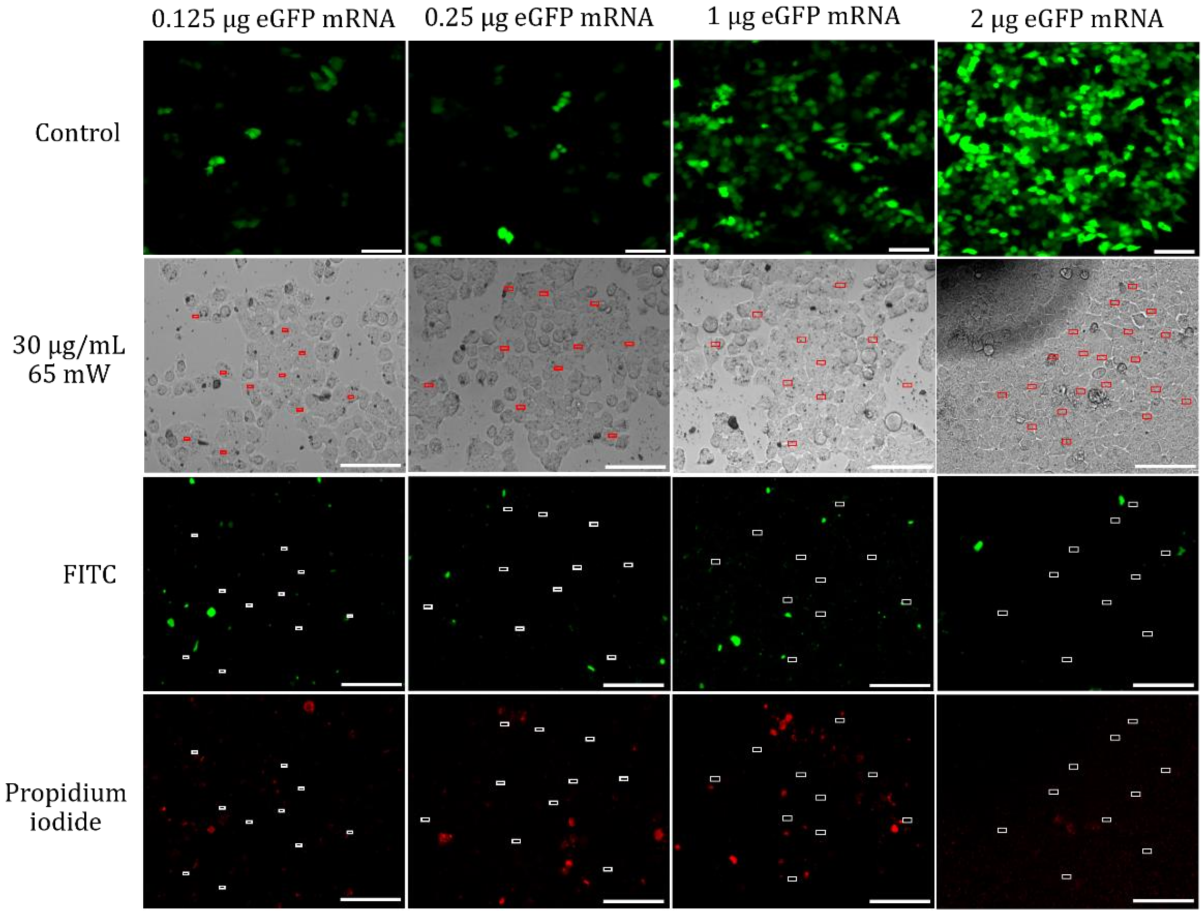

Figure 48: Influence of increasing eGFP mRNA concentration on transfection efficiency. FITC imaging for GFP expression and propidium iodide probing for dead cells at 24 hours post-optoporation.

5.5.2 Imaging and Laser Impact on eGFP mRNA Expression

A critical first step was identifying factors that could be impacting GFP expression after the mRNA delivery into the cells via optoporation. I hypothesised that the laser pulses and imaging process may be degrading the GFP mRNA before it could be translated. To test the impact of both processes, I transfected cells with eGFP mRNA using lipofectamine as a positive control in the presence of nanoparticles. In one experiment, lipofectamine transfection was immediately imaged with Cy5 channel (**Figure 49a**). Monitoring the GFP expression 24 hours after this process, demonstrated that even minimal light intensity of 30% and a short exposure time of 200 ms led to a reduction in the GFP expression when imaged with the Cy5 channel (651 nm). A clear indication that the imaging process was leaving a negative impact on the GFP expression, possibly due to photobleaching. It is important to note that imaging with other channels such as FITC (488 nm) did not result in an observable decline in the GFP expression. Attempts to enhance imaging quality by introducing bright cell MEMO photostable media did not yield improvements. Therefore, I only pursued fluorescence imaging at 24 hours post-optoporation to allow enough time for any eGFP mRNA within the cells to be expressed. In a separate experiment, I followed lipofectamine transfection with laser-targeting 20 cells at 65mW to mimic the process of optoporation transfection. In this instance, I used only bright-field for imaging to protect the integrity of the mRNA and its ability to be expressed. The results suggested that the laser irradiation at 65 mW had no discernible effect on the ability of cells in the scanned area to express GFP (**Figure 49b**). This demonstrated that the set laser parameters did not compromise or damage the transfected mRNA, allowing it to successfully express the GFP protein. Ensuring that the laser itself did not negatively impact the mRNA integrity and downstream expression was vital to properly assess the optoporation effectiveness as a transfection method.

In conclusion, monitoring the mRNA delivery into the cytosol through fluorescent imaging immediately after optoporation impacted negatively the eGFP mRNA integrity and its downstream expression. Therefore, restricting fluorescent imaging to at least 24 hours post-optoporation allowed enough time for the eGFP mRNA to translate before imaging. The optimised laser conditions were suitable and did not require any alterations at this stage.

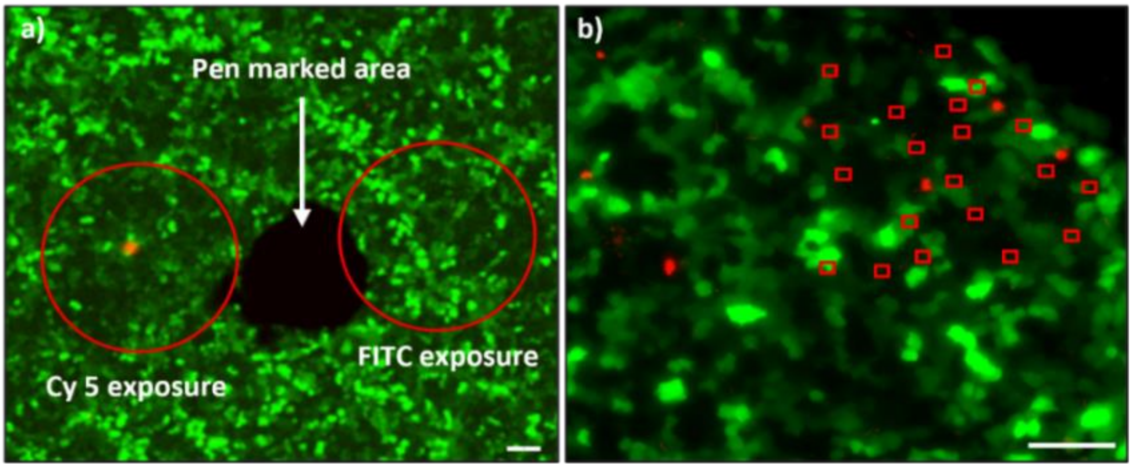

Figure 49: GFP expression in lipofectamine treated cells after 24 hours. a) A comparison between two areas, one exposed to Cy5 (651 nm) and the other to FITC (488 nm) for 200 ms at 30% intensity immediately after lipofectamine treatment. b) An area scanned with a 65 mW laser shortly after lipofectamine treatment. Scale bar: 100 µm.

5.5.3 Loading of pSi Nanoparticles with eGFP mRNA

This section focused on loading the negatively charged mRNA into nanoparticles to increase localisation of mRNA near the cell membrane as a strategy to further enhance mRNA delivery via optoporation.

The loading process relies on the electrostatic interaction between the negatively charged nucleic acids and the modified positively charged APTES functionalised pSi nanoparticles (Kamegawa et al., 2018). Herein, I incorporated the mRNA into the nanoparticles and measured the loading success using Qubit Fluorometer Assays by quantifying the residual mRNA in the supernatant after nanoparticle loading. Comparison of the mRNA concentration in the initial solution with that of the supernatant solution suggests a 95% loading efficiency of mRNA onto the nanoparticles (**Figure 50a**). Fluorescence in the Cy5 channel confirmed the loading of the Cy5 tagged eGFP mRNA onto the nanoparticles (**Figure 50b**).

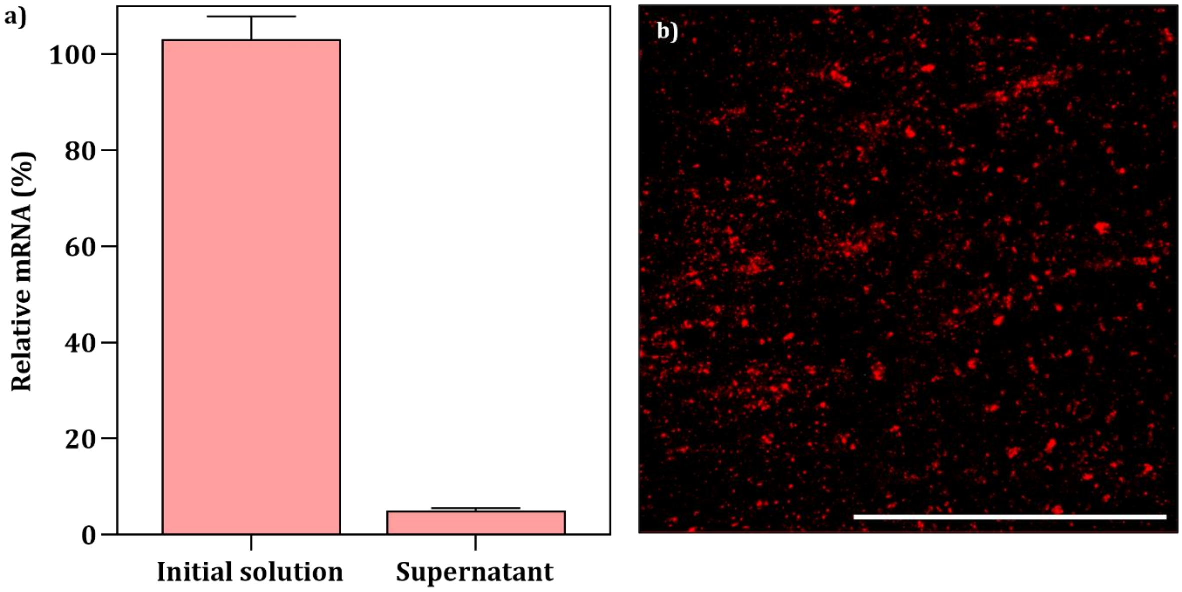

Figure 50: Loading of the mRNA into the pSi nanoparticles. a) The concentration of eGFP mRNA measured through Qubit Fluorometer Assay before complexation (initial solution) and after complexation (supernatant). b) Fluorescent image of the loaded nanoparticles with eGFP Cy5–tagged mRNA. Scale bar: 100 µm.

Cells treated with a 1:1 ratio of mRNA loaded nanoparticles and FITC tagged nanoparticles (for visualisation purposes) lacked GFP expression when imaged 24 hours post-optoporation. Any green fluorescence in the image was primarily stemming from the FITC–tagged nanoparticles (**Figure 51b**). Additionally, the detection of Cy5-tagged mRNA inside the targeted cells suggested successful membrane poration via optoporation (**Figure 51c**). However, assessing viability after 24 hours revealed that the cells containing Cy5-tagged mRNA were the same cells that had taken up propidium iodide (**Figure 51d**). Hence, indicating that the optoporation treatment under the current conditions, compromised cell survival underscoring the need for further optimisation of the laser system.

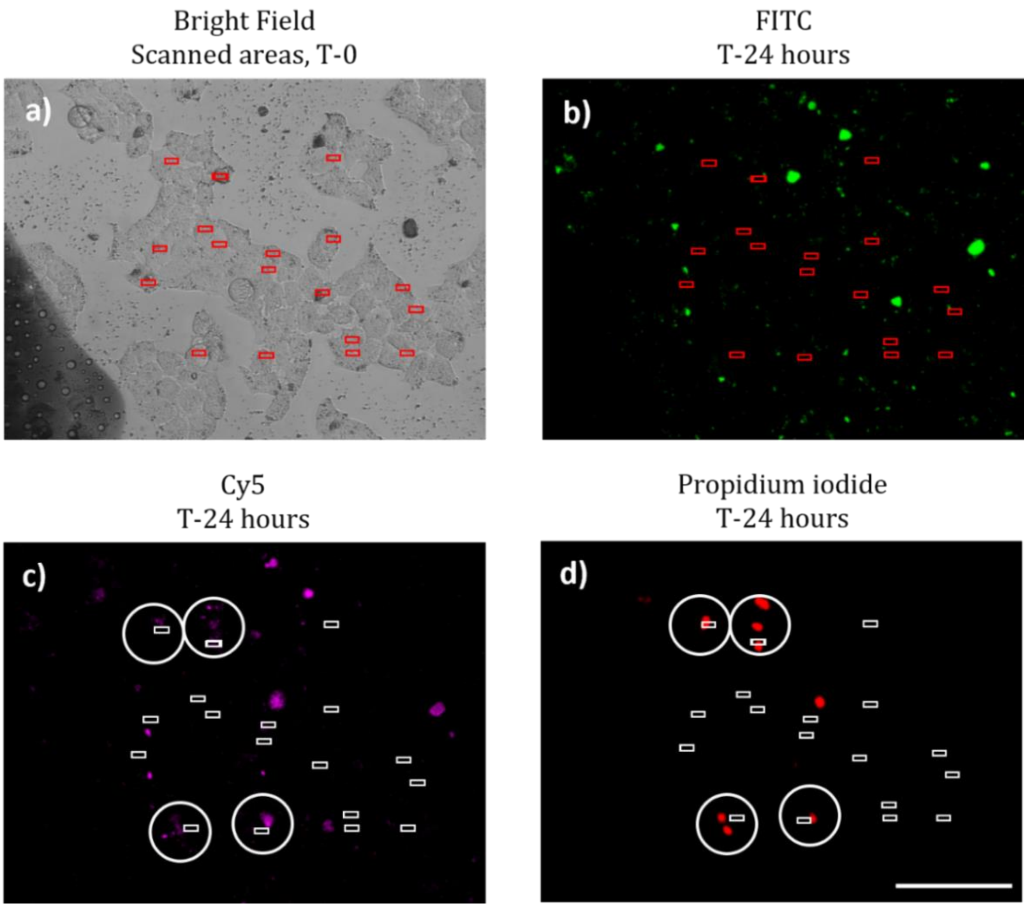

Figure 51: Visualisation of Cy5–tagged eGFP mRNA delivery in MCF–7 cells. a) Immediate imaging of laser–scanned areas post–optoporation and b) imaging after 24 hours of optoporation. c) Absence of GFP expression with observed green fluorescence attributed to FITC–tagged EC nanoparticles and d) cell viability assessed with propidium iodide staining after 24 hours. The white circles on images c and d represent the cells that were positive for both Cy-5 and propidium iodide uptake. Scale bar: 100 µm.

5.6 Optimisations for Nucleic Acid Delivery and Protein Translation

The selected laser power and nanoparticle concentration required further optimisation because the cells were not expressing the GFP protein and were indeed dying after 24 hours post-optoporation. To mitigate the adverse effects of the laser, I sought more favourable optoporation conditions than the current 65 mW and 30 µg/mL of nanoparticles. These conditions included scanning smaller target areas, investigating the impact of incubation time, altering the scanning speed, and concurrently increasing nanoparticle concentration while lowering the laser power. Further elaboration on these adjustments is provided below.

5.6.1 Laser Scanning Area

I hypothesised that the area scanned by the laser could impact cellular damage, as a larger scanned area would expose a greater portion of the cells to laser irradiation. To investigate the effect of scanned area size on optoporation efficiency, I quantified the propidium iodide uptake in the laser targeted cells for each scan area size.

The difference between the size of the areas selected was both in the x and in the y axis. Changes in the y-axis altered the number of scanned lines (horizontal axis). For example, changes involved from scanning a single horizontal line (35 × 10 pixels) to scanning the cells with two horizontal lines (35 × 30, 40 × 30, 45 × 30 pixels) and three horizonal lines (60 × 50 pixels). Along the x-axis, changes were minute by scanning different lengths of the cell ranging between 35 – 65 pixels. The largest scanned area, that of 60 by 50 pixels equivalent to 10 µm by 8.3 µm, exhibited a mean poration efficiency of 43%, while the smallest area yielded a very similar mean poration efficiency of 37% (**Figure 52**). Overall, there was no significant difference in the percentage of porated cells among the tested scanning areas, indicating similar cell membrane permeability efficiency.

Given the marginal difference between the different scanned sizes, I selected the smallest scanning area of 35 by 10 pixels, equivalent to 5.8 µm by 1.7 µm for the following experiments. The scope for selecting this scanning area was to enhance repeatability and reduce the risk of cellular damage, while having minimal impact on declining the poration efficiency.

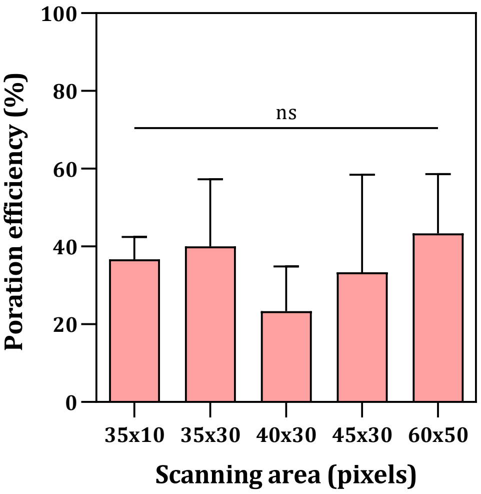

Figure 52: Optimisation of laser scanning area. The poration efficiency across five difference laser scanning areas as assessed through propidium iodide uptake. The ordinary one–way ANOVA test determined no significant difference among the various scanned areas.

5.6.2 The effect of pSi Nanoparticles Incubation Time on the Loading Density

The incubation time of nanoparticles with cells can impact the nanoparticle loading density on the cells, which may influence optoporation efficiency. To determine this relationship between incubation time and the amount of nanoparticles settling on the cells, I incubated cells with fluorescently labelled EC nanoparticles and measured fluorescence at varying incubation times. The fluorescence provided an indirect measurement for the amount of nanoparticle settling on the cells. Subsequently, I explored the relationship between loading density and optoporation efficiency through the quantification of propidium iodide delivery in the laser-targeted cells.

Literature reports have used various incubation times for different nanoparticle-cell systems, typically ranging from 30 minutes to 4 hours (Baumgart et al., 2012; Lachaine et al., 2016; Patskovsky et al., 2020; Schomaker et al., 2015; Wayteck et al., 2017). Therefore, I incubated cells with FITC-tagged nanoparticles for 30 minutes, 1 hour, 2 hours or 4 hours, followed by a washing step to remove unbound nanoparticles. Analysis of the total fluorescence at the four time points following image processing in ImageJ, resulted in the determination of the relative loading density. This involved background subtraction, threshold application to generate a binary image separating the object from the background and the removal of isolated single pixels. The results indicated that there was no significant difference between the 30 minutes and 1 hour time points but a significant difference in fluorescence emerged between 1–hour and longer incubation time (**Figure 53**). Thus, the prolonged incubation time allowed for more nanoparticles to settle on the cells. Importantly, this prolonged incubation did not induce cytotoxicity (**Figure 54**).

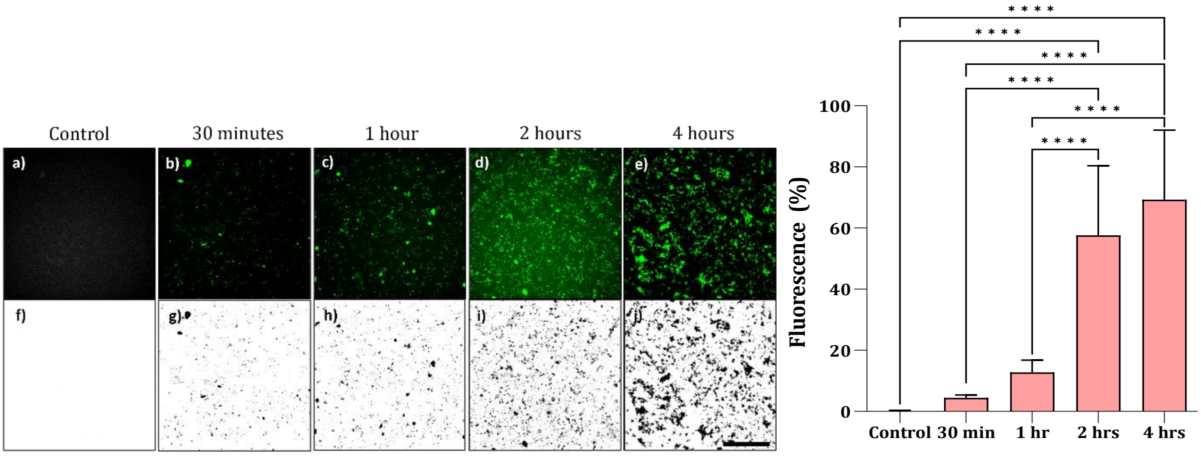

Figure 53: Impact of incubation time on nanoparticles' loading density. a–e) Fluorescence imaging of FITC–tagged nanoparticles post–washing at specified time intervals. f–j) Processed images showcasing background subtraction, threshold and single pixel removal. The bar chart summarises the findings and offers a relative comparison. Statistical analysis using a one–way ANOVA test determined significant difference between incubation periods of one hour or less and extended incubation times. Scale bar: 100 µm. ****p<0.0001, n=3.

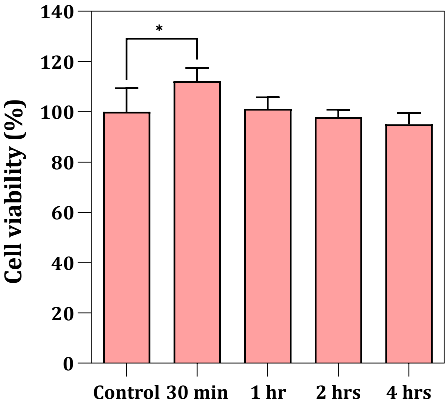

Figure 54: Cell viability assay for EC–nanoparticles after different incubation times. Determined with the Cell Titer–Glo assay and expressed relative to the untreated control group. Statistical analysis using a one–way ANOVA test determined no significant difference between the different incubation periods except for the minor difference between the control and 30 minutes. *p = 0.0243, n=3.

The significant difference in the loading density between one hour and longer incubation time led to the investigation of the optoporation efficiency between the one hour and the four-hour time point. This comparison involved incubating 30 µg/mL of pSi nanoparticles for either one hour or four hours followed by optoporation with a range of laser power. The area scanned per cell was 35 by 10 pixels, with a scanning time of 1.40 seconds per area. I observed three distinct field of view for each biological replicate and laser targeted ten cells in each field of view. As a result, each biological replicate consisted of laser-targeting 30 cells. Overall, the four-hour incubation timepoint performed better than the one hour timepoint with higher percentage of laser-targeted cell taking up propidium iodide (**Figure 55**). The difference in poration efficiency between the two incubation times varied by less than 10% at pulse energy below 39 mW. However, the disparity became more pronounced at higher pulse energy of 52 and 65 mW. At these setting, the four-hour incubation timepoint showed 24% and 43% higher cell poration efficiency, respectively, compared to the one-hour incubation.

In conclusion, the higher nanoparticle concentration positively impacted optoporation efficiency. This suggested that increasing the nanoparticle-cell interactions by elevating nanoparticle concentration could further improve efficiency.

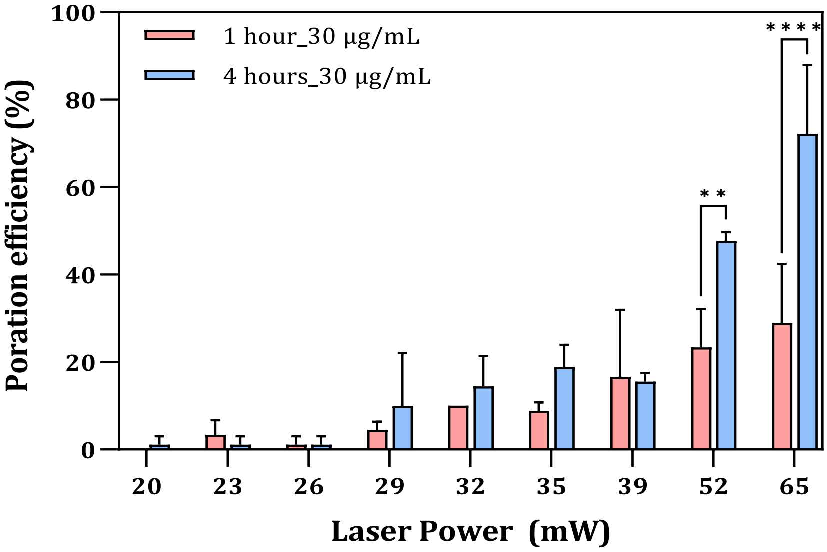

Figure 55: The effect of different incubation times on cell poration efficiency. Poration efficiency of cells at different laser fluences when incubated with 30 µg/mL of EC nanoparticles for one hour vs four hours. Statistical analysis using the ordinary two–way ANOVA with Tukey's post–hoc test determined there is a significant difference between one hour and four hours incubation time with laser powers of 52 and 65 mW. **p<0.01, ****p<0.0001.

5.6.3 Laser Power and EC Nanoparticle Concentrations Impact

A key aim was accelerating the experimental workflow by reducing incubation time while maintaining similar nanoparticle loading density to that obtained within the four-hour time frame. This prompted further exploration into using higher initial nanoparticle concentrations with a shorter incubation period. A short incubation period for the nanoparticles is convenient, as it allows the nanoparticles to adhere to the cell membrane and if endocytosed, the nanoparticles would remain in close proximity to the cell surface membrane (Raes et al., 2019). This positioning of the nanoparticles near the cell surface is desirable as it makes them easily accessible for their interaction with the laser. In contrast longer incubation times increase the chances of the nanoparticles to be endocytosed deep within the cell which would be less favourable for the optoporation process.

The approach was to evaluate the propidium iodide delivery efficiency at three different concentrations of 30, 100 and 150 µg/mL of EC-nanoparticles still with one hour incubation. In parallel I also investigated the poration efficiency at each nanoparticle concentration with a range of laser powers. At a concentration of 30 µg/mL EC nanoparticles and 65 mW exposure, ~30% of cells exhibited propidium iodide uptake (**Figure 56**). In comparison, increasing the nanoparticle concentration also increased the poration efficiency, particularly with increasing laser powers. Below 26 mW, there was a similar trend of low poration efficiency not exceeding 10% at all of the three nanoparticle concentrations. In fact, there was no significant difference in the poration efficiency between the three concentrations when exposed to laser powers of 20 to 26 mW. Focusing solely on the 100 µg/mL concentration, the uptake increased to 22% when using 29 mW. The delivery efficiency remained relatively constant until 52 mW which resulted in an increase to 43% and then to 62% at 65 mW. Similarly, at 150 µg/mL the uptake increased to 31% at 29 mW and remained constant up until 52 mW at which the poration efficiency increased to 71%. This suggests there is an energy input threshold that must be overcome to effectively porate the cell membrane and facilitate uptake. Once this threshold was exceeded at 29 mW and at 52 mW, the delivery efficiency continued to improve. Interestingly, the optoporation efficiency achieved with a four hour incubation at 30 µg/mL was very similar to the efficiency obtained at the higher concentrations of 100 and 150 µg/mL with one hour incubation. Therefore this suggests that increasing the initial loading density of the one hour incubation achieved similar amounts of nanoparticles settling on the cells as the four hours incubation period.

Overall, the results obtained were in line with those of other nanoparticles used in optoporation (Holguin et al., 2018). Whereby increasing the pulse energy and the EC nanoparticle concentration caused for a greater amount of energy to be absorbed by the nanoparticles that transduced into other energy forms and impacted the cells' permeability. As a result, the selected nanoparticle concentrations were that of 100 µg/mL with an incubation time of one hour. Furthermore, the greatest difference in poration efficiency occurred at 29 mW and 65 mW. Therefore, I selected these two power levels for further optimisation experiments to refine the optoporation system parameters.

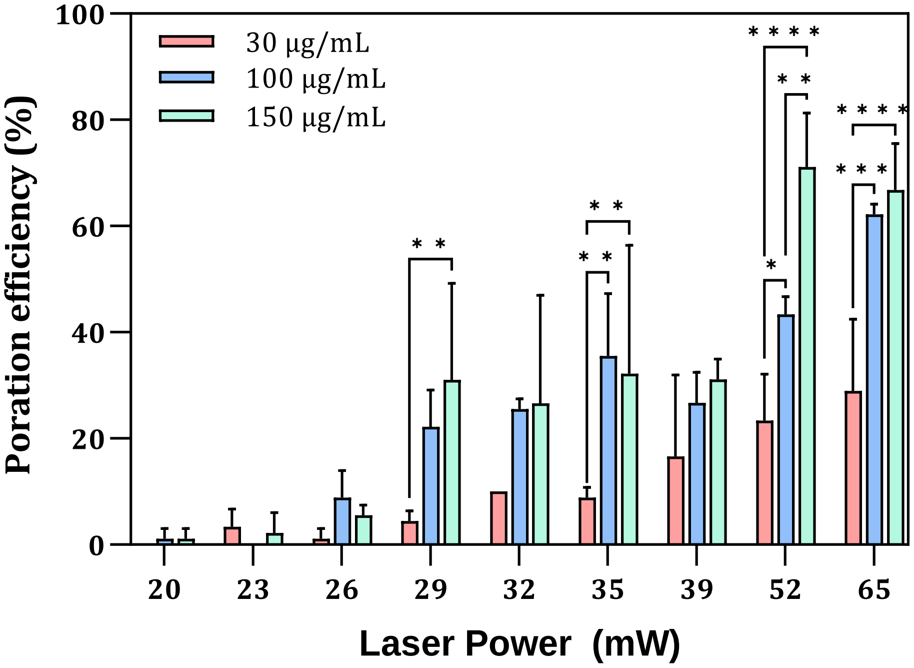

Figure 56: The effect of EC–nanoparticle concentration on cell poration efficiency. Poration of cells at different laser fluences with 30, 100 and 150 µg/mL of EC–nanoparticles and one hour incubation. Statistical analysis using the ordinary two–way ANOVA with Tukey's post–hoc test determined there is a significant difference between 30 µg/mL and the two concentrations of 100 and 150 µg/mL at most of the high laser powers (above 29 mW). A significant difference between 100 and 150 µg/mL was only observed at 52 mW. *p<0.05, **p<0.01, ***p<0.001, ****p<0.0001.

5.6.4 Scanning Speed Impact on Uptake Efficiency

High–repetition rate femtosecond lasers operating in the MHz range can have a high number of overlapping pulses during laser irradiation resulting in heat accumulation (Talone et al., 2021). The localised thermal accumulation might induce cellular damage, leading to altered cell behaviour or even cell death. Aiming at minimising the laser's exposure time, thereby reducing the generated thermal energy, I systematically varied the scanning speed and measured the poration efficiency for each condition. The explored scanning speed ranged between 50 pixels/s to the maximum scanning speed supported by the system that of 2000 pixels/s. The time required to scan an area at a scanning speed of 50 pixels/s was 0.7 seconds at a rate of 8.4 μm/s, while 2000 pixels/s took 0.0171 seconds (17.1 ms) per area at a rate of 340 μm/s.

I performed a comparative study to investigate the scanning speeds impact on poration efficiency at 29 mW (**Figure 57**) and 65 mW (**Figure 58**) in the presence of 30, 100 and 150 μg/mL of EC nanoparticles. Aligning with previous results, increasing the nanoparticle concentration from 30 μg/mL to 100 μg/mL or 150 μg/mL significantly enhanced the propidium iodide uptake. Although not statistically significant, the 150 μg/mL concentration yielded slightly higher poration efficiency over 100 μg/mL at both power levels. Importantly, the scanning speed did not impact poration efficiency for any of the nanoparticle concentrations, achieving less than 10% difference in efficiency between 50 pixels/s and 2000 pixels/s. Therefore, I selected 2000 pixels/s as the optimum scanning speed because the higher scanning speed minimised laser exposure time and potentially reduced damage without compromising poration efficiency. Additionally, higher scanning speeds allowed for greater throughput since it took less time to scan a given area.

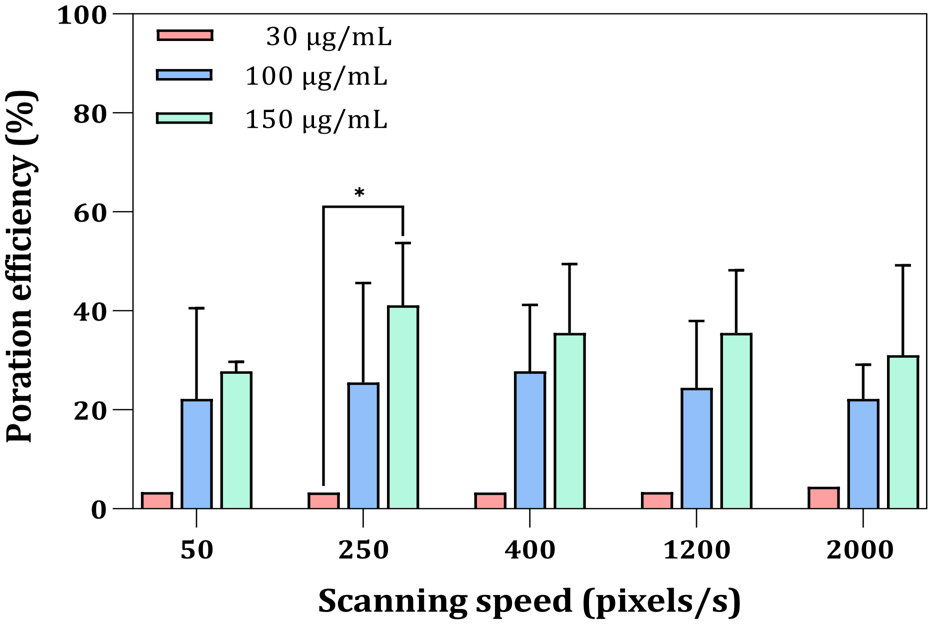

Figure 57: The effect of scanning speed on the poration efficiency at 29 mW. Cells incubated with different concentrations of nanoparticles and porated at 29 mW at different laser scanning speeds. Statistical analysis using the ordinary two–way ANOVA with Tukey's post–hoc test determined there is no significant difference between the same concentration of nanoparticles at different scanning speeds. *$p<0.05$.

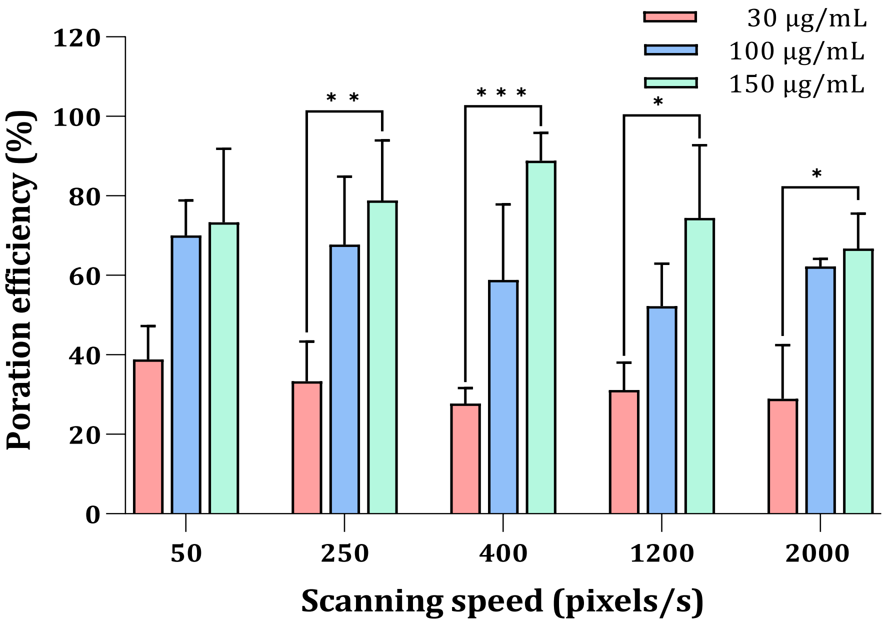

Figure 58: The effect of scanning speed on the poration efficiency at 65 mW. Porated cells at 65 mW and at different laser scanning speeds. Statistical analysis using the ordinary two–way ANOVA with Tukey's post–hoc test determined there is no significant difference between the same concentration of nanoparticles at different scanning speeds. $*p<0.05$, $**p<0.01$, $***p<0.001$.

5.6.5 Short–term Cell Viability

Once the conditions had been optimised to maximise optoporation efficiency, the next crucial step was determining whether these optimised conditions were suitable for the disrupted membrane to recover post–optoporation. Experiments exploring the cell's resilience to the optoporation treatment included examining the cells for their ability to hydrolyse calcein-AM. The calcein–AM experiments at 29 mW with 100 µg/mL determined cellular viability (**Figure 59**). The merged image of propidium iodide and calcein–AM showed cells retaining both dyes indicating that cells remained viable for at least 30 minutes post–optoporation. Analysis of the images showed that ~30% of the targeted cells had propidium iodide delivery and ~20% of the targeted cells had both dyes present (**Figure 60**). This consistent trend across various scanning speeds aligned with the earlier data, indicating that scanning speed did not affect the poration outcome.

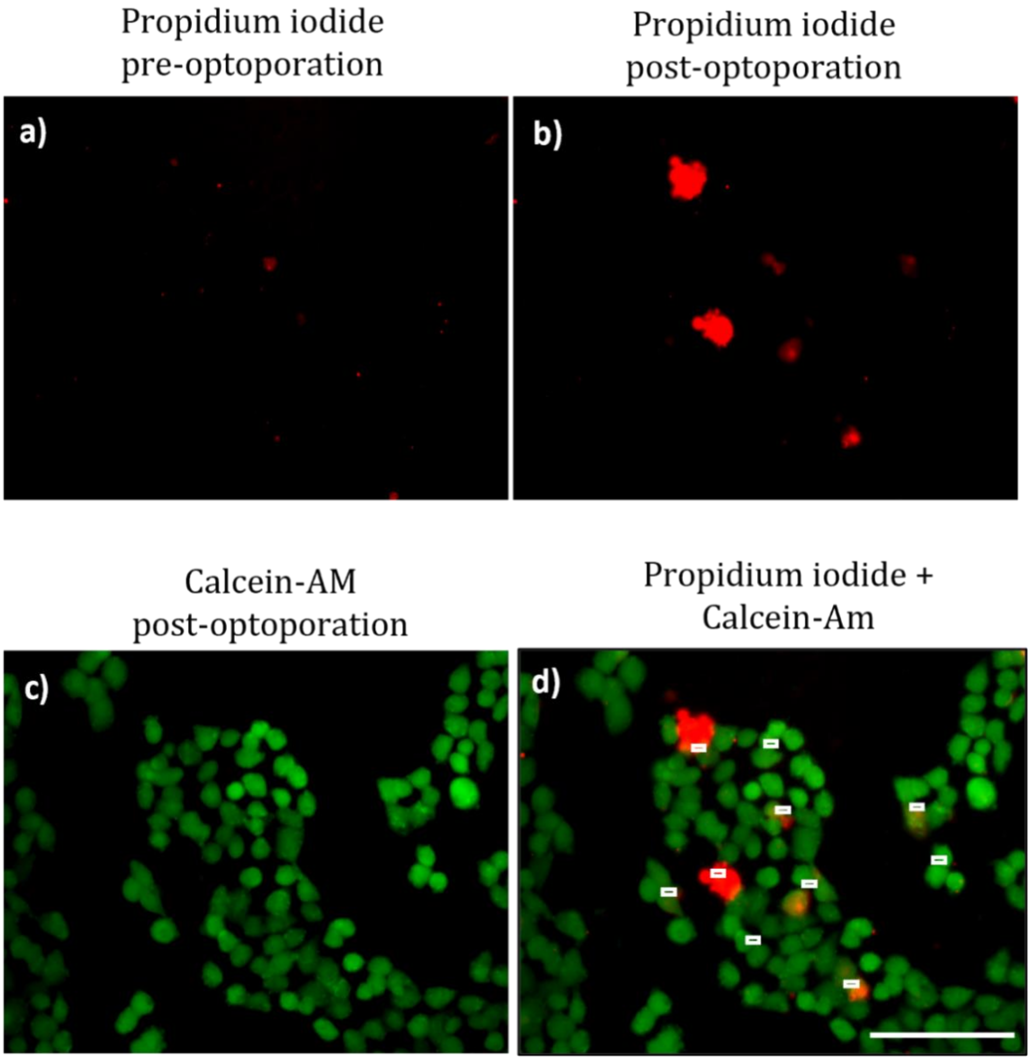

Figure 59: Short term viability assay at 29 mW with 100 µg/mL EC–nanoparticles. a) Pre–optoporation and b) post–optoporation imaging for propidium iodide to compare and avoid false–positive results. c) The retention of calcein and d) merge of the propidium iodide with calcein–AM showing cells that have taken up propidium iodide after poration and retained the green fluorescence. Scale bar: 100 µm.

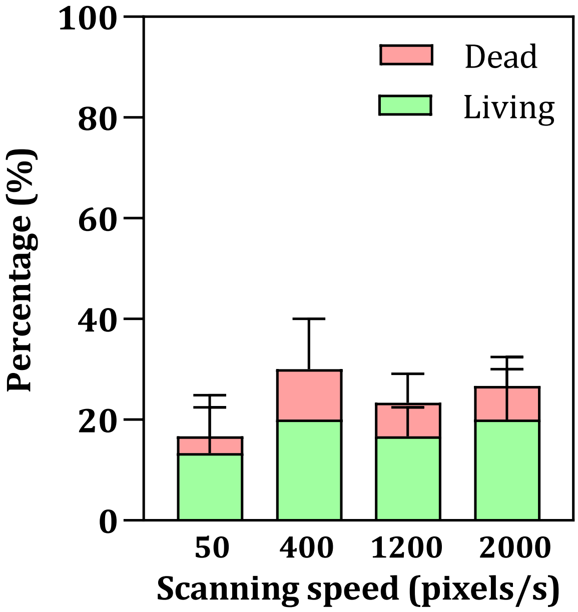

Figure 60: Short term viability at different scanning speed at 29 mW with 100 µg/mL. Dead cells refer to porated cells with propidium iodide delivered without calcein retention, while live cells denote porated cells with propidium iodide delivered and calcein retention. The calculated percentage is derived from the total number of targeted cells, regardless of whether they are porated or not.

5.6.6 Reactive Oxygen Species and Apoptosis

Further verification of the cells' viability was through the detection of ROS and caspase 3/7. The presence of ROS is commonly assessed by small–molecule fluorescent probes including the fluorescence probe 2'7'–dichlorodihydrofluorescein diacetate (DCFH–DA) that I used in this study.

DCFH–DA readily enters cells and upon encountering ROS it is oxidised to the impermeable and fluorescent 2',7'–dichlorofluorescein. It is important to note that this assay serves solely as an indicator of altered ROS levels as it is not specific to any particular ROS and is sensitive to local oxygen levels and pH (Brandes et al., 2015; Kowaltowski, 2019). Thus, implementing suitable controls is crucial to ensure that positive results stem only from the optoporation treatment (Murphy et al., 2022). Negative controls to account for background fluorescence included imaging cells with and without DCFH–DA but without the optoporation treatment (**Figure 61a–d**). A positive control using hydrogen peroxide (**Figure 61e, f**) yielded the anticipated green fluorescence signal indicating the presence of reactive oxygen species. It is important to note that DCFH–DA is not directly oxidised by peroxide but the peroxide is converted to other reactive species facilitated by proteins like cellular peroxidases, cytochrome C and redox–active metals (Dikalov & Harrison, 2014; Murphy et al., 2022). Irradiation of cells with 65 mW in the presence of 30 µg/mL of EC–nanoparticles resulted in the detection of ROS within two minutes post–optoporation as a green fluorescence signal appeared in the laser–irradiated cells (**Figure 61g, h**). In contrast, irradiation of cells with a lower laser power, specifically 29 mW at 100 µg/mL, did not exhibit a green fluorescence signal even after a 10 minute incubation period (**Figure 61i, j**).

Accumulation of ROS within cells can lead to oxidative stress and damage in vital macromolecules like proteins, nucleic acids and lipids. This damage, in turn has the potential to trigger cell death processes including apoptosis (Redza–Dutordoir & Averill–Bates, 2016). Therefore, I assessed cellular viability by probing for the apoptotic markers caspase 3/7. Irradiating the cells with 65 mW at 30 µg/mL of EC nanoparticles resulted in green fluorescent cells representing the presence of caspase 3/7 (**Figure 62a–d**). Subsequently, the same cells had tested positive for propidium iodide uptake one hour post–optoporation, signifying cell death. Remarkably, there was no visible apoptotic cells or propidium iodide uptake for the conditions of 29 mW at 100 µg/mL (**Figure 62e–h**). This served to confirm the maintenance of cell viability and the reversible membrane damage caused by the laser as indicated by the absence of propidium iodide uptake one hour post–optoporation.

Cellular viability remained unaffected under these newly optimised conditions. Consequently, the laser-induced transfection of eGFP mRNA could be reattempted by exposing the cells to 100 µg/mL of EC nanoparticles at 29 mW, 2000 pixel/s scanning speed and a scan area of 35 × 10 pixels.

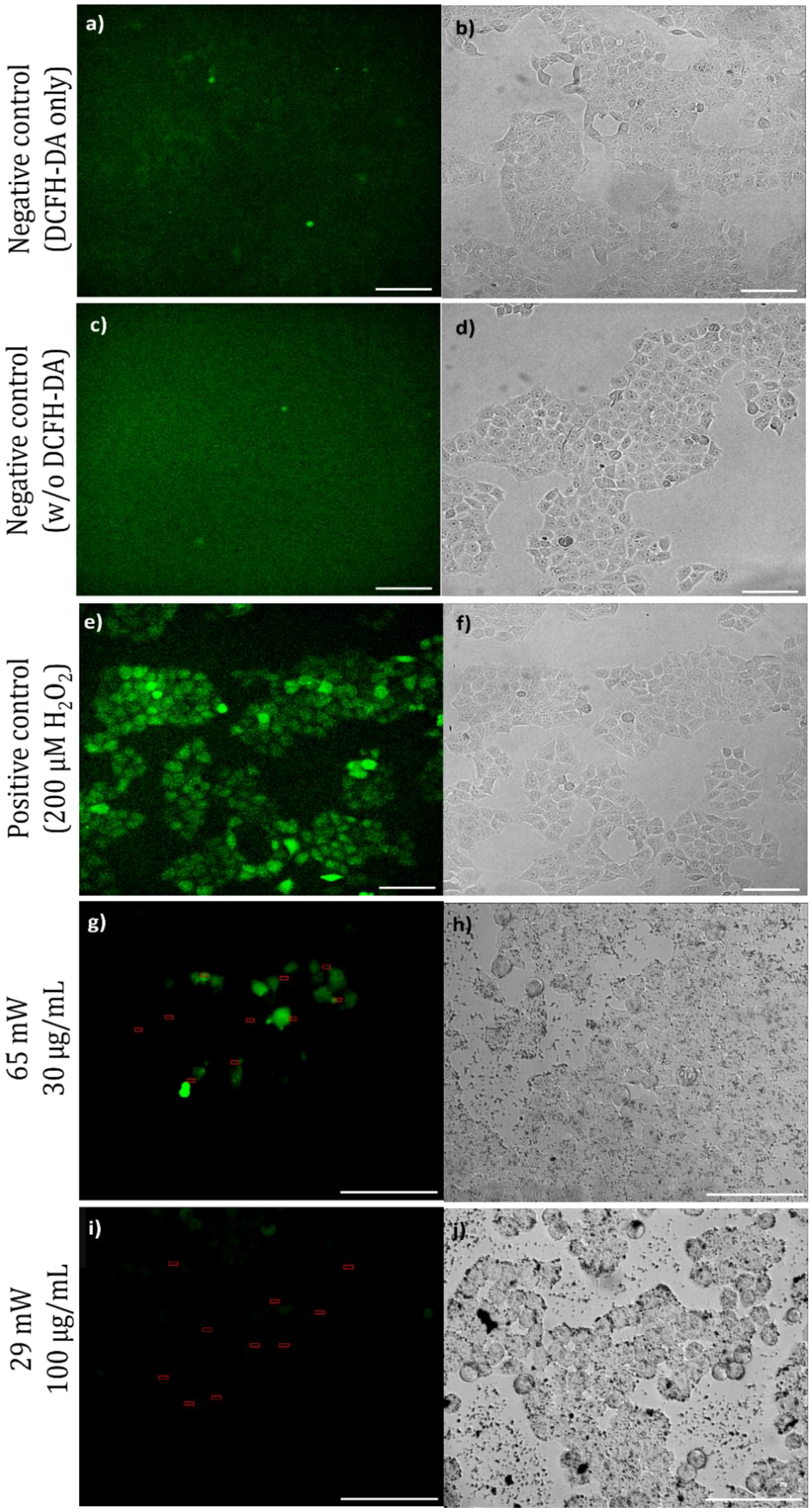

Figure 61: ROS detection using DCFH–DA. Fluorescent and bright field imaging of: a–d) Negative controls with and without DCFH–DA respectively, e, f) Positive control in the presence of 200 µM H_2O_2, g, h) Optoporation areas at 65 mW with 30 µg/mL EC–nanoparticles and i, j) optoporation areas at 29 mW with 100 µg/mL EC–nanoparticles. Scale bar: 100 µm.

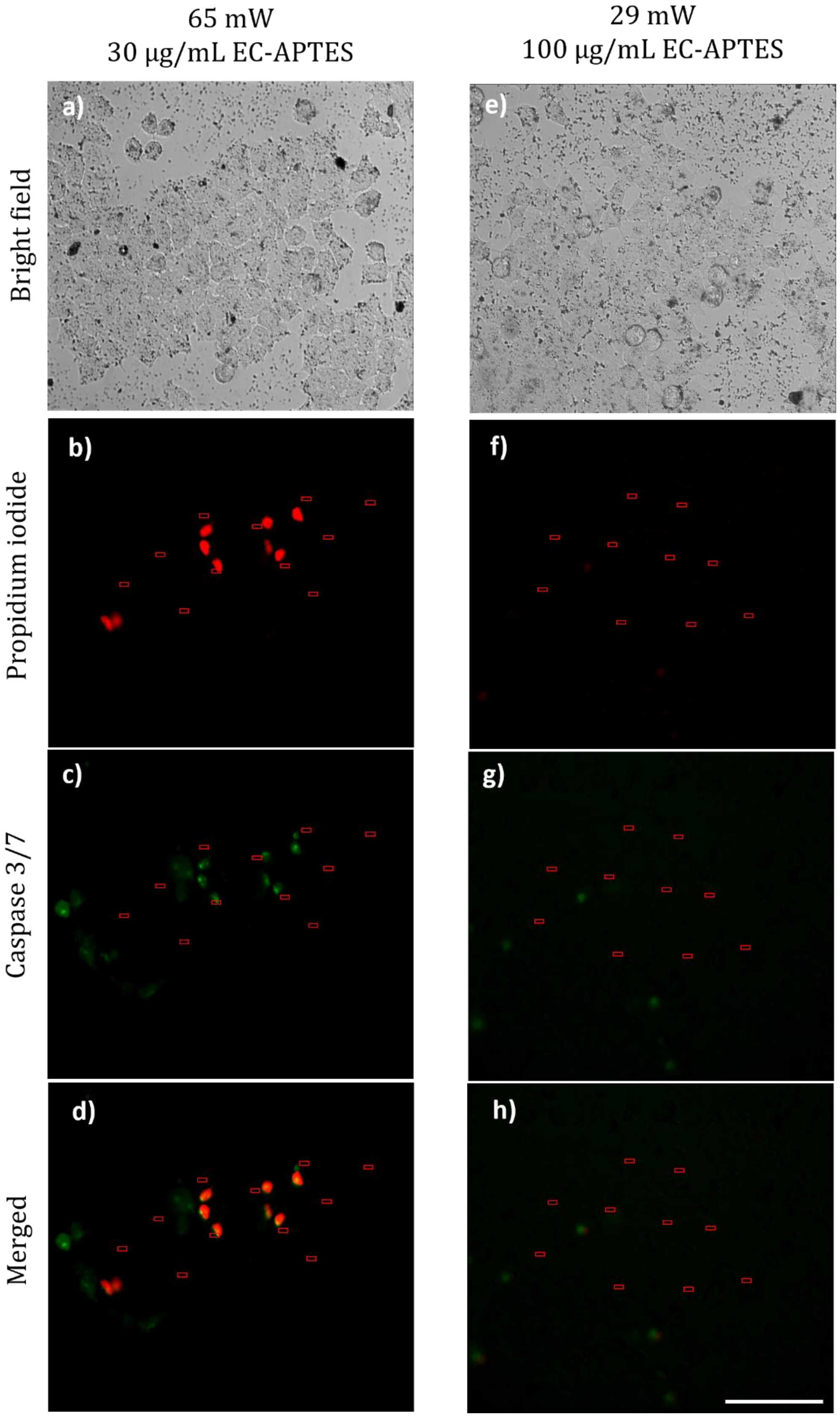

Figure 62: Caspase 3/7 detection. Fluorescent and bright field imaging of: a–d) laser–irradiated areas at 65 mW with 30 µg/mL EC–nanoparticles and e–h) laser–irradiated areas at 29 mW with 100 µg/mL EC–nanoparticles. Scale bar: 100 µm.

5.7 Altering the Functionalisation of the EC Nanoparticles

Proceeding to transfecting the cells with eGFP mRNA using 100 µg/mL of EC FITC tagged nanoparticles revealed a substantial increase in the fluorescent background within the green channel. This increase in background fluorescence interfered with the GFP protein's fluorescent signal, resulting in challenges when identifying the level of GFP expression. In fact, control experiments of the lipofectamine with GFP mRNA (**Figure 63a**) showed that it was difficult to distinguish between the signal originating from the tagged nanoparticles (**Figure 63c**) and that from the cells. This was not an issue with 30 µg/mL (**Figure 63b**). An alternative approach was to use ocean blue–tagged (OB) nanoparticles (**Figure 63d, e**), and APTES functionalised nanoparticles (**Figure 63f, g**) aiming at assessing whether dye functionalisation had any adverse impact on the GFP signal.

Overall, both APTES and ocean–blue tagged nanoparticles showed unhindered GFP expression suggesting that both type of nanoparticles were suitable replacements for the FITC–tagged EC-nanoparticles. Given that the cells appeared adhered better to the well plate in the presence of APTES-nanoparticles, I selected these nanoparticles for the following experiments.

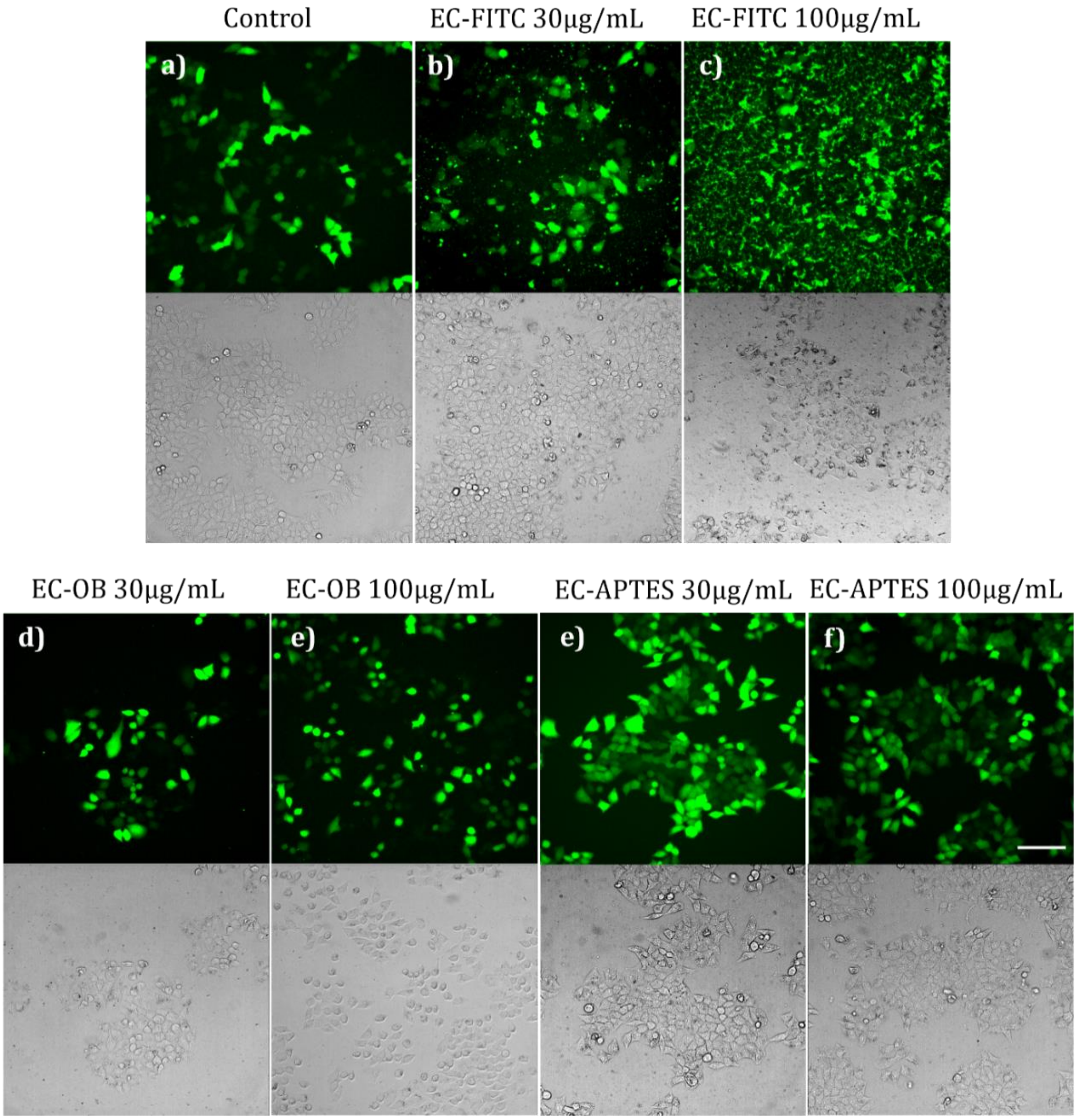

Figure 63: GFP mRNA transfection using lipofectamine. Three distinct type of functionalised nanoparticles – FITC, OB and APTES tagged at concentrations of 30 μg/mL and 100 μg/mL incubated with the cells in the presence of lipofectamine. Scale bar: 100 μm.

5.8 GFP mRNA Transfection via Optoporation

Once all the conditions were set, laser-induced eGFP transfection could be tested at a laser power of 29 mW at 2000 pixels/s. To achieve maximum output, I tested a series of laser powers within ±10 mW range of the 29 mW at nanoparticles concentrations of both 100 and 150 μg/mL. Successful experiments resulted in the delivery and expression of eGFP mRNA. One experimental approach involved laser-targeting individual cells by using the 35 x 10 pixels box dimensions (**Figure 64a and Figure 65a**). An alternative approach involved scanning a larger area thereby targeting a greater portion of the cells within the field of view (**Figure 64b and Figure 65b**). I took this decision based on the previous understanding that the scanning area had no significant impact on the cells. Additionally, it was challenging to focus on the cells when 150 µg/mL of nanoparticles covered the cells. Within both approaches, a pulse energy of 35 mW led to considerable cell death, with occasional cells fluorescing green indicative of GFP expression suggesting that some cells were surviving the optoporation process.

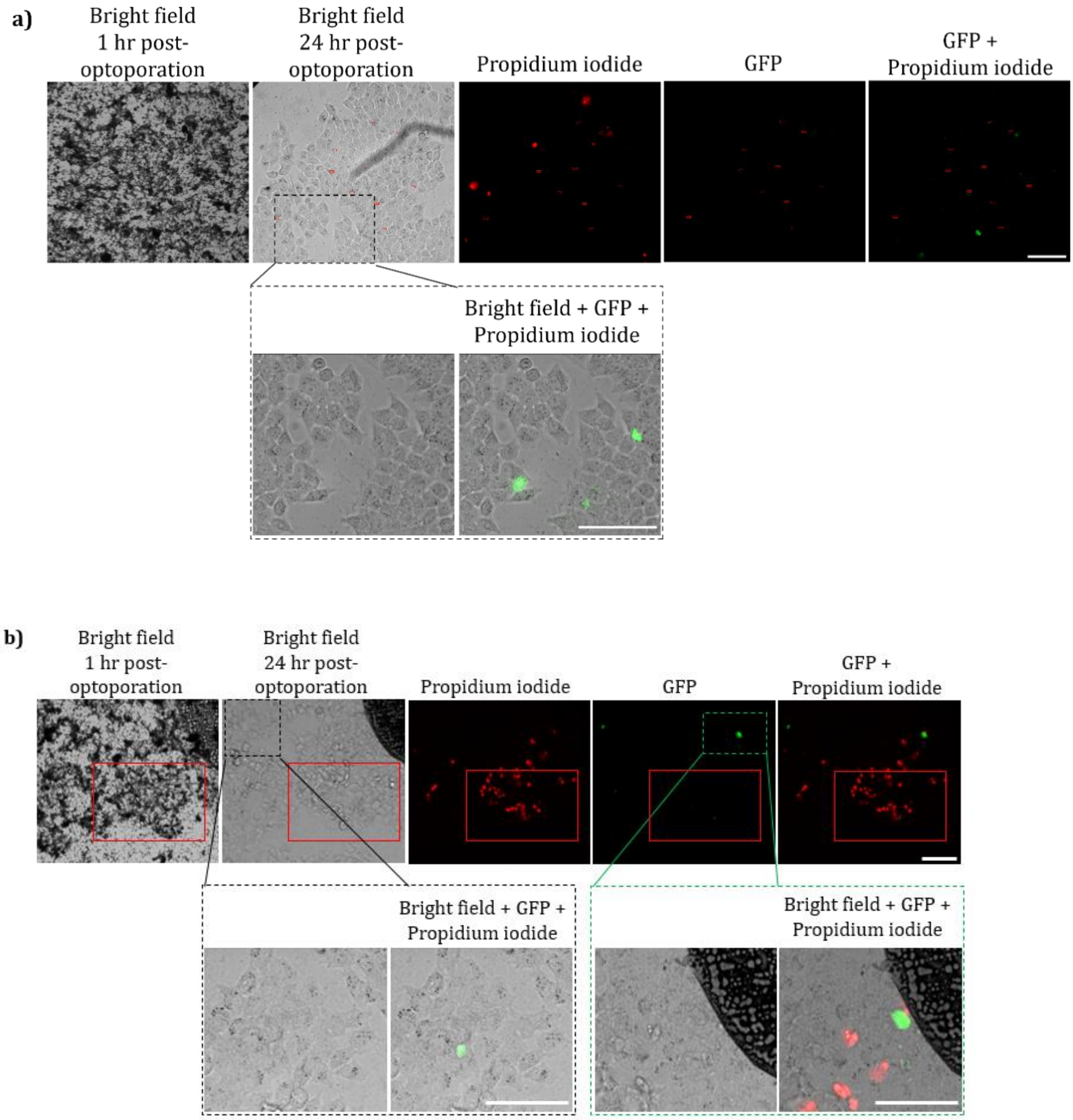

Figure 64: GFP mRNA transfection via optoporation at 35 mW and 100 µg/mL of EC nanoparticles. a) Laser scanning of 10 areas, each measuring 35 × 10 pixels and b) laser scanning of larger areas. Scale bar: 100 µm.

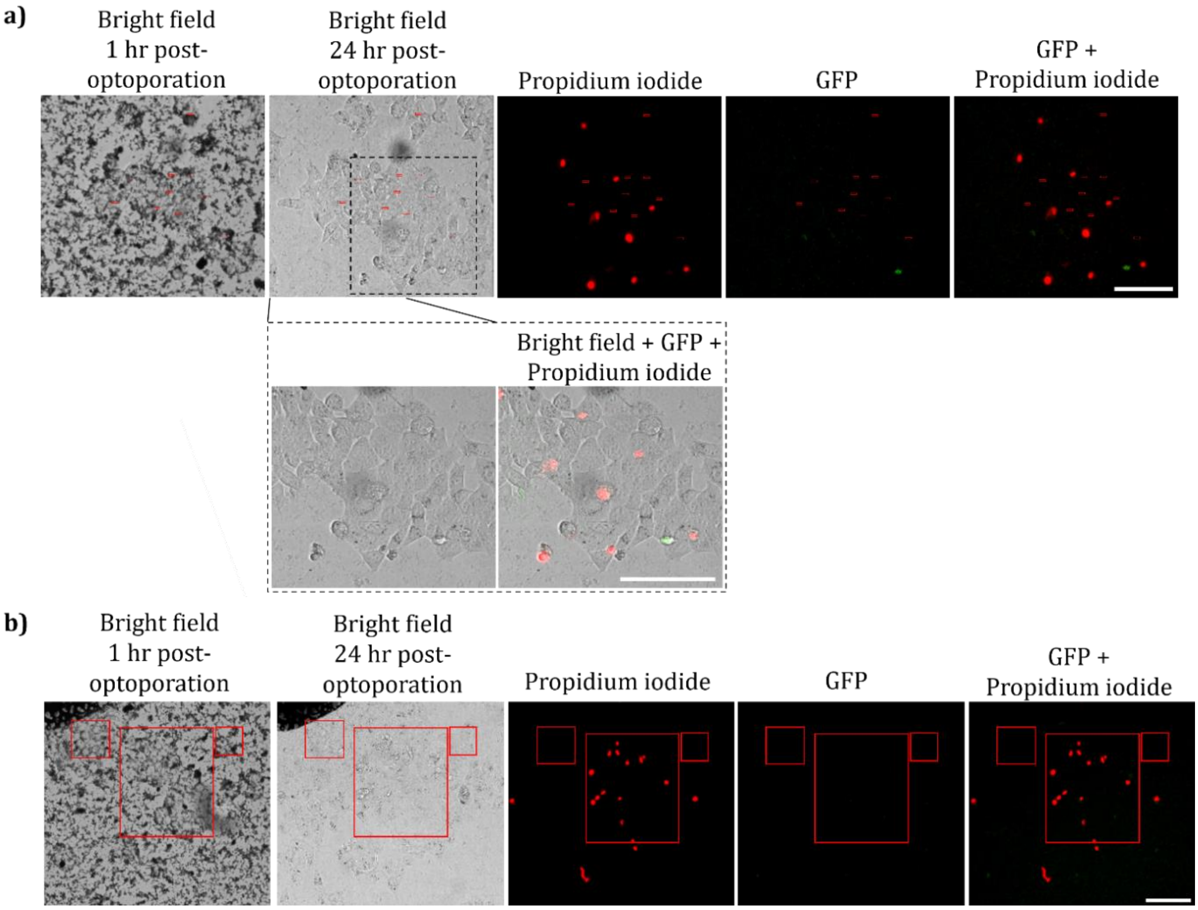

Figure 65: GFP mRNA transfection via optoporation at 35 mW and 150 µg/mL of EC–nanoparticles. a) Laser scanning of 10 areas, each measuring 35 × 10 pixels and b) laser scanning of larger areas. Scale bar: 100 µm.

Nonetheless, the extensive cell death seen through propidium iodide uptake at 24 hours post-optoporation highlighted the need to use lower laser power. To identify conditions enabling GFP expression with minimal cell death, I tested a range of laser powers from 20-32 mW in 3 mW intervals at both 100 and 150 µg/mL nanoparticles. **Figure 66** presents only the positive results obtained with cells expressing GFP 24 hours post-optoporation. In summary, the 100 and the 150 µg/mL nanoparticles concentrations resulted in only 1 to 3 cells expressing GFP (~4%) within the targeted field of view, 24 hours post-optoporation. This data demonstrates that while there is successful delivery and reversible membrane permeability, as evidenced by the cells expressing GFP, the level of GFP expression remained constant across the different parameters tested. This suggests that the optoporation system has reached a plateau as the nanoparticles concentration, laser power and scanning speed had all been extensively investigated, yet GFP expression remained limited.

Compared to a similar near-infrared femtosecond laser for the target-based approach utilising polystyrene-based plasmid-coated microparticles on MCF-7 cells also achieved a rather low transfection efficiency of 12.7% (Waleed et al., 2013). In contrast, methods employing bulk optoporation have reported higher mRNA delivery efficiencies, such as ~38% in adherent HeLa cells and 20% in suspension Jurkat cells using gold vapour nanobubble–mediated optoporation (Raes et al., 2020). Similarly coupling polydopamine nanosensitisers and black phosphorus under near–infrared radiation resulted in a ~40% transfection efficiency for eGFP mRNA (Harizaj et al., 2021; Wang et al., 2021). Meanwhile, a gold plasmonic-enhanced femtosecond laser method achieved an average transfection rate of 23% in human cancer melanoma cells (Baumgart et al., 2012).

It is worth noting that some studies have reported even higher transfection rates by directing the laser straight onto the targets cells. However, this may come at the cost of greater labour intensity in focusing onto the cell membrane. Some results worth highlighting include the transfection of human hepatocarcinoma cells (HepG2) using a femtosecond laser at a longer wavelengths of 1554 nm, achieving a remarkable 77% transfection rate with a DNA plasmid containing the GFP gene (He et al., 2011). Similarly, canine mammary cells achieved a 30% cell transfection rate with plasmid DNA encoding GFP (Baumgart et al., 2008). Previous studies involving plasmids encoded eGFP have also reported transfection rates around 30% (Davis et al., 2013; Schneckenburger et al., 2002).

The transfection results obtained here were low compared to other methods, however, it may not be just to compare these technique in terms of efficiency alone. This is primarily because transfection efficiency varies greatly between mammalian cell lines and MCF–7 cells are considered as hard to transfect (Uchida et al., 2009). Secondly, there were discrepancies in the way that researchers reported transfection efficiency. Some of the reported efficiencies included all the targeted cells by the laser regardless of whether membrane permeabilisation has occurred or whether the cell had died (Stevenson et al., 2006). Additionally, a 24 – 48 hour incubation period is required to monitor GFP expression. During this time, cell division occur, producing daughter cells that also express GFP. Counting all GFP-expressing cells at the endpoint, could result in a higher calculated efficiency (Stevenson et al., 2006). This all also contributed to a large range in the transfection efficiency reported among the various literature.

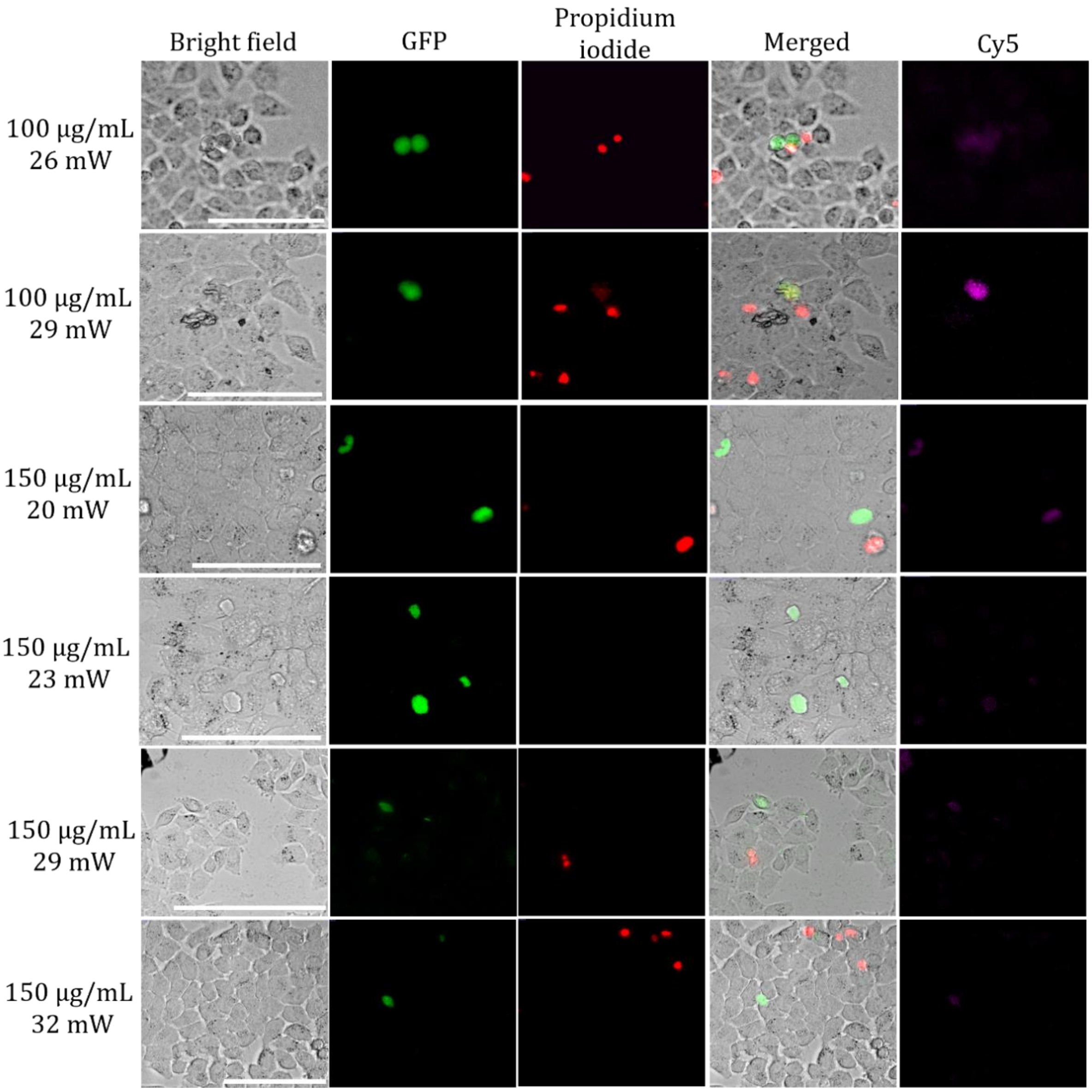

Figure 66: GFP mRNA transfection via optoporation. Optoporation with laser powers ranging between 20 – 32mW with 100 and 150 µg/mL of EC nanoparticles resulted in GFP expression. Scale bar: 100 µm.

5.9 Optoporation of 3D MCF–7 Spheroids

Research on optoporation delivery efficiency within three dimensional tissue model has not been well explored. The optimised optoporation methodology developed herein served as an avenue for exploring the feasibility of laser–targeting individual cells within spheroids. I reverted to FITC-tagged EC nanoparticles to better visualise the nanoparticles within this new cellular environment, ensuring focusing on the nanoparticles and thus improving the success of optoporation. Once again, the propidium iodide uptake by the laser-targeted cells gave an indication of the poration efficiency in these 3D spheroid models.

Leaving the spheroids growing for 24 hours ensured that the spheroids were compact enough for handling and maintaining their integrity. Such a time frame also prevented the spheroids from developing a necrotic core accompanied by cell apoptosis (Alves et al., 2023). Consequently, irradiation occurred 24 hours post-cell seeding. In accordance with the conclusions outlined in Chapter 4, the introduction of 100 µg/mL of EC-nanoparticles hindered spheroid formation. A comparison between the additions of 30 µg/mL and 60 µg/mL resulted for the 60 µg/mL to generate structurally irregular spheroids with increased cell death. Consequently, I opted for the use of 30 µg/mL of EC nanoparticles in these 3D models.

I implemented two concurrent strategies for optoporation in the 3D spheroids. The first involved incorporating 30 µg/mL FITC tagged EC-nanoparticles to the cells, followed by a 24 hours hanging drop incubation. This yielded a uniform distribution of the nanoparticles throughout the spheroid (**Figure 67a**). Alternatively, the second approach involved first forming the spheroid and then after 24 hours loading a higher nanoparticle concentration of 200 µg/mL resulting for the nanoparticles to primarily localise to the spheroid's periphery (**Figure 67b**).

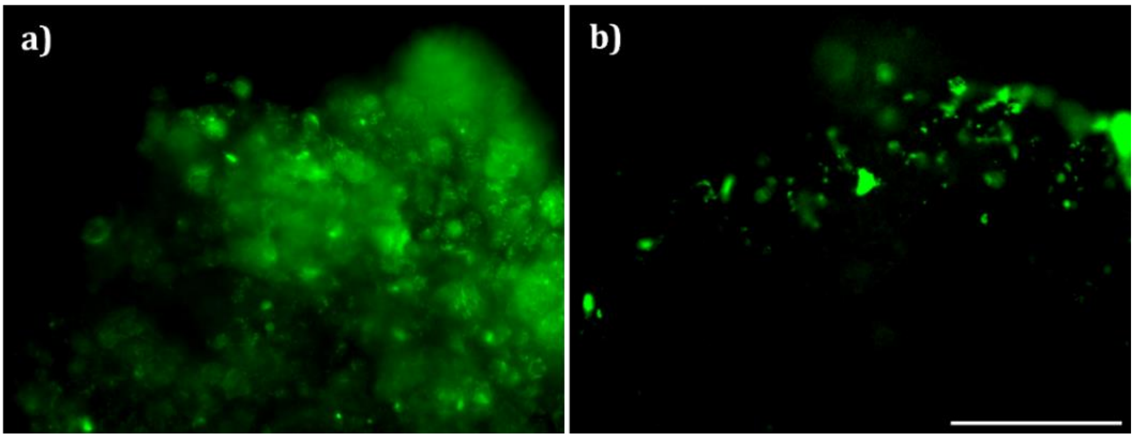

Figure 67: Interaction of EC–nanoparticles with spheroids. a) Uniform mixing of 30 µg/mL FITC–tagged nanoparticles with the cells suspension, followed by a 24 hour incubation using the hanging drop method. b) Concentration of 200 µg/mL FITC–tagged nanoparticles added post-spheroid formation. Scale bar: 100 µm.

I hypothesised that higher laser power would be needed for successful permeation given the dense and compact structure of 3D spheroids. Therefore, I investigated a range of laser powers including 39 mW, 55 mW and 65 mW and in fact propidium iodide uptake occurred exclusively at 55 mW and 65 mW. Spheroids with uniformly mixed nanoparticles displayed spatially selective dye delivery throughout the full spheroid depth (**Figure 68**). In contrast, spheroids with EC nanoparticles concentrated at the periphery achieved spatially restricted propidium iodide delivery penetrating around 20 µm (**Figure 69, Figure 70**). The lack of propidium iodide uptake by the targeted cells cannot be due to the dye's inability to penetrate or diffuse through the spheroid's core. This is because the naturally occurring dead cells within the core of the spheroid exhibited positive propidium iodide uptake. Despite the small number of porated cells, the results hold promise as it signified access to individually targeted cells within the spheroid.

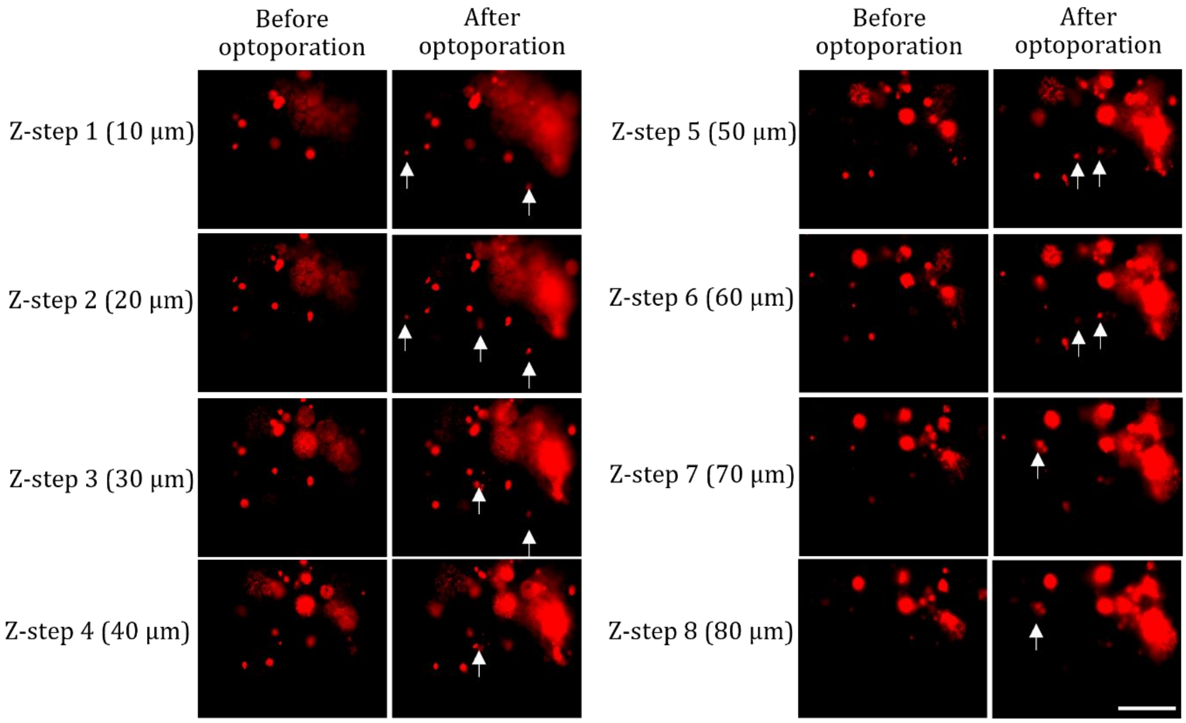

Figure 68: Optoporation on spheroids with uniformly mixed EC–nanoparticles. The spatial selective delivery of propidium iodide at 65 mW with 30 µg/mL as seen throughout the full spheroid depth. The Z-step represents the sequential image acquisition at each 10 µm along the optical axis. Scale bar: 100 µm.

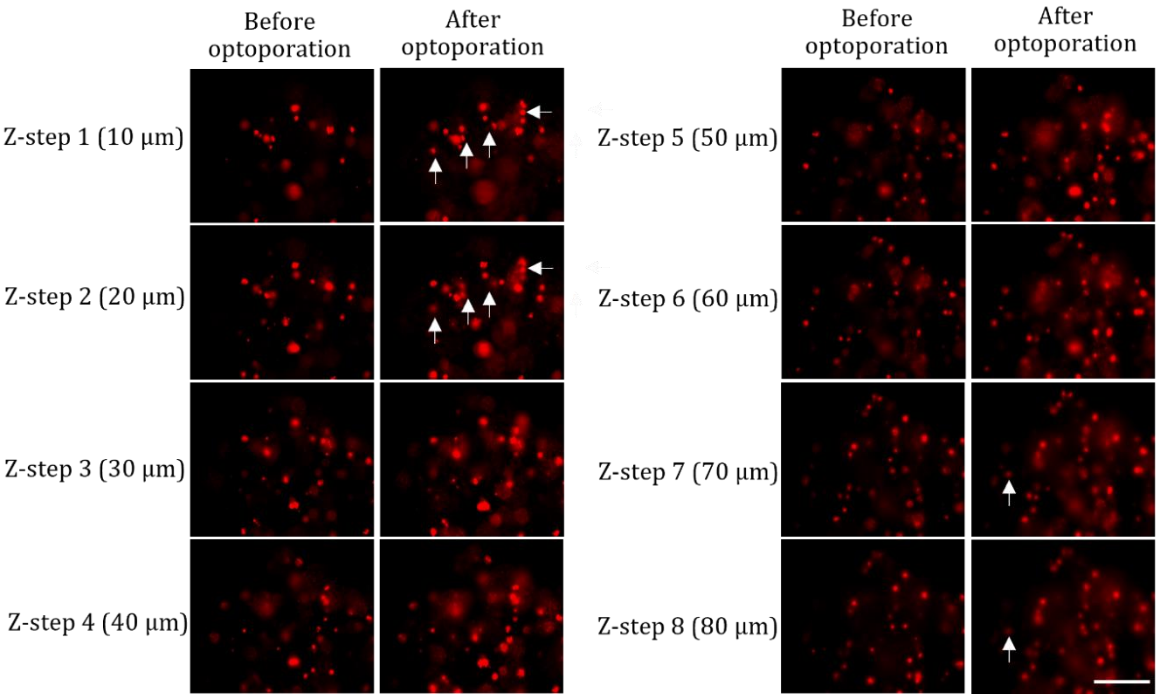

Figure 69: Optoporation on spheroids with EC nanoparticles at its periphery. The spatial selective delivery of propidium iodide at 65 mW with 200 μg/mL as seen only at ~20 μm in depth. The Z-step represents the sequential image acquisition at each 10 μm along the optical axis. Scale bar: 100 μm.

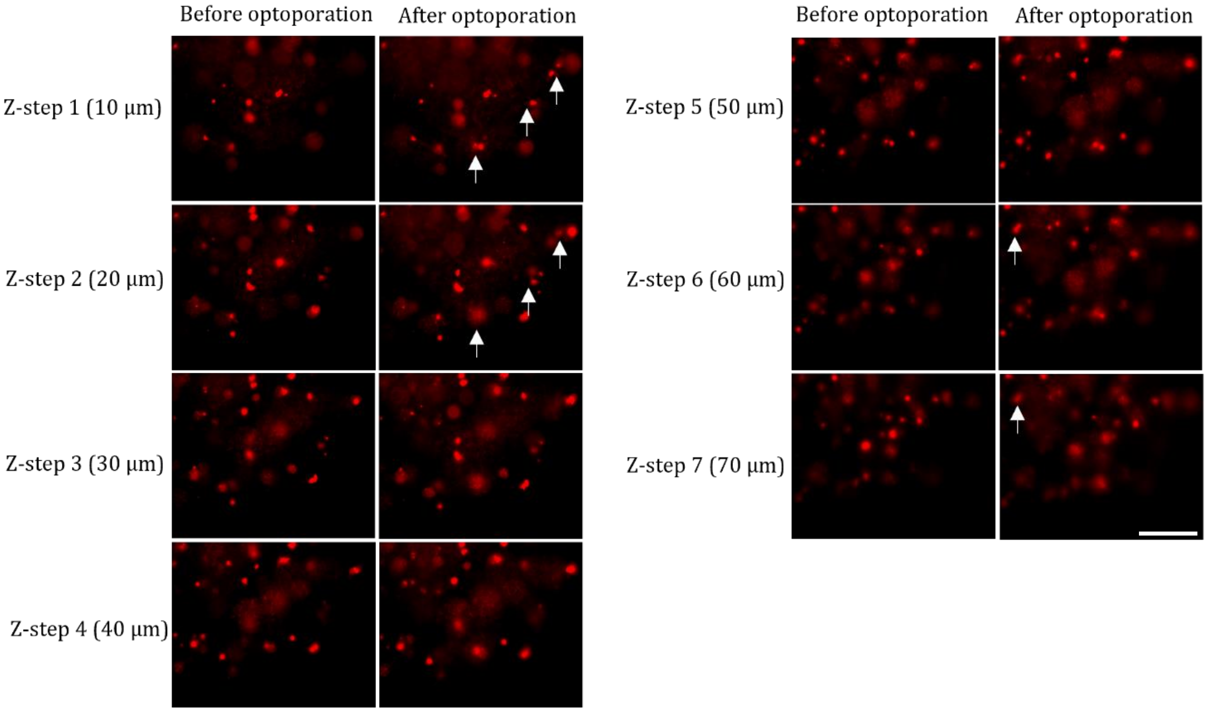

Figure 70: Optoporation on spheroids with EC nanoparticles at its periphery. The spatial selective delivery of propidium iodide at 55 mW with 200 μg/mL as seen only at ~20 μm in depth. The Z-step represents the sequential image acquisition at each 10 μm along the optical axis. Scale bar: 100 μm.

The next step would be to deliver eGFP mRNA in 3D spheroids. However, considering the previous discussions, it was highly probable that cells underwent cell death during optoporation process due to the high laser power needed for inducing membrane permeability in the 3D spheroid. As a result, I did not attempt mRNA delivery into the 3D spheroid model with these EC-nanoparticles.

Despite optimising the laser parameters, nanoparticle concentration and imaging concentration, mRNA delivery efficiency remained low. The current system appeared to reach its limits as higher laser powers to improve cellular delivery induced cell death while increased nanoparticle concentration impacted visibility. Additionally, laser scanning speed was already maximised in this setup. Thus, alternative nanoparticle surface functionalisation approaches that interact better with the laser and induce the transient pore formation could be potential solutions to overcome the delivery efficiency barrier without causing extensive damage to the cell.

5.10 Concluding Remarks

In summary, I have demonstrated that pSi nanoparticles interact with the laser, resulting in the formation of transient pores within the cell membrane. The nanoparticles enabled pore formation at lower laser energies compared to without nanoparticles present. In fact, optoporation in the controls (without nanoparticles) occurred at laser powers of 78 mW and higher due to the excessive energy input. Of the two nanoparticles types, EC nanoparticles achieved slightly better optoporation efficiency than MACE nanoparticles overall, although the difference between the two was not significant.

Numerous parameters underwent fine–tuning to enable successful eGFP mRNA delivery and expression. These adjustments included assessing the impact of laser scanning area and the laser scanning speed. Both had negligible influence on the poration efficiency, therefore I opted for the fastest scanning speed (2000 pixels/s) to minimise thermal energy generated due to prolonged laser exposure. Additionally, the control experiments showed that restricting fluorescent imaging to 24 hours improved GFP expression. Throughout the optimisation process, it became evident that prolonging the incubation time from one hour to four hours allowed more time for the 30 µg/mL nanoparticles to settle onto the cells. This longer incubation resulted in more nanoparticles settling on the cells which correlated with greater poration efficiency as evidenced by the higher propidium iodide uptake in the laser-targeted cells. This higher nanoparticle amount on the cells could still be achieved within one hour of incubation by increasing the initial concentration of nanoparticles with the cells to 100 and 150 µg/mL.

I tested these optimised conditions with various laser powers and identified that increasing the laser power progressively from 26 to 29 mW and from 52 to 65 mW rendered more than 15% increase in poration efficiency. Assessing both the 29 and 65 mW on cellular viability revealed that the 65 mW treated cells did not remain viable post-optoporation which also resulted in the production of ROS and cellular apoptosis markers. In contrast, the 29 mW treated cells exhibited short-term viability and tested negative for ROS generation and cellular apoptosis post-optoporation, affirming the suitability of this laser power. Moving forward, delivery and transfection of eGFP mRNA was successful with both the 100 and 150 µg/mL concentration. The efficiency was 1-3 cells within each field of view regardless of the laser power used within the 20-32 mW range. This transfection efficiency aligned with results typically reported in literature for indirect optoporation utilising nanomaterials demonstrating that the approach taken here performed on par with existing optoporation techniques. Therefore these results suggest the feasibility of optoporation in the presence of porous silicon nanoparticles as an alternate transfection approach. Lastly, I demonstrated optoporation in a 3D context through the spatially selective uptake of propidium iodide. Uniform nanoparticle within the spheroid yielded propidium iodide delivery across the entire spheroid depth, whereas nanoparticles localised at the periphery resulted in propidium iodide delivery within approximately 20 μm depth.

Collectively, this chapter underscored the suitability of pSi nanoparticles for achieving spatially selective delivery of propidium iodide in both the 2D and the 3D models. More importantly, I have also demonstrated the selective delivery of nucleic acid and subsequently the GFP expression post-optoporation in the 2D system. However, low delivery efficiency poses a central limitation necessitating further exploration as even upon optimising laser parameters, nanoparticle concentration and imaging conditions, efficiency remained low. Determining functional groups that elicit greater responses without inducing cytotoxicity could optimise the present nanoparticles efficiency which would enable application for the delivery of nucleic acids in the 3D system. Thus, in the next chapter I investigated chemical moieties for grafting onto the nanoparticles surface that heightened laser interaction without raising the 32 mW or 100 μg/mL limits.

Chapter 6 – Photo-switchable Molecule for Controllable mRNA Release

6.1 Introduction

Light-controlled release of nucleic acids has gained popularity in recent years as a means to manipulate biological processes under precise spatial and temporal control (Spiteri et al., 2020). The objective of this chapter was to investigate the light-controlled nucleic acid release approach in combination with optoporation to enhance the efficiency of nucleic acid delivery. To accomplish this, I synthesised a molecule capable of attracting nucleic acids and releasing them when exposed to NIR.

Light-controlled delivery of nucleic acid encompasses various mechanisms, including photocleavage of light-sensitive groups (Foster et al., 2015; Wang et al., 2017; Yu et al., 2018), photochemical internalisation (Jerjes et al., 2020) and the previously discussed plasmonic-heated systems. The photocleavable strategies involve the use of photocaging where caged molecules are released by covalent bond cleavage upon UV light exposure. This release allows the molecules to perform their intended function, resulting in a high spatiotemporal resolution of their activity (Chen et al., 2018; Nalluri et al., 2011). However, a major limitation of this method is the exclusive responsiveness to UV irradiation, which can potentially cause DNA damage, tissue damage and significantly restrict tissue penetrability (Adeyemi, 2023).

An alternative approach involves isomerisation of photo-switchable molecules that can tune their affinity for nucleic acids when exposed to light. Among these molecules, azobenzene is a widely employed photo-switchable agent in biological research. For instance, researchers harnessed azobenzene trimethylammonium bromide surfactant, a cationic surfactant, to achieve reversible binding and unbinding of nucleic acids (Estévez-Torres et al., 2009). Azobenzene transitioned reversibly between the thermodynamically stable trans configuration and the metastable cis configuration. The trans state exposes the hydrophobic apolar group resulting in a strong affinity for nucleic acids and thus inhibit translation (Estévez-Torres et al., 2009). Upon brief exposure to UV radiation, azobenzene molecules shifted to their cis state which weakened their interactions with the nucleic acid. This enabled the mRNA to unfold thereby activating the translation reaction (Rudiuk et al., 2011).

Despite providing spatiotemporal control over the delivery, the limitation is once again the use of UV irradiation highlighting the need to shift to longer wavelengths in the NIR region that offer deeper tissue penetration with minimal biological system disruption.

Recent approaches have adapted the above photocaging and isomerisation techniques to respond to near-infrared light and overcome the limitations of UV-visible light approaches. One strategy uses upconverting nanoparticles that can convert low-energy near-infrared excitation photons into shorter wavelength ultraviolet-visible emissions (Chen et al., 2014). This energy conversion is possible through the unique ladder-like energy level structure of lanthanide ions (Haase & Schäfer, 2011). Near-infrared photoactivation of caged siRNA conjugated to upconverting nanoparticles enabled the controlled release of the siRNA to direct osteogenic differentiation of human mesenchymal stem cells (Li et al., 2019). Similarly, NIR irradiation cleaved the photocaged linker on the upconversion nanoparticles and led to the intracellular release of siRNA that successfully silenced eGFP gene expression in the targeted cells (Yang et al., 2013). This serves as a potential platform for biomedical research and therapeutic application. However, concerns about their non-biodegradability and biocompatibility may restrict their use in biological settings (Rwei et al., 2015).

Some studies have employed direct two-photon excitation in the near-infrared (NIR) region to achieve spatial precision in delivering nucleic acids with 3D spatial resolution (Cueto Díaz et al., 2015; Yang et al., 2015). These studies used two-photon cleavage of the 4,5-dimethoxy-2-nitrobenzyle group to release the nucleic acids. However, this approach has encountered limitations primarily related to the low two-photon decaging cross-section of this group, which necessitates long irradiation times that risk cellular damage (Yang et al., 2015).

Interestingly, porous silicon nanoparticles offer an alternative avenue for two-photon excitation. These nanoparticles have the unique property of being excited by two near-infrared light photons and transfer the absorbed energy to the anchored absorbing molecules (Létant & Vial, 1997, Park et al., 2009; Secret et al., 2014). Since azobenzene has a limited two-photon absorption in the NIR region (De Boni et al., 2002), the porous silicon nanoparticles act as a two-photon transducer for azobenzene thereby changing its conformation. In fact, this energy transfer process could be demonstrated by the fluorescence quenching of pSi nanoparticles in the presence of azobenzene (Chaix et al., 2023). To further support their claim that azobenzene isomerisation plays a role in adjusting the affinity towards the nucleic acids, they substituted the azobenzene ring with a benzene ring. As expected, the substitution did not result in gene-silencing effects because the benzene ring did not undergo isomerisation. Hence, the nucleic acid was not released upon irradiation (Chaix et al., 2023).

The synthesis of functionalised pSi nanoparticles containing azobenzene (**Figure 71**) described in this chapter was a collaborative effort recently included in a publication in *Advanced Healthcare Materials*. These functionalised nanoparticles have been shown to be effective in delivering the siRNA targeting the inhibitory apoptotic protein (IAP) leading to over 70% cell death among the MCF-7 cells (Chaix et al., 2023). The objective of this chapter was to initially assess the newly functionalised nanoparticles through a cell viability assay. I also investigated the effects of laser interaction with the cells in the presence of nanoparticles by measuring ROS generation and caspase 3/7 activity. After optimising the conditions for cell viability post-optoporation, the investigations progressed to the delivery of eGFP mRNA in a 2D cell culture system and monitoring the resulting GFP expression. Subsequently, I also attempted the delivery of the mRNA in a 3D MCF-7 spheroid model.

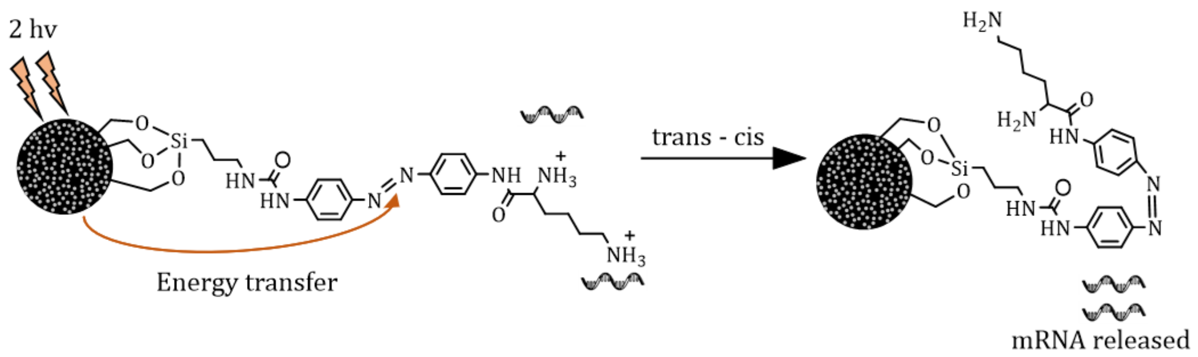

Figure 71: A schematic representation of reversible trans-cis isomerisation of azobenzene. The laser irradiation induces a conformational change of the azobenzene from a trans to a cis conformation, subsequently initiating the nucleic acid release mechanisms.

6.2 Synthesis of ICPES–azobenzene–lys pSi Nanoparticles

In this section, the aim was to enhance the optoporation efficiency by functionalising the porous silicon nanoparticle with a photo-switchable molecule capable of interacting with nucleic acids. For this purpose, the photo-switchable molecule needed to be able to releases nucleic acid when exposed to irradiation, contain an amine group capable of electrostatically attracting nucleic acids and have a silyl ether group suitable for grafting the molecule onto the nanoparticles.

Diaminoazobenzene is a photo-switchable molecule that can undergo a conformation change upon irradiation and could react with lysine via a peptide bond. The importance of incorporating lysine into the photo-switchable molecule structure lies in the introduction of two amine groups on the surface of the pSi nanoparticles, enabling electrostatic interactions with nucleic acids. The addition of Boc groups shielded the amine groups of the lysine molecule as a protective measure to ensure that lysine selectively reacted with the amine groups on diaminoazobenzene. The resulting compound containing the diaminoazobenzene and lysine was then silylated because the silyl ether group allowed for conjugation with the porous silicon nanoparticles. After conjugation, the Boc groups were removed to expose the amine groups enabling the electrostatic interaction of nucleic acids with the nanoparticles. Consequently, as the pSi nanoparticles rested on the cell surface membrane during cell-nanoparticle incubation, they brought the nucleic acids into close proximity to the cell membrane.

The multistep chemical reactions used to obtain ICPES (isocyanatopropyltriethoxysilane)-azobenzene–lys, a molecule containing azobenzene, lysine and the silyl ether group, are summarised in **Figure 72.** The resulting chemical structure was the conjugated group on the surface of the pSi nanoparticles.

6.2.1 Synthesis of ICPES–azobenzene–lys–diBoc

Dr Sofia Domínguez Gil from the research group of Dr Frédérique Cunin at Charles Gerhardt Institute Montpellier provided the product synthesised from the first reaction step which involved an azobenzene (4,4-diaminoazobenzene) reacting with a lysine amino acid. The lysine had the two amine groups protected with a Boc group (Boc–lys–(Boc)–OH) (Chaix et al., 2023; Rahim et al., 2011). The resulting compound, azobenzene–

lys–diBoc (**1**) was characterised via a ^{1}H NMR (**Figure 73**) and obtained the characteristic peaks corresponding to the product. The 18H at 1.4 ppm was characteristic of the two Boc groups, the peaks between 7.7 – 6.6 ppm represented the 8H from the two benzene groups and the remaining peaks corresponded to the four $–CH_2$ groups in the lysine part of the structure.

The subsequent synthesis step was reacting azobenzene–lys–diBoc (**1**) with ICPES to produce ICPES–azobenzene–lys–diBoc (**2**) (Chaix et al., 2023; Rahim et al., 2011). The resulting compound was characterised via a ^{1}H NMR (**Figure 74**) and obtained the characteristic peaks corresponding to the product. The 18H at 1.4 ppm were characteristic of the two Boc groups, the 6H at 3.7 ppm and the 9H at 1.1 ppm represented the triethyl part of the triethoxysilyl structure. The peaks between 7.7 - 6.6 ppm represented the 8H from the two benzene groups and the remaining peaks corresponded to the $-CH_2$ groups in the lysine and the propyl structure.

The successfully synthesised photo-switchable molecule contained all the desired functional groups as confirmed by the NMR spectra and could be grafted onto the porous silicon nanoparticles.

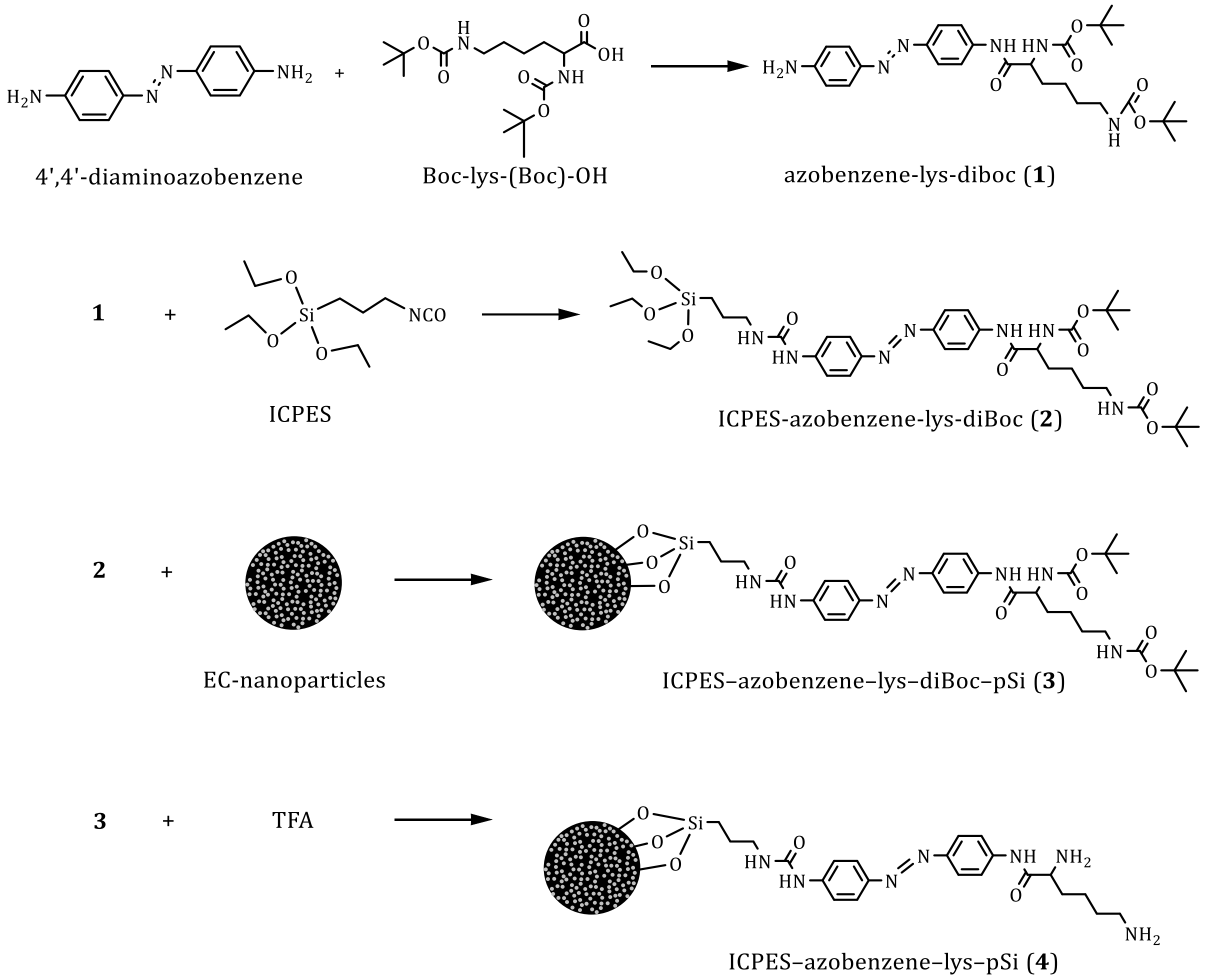

Figure 72: A schematic representation of ICPES–azobenzene–lys pSi nanoparticle synthesis. This figure illustrates a four-step chemical synthesis pathway to create ICPES–azobenzene–lys pSi nanoparticles. The process begins with the synthesis of azobenzene-lys-diboc (**1**), which is then subjected to a reaction with ICPES, resulting in ICPES-azobenzene-lys-diBoc (**2**). Subsequently, (**2**) is reacted with the pSi nanoparticles (**3**), followed by a deprotection step involving the addition of TFA, ultimately yielding the final product ICPES–azobenzene–lys pSi nanoparticles (**4**).

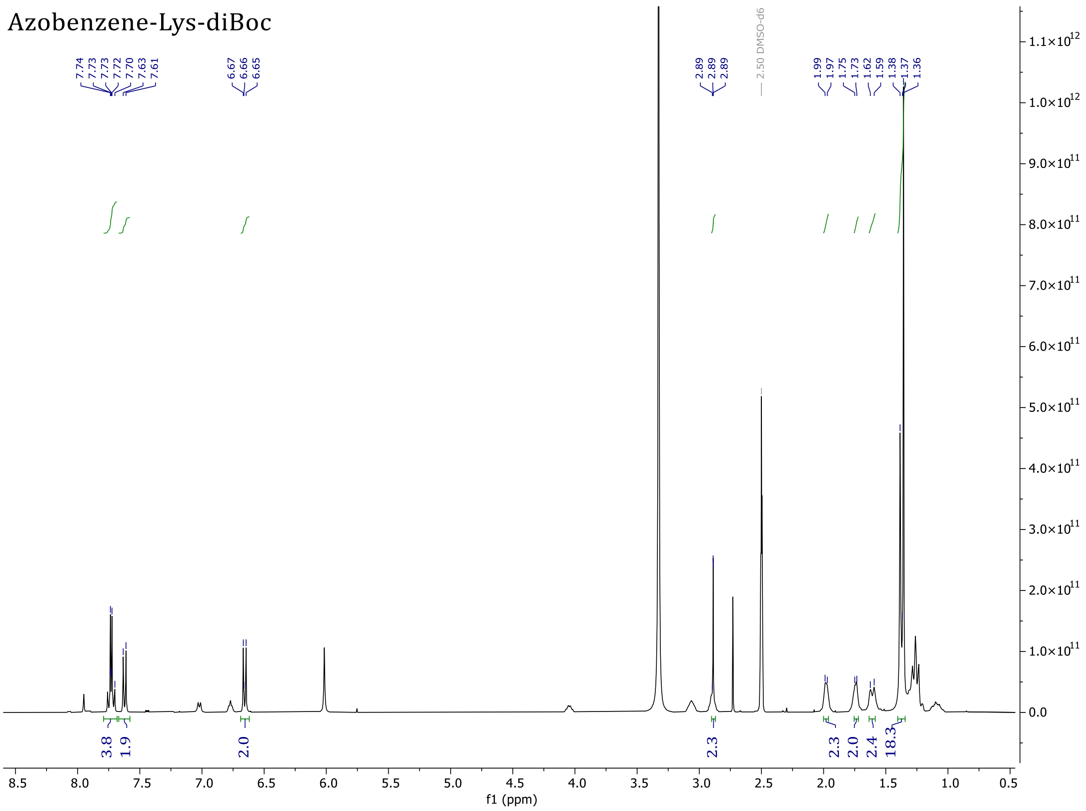

Figure 73: ¹H NMR of azobenzene-lys-diBoc (1).

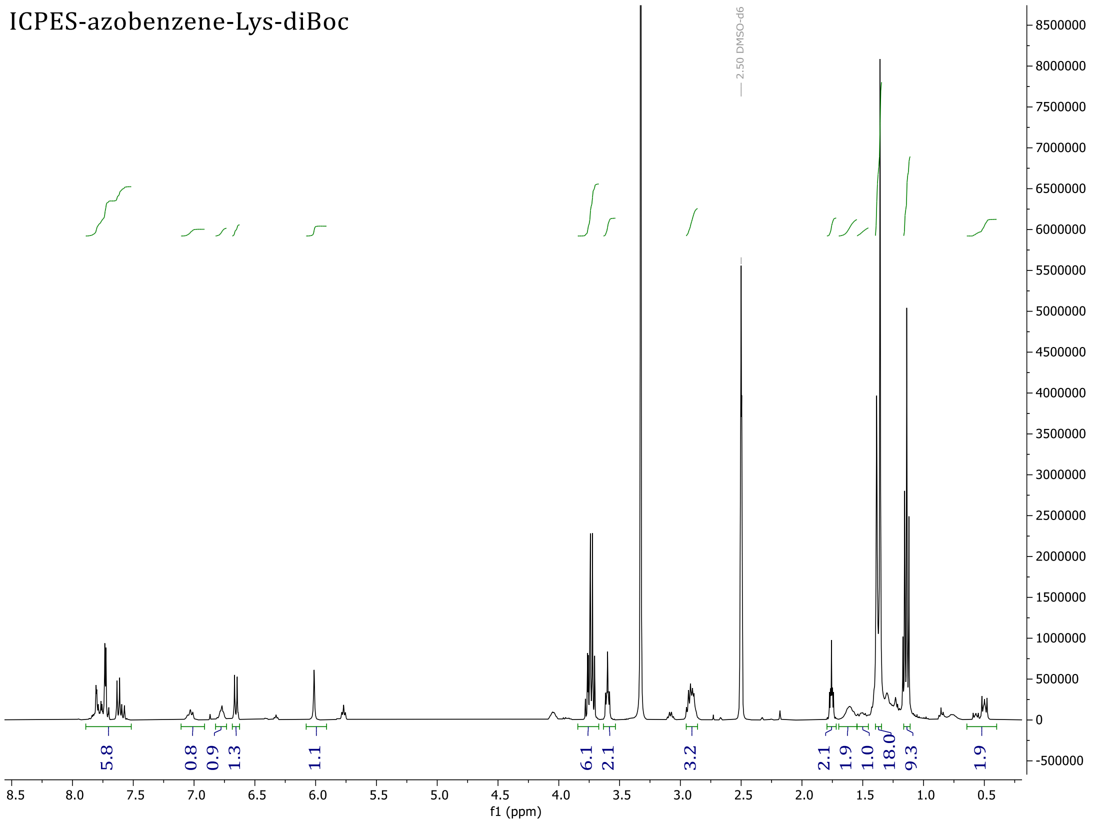

Figure 74: ¹H NMR of ICPES–azobenzene–lys–diBoc (2).

6.2.2 Grafting of ICPES-azobenzene-lys and Characterisation

The aim herein was to graft the photo-switchable molecule to the surface of the nanoparticles and thus generate nanoparticles that could release nucleic acid when exposed to light. Subsequently, the resulting nanoparticles were characterised to confirm the success of the grafting process.

The synthesised photo-switchable molecule (**2**) was grafted to the EC–nanoparticles via a hydrolytic condensation reaction of the silyl ether group forming ICPES–azobenzene–lys–diBoc pSi nanoparticles (**3**). The last step in the chemical reaction pathway involved adding TFA for the removal of the BOC group leading to the formation of ICPES–azobenzene–lys pSi nanoparticles (**4**), referred to as grafted EC-nanoparticles. The non-grafted EC-nanoparticles and the ICPES–azobenzene–lys pSi EC-nanoparticles (**4**) were characterised and compared through Fourier Transform Infrared Spectroscopy (FTIR) (**Figure 75**). The characteristic peaks for the grafting of the linker are summarised in **Table 4**. The broad peak of the EC-nanoparticles at 2115 cm^{-1} represented the Si–H bonds on the surface of the nanoparticles. The reduction in the predominance of these Si-H bonds with grafting was due to their replacement with Si–O bonds from the ICPES–azobenzene–lys photo-switchable molecule. The strong peaks at ~632 and ~1065 cm^{-1} were assigned to the bending and stretching vibration mode of S–H and Si–O respectively, representing the partial oxidation of pSi nanoparticles. The broad Si–O stretching vibration peak likely obscured the C–N stretching vibration, which would typically occur at around 1250 cm^{-1}. The peaks at 1392 cm^{-1} represented the stretching vibrations of N=N from the azide, the peak at 1552 cm^{-1} corresponded to N-H bending and the peak at 1675 cm^{-1} indicated the C=O stretching vibrations. Overall, the presence of these characteristic peaks from the FTIR analysis confirmed the successful grafting of the photo-switchable molecule to the nanoparticles.

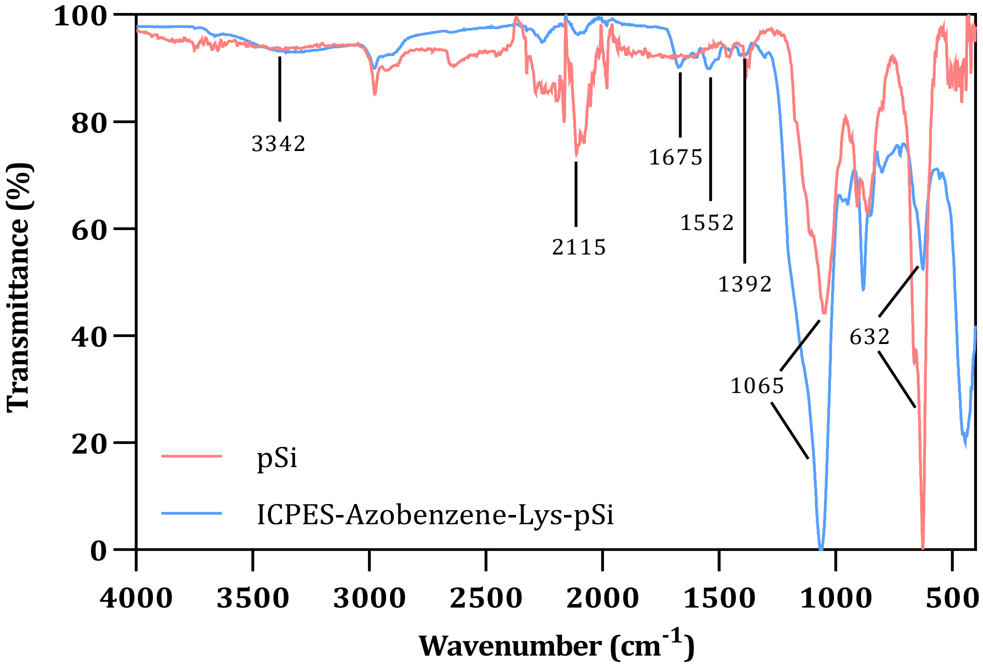

Figure 75: FTIR spectra for pSi and ICPES-azobenzene-lys pSi.

Table 4: Main peaks of interest from the ICPES–azobenzene–lys pSi nanoparticles FTIR. Unless otherwise stated, references values from (Merck, 2023b).

Absorbance cm^{-1}	**Group**
632	S–H bending vibration (Cardona, 1983; Jafari et al., 2019)
1270 – 1000	Si–O stretching vibration
1250	C–N stretching vibration (masked peak)
1392	N=N stretching vibration
1552	N–H bending vibration
1675	C=O stretching vibration
2115	S–H stretching vibration (Cardona, 1983; Jafari et al., 2019)
3342	Secondary amine stretching vibration

The changes in the hydrodynamic diameter and the surface charge of the nanoparticles also confirmed the grafting of the photo-switchable molecule to the EC-nanoparticles. The hydrodynamic diameter of the EC-nanoparticles changed from 282 ± 2.5 to 463.6 nm ± 42.6 when grafted (**3**). The increase in size could be a result of the π-stacking of the azobenzene groups (Chaix et al., 2023). The zeta potential values were negative for both non-grafted EC-nanoparticles and the ICPES–azobenzene–lys–diBoc pSi EC-nanoparticles, with a surface charge of − 20.8 mV ± 0.4 to − 40.23 mV ± 1.2 respectively. This is attributed to the partial oxidation of the nanoparticle surface and the presence of the silyl ether group. After the deprotection step, the hydrodynamic diameter of ICPES–azobenzene–lys pSi nanoparticles (**4**) decreased to 376.0 nm ± 24.5, which was in line with the particle sizes observed through SEM (**Figure 76**). The zeta potential increased to 42.0 mV ± 2.6, an indication that the amine groups (–NH_2) were now exposed forming an ammonium group.

In summary, the synthesis process resulted in the functionalisation of the EC-nanoparticles with the photo-switchable ICPES–azobenzene–lys molecule and could then be tested for its application with the MCF-7 cells.

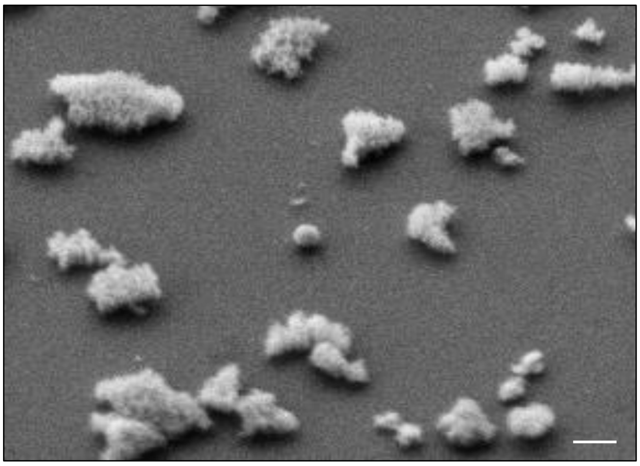

Figure 76: SEM images of ICPES–azobenzene–lys pSi nanoparticles. Scale bar: 100 nm.

6.3 Toxicity of the Nanoparticles

The ICPES–azobenzene–lys pSi nanoparticles were assessed through a cell-viability assay to determine if the same concentration established earlier induced cytotoxic effects. MCF-7 cells not treated with the nanoparticles served as the control and represented 100% viability (**Figure 77**). The cytotoxicity levels remained below 20% for concentrations up to 200 µg/mL and there was no significant difference between the control and the tested concentrations up to 150 µg/mL. In particular, the concentration of 100 µg/mL did not induce a cytotoxic effect hence, the previously established parameters for optoporation could be used here.

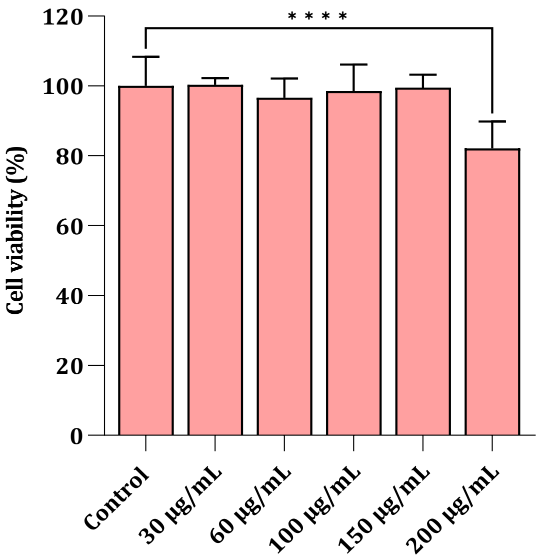

Figure 77: Cell viability assay for ICPES–azobenzene–lys pSi nanoparticles. Determined with the Cell Titer-Glo assay and expressed relative to the untreated control group.

6.4 Reactive Oxygen Species and Apoptosis

Once the nanoparticle concentration was established, the interaction of the grafted nanoparticles with the laser power needed to be tested for its suitability in maintaining cellular viability. The laser powers of 29 and 65 mW were previously tested with the APTES nanoparticles described in Chapter 5. Herein, these laser powers were also investigated to determine whether the same laser power could be used without inducing ROS or apoptosis and thus preserving cellular viability.

The assessment of ROS presence resulting from the optoporation treatment involved the use of DCFH-DA in conjunction with 100 µg/mL ICPES-azobenzene-lys pSi nanoparticles. At laser power of 65 mW ROS were generated within the first 2 minutes post-optoporation (**Figure 78**). However, cells irradiated with 29 mW laser power did not show any ROS production within the 10 minutes post-optoporation. This outcome was consistent with previous results reported by Chaix et al., 2023 highlighting the reliability of the experimental delivery approach. Furthermore, little to no apoptosis was detected one hour post-optoporation (**Figure 78**) suggesting that when subjected to laser irradiation under these conditions, the nanoparticles did not exert any adverse effects on cellular viability. Consequently, these specific experimental conditions of 29 mW and 100 µg/mL of ICPES-azobenzene-lys pSi nanoparticles were considered appropriate for attempting the delivery of eGFP mRNA to the MCF-7 cells.

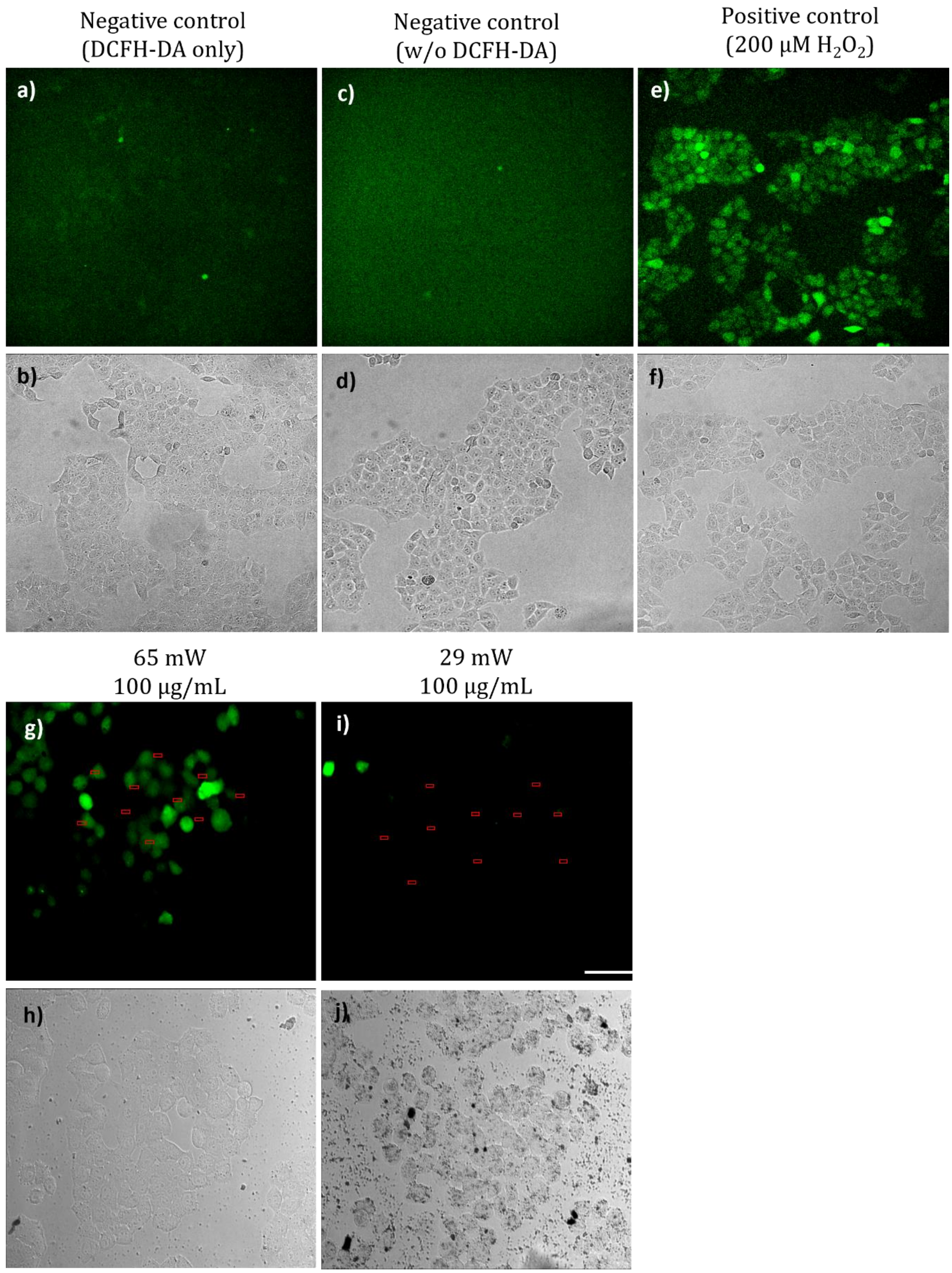

Figure 78: ROS detection using DCFH–DA. Fluorescent and bright field imaging of: a–d) Negative controls with and without DCFH–DA respectively, e, f) Positive control in the presence of 200 µM H_2O_2. Optoporation area at g, h) 65 mW with 100 µg/mL ICPES-azobenzene-lys pSi nanoparticles and i, j) 29 mW with 100 µg/mL ICPES-azobenzene-lys pSi. Scale bar: 100 µm.

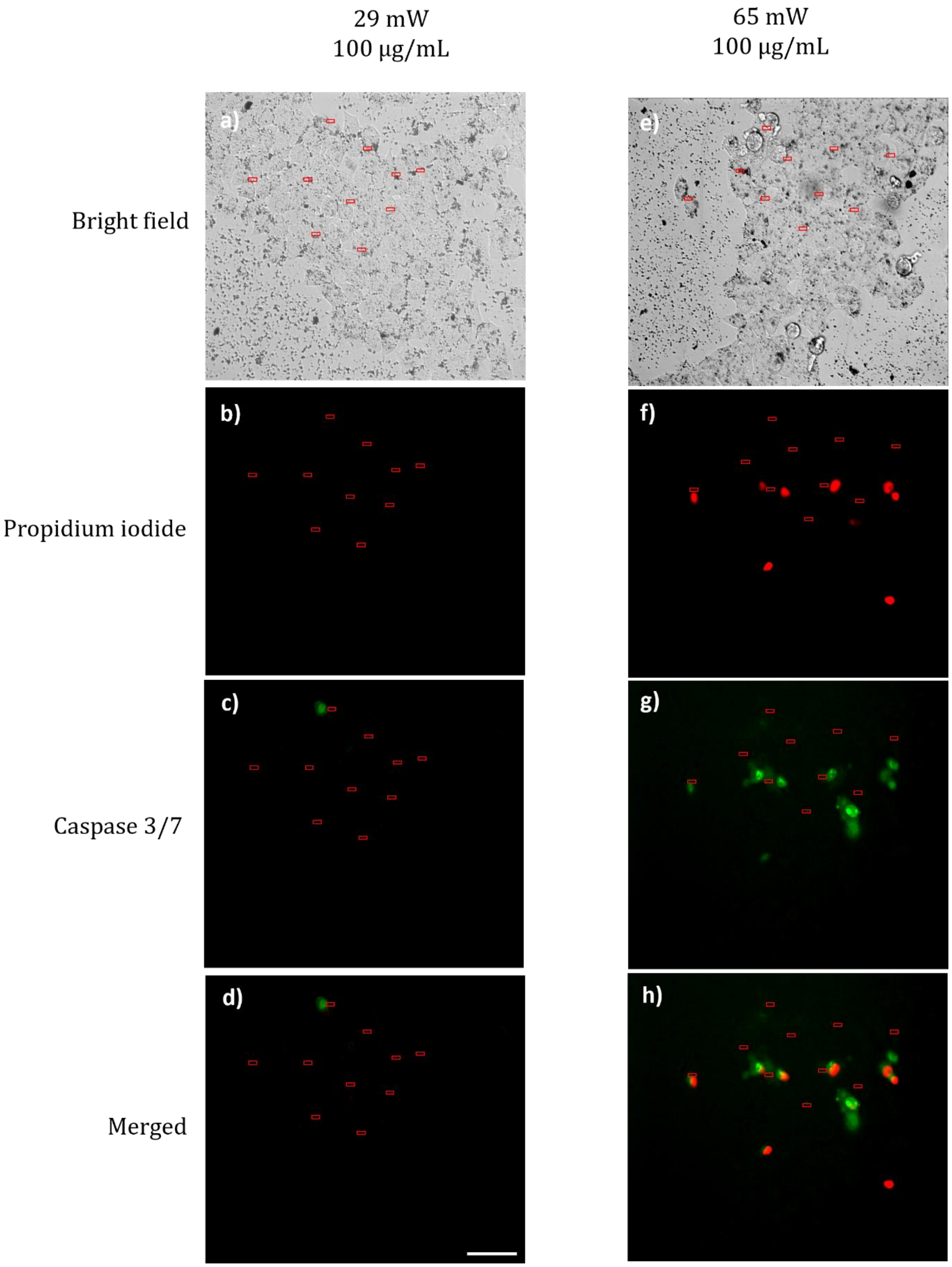

Figure 79: Caspase 3/7 assay. Fluorescent and bright field imaging of: a–d) laser–irradiated areas at 29 mW and e-h) laser-irradiated areas at 65 mW, both with 100 µg/mL ICPES-azobenzene-lys pSi nanoparticles. Scale bar: 100 µm.

6.5 Complexation with mRNA

Delivery of mRNA into porated cells can be facilitated by immobilising the mRNA onto the internal and external surfaces of the nanoparticles. The two positively charged amine groups in the lysine moiety enabled electrostatic attraction with the negatively charged mRNA. This allowed localised concentration of mRNA near a perforated membrane.

The eGFP mRNA was incubated with ICPES-azobenzene-lys pSi nanoparticles in the ratio of 1: 10, 1: 25, and 1: 50. After 1 hour of incubation, an agarose RNA gel determined the effectiveness of forming mRNA complexes with ICPES-azobenzene-lys pSi nanoparticles. In the 1: 10 ratio a prominent band similar to the control (mRNA without nanoparticles) indicated that the mRNA was in large quantities and the excess of mRNA remained non-complexed (**Figure 80**). The 1: 25 ratio produced a faint migration band and the migration band was absent for the 1: 50 ratio. The vanishing of the mRNA band confirmed successful complexation with pSi nanoparticles, consequently hindering the migration of the mRNA through the agarose gel. Given that the 1: 25 resulted in maximal complexation with the least mRNA waste, I selected the 1: 25 complexation ratio.

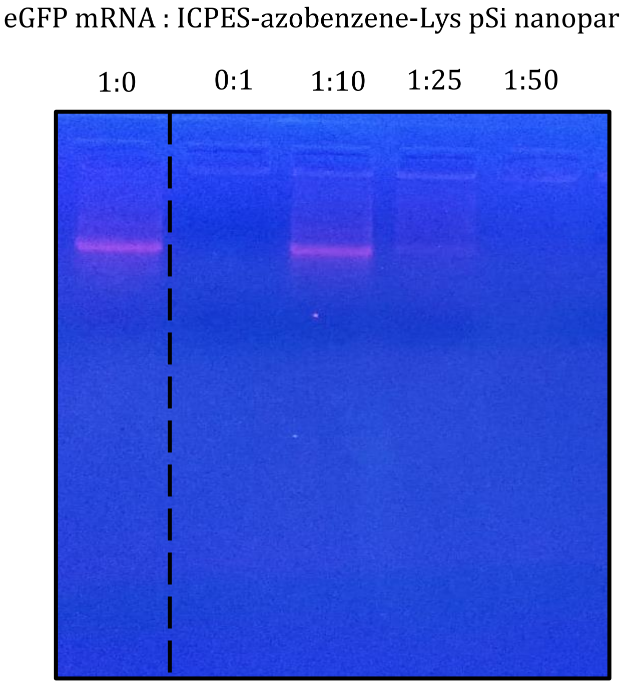

Figure 80: RNA gel for eGFP mRNA complexation with ICPES-azobenzene-lys pSi nanoparticles. The different ratios of eGFP mRNA to ICPES-azobenzene-lys pSi nanoparticles where the presence of fluorescence along the gel marks the excess unbound mRNA.

6.6 Delivery of eGFP mRNA in 2D Cell Culture System

The ICPES-azobenzene-lys pSi nanoparticles complexed with the mRNA were assessed for their ability to trigger laser-induced spatial-temporal nucleic acid delivery. I investigated the effectiveness of these nanoparticles in delivering eGFP mRNA by irradiating in the NIR region-specific areas within the well and monitoring GFP expression the following day.

Cells were treated with 100 μg/mL of nanoparticles and specific areas were subjected to 29 mW laser irradiation. Regions not exposed to the laser did not exhibit any GFP expression. Similarly, free mRNA (negative control) in the absence of nanoparticles did not result in delivery to the cells nor expression of GFP. In contrast, the laser-irradiated areas expressed GFP (**Figure 81**) and demonstrated a much higher proportion of the cells producing the GFP as compared to the outcomes described in Chapter 5 with the EC APTES tagged nanoparticles. This increase in efficiency was attributed to the photo-isomerisation of the azobenzene group induced by NIR irradiation that released the mRNA in solution. The free mRNA was therefore readily available to enter the cytosol of the perforated cell.

The large proportion of targeted cells successfully transfected with GFP in the 2D system was a promising outcome that motivated the exploration of mRNA delivery into the more complex 3D tumour models.

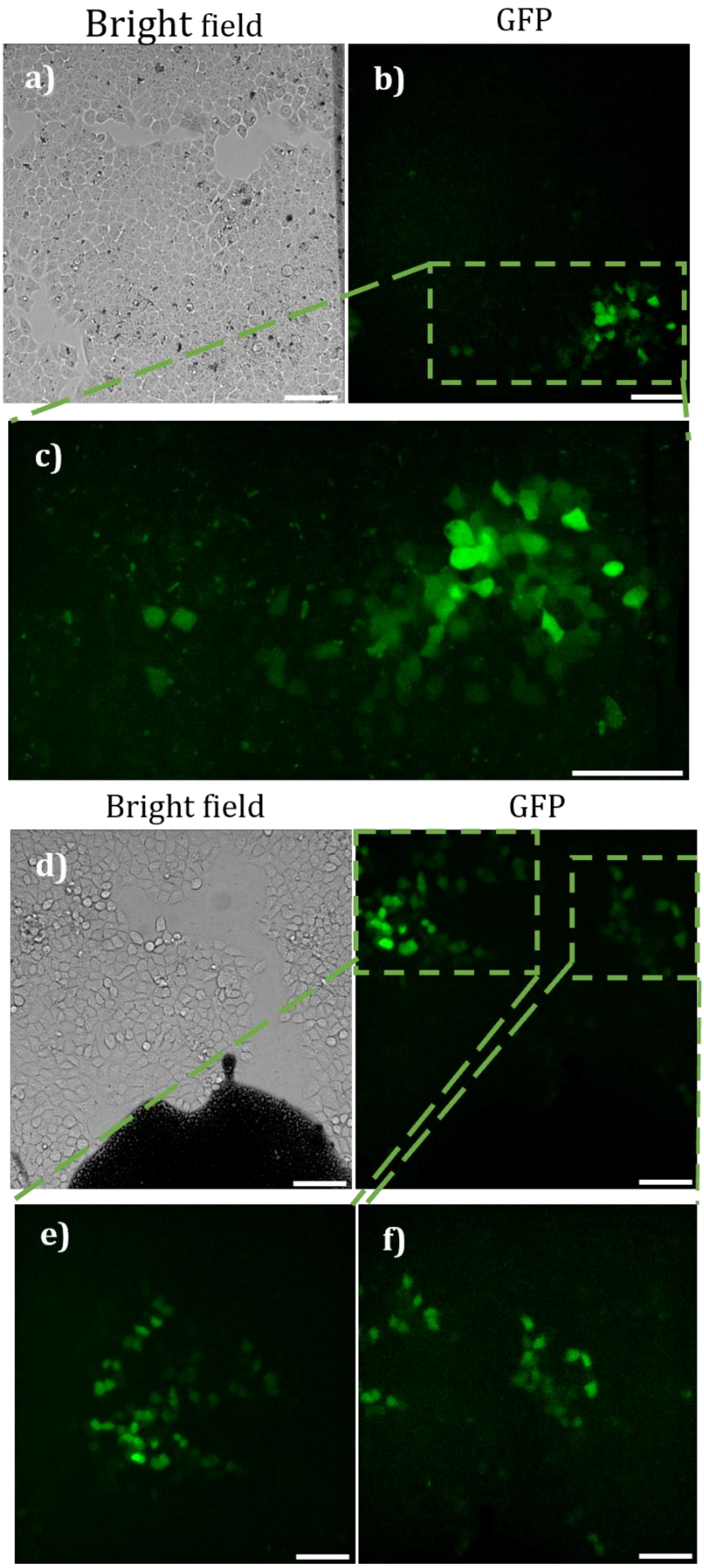

Figure 81: GFP mRNA transfection via optoporation. GFP expression in the 2D cell culture model when optoproating the cells with laser powers ranging between 26–32 mW in the presence of 100 µg/mL of ICPES-azobenzene-lys pSi nanoparticles . Scale bar: 100 µm.

6.7 Delivery of eGFP mRNA in 3D Tumour Models

Achieving spatially selective mRNA delivery within a 3D model was a critical step for the potential use of this optoporation tool in in vitro modelling. Various strategies were explored in attempts to achieve mRNA delivery and subsequent expression. As part of the approach, the mRNA was complexed with the nanoparticles and incubated with the cells for 24 hours during the spheroid formation period. This step was implemented to facilitate the transport of mRNA to the spheroid's core. However, there was concern regarding the stability of the mRNA attached to the nanoparticles throughout the 24-hour incubation. For this reason, an additional 1 μg of mRNA was introduced immediately before the optoporation experiment. Post-optoporation, the cells were allowed to incubate for 24 hours, followed by cryosectioning, staining and imaging of the 10 μm thick cryosections.

The experimental parameters optimised for 2D culture systems were largely applied with the primary difference being the laser power. I hypothesised that successful optoporation in 3D systems might be more challenging due to the greater cell-to-cell interactions. Therefore, in addition to the established 29 mW I also tested the 39 and 52 mW as the higher laser powers. Positive results were only obtained with the 39 mW, as 29 mW appeared insufficient to induce poration, while 52 mW likely led to cell death.

Three control groups were established to ensure that any observed fluorescence in the green channel could be only attributed to the GFP expression. The first control was negative for eGFP mRNA and for the grafted nanoparticles, and absence of irradiation. The second control had the grafted nanoparticles but without the eGFP mRNA and without the irradiation. The third control had both the eGFP mRNA and the grafted nanoparticles but did not undergo irradiation. As expected, none of the control groups exhibited GFP expression because no laser irradiation occurred in all three cases (**Figure 82a-l**). This observation underscores the importance of NIR irradiation for facilitating the delivery and expression of GFP mRNA. In contrast, irradiation of the periphery of the spheroids in the presence of grafted nanoparticles and eGFP mRNA resulted in the GFP expression (**Figure 83a-f**). In a separate experiment, the laser was irradiated to other areas of the spheroid, this time excluding the periphery. In this case, a subset of cells were transfected deeper into the core of the spheroid (**Figure 83g-l**), however, the efficiency of the delivery was lower than that of the periphery.

These positive results mark a significant milestone, representing the first successful demonstration of mRNA delivery and expression within a 3D spheroid model using pSi optoporation. While further work is needed to establish the reliability and robustness of this tool, these initial findings are highly encouraging.

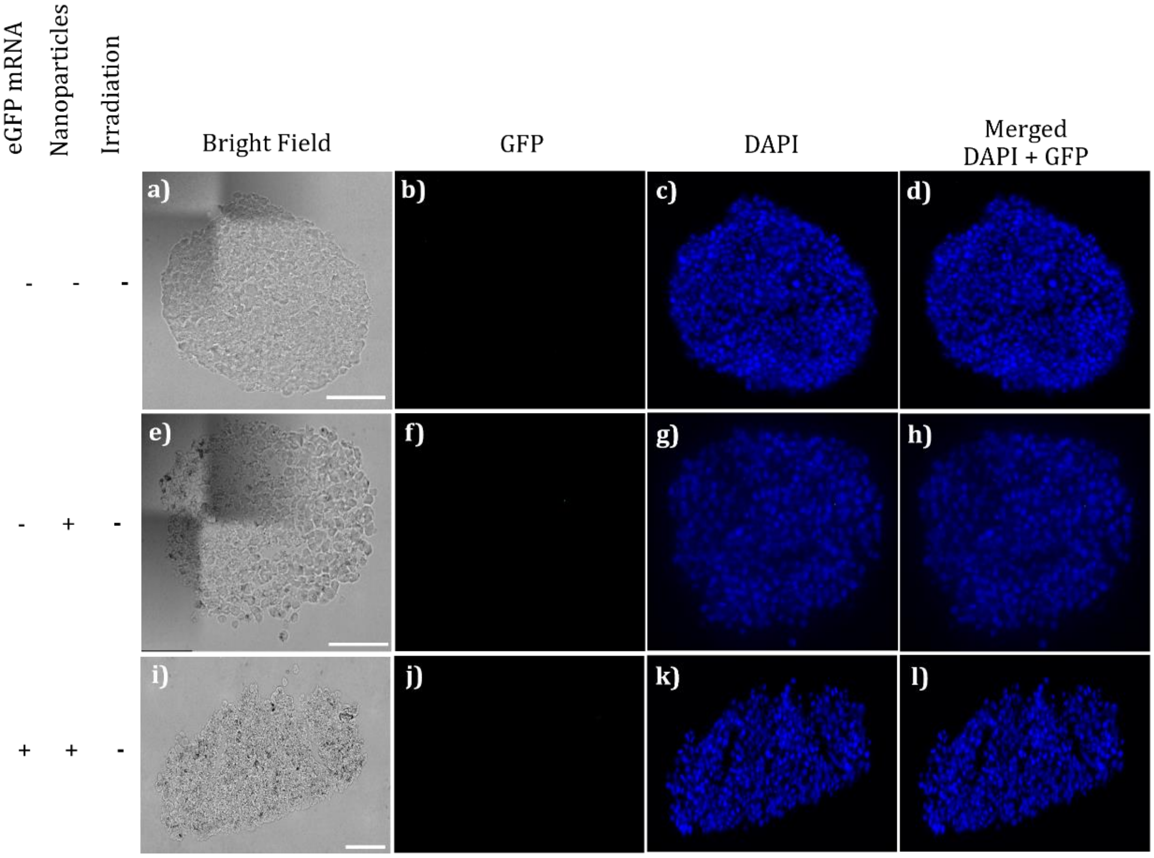

Figure 82: Controls for optoporation-mediated GFP mRNA delivery into MCF-7 spheroids. The first column shows the parameters that were controlled in each experiment: a negative sign (-) indicates the parameter was omitted, while a positive sign (+) indicates it was included. Bright field, GFP, DAPI and Merged DAPI + GFP indicate the imaging channel. a-d) Spheroids without mRNA, nanoparticles or laser (negative controls). e-h) Spheroids with nanoparticles but no mRNA or laser. i-l) Spheroids with mRNA and nanoparticles but no laser. Scale bar: 100 µm.

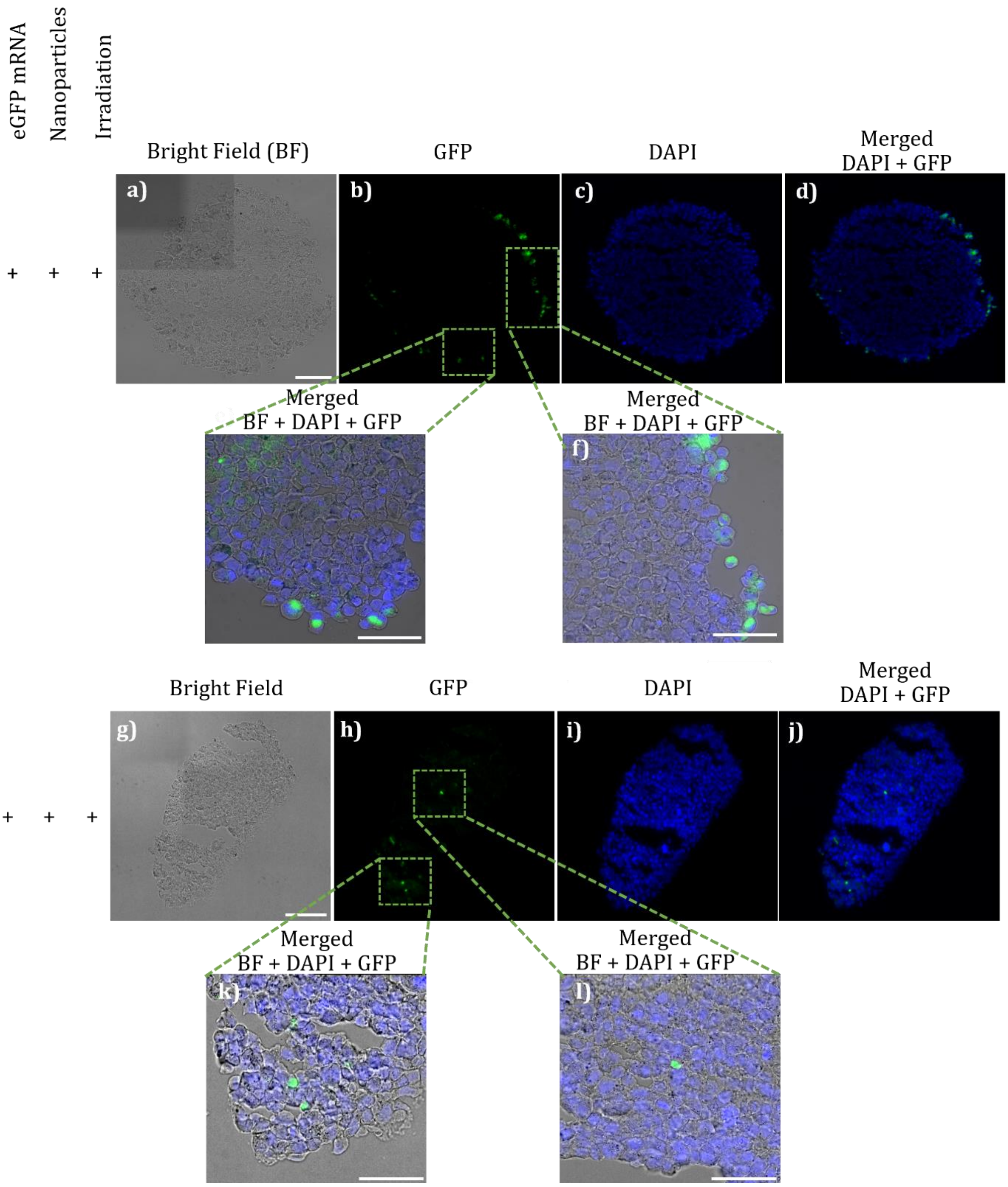

Figure 83: GFP mRNA transfection via optoporation in MCF-7 spheroids. The first column shows the parameters controlled in each experiment, with a + sign indicating they were included. a-d) Spheroids irradiated at the periphery with 39 mW laser power and 100 µg/mL ICPES-azobenzene-lys pSi nanoparticles, resulting in GFP expression. e-f) Zoomed images of GFP-expressing cells. g-j) Spheroids irradiated in areas other than the periphery using the same laser power and nanoparticle concentration. k-l) Zoomed images of GFP-expressing cells. Scale bar: 100 µm.

6.8 Concluding Remarks

The multistep chemical synthesis aimed at functionalising pSi nanoparticles with ICPES-azobenzene-lysine moiety was successful, as confirmed by NMR and FTIR spectra. Additionally, observable alterations in the surface charge of the nanoparticles following grafting further substantiated this success. The positive charge measuring 44.0 mV indicated that the amino groups from the lysine moiety had been exposed, rendering them available for complexing with the negatively charged mRNA. Indeed, the gel electrophoresis revealed that the optimal complexation ratio of mRNA with the nanoparticles was 1: 25. The chemical functionalised pSi nanoparticles displayed no significant cytotoxic effects, even at concentrations as high as 150 µg/mL, well beyond the working concentration of 100 µg/mL needed for optoporation. Furthermore, laser irradiation in conjunction with the nanoparticles demonstrated no generation of ROS and did not induce apoptosis in cells irradiated with 29 mW in the presence of the nanoparticles.

Spatiotemporal mRNA delivery was successfully carried out under the optimised conditions for the GFP expression in the 2D cell model. This demonstrated that the pSi nanoparticles could complex and deliver mRNA to MCF-7 breast cancer cells when irradiated with a two-photon NIR laser. Importantly, mRNA release occurred exclusively upon cell irradiation, as validated by control results. This release mechanism hinges on the photoisomerisation of the functionalised azobenzene, facilitated by resonance energy transfer from pSi nanoparticles to the ICPES-azobenzene-lysine moiety. Consequently, a significant number of cells were successfully transfected with GFP mRNA, more than that observed in the previous result chapter. This outcome holds considerable promise for nucleic acid delivery in 3D tumour models, due to the GFP expression both at the periphery and within greater depths of the spheroid.

In summary, the development of a light-triggered system capable of transfecting cells in both 2D and 3D models with precise spatiotemporal control has been achieved. This nano-sensitised optoporation method sets the stage for patterned mRNA delivery within 3D cell systems, offering substantial potential for advancements in biomedical research and cell-based engineering applications.

Chapter 7 - Conclusion

Techniques that enable the intracellular delivery of nucleic acids are key to modifying gene function and expression within cells. While some of these techniques facilitate bulk delivery such as viral vectors, carrier mediated techniques, nanoneedles, bulk electroporation and sonoporation, others like microinjection, nanostraw and nanochannel based electroporation techniques and optoporation show promise for in vitro single-cell delivery. Optoporation is particularly promising for delivering biochemical cargo to specific cells, providing well-defined spatiotemporal control for nucleic acid delivery at the single cell level. However, optoporation throughput has previously remained low, and although nanomaterials such as gold, carbon-based, black phosphorus and titanium nanoparticles have improved delivery efficiency, most of these nanomaterials are cytotoxic and non-biodegradable.

The research presented within this thesis utilises mesoporous silicon nanoparticles as sensitisers during optoporation for single-cell targeted delivery. Specifically, upon femtosecond 800 nm laser excitation, the nontoxic biodegradable nanoparticles generate transient pores in cell membranes. Developing this delivery system required several key steps. Firstly was the fabrication of porous silicon nanoparticles with varying aspect ratios and determination of a suitable nanoparticle concentration range that can be incubated with the cells without inducing cytotoxicity. The following steps involved optimising the optoporation conditions for intracellular delivery of propidium iodide and eGFP mRNA in 2D MCF-7 cells by tuning parameters like laser power, nanoparticle concentration and laser scanning speed. This was followed by propidium iodide delivery in 3D cancer spheroids. Finally, to improve the transfection efficiency of eGFP mRNA in 2D and 3D cell cultures, I investigated optoporation with ICPES–azobenzene–lysine functionalised EC nanoparticles.

In Chapter 4, I reported on the fabrication of mesoporous silicon nanoparticles and their interaction with MCF-7 cells. Discoidal and rod-shaped nanoparticles, with varying aspect ratios and pore size structures, were fabricated using electrochemical etching and metal-assisted chemical etching techniques respectively. Identifying a suitable solvent system that prevents aggregation and sedimentation of the nanoparticles was one of the key challenges faced, as nanoparticles with differing aspect ratios showed distinct dispersant stabilities. Specifically, I demonstrated how improved stability was obtained by dispersing rod-shaped nanoparticles in ethanol, and discoidal nanoparticles in IPA. Using SEM, the mean nanoparticle size was estimated to be 323 nm for EC and 404 nm in length and 171 nm in width for MACE nanoparticles. SEM imaging was used to measure the aspect ratios of the nanoparticles, with EC nanoparticles showing a median aspect ratio of 1.26 within a range of 1 – 1.5, whilst MACE nanoparticles showed a median aspect ratio of 2.2 within a range of 1 – 2.5. EC-nanoparticles were shown to have larger pore sizes (12 nm) than MACE nanoparticles (7.9 nm) using nitrogen sorption isotherms. SEM and EDX imaging was used to show that after 1 hour of incubation with either EC or MACE nanoparticles, both nanoparticle types distributed on the surface of the MCF-7 cells. Also both EC and MACE nanoparticles were deemed non-toxic to the MCF-7 cells up to the tested concentration of 200 µg/mL. Finally, the interaction of EC nanoparticles with MCF-7 spheroids was investigated and identified that concentration beyond 30 µg/mL compromised spheroid morphological integrity, and cell viability dropped below 80%. In an attempt to increase nanoparticle levels within spheroids, I added nanoparticles after spheroid formation. However, this restricted nanoparticle penetration caused an accumulation of the nanoparticles at the periphery of the spheroid.

In the second phase of work (Chapter 5), I investigated the spatially-selective delivery of propidium iodide and nucleic acids using mesoporous silicon nanoparticles as sensitisers in optoporation. I initially investigated how the delivery efficiency of propidium iodide is impacted by the nanoparticle structure. The MCF-7 cells were optoporated using laser powers in the range of 39–91 mW. Although the EC nanoparticles outperformed the delivery of the MACE nanoparticles, this was not found to be statistically significant at the 95% confidence interval. Consequently, EC nanoparticles were identified as the particle of choice for subsequent work due to their simpler synthesis route.

In order to optimise the optoporation parameters, a systematic investigation was conducted to identify the optimal laser power, scanning speed, scanning area, nanoparticle concentration and nanoparticle incubation time. The investigation identified 29 mW laser power, 100 µg/mL nanoparticle concentration, 2000 px/s scanning speed, and 1 hour incubation time as the optimal conditions. To assess the short-term viability of MCF-7 cells after optoporation, I imaged the cells 30 minutes after treatment to see if they retained the calcein dye. The presence of green fluorescence in the cells indicated that they were still viable, as the calcein was retained inside the cells. This shows that the increased permeability caused by optoporation was transient and short-lived, as the pores resealed within 30 minutes without compromising overall cell viability. Moreover, no reactive oxygen species were detected with DCFH-DA, and caspase 3/7 assays for apoptosis gave negative results, further suggesting good cell viability after optoporation. The EC nanoparticles and the established optimised conditions were used to spatially transfect mRNA into the laser targeted 2D cell culture by optoporation

The next challenge was optimising delivery of nanoparticles and cargo to 3D cell spheroids while maintaining spheroid integrity. To address spatial selectivity, I delivered nanoparticles to spheroids in two distinct methods. First, I added nanoparticles to free floating cells at a concentration of 30 μg/mL, resulting in uniform nanoparticle distribution within the spheroids. Alternatively, I added nanoparticles at 200 μg/mL concentration to the formed spheroids, where the nanoparticles remained adhered to periphery of the spheroids. I accomplished propidium iodide delivery to cells within the 3D spheroid model using 55-65 mW laser power and 2000 pixels/s line speed. Spheroids with uniformly distributed nanoparticles showed greater depth of delivery compared to those with peripheral nanoparticles only. However, I had previously shown that optoporation above 35 mW resulted in low cell viability, despite being effective for cargo delivery. Thus, I ultimately concluded that the original parameters of 55-65 mW laser power and 30 μg/mL nanoparticles, while enabling propidium iodide delivery to spheroid cores, were not suitable for viable mRNA delivery. Having established an initial optoporation platform in Chapter 5, Chapter 6 of this thesis focused on enhancing the transfection efficiency of the nanoparticle-mediated optoporation method. The key innovation was synthesising a photo-switchable ICPES-Azobenzene–Lysine moiety and grafting it to the nanoparticles. This allowed binding of the mRNA directly to the ligand on the nanoparticle surface, thus concentrating mRNA at the cell membrane. Upon NIR laser irradiation, the azobenzene ligand underwent isomerisation to release the mRNA for cellular uptake. Prior to mRNA delivery, it was shown that the addition of the photoswitchable ligand did not impact cell viability or ROS/caspase levels under the previously optimised conditions. The improved mRNA delivery efficiency with the photoswitchable nanoparticles reached ~80% in 2D cell cultures. More significantly, this mRNA delivery platform enabled the first demonstration of spatially selective mRNA delivery and expression in 3D spheroid models using mesoporous silicon-mediated optoporation.

Overall, this work has achieved the key aim of developing a novel optoporation platform with spatiotemporal control for targeted biomolecule delivery. Specifically, I made use of biodegradable porous silicon nanoparticles that couple with multiphoton near-infrared irradiation to create transient pores within cell membranes. This allows cargo delivery with precise spatial and temporal control into individual cells in 2D and 3D cultures, which is essential for dissecting complex gene regulatory pathways that control cellular functions.

Chapter 8 - Future Work

While the work within this thesis has demonstrated feasible optoporation and gene delivery in cells, there remain several open questions and avenues for future development. Future work will focus on gaining a mechanistic understanding of the optoporation process, characterising its effects on cells, and translating the approach to complex 3D cultures. Furthermore, assessing functional impacts will provide insights into potential limitations and guide strategies to maximise optoporation efficacy. Overall, this continued research will establish nanoparticle-mediated optoporation as a versatile platform for precision intracellular delivery in diverse cell types and culture models.

This study optimised several parameters, principally laser power and nanoparticle concentration, using silicon nanoparticles of fixed pore sizes. Further work could investigate how pore size influences nanoparticle-laser interactions and thus overall cell delivery efficiency. This would test the hypothesis that altering the pore size has an impact on the light absorption and cell delivery efficiency. The pore size distribution of mesoporous silicon nanoparticles can be tuned by changing the HF: ethanol ratio during electrochemical etching, with higher ethanol proportions increasing average pore diameter (Burham et al., 2014). By synthesising nanoparticles over a range of HF: ethanol ratios, the relationship between pore size, light absorption, and eventual cell delivery could be determined.

This work has demonstrated efficient optoporation and gene delivery but the mechanism behind membrane pore formation in cells during optoporation remains unclear, whether it is arising from photothermal or photochemical effects. Determining whether this occurs through photothermal or photochemical effects would allow more informed optimisation of optoporation conditions to maximise delivery efficiency while retaining cell viability. The lack of detectable ROS generation at 29 mW suggests a photothermal mechanism rather than oxidative damage. However, definitively testing this hypothesis requires measuring singlet oxygen ($^1O_2$) with a selective sensor like Singlet Oxygen Sensor Green (Xiao et al., 2011). Meanwhile, temperature increases during optoporation can be monitored in situ with a nanodiamond thermometer (Romshin et al., 2021, 2023). Understanding the roles of heat and reactive species in optoporation will clarify whether parameter optimisation should focus on thermal management or mitigating photochemical damage.

This optoporation approach relies on the temporary formation and resealing of pores in the cell membrane, which must occur before cell death. Studying the dynamics of these pores, including sealing time and size, would enable better control over delivery amount and cargo size while minimising disruption. I hypothesise pores reseal within 30 minutes based on retained calcein fluorescence after optoporation. To test this, future work could add propidium iodide at intervals following optoporation. The time point at which propidium iodide is no longer delivered intracellularly suggests the time taken for the optoporation to reseal (Messina et al., 2015). The membrane repair kinetics could also be monitored with FM1-43, a fluorescent dye that inserts into lipid membranes. Its fluorescence intensity would increase upon compromising membrane integrity and plateau upon resealing (Bouter et al., 2011).

In addition to studying pore resealing dynamics, characterising the size of the optoporation pores would reveal the maximum cargo size for delivery into cells. To test this, dextrans of increasing molecular weight could be added during optoporation to determine the size exclusion limit (Kalies et al., 2014). When a dextran is too large to enter the cell, the maximum pore diameter can be approximated. Combined with the sealing dynamics, the pore size characterisation would determine the critical parameters governing efficient cytoplasmic delivery while retaining viability.

Additionally, future work can aim to drive controlled changes in cell function within organotypic systems through optoporation. Cell functionality can then be evaluated by monitoring downstream protein expression post-transfection. For instance, cells can be transfected with a single construct containing SNAIL and GFP mRNA where GFP serves as a reporter to label cells receiving the effector SNAIL gene. SNAIL expression promotes epithelial-mesenchymal transition (EMT), inducing cell migration and repressing E-cadherin transcription (Barrallo-Gimeno & Nieto, 2005). Therefore, live-cell imaging of optoporated cells can reveal if both migration and GFP expression occur, indicating successful SNAIL delivery. Alternatively, we can directly assay EMT by checking for downregulation of epithelial E-cadherin and upregulation of mesenchymal markers like vimentin and fibronectin (Smith et al., 2014) after optoporation.

Further optimisation of the 3D optoporation system is required. While I have demonstrated feasibility of mRNA transfection in 3D cultures, efficient delivery to the core regions needs improvement. I was unable to investigate optoporation of collagenase-treated cells, which may enhance transfection efficiency after undergoing the enzymatic treatment. Next steps will include optimising optoporation parameters in collagenase-treated 3D cultures to improve core transfection efficiency. This will establish optoporation as a versatile platform for 3D tissue engineering and developmental models.

Testing optoporation on stem cells could both demonstrate efficacy in hard-to-transfect cell types and showcase potential for modelling early developmental differentiation processes through precise spatiotemporal control of signaling. Despite advances, current in vitro models struggle to replicate the asymmetric developmental signaling to replicate the in vivo embryogenesis environment. Optoporation may provide the opportunity to deploy spatiotemporal cues directing cell fate and mimicking cues that guide symmetry breaking events and germ layer formation. Improved control over signalling and differentiation in embryonic stem cells could provide new findings on the specific pathways driving early embryogenesis. This would facilitate platforms to uncover details of human development while enabling new studies into regeneration, birth defects, and developmental diseases. Therefore, refining optoporation for use in stem cells and organoid structures holds tremendous opportunity to probe spatiotemporal signals governing cell fate and morphogenesis in embryological contexts difficult to recreate using other means.

In summary, future work will build upon the feasibility demonstrated within this thesis to gain a comprehensive understanding of nanoparticle-mediated optoporation, from pore formation dynamics to downstream cellular impacts. Methodical characterisation paired with optimisation of delivery parameters and functional assays will aim to demonstrate optoporation as a tuneable, universal technology for targeted gene editing and reprogramming within single cells. Hence, facilitating transformative applications in synthetic biology and regenerative medicine.

Chapter 9 – References

Abreu-Blanco, M. T., Verboon, J. M., & Parkhurst, S. M. (2014). Coordination of Rho family GTPase activities to orchestrate cytoskeleton responses during cell wound repair. Current Biology, 24(2), 144–155. https://doi.org/10.1016/j.cub.2013.11.048

Adamo, A., Roushdy, O., Dokov, R., Sharei, A., & Jensen, K. F. (2013). Microfluidic jet injection for delivering macromolecules into cells. Journal of Micromechanics and Microengineering, 23(3), 035026. https://doi.org/10.1088/0960-1317/23/3/035026

Adeyemi, R. O. (2023). Transcription and DNA repair collide after UV exposure. Proceedings of the National Academy of Sciences of the United States of America, 120(16), e2303201120. https://doi.org/10.1073/pnas.2303201120

Ahuja, G., & Pathak, K. (2009). Porous carriers for controlled and modulated drug delivery. Indian Journal of Pharmaceutical Sciences, 71, 599–607. https://doi.org/10.4103/0250-474X.59540

Ali, F., Reinert, L., Lévêque, J., Duclaux, L., Muller, F., Saeed, S., & Sakhawat Shah, S. (2014). Effect of sonication conditions: solvent, time, temperature and reactor type on the preparation of micron sized vermiculite particles. Ultrasonics Sonochemistry, 21(3), 1002–1009. https://doi.org/10.1016/j.ultsonch.2013.10.010

Alves, S. R., Calori, I. R., Bi, H., & Tedesco, A. C. (2023). Characterization of glioblastoma spheroid models for drug screening and phototherapy assays. OpenNano, 9, 100116. https://doi.org/10.1016/j.onano.2022.100116

Anglin, E. J., Cheng, L., Freeman, W. R., & Sailor, M. J. (2008). Porous silicon in drug delivery devices and materials. Advanced Drug Delivery Reviews, 60(11), 1266–1277. https://doi.org/10.1016/j.addr.2008.03.017

Antkowiak, M., Torres-Mapa, M. L., Gunn-Moore, F., & Dholakia, K. (2010). Application of dynamic diffractive optics for enhanced femtosecond laser based cell transfection. Journal of Biophotonics, 3(10–11), 696–705. https://doi.org/10.1002/jbio.201000052

Antkowiak, M., Torres-Mapa, M. L., Stevenson, D. J., Dholakia, K., & Gunn-Moore, F. J. (2013). Femtosecond optical transfection of individual mammalian cells. Nature Protocols, 8(6), 1216–1233. https://doi.org/10.1038/nprot.2013.071

Azizipour, N., Avazpour, R., Sawan, M., Rosenzweig, D. H., & Ajji, A. (2022). Uniformity of spheroids-on-a-chip by surface treatment of PDMS microfluidic platforms. Sensors and Diagnostics, 1(4), 750–764. https://doi.org/10.1039/d2sd00004k

Babiychuk, E. B., Monastyrskaya, K., Potez, S., & Draeger, A. (2009). Intracellular Ca2+ operates a switch between repair and lysis of streptolysin O-perforated cells. Cell Death and Differentiation, 16(8), 1126–1134. https://doi.org/10.1038/cdd.2009.30

Bai, F., Li, M., Song, D., Yu, H., Jiang, B., & Li, Y. (2013). Metal-assisted homogeneous etching of single crystal silicon: A novel approach to obtain an ultra-thin silicon wafer. Applied Surface Science, 273, 107–110. https://doi.org/10.1016/j.apsusc.2013.01.196

Barisch, C., Holthuis, J. C. M., & Cosentino, K. (2023). Membrane damage and repair: A thin line between life and death. Biological Chemistry, 404(5), 467–490. https://doi.org/10.1515/hsz-2022-0321

Barrallo-Gimeno, A., & Nieto, M. A. (2005). The Snail genes as inducers of cell movement and survival: Implications in development and cancer. Development, 132, 3151–3161. https://doi.org/10.1242/dev.01907

Barrett, D. M., Grupp, S. A., & June, C. H. (2016). Chimeric antigen receptor (CAR) and T cell receptor (TCR) Modified T cells Enter Main Street and Wall Street. Journal of Immunology, 195(3), 755–761. https://doi.org/10.4049/jimmunol.1500751.Chimeric

Barrett, L. E., Sul, J. Y., Takano, H., Van Bockstaele, E. J., Haydon, P. J., & Eberwine, J. H. (2006). Region-directed phototransfection reveals the functional significance of a dendritically synthesized transcription factor. Nature Methods, 3(6), 455–460. https://doi.org/10.1038/nmeth885

Baumgart, J., Bintig, W., Ngezahayo, A., Willenbrock, S., Murua Escobar, H., Ertmer, W., Lubatschowski, H., Heisterkamp, A., Wold, W., Doronin, K., Toth, K., Kuppuswamy, M., Lichtenstein, D., Tollefson, A., Kohli, V., Acker, J., & Elezzabi, A. (2008). Quantified femtosecond laser based opto-perforation of living GFSHR-17 and MTH53a cells. Optics Express, 16(5), 3021–3033.

Baumgart, J., Humbert, L., Boulais, É., Lachaine, R., Lebrun, J. J., & Meunier, M. (2012). Off-resonance plasmonic enhanced femtosecond laser optoporation and transfection of cancer cells. Biomaterials, 33(7), 2345–2350. https://doi.org/10.1016/j.biomaterials.2011.11.062

Baumgart, J., Kuetemeyer, K., Bintig, W., Ngezahayo, A., Ertmer, W., Lubatschowski, H., & Heisterkamp, A. (2009). Repetition rate dependency of reactive oxygen species formation during femtosecond laser–based cell surgery. Journal of Biomedical Optics, 14(5), 054040. https://doi.org/10.1117/1.3253382

Baumgärtel, T., & von Borczyskowski, C. (2013). Selective surface modification of lithographic silicon oxide nanostructures by organofunctional silanes. Beilstein Journal of Nanotechnology, 4(1), 218–226. https://doi.org/10.3762/bjnano.4.22

Behr, J.-P. (1997). The Proton Sponge: a trick to enter cells the viruses did not exploit. Chimia, 51, 34–36.

Belton, D. J., Deschaume, O., & Perry, C. C. (2012). An overview of the fundamentals of the chemistry of silica with relevance to biosilicification and technological advances. FEBS Journal, 279(10), 1710–1720. https://doi.org/10.1111/j.1742-4658.2012.08531.x

Berdecka, D., Harizaj, A., Goemaere, I., Punj, D., Goetgeluk, G., De Munter, S., De Keersmaecker, H., Boterberg, V., Dubruel, P., Vandekerckhove, B., De Smedt, S. C., De Vos, W. H., & Braeckmans, K. (2023). Delivery of macromolecules in unstimulated T cells by photoporation with polydopamine nanoparticles. Journal of Controlled Release, 354, 680–693. https://doi.org/10.1016/j.jconrel.2023.01.047

Bergeron, E., Boutopoulos, C., Martel, R., Torres, A., Rodriguez, C., Niskanen, J., Lebrun, J. J., Winnik, F. M., Sapieha, P., & Meunier, M. (2015). Cell-specific optoporation with near-infrared ultrafast laser and functionalized gold nanoparticles. Nanoscale, 7(42), 17836–17847. https://doi.org/10.1039/c5nr05650k

Bhattacharjee, N., Horowitz, L. F., & Folch, A. (2016). Continuous-flow multi-pulse electroporation at low DC voltages by microfluidic flipping of the voltage space topology. Applied Physics Letters, 109(16), 163702. https://doi.org/10.1063/1.4963316

Bhattacharjee, S. (2016). DLS and zeta potential - What they are and what they are not? Journal of Controlled Release, 235, 337–351. https://doi.org/10.1016/j.jconrel.2016.06.017

Bhutto, D. F., Murphy, E. M., Priddy, M. C., Centner, C. C., Moore IV, J. B., Bolli, R., & Kopechek, J. A. (2018). Effect of Molecular Weight on Sonoporation-Mediated Uptake in Human Cells. Ultrasound in Medicine and Biology, 44(12), 2662–2672. https://doi.org/10.1016/j.ultrasmedbio.2018.08.008

Bibikova, O., Singh, P., Popov, A., Akchurin, G., Skaptsov, A., Skovorodkin, I., Khanadeev, V., Mikhalevich, D., Kinnunen, M., Akchurin, G., Bogatyrev, V., Khlebtsov, N., Vainio, S. J., Meglinski, I., & Tuchin, V. (2017). Shape-dependent interaction of gold nanoparticles with cultured cells at laser exposure. Laser Physics Letters, 14(5), 055901. https://doi.org/10.1088/1612-202X/aa63ae

Bischofberger, M., Iacovache, I., & Gisou Van Der Goot, F. (2012). Pathogenic pore-forming proteins: Function and host response. Cell Host and Microbe, 12(3), 266–275. https://doi.org/10.1016/j.chom.2012.08.005

Blazek, A. D., Paleo, B. J., & Weisleder, N. (2015). Plasma membrane repair: A central process for maintaining cellular homeostasis. Physiology, 30(6), 438–448. https://doi.org/10.1152/physiol.00019.2015

Bonanno, L. M., & Segal, E. (2011). Nanostructured porous silicon-polymer-based hybrids: From biosensing to drug delivery. Nanomedicine, 6(10), 1755–1770. https://doi.org/10.2217/nnm.11.153

Boroviak, T. E. (2022). A human embryo model cracks symmetry breaking. Cell Stem Cell, 29(6), 869–870. https://doi.org/10.1016/j.stem.2022.05.009

Boukany, P. E., Morss, A., Liao, W. C., Henslee, B., Jung, H., Zhang, X., Yu, B., Wang, X., Wu, Y., Li, L., Gao, K., Hu, X., Zhao, X., Hemminger, O., Lu, W., Lafyatis, G. P., & Lee, L. J. (2011). Nanochannel electroporation delivers precise amounts of biomolecules into living cells. Nature Nanotechnology, 6(11), 747–754. https://doi.org/10.1038/nnano.2011.164

Boulais, É., Lachaine, R., & Meunier, M. (2012). Plasma mediated off-resonance plasmonic enhanced ultrafast laser-induced nanocavitation. Nano Letters, 12(9), 4763–4769. https://doi.org/10.1021/nl302200w

Bouter, A., Gounou, C., Bérat, R., Tan, S., Gallois, B., Granier, T., D'Estaintot, B. L., Pöschl, E., Brachvogel, B., & Brisson, A. R. (2011). Annexin-A5 assembled into two-dimensional arrays promotes cell membrane repair. Nature Communications, 2(1), 270. https://doi.org/10.1038/ncomms1270

Brandes, R. P., Rezende, F., & Schroder, K. (2015). Redox regulation beyond ROS: why ROS should not be measured as often. Circulation Research, 116(3), 531–549. https://doi.org/10.1161/CIRCRESAHA.116.303584

Braun, J. S., Hoffmann, O., Schickhaus, M., Freyer, D., Dagand, E., Bermpohl, D., Mitchell, T. J., Bechmann, I., & Weber, J. R. (2007). Pneumolysin causes neuronal cell death through mitochondrial damage. Infection and Immunity, 75(9), 4245–4254. https://doi.org/10.1128/IAI.00031-07

Breunig, H. G., Uchugonova, A., Batista, A., & König, K. (2014). High-throughput continuous flow femtosecond laser-assisted cell optoporation and transfection. Microscopy Research and Technique, 77(12), 974–979. https://doi.org/10.1002/jemt.22423

Breunig, H. G., Uchugonova, A., Batista, A., & König, K. (2015). Software-aided automatic laser optoporation and transfection of cells. Scientific Reports, 5, 11185. https://doi.org/10.1038/srep11185

Brooks, J., Minnick, G., Mukherjee, P., Jaberi, A., Chang, L., Espinosa, H. D., & Yang, R. (2020). High Throughput and Highly Controllable Methods for In Vitro Intracellular Delivery. Small, 16(51), 2004917. https://doi.org/10.1002/smll.202004917

Brunner, S., Sauer, T., Carotta, S., Cotten, M., Saltik, M., & Wagner, E. (2000). Cell cycle dependence of gene transfer by lipoplex, polyplex and recombinant adenovirus. Gene Therapy, 7, 401–407. www.nature.com/gt

Bucharskaya, A., Maslyakova, G., Terentyuk, G., Yakunin, A., Avetisyan, Y., Bibikova, O., Tuchina, E., Khlebtsov, B., Khlebtsov, N., Tuchin, V., & Sivakov, V. (2016). Towards effective photothermal/photodynamic treatment using plasmonic gold nanoparticles. International Journal of Molecular Sciences, 17(8), 1295. https://doi.org/10.3390/ijms17081295

Bulcha, J. T., Wang, Y., Ma, H., Tai, P. W. L., & Gao, G. (2021). Viral vector platforms within the gene therapy landscape. Signal Transduction and Targeted Therapy, 6(1), 53. https://doi.org/10.1038/s41392-021-00487-6

Burham, N., Hamzah, A. A., & Majlis, B. Y. (2014). Effect of hydrofluoric acid (HF) concentration to pores size diameter of silicon membrane. Bio-Medical Materials and Engineering, 24(6), 2203–2209. https://doi.org/10.3233/BME-141032

Buschmann, M. D., Carrasco, M. J., Alishetty, S., Paige, M., Alameh, M. G., & Weissman, D. (2021). Nanomaterial Delivery Systems for mRNA Vaccines. Vaccines, 9, 65. https://doi.org/10.3390/vaccines

Cao, Y., Chen, H., Qiu, R., Hanna, M., Ma, E., Hjort, M., Zhang, A., Lewis, R. S., Wu, J. C., & Melosh, N. A. (2018). Universal intracellular biomolecule delivery with precise dosage control. Science Advances, 4, eaat8131.

Caprettini, V., Cerea, A., Melle, G., Lovato, L., Capozza, R., Huang, J. A., Tantussi, F., Dipalo, M., & De Angelis, F. (2017). Soft electroporation for delivering molecules into tightly adherent mammalian cells through 3D hollow nanoelectrodes. Scientific Reports, 7(1), 8524. https://doi.org/10.1038/s41598-017-08886-y

Cardona, M. (1983). Vibrational Spectra of Hydrogen in Silicon and Germanium. Physica Status Solidi (B), 118(3), 463–481. https://doi.org/10.1002/pssb.2221180202

Chaix, A., Cueto-Diaz, E., Delalande, A., Knezevic, N., Midoux, P., Durand, J. O., Pichon, C., & Cunin, F. (2019). Amino-acid functionalized porous silicon nanoparticles for the delivery of pDNA. RSC Advances, 9(55), 31895–31899. https://doi.org/10.1039/c9ra05461h

Chaix, A., Cueto-Diaz, E., Dominguez-Gil, S., Spiteri, C., Lichon, L., Maynadier, M., Dumail, X., Aggad, D., Delalande, A., Bessière, A., Pichon, C., Chiappini, C., Sailor, M. J., Bettache, N., Gary-Bobo, M., Durand, J. O., Nguyen, C., & Cunin, F. (2023). Two-Photon Light Trigger siRNA Transfection of Cancer Cells Using Non-Toxic Porous Silicon Nanoparticles. Advanced Healthcare Materials, 12(27), 2301052. https://doi.org/10.1002/adhm.202301052

Chakravarty, P., Qian, W., El-Sayed, M. A., & Prausnitz, M. R. (2010). Delivery of molecules into cells using carbon nanoparticles activated by femtosecond laser pulses. Nature Nanotechnology, 5(8), 607–611. https://doi.org/10.1038/nnano.2010.126

Chan, S., Li, Y., Rothberg, L. J., Miller, B. L., & Fauchet, P. M. (2001). Nanoscale silicon microcavities for biosensing. Materials Science and Engineering C, 15(1–2), 277–282. https://doi.org/10.1016/s0928-4931(01)00219-3

Chang, L., Bertani, P., Gallego-Perez, D., Yang, Z., Chen, F., Chiang, C., Malkoc, V., Kuang, T., Gao, K., Lee, L. J., & Lu, W. (2016). 3D nanochannel electroporation for high-throughput cell transfection with high uniformity and dosage control. Nanoscale, 8(1), 243–252. https://doi.org/10.1039/c5nr03187g

Chang, L., Gallego-Perez, D., Chiang, C. L., Bertani, P., Kuang, T., Sheng, Y., Chen, F., Chen, Z., Shi, J., Yang, H., Huang, X., Malkoc, V., Lu, W., & Lee, L. J. (2016). Controllable Large-Scale Transfection of Primary Mammalian Cardiomyocytes on a Nanochannel Array Platform. Small, 12(43), 5971–5980. https://doi.org/10.1002/smll.201601465

Chattopadhyay, S., Li, X., & Bohn, P. W. (2002). In-plane control of morphology and tunable photoluminescence in porous silicon produced by metal-assisted electroless chemical etching. Journal of Applied Physics, 91(9), 6134–6140. https://doi.org/10.1063/1.1465123

Chen, G., Ma, B., Xie, R., Wang, Y., Dou, K., & Gong, S. (2018). NIR-induced spatiotemporally controlled gene silencing by upconversion nanoparticle-based siRNA nanocarrier. Journal of Controlled Release, 282, 148–155. https://doi.org/10.1016/j.jconrel.2017.12.028

Chen, G., Qiu, H., Prasad, P. N., & Chen, X. (2014). Upconversion nanoparticles: Design, nanochemistry, and applications in Theranostics. Chemical Reviews, 114(10), 5161–5214. https://doi.org/10.1021/cr400425h

Chen, H., McGrath, T., & Diebold, G. J. (1997). Laser Chemistry in Suspensions: New Products and Unique Reaction Conditions for the Carbon-Steam Reaction. Angewandte Chemie, 36(1–2), 163–166. https://doi.org/10.1002/anie.199701631

Chen, J., Wang, D., Xi, J., Au, L., Siekkinen, A., Warsen, A., Li, Z.-Y., Zhang, H., Xia, Y., & Li, X. (2007). Immuno Gold Nanocages with Tailored Optical Properties for Targeted Photothermal Destruction of Cancer Cells. Nano Letters, 7(5), 1318–1322. https://doi.org/10.1021/nl070345g

Chen, X., He, L., Zhao, Y., Li, Y., Zhang, S., Sun, K., So, K., Chen, F., Zhou, L., Lu, L., Wang, L., Zhu, X., Bao, X., Esteban, M. A., Nakagawa, S., Prasanth, K. V., Wu, Z., Sun, H., & Wang, H. (2017). Malat1 regulates myogenic differentiation and muscle regeneration through modulating MyoD transcriptional activity. Cell Discovery, 3(1), 1–23. https://doi.org/10.1038/celldisc.2017.2

Chen, Y., Aslanoglou, S., Murayama, T., Gervinskas, G., Fitzgerald, L. I., Sriram, S., Tian, J., Johnston, A. P. R., Morikawa, Y., Suu, K., Elnathan, R., & Voelcker, N. H. (2020). Silicon-Nanotube-Mediated Intracellular Delivery Enables Ex Vivo Gene Editing. Advanced Materials, 32(24), 2000036. https://doi.org/10.1002/adma.202000036

Chhasatia, R., Sweetman, M. J., Harding, F. J., Waibel, M., Kay, T., Thomas, H., Loudovaris, T., & Voelcker, N. H. (2017). Non-invasive, in vitro analysis of islet insulin production enabled by an optical porous silicon biosensor. Biosensors and Bioelectronics, 91, 515–522. https://doi.org/10.1016/j.bios.2017.01.004

Chiappini, C., DeRosa, E., Martinez, J. O., Liu, X., Steele, J., Stevens, M. M., & Tasciotti, E. (2015). Biodegradable silicon nanoneedles delivering nucleic acids intracellularly induce localized in vivo neovascularization. Nature Materials, 14(5), 532–539. https://doi.org/10.1038/nmat4249

Chiappini, C., Liu, X., Fakhoury, J. R., & Ferrari, M. (2010). Biodegradable porous silicon barcode nanowires with defined geometry. Advanced Functional Materials, 20(14), 2231–2239. https://doi.org/10.1002/adfm.201000360

Chiappini, C., Martinez, J. O., De Rosa, E., Almeida, C. S., Tasciotti, E., & Stevens, M. M. (2015). Biodegradable nanoneedles for localized delivery of nanoparticles in vivo: Exploring the biointerface. ACS Nano, 9(5), 5500–5509. https://doi.org/10.1021/acsnano.5b01490

Chow, Y. T., Chen, S., Wang, R., Liu, C., Kong, C. W., Li, R. A., Cheng, S. H., & Sun, D. (2016). Single cell transfection through precise microinjection with quantitatively controlled injection volumes. Scientific Reports, 6(1), 24127. https://doi.org/10.1038/srep24127

Chu, M., Shao, Y., Peng, J., Dai, X., Li, H., Wu, Q., & Shi, D. (2013). Near-infrared laser light mediated cancer therapy by photothermal effect of Fe3O4 magnetic nanoparticles. Biomaterials, 34(16), 4078–4088. https://doi.org/10.1016/j.biomaterials.2013.01.086

Cooper, S. T., & Mcneil, P. L. (2015). Membrane Repair: Mechanisms and Pathophysiology. Physiological Reviews, 95(4), 1205–1240. https://doi.org/10.1152/physrev.00037.2014.-Eukaryotic

Cueto Díaz, E. J., Picard, S., Chevasson, V., Daniel, J., Hugues, V., Mongin, O., Genin, E., & Blanchard-Desce, M. (2015). Cooperative Dyads for Two-Photon Uncaging. Organic Letters, 17(1), 102–105. https://doi.org/10.1021/ol5033046

Davis, A. A., Farrar, M. J., Nishimura, N., Jin, M. M., & Schaffer, C. B. (2013). Optoporation and genetic manipulation of cells using femtosecond laser pulses. Biophysical Journal, 105(4), 862–871. https://doi.org/10.1016/j.bpj.2013.07.012

De Boni, L., Rodrigues Jr, J., dos Santos Jr, D., Silva, C., Balogh, D., Oliveira Jr, O., Zilio, S., Misoguti, L., & Mendonc ßa, C. (2002). Two-photon absorption in azoaromatic compounds. Chemical Physics Letters, 361(3–4), 209–213. https://doi.org/10.1016/s0009-2614(02)00892-8

De La Haba, C., Palacio, J. R., Martínez, P., & Morros, A. (2013). Effect of oxidative stress on plasma membrane fluidity of THP-1 induced macrophages. Biochimica et Biophysica Acta - Biomembranes, 1828(2), 357–364. https://doi.org/10.1016/j.bbamem.2012.08.013

Delalande, A., Kotopoulis, S., Postema, M., Midoux, P., & Pichon, C. (2013). Sonoporation: Mechanistic insights and ongoing challenges for gene transfer. Gene, 525(2), 191–199. https://doi.org/10.1016/j.gene.2013.03.095

Delcea, M., Sternberg, N., Yashchenok, A. M., Georgieva, R., Bäumler, H., Möhwald, H., & Skirtach, A. G. (2012). Nanoplasmonics for dual-molecule release through nanopores in the membrane of red blood cells. ACS Nano, 6, 4169–4180. https://doi.org/10.1021/nn3006619

Dhakal, K., Black, B., & Mohanty, S. (2014). Introduction of impermeable actin-staining molecules to mammalian cells by optoporation. Scientific Reports, 4(1), 6553. https://doi.org/10.1038/srep06553

Di Francia, G., La Ferrara, V., Manzo, S., & Chiavarini, S. (2005). Towards a label-free optical porous silicon DNA sensor. Biosensors and Bioelectronics, 21(4), 661–665. https://doi.org/10.1016/j.bios.2004.12.008

Dikalov, S. I., & Harrison, D. G. (2014). Methods for detection of mitochondrial and cellular reactive oxygen species. Antioxidants and Redox Signaling, 20(2), 372–382. https://doi.org/10.1089/ars.2012.4886

Ding, J., Chen, J., Gao, L., Jiang, Z., Zhang, Y., Li, M., Xiao, Q., Lee, S. S., & Chen, X. (2019). Engineered nanomedicines with enhanced tumor penetration. Nano Today, 29, 100800. https://doi.org/10.1016/j.nantod.2019.100800

Djomehri, S. I., Burman, B., Gonzalez, M. E., Takayama, S., & Kleer, C. G. (2019). A reproducible scaffold-free 3D organoid model to study neoplastic progression in breast cancer. Journal of Cell Communication and Signaling, 13(1), 129–143. https://doi.org/10.1007/s12079-018-0498-7

Dong, Z., & Chang, L. (2021). Recent electroporation-based systems for intracellular molecule delivery. Nanotechnology and Precision Engineering, 4(4). https://doi.org/10.1063/10.0005649

Draeger, A., Monastyrskaya, K., & Babiychuk, E. B. (2011). Plasma membrane repair and cellular damage control: The annexin survival kit. Biochemical Pharmacology, 81(6), 703–712. https://doi.org/10.1016/j.bcp.2010.12.027

Draeger, A., Schoenauer, R., Atanassoff, A. P., Wolfmeier, H., & Babiychuk, E. B. (2014). Dealing with damage: Plasma membrane repair mechanisms. Biochimie, 107, 66–72. https://doi.org/10.1016/j.biochi.2014.08.008

Duan, X., Chan, K. T., Lee, K. K. H., & Mak, A. F. T. (2015). Oxidative Stress and Plasma Membrane Repair in Single Myoblasts After Femtosecond Laser Photoporation. Annals of Biomedical Engineering, 43(11), 2735–2744. https://doi.org/10.1007/s10439-015-1341-4

Duckert, B., Vinkx, S., Braeken, D., & Fauvart, M. (2021). Single-cell transfection technologies for cell therapies and gene editing. Journal of Controlled Release, 330, 963–975. https://doi.org/10.1016/j.jconrel.2020.10.068

Durymanov, M., & Reineke, J. (2018). Non-viral delivery of nucleic acids: Insight into mechanisms of overcoming intracellular barriers. Frontiers in Pharmacology, 9, 971. https://doi.org/10.3389/fphar.2018.00971

Duval, K., Grover, H., Han, L. H., Mou, Y., Pegoraro, A. F., Fredberg, J., & Chen, Z. (2017). Modeling physiological events in 2D vs. 3D cell culture. Physiology, 32(4), 266–277. https://doi.org/10.1152/physiol.00036.2016

Elango, N., Elango, S., Shivshankar, P., & Katz, M. S. (2005). Optimized transfection of mRNA transcribed from a d(A/T)100 tail-containing vector. Biochemical and Biophysical Research Communications, 330(3), 958–966. https://doi.org/10.1016/j.bbrc.2005.03.067

Elnathan, R., Barbato, M. G., Guo, X., Mariano, A., Wang, Z., Santoro, F., Shi, P., Voelcker, N. H., Xie, X., Young, J. L., Zhao, Y., Zhao, W., & Chiappini, C. (2022). Biointerface design for vertical nanoprobes. Nature Reviews Materials, 7(12), 953–973. https://doi.org/10.1038/s41578-022-00464-7

Elnathan, R., Delalat, B., Brodoceanu, D., Alhmoud, H., Harding, F. J., Buehler, K., Nelson, A., Isa, L., Kraus, T., & Voelcker, N. H. (2015). Maximizing transfection efficiency of vertically aligned silicon nanowire arrays. Advanced Functional Materials, 25(46), 7215–7225. https://doi.org/10.1002/adfm.201503465

Estelrich, J., & Antònia Busquets, M. (2018). Iron oxide nanoparticles in photothermal therapy. Molecules, 23(7), 1567. https://doi.org/10.3390/molecules23071567

Estévez-Torres, A., Crozatier, C., Diguet, A., Hara, T., Saito, H., Yoshikawa, K., & Baigl, D. (2009). Sequence-independent and reversible photocontrol of transcription/ expression systems using a photosensitive nucleic acid binder. Proceedings of the National Academy of Sciences of the United States of America, 106(30), 12219–12223. https://doi.org/10.1073/pnas.0904382106

Eversole, D., Subramanian, K., Harrison, R. K., Bourgeois, F., Yuksel, A., & Ben-Yakar, A. (2020). Femtosecond Plasmonic Laser Nanosurgery (fs-PLN) mediated by molecularly targeted gold nanospheres at ultra-low pulse fluences. Scientific Reports, 10(1), 12387. https://doi.org/10.1038/s41598-020-68512-2

Fan, Z., Chen, D., & Deng, C. X. (2013). Improving ultrasound gene transfection efficiency by controlling ultrasound excitation of microbubbles. Journal of Controlled Release, 170(3), 401–413. https://doi.org/10.1016/j.jconrel.2013.05.039

Fan, Z., Liu, H., Mayer, M., & Deng, C. X. (2012). Spatiotemporally controlled single cell sonoporation. Proceedings of the National Academy of Sciences, 109(41), 16486–16491. https://doi.org/10.1073/pnas.1208198109/-/DCSupplemental

Fang, H., & Chen, Q. (2022). Applications and challenges of biomaterial mediated mRNA delivery. Exploration of Targeted Anti-Tumor Therapy, 3(4), 428–444. https://doi.org/10.37349/etat.2022.00093

Foster, A. A., Greco, C. T., Green, M. D., Epps, T. H., & Sullivan, M. O. (2015). Light-mediated activation of siRNA release in diblock copolymer assemblies for controlled gene silencing. Advanced Healthcare Materials, 4(5), 760–770. https://doi.org/10.1002/adhm.201400671

Froehlich, K., Haeger, J. D., Heger, J., Pastuschek, J., Photini, S. M., Yan, Y., Lupp, A., Pfarrer, C., Mrowka, R., Schleußner, E., Markert, U. R., & Schmidt, A. (2016). Generation of Multicellular Breast Cancer Tumor Spheroids: Comparison of Different Protocols. Journal of Mammary Gland Biology and Neoplasia, 21(3–4), 89–98. https://doi.org/10.1007/s10911-016-9359-2

Fujii, M., Kovalev, D., Goller, B., Minobe, S., Hayashi, S., & Timoshenko, V. Y. (2005). Time-resolved photoluminescence studies of the energy transfer from excitons confined in Si nanocrystals to oxygen molecules. Physical Review B - Condensed Matter and Materials Physics, 72(16), 165321. https://doi.org/10.1103/PhysRevB.72.165321

Fus-Kujawa, A., Prus, P., Bajdak-Rusinek, K., Teper, P., Gawron, K., Kowalczuk, A., & Sieron, A. L. (2021). An Overview of Methods and Tools for Transfection of Eukaryotic Cells in vitro. Frontiers in Bioengineering and Biotechnology, 9, 701031. https://doi.org/10.3389/fbioe.2021.701031

Gac, S. Le, Zwaan, E., Berg, A. Van Den, & Ohl, C. D. (2007). Sonoporation of suspension cells with a single cavitation bubble in a microfluidic confinement. Lab on a Chip, 7(12), 1666–1672. https://doi.org/10.1039/b712897p

Geng, T., Zhan, Y., Wang, H. Y., Witting, S. R., Cornetta, K. G., & Lu, C. (2010). Flow-through electroporation based on constant voltage for large-volume transfection of cells. Journal of Controlled Release, 144(1), 91–100. https://doi.org/10.1016/j.jconrel.2010.01.030

Gessner, I., Klimpel, A., Klußmann, M., Neundorf, I., & Mathur, S. (2020). Interdependence of charge and secondary structure on cellular uptake of cell penetrating peptide functionalized silica nanoparticles. Nanoscale Advances, 2(1), 453–462. https://doi.org/10.1039/c9na00693a

Gilleron, J., Querbes, W., Zeigerer, A., Borodovsky, A., Marsico, G., Schubert, U., Manygoats, K., Seifert, S., Andree, C., Stöter, M., Epstein-Barash, H., Zhang, L., Koteliansky, V., Fitzgerald, K., Fava, E., Bickle, M., Kalaidzidis, Y., Akinc, A., Maier, M., & Zerial, M. (2013). Image-based analysis of lipid nanoparticle-mediated siRNA delivery, intracellular trafficking and endosomal escape. Nature Biotechnology, 31(7), 638–646. https://doi.org/10.1038/nbt.2612

Godin, B., Gu, J., Serda, R. E., Bhavane, R., Tasciotti, E., Chiappini, C., Liu, X., Tanaka, T., Decuzzi, P., & Ferrari, M. (2010). Tailoring the degradation kinetics of mesoporous silicon structures through PEGylation. Journal of Biomedical Materials Research - Part A, 94(4), 1236–1243. https://doi.org/10.1002/jbm.a.32807

Golshadi, M., Wright, L. K., Dickerson, I. M., & Schrlau, M. G. (2016). High-Efficiency Gene Transfection of Cells through Carbon Nanotube Arrays. Small, 12(22), 3014–3020. https://doi.org/10.1002/smll.201503878

Goodman, T. T., Olive, P. L., & Pun, S. H. (2007). Increased nanoparticle penetration in collagenase-treated multicellular spheroids. International Journal of Nanomedicine, 2(2), 265–274. https://doi.org/10.2147/IJN.S2.2.265

Gratton, S. E. A., Ropp, P. A., Pohlhaus, P. D., Luft, J. C., Madden, V. J., Napier, M. E., & DeSimone, J. M. (2008). The effect of particle design on cellular internalization pathways. Proceedings of the National Academy of Sciences of the United States of America, 105(33), 11613–11618. https://doi.org/10.1073/PNAS.0801763105

Gross, E., Kovalev, D., Künzner, N., Diener, J., Koch, F., Timoshenko, Y., & Fujii, M. (2003). Spectrally resolved electronic energy transfer from silicon nanocrystals to molecular oxygen mediated by direct electron exchange. Physical Review B - Condensed Matter and Materials Physics, 68(11), 115405. https://doi.org/10.1103/PhysRevB.68.115405

Grumezescu, A. Mihai. (2016). Antimicrobial photoinactivation with functionalized fullerenes. In A. M. Grumezescu (Ed.), Nanobiomaterials in antimicrobial therapy: applications of nanobiomaterials (pp. 1–27). William Andrew is an imprint of Elsevier.

Gupta, N., & Malviya, R. (2021). Understanding and advancement in gold nanoparticle targeted photothermal therapy of cancer. Biochimica et Biophysica Acta - Reviews on Cancer, 1875(2), 188532. https://doi.org/10.1016/j.bbcan.2021.188532

Gupta, P., Kar, S., Kumar, A., Tseng, F. G., Pradhan, S., Mahapatra, P. S., & Santra, T. S. (2021). Pulsed laser assisted high-throughput intracellular delivery in hanging drop based three dimensional cancer spheroids. Analyst, 146(15), 4756–4766. https://doi.org/10.1039/d0an02432e

Haase, M., & Schäfer, H. (2011). Upconverting nanoparticles. Angewandte Chemie - International Edition, 50(26), 5808–5829. https://doi.org/10.1002/anie.201005159

Haggerty, D. L., Grecco, G. G., Reeves, K. C., & Atwood, B. (2020). Adeno-Associated Viral Vectors in Neuroscience Research. Molecular Therapy - Methods and Clinical Development, 17, 69–82. https://doi.org/10.1016/j.omtm.2019.11.012

Hansen, S. F., & Lennquist, A. (2020). Carbon nanotubes added to the SIN List as a nanomaterial of Very High Concern. Nature Nanotechnology, 15(1), 3–4. https://doi.org/10.1038/s41565-019-0613-9

Harizaj, A., Van Hauwermeiren, F., Stremersch, S., De Rycke, R., De Keersmaecker, H., Brans, T., Fraire, J. C., Grauwen, K., De Smedt, S. C., Lentacker, I., Lamkanfi, M., & Braeckmans, K. (2021). Nanoparticle-sensitized photoporation enables inflammasome activation studies in targeted single cells. Nanoscale, 13(13), 6592–6604. https://doi.org/10.1039/d0nr05067a

Harizaj, A., Wels, M., Raes, L., Stremersch, S., Goetgeluk, G., Brans, T., Vandekerckhove, B., Sauvage, F., De Smedt, S. C., Lentacker, I., & Braeckmans, K. (2021). Photoporation with Biodegradable Polydopamine Nanosensitizers Enables Safe and Efficient Delivery of mRNA in Human T Cells. Advanced Functional Materials, 31(28), 2102472. https://doi.org/10.1002/adfm.202102472

Hasanzadeh Kafshgari, M., Agiotis, L., Largillière, I., Patskovsky, S., & Meunier, M. (2021a). Antibody-Functionalized Gold Nanostar-Mediated On-Resonance Picosecond Laser Optoporation for Targeted Delivery of RNA Therapeutics. Small, 17(19), 2007577. https://doi.org/10.1002/smll.202007577

Hashemi, A., Roohvand, F., Ghahremani, M. H., Aghasadeghi, M. R., Vahabpour, R., Motevali, F., & Memarnejadian, A. (2012). Optimization of transfection methods for Huh-7 and Vero cells: A comparative study. Cytology and Genetics, 46(6), 347–353. https://doi.org/10.3103/S0095452712060035

Hatef, A., Fortin-Deschênes, S., Boulais, E., Lesage, F., & Meunier, M. (2015). Photothermal response of hollow gold nanoshell to laser irradiation: Continuous wave, short and ultrashort pulse. International Journal of Heat and Mass Transfer, 89, 866–871. https://doi.org/10.1016/j.ijheatmasstransfer.2015.05.071

He, H., Kong, S. K., & Chan, K. T. (2011). Transfection and cell fusion by femtosecond lasers. Journal of Innovative Optical Health Sciences, 4(2), 113–125. https://doi.org/10.1142/S179354581100123X

He, Y., Zhang, W., Xiao, Q., Fan, L., Huang, D., Chen, W., & He, W. (2022). Liposomes and liposome-like nanoparticles: From anti-fungal infection to the COVID-19 pandemic treatment. Asian Journal of Pharmaceutical Sciences, 17(6), 817–837. https://doi.org/10.1016/j.ajps.2022.11.002

Hecht, J. (2019). Understanding Lasers: An Entry-Level Guide. John Wiley & Sons.

Heinemann, D., Kalies, S., Schomaker, M., Ertmer, W., Murua Escobar, H., Meyer, H., & Ripken, T. (2014). Delivery of proteins to mammalian cells via gold nanoparticle mediated laser transfection. Nanotechnology, 25. https://doi.org/10.1088/0957-4484/25/24/245101

Heinemann, D., Schomaker, M., Kalies, S., Schieck, M., Carlson, R., Escobar, H. M., Ripken, T., Meyer, H., & Heisterkamp, A. (2013). Gold Nanoparticle Mediated Laser Transfection for Efficient siRNA Mediated Gene Knock Down. PLoS ONE, 8, 1–9. https://doi.org/10.1371/journal.pone.0058604

Heinrich, J. L., Curtis, C. L., Credo, G. M., Kavanagh, K. L., & Sailor, M. J. (1992). Luminescent colloidal silicon suspensions from porous silicon. Science, 255(5040), 66–68. https://doi.org/10.1126/SCIENCE.255.5040.66

Hirschhaeuser, F., Menne, H., Dittfeld, C., West, J., Mueller-Klieser, W., & Kunz-Schughart, L. A. (2010). Multicellular tumor spheroids: An underestimated tool is catching up again. Journal of Biotechnology, 148(1), 3–15. https://doi.org/10.1016/j.jbiotec.2010.01.012

Holguin, S. Y., Gray, M. D., Joseph, P., Thadhani, N. N., & Prausnitz, M. R. (2018). Photoporation Using Carbon Nanotubes for Intracellular Delivery of Molecules and Its Relationship to Photoacoustic Pressure. Advanced Healthcare Materials, 7(5), 1–10. https://doi.org/10.1002/adhm.201701007

Hong, C., Kang, J., Kim, H., & Lee, C. (2012). Photothermal properties of inorganic nanomaterials as therapeutic agents for cancer thermotherapy. Journal of Nanoscience and Nanotechnology, 12(5), 4352–4355. https://doi.org/10.1166/jnn.2012.5883

Hong, C., Lee, J., Zheng, H., Hong, S. S., & Lee, C. (2011). Porous silicon nanoparticles for cancer photothermotherapy. Nanoscale Research Letters, 6(1), 2–9. https://doi.org/10.1186/1556-276X-6-321

Hong, G., Diao, S., Antaris, A. L., & Dai, H. (2015). Carbon Nanomaterials for Biological Imaging and Nanomedicinal Therapy. Chemical Reviews, 115(19), 10816–10906. https://doi.org/10.1021/acs.chemrev.5b00008

Hosokawa, Y., Ochi, H., Iino, T., Hiraoka, A., & Tanaka, M. (2011). Photoporation of biomolecules into single cells in living vertebrate embryos induced by a femtosecond laser amplifier. PLoS ONE, 6(11), e27677. https://doi.org/10.1371/journal.pone.0027677

Hosseinpour, S., & Walsh, L. J. (2021). Laser-assisted nucleic acid delivery: A systematic review. Journal of Biophotonics, 14(1). https://doi.org/10.1002/jbio.202000295

Houthaeve, G., De Smedt, S. C., Braeckmans, K., & De Vos, W. H. (2022). The cellular response to plasma membrane disruption for nanomaterial delivery. Nano Convergence, 9(1), 1–17. https://doi.org/10.1186/s40580-022-00298-7

Howard, A. C., McNeil, A. K., & McNeil, P. L. (2011). Promotion of plasma membrane repair by vitamin e. Nature Communications, 2(1), 597. https://doi.org/10.1038/ncomms1594

Huang, X., Teng, X., Chen, D., Tang, F., & He, J. (2010). The effect of the shape of mesoporous silica nanoparticles on cellular uptake and cell function. Biomaterials , 31(3), 438–448. https://doi.org/10.1016/j.biomaterials.2009.09.060

Hur, J., & Chung, A. J. (2021). Microfluidic and Nanofluidic Intracellular Delivery. Advanced Science, 8(15), 2004595. https://doi.org/10.1002/advs.202004595

Jafari, S., Hirsch, J., Lausch, D., John, M., Bernhard, N., & Meyer, S. (2019). Composition limited hydrogen effusion rate of a-SiNx:H passivation stack. AIP Conference Proceedings, 2147, 0500041–0500048. https://doi.org/10.1063/1.5123853

Jaque, D., Martínez Maestro, L., Del Rosal, B., Haro-Gonzalez, P., Benayas, A., Plaza, J. L., Martín Rodríguez, E., & García Solé, J. (2014). Nanoparticles for photothermal therapies. Nanoscale, 6(16), 9494–9530. https://doi.org/10.1039/c4nr00708e

Jerjes, W., Theodossiou, T. A., Hirschberg, H., Høgset, A., Weyergang, A., Selbo, P. K., Hamdoon, Z., Hopper, C., & Berg, K. (2020). Photochemical internalization for intracellular drug delivery. From basic mechanisms to clinical research. Journal of Clinical Medicine, 9(2), 1–51. https://doi.org/10.3390/jcm9020528

Jia, S., Fong, W. K., Graham, B., & Boyd, B. J. (2018). Photoswitchable Molecules in Long-Wavelength Light-Responsive Drug Delivery: From Molecular Design to Applications. Chemistry of Materials, 30(9), 2873–2887. https://doi.org/10.1021/acs.chemmater.8b00357

Jimenez, A. J., Maiuri, P., Lafaurie-Janvore, J., Divoux, S., Piel, M., & Perez, F. (2014). ESCRT machinery is required for plasma membrane repair. Science, 343(6174). https://doi.org/10.1126/science.1247136

Jones, K. H., & Senft, J. A. (1985). An Improved Method to Determine Cell Viability by Simultaneous Staining with Fluorescein Diacetate-Propidium Iodide. Journal of Histochemistry & Cytochemistry, 33(1), 77–79. https://doi.org/10.1177/33.1.2578146

Jung, H., Moon, D., & Lee, J. (2012). Quantitative analysis and efficient surface modification of silica nanoparticles. Journal of Nanomaterials, 2012, 48. https://doi.org/10.1155/2012/593471

Kalies, S., Birr, T., Heinemann, D., Schomaker, M., Ripken, T., Heisterkamp, A., & Meyer, H. (2014). Enhancement of extracellular molecule uptake in plasmonic laser perforation. Journal of Biophotonics, 7, 474–482. https://doi.org/10.1002/jbio.201200200

Kam, W. N. S., O'connell, M., Wisdom, J. A., & Dai, H. (2005). Carbon nanotubes as multifunctional biological transporters and near-infrared agents for selective cancer cell destruction. Proceedings of the National Academy of Sciences, 102(33), 11600–11605. www.pnas.orgcgidoi10.1073pnas.0502680102

Kamegawa, R., Naito, M., & Miyata, K. (2018). Functionalization of silica nanoparticles for nucleic acid delivery. Nano Research, 11(10), 5219–5239. https://doi.org/10.1007/s12274-018-2116-7

Kar, S., Loganathan, M., Dey, K., Shinde, P., Chang, H. Y., Nagai, M., & Santra, T. S. (2018). Single-cell electroporation: Current trends, applications and future prospects. Journal of Micromechanics and Microengineering, 28(12), 123002. https://doi.org/10.1088/1361-6439/aae5ae

Karki, A., Giddings, E., Carreras, A., Champagne, D., Fortner, K., Rincon, M., & Wu, J. (2019). Sonoporation as an Approach for siRNA delivery into T cells. Ultrasound in Medicine and Biology, 45(12), 3222–3231. https://doi.org/10.1016/j.ultrasmedbio.2019.06.406

Katsen-Globa, A., Puetz, N., Gepp, M. M., Neubauer, J. C., & Zimmermann, H. (2016). Study of SEM preparation artefacts with correlative microscopy: Cell shrinkage of adherent cells by HMDS-drying. Scanning, 38(6), 625–633. https://doi.org/10.1002/sca.21310

Katti, A., Diaz, B. J., Caragine, C. M., Sanjana, N. E., & Dow, L. E. (2022). CRISPR in cancer biology and therapy. Nature Reviews Cancer, 22(5), 259–279. https://doi.org/10.1038/s41568-022-00441-w

Koloskova, O. O., Gileva, A. M., Drozdova, M. G., Grechihina, M. V., Suzina, N. E., Budanova, U. A., Sebyakin, Y. L., Kudlay, D. A., Shilovskiy, I. P., Sapozhnikov, A. M., Kovalenko, E. I., Markvicheva, E. A., & Khaitov, M. R. (2018). Effect of lipopeptide structure on gene delivery system properties: Evaluation in 2D and 3D in vitro models. Colloids and Surfaces B: Biointerfaces, 167, 328–336. https://doi.org/10.1016/j.colsurfb.2018.04.003

Korhonen, E., Rönkkö, S., Hillebrand, S., Riikonen, J., Xu, W., Järvinen, K., Lehto, V. P., & Kauppinen, A. (2016). Cytotoxicity assessment of porous silicon microparticles for ocular drug delivery. European Journal of Pharmaceutics and Biopharmaceutics, 100, 1–8. https://doi.org/10.1016/j.ejpb.2015.11.020

Kovalev, D., & Fujii, M. (2005). Silicon nanocrystals: Photosensitizers for oxygen molecules. Advanced Materials, 17(21), 2531–2544. https://doi.org/10.1002/adma.200500328

Kowaltowski, A. J. (2019). Strategies to detect mitochondrial oxidants. Redox Biology, 21, 101065. https://doi.org/10.1016/j.redox.2018.101065

Koynov, S., Pereira, R. N., Crnolatac, I., Kovalev, D., Huygens, A., Chirvony, V., Stutzmann, M., & De Witte, P. (2011). Purification of nano-porous silicon for biomedical applications. Advanced Engineering Materials, 13(6), B225–B233. https://doi.org/10.1002/adem.201080091

Kozlowski, M. T., Crook, C. J., & Ku, H. T. (2021). Towards organoid culture without Matrigel. Communications Biology, 4(1), 1387. https://doi.org/10.1038/s42003-021-02910-8

Kulyavtsev, P. A., & Spencer, R. P. (2017). Drug delivery via porous silicon: a focused patent review. Pharmaceutical Patent Analyst, 6(2), 77–85. https://doi.org/10.4155/ppa-2016-0042

Kumar, S., Lazau, E., Kim, C., Thadhani, N. N., & Prausnitz, M. R. (2021). Serum protects cells and increases intracellular delivery of molecules by nanoparticle-mediated photoporation. International Journal of Nanomedicine, 16, 3707–3724. https://doi.org/10.2147/IJN.S307027

Kumara, M., Jayakumar, G., Muhammad Idris, N., & Zhang, Y. (2012). Remote activation of biomolecules in deep tissues using near-infrared-to-UV upconversion nanotransducers. Proceedings of the National Academy of Sciences, 109(22), 8483–8488. https://doi.org/10.1073/pnas.1114551109

Kumeria, T., McInnes, S. J. P., Maher, S., & Santos, A. (2017). Porous silicon for drug delivery applications and theranostics: recent advances, critical review and perspectives. Expert Opinion on Drug Delivery, 14(12), 1407–1422. https://doi.org/10.1080/17425247.2017.1317245

Laaksonen, T., Santos, H., Vihola, H., Salonen, J., Riikonen, J., Heikkilä, T., Peltonen, L., Kumar, N., Murzin, D. Y., Lehto, V.-P., & Hirvonen, J. (2007). Failure of MTT as a toxicity testing agent for mesoporous silicon microparticles. Chemical Research in Toxicology, 20(12), 1913–1918. https://doi.org/10.1021/tx700326b

Lachaine, R., Boulais, É., & Meunier, M. (2014). From Thermo- to Plasma-Mediated Ultrafast Laser-Induced Plasmonic Nanobubbles. ACS Photonics, 1(4), 331–336. https://doi.org/10.1021/ph400018s

Lachaine, R., Boutopoulos, C., Lajoie, P. Y., Boulais, É., & Meunier, M. (2016). Rational Design of Plasmonic Nanoparticles for Enhanced Cavitation and Cell Perforation. Nano Letters, 16(5), 3187–3194. https://doi.org/10.1021/acs.nanolett.6b00562

Lai, W. F., & Wong, W. T. (2018). Design of Polymeric Gene Carriers for Effective Intracellular Delivery. Trends in Biotechnology, 36(7), 713–728. https://doi.org/10.1016/j.tibtech.2018.02.006

Lapotko, D. (2009). Optical excitation and detection of vapor bubbles around plasmonic nanoparticles. Optics Express, 17(4), 2538–2556. https://doi.org/10.1364/oe.17.002538

Lechardeur, D., Sohn, K.-J., Haardt, M., Joshi, P. B., Monck, M., Graham, R. W., Beatty, B., Squire, J., O'brodovich, H., & Lukacs, G. L. (1999). Metabolic instability of plasmid DNA in the cytosol: a potential barrier to gene transfer. Gene Therapy, 6(4), 482–497. https://doi.org/10.1038/sj.gt.3300867

Lee, C., Hong, C., Lee, J., Son, M., & Hong, S. S. (2012). Comparison of oxidized porous silicon with bare porous silicon as a photothermal agent for cancer cell destruction based on in vitro cell test results. Lasers in Medical Science, 27(5), 1001–1008. https://doi.org/10.1007/s10103-011-1032-9

Lee, C., Kim, H., Cho, Y., & Lee, W. I. (2007). The properties of porous silicon as a therapeutic agent via the new photodynamic therapy. Journal of Materials Chemistry, 17(2), 2648–2653. https://doi.org/10.1039/b700892a

Lee, S. H., Kang, J. S., & Kim, D. (2018). A mini review: Recent advances in surface modification of porous silicon. Materials, 11(12), 1–14. https://doi.org/10.3390/ma11122557

Lee, S., Kim, S., Kim, D., You, J., Kim, J. S., Kim, H., Park, J., Song, J., & Choi, I. (2023). Spatiotemporally controlled drug delivery via photothermally driven conformational change of self-integrated plasmonic hybrid nanogels. Journal of Nanobiotechnology, 21(1), 1–20. https://doi.org/10.1186/s12951-023-01935-x

Lentacker, I., De Cock, I., Deckers, R., De Smedt, S. C., & Moonen, C. T. W. (2014). Understanding ultrasound induced sonoporation: Definitions and underlying mechanisms. Advanced Drug Delivery Reviews, 72, 49–64. https://doi.org/10.1016/j.addr.2013.11.008

Leonardi, A. A., Lo Faro, M. J., & Irrera, A. (2021). Biosensing platforms based on silicon nanostructures: A critical review. Analytica Chimica Acta, 1160, 338393. https://doi.org/10.1016/j.aca.2021.338393

Leung, B. M., Lesher-Perez, S. C., Matsuoka, T., Moraes, C., & Takayama, S. (2015). Media additives to promote spheroid circularity and compactness in hanging drop platform. Biomaterials Science, 3(2), 336–344. https://doi.org/10.1039/c4bm00319e

Levy-Clement, C. (2014). Porous silicon formation by metal nanoparticle-assisted etching. In L. Canham (Ed.), Handbook of Porous Silicon (pp. 49–67). https://doi.org/10.1007/978-3-319-05744-6

Li, B., Luo, X., & Dong, Y. (2016). Effects of Chemically Modified Messenger RNA on Protein Expression. Bioconjugate Chemistry, 27(3), 849–853. https://doi.org/10.1021/acs.bioconjchem.6b00090

Li, J. J., Zou, L., Hartono, D., Ong, C. N., Bay, B. H., & Yung, L. Y. L. (2008). Gold nanoparticles induce oxidative damage in lung fibroblasts in vitro. Advanced Materials, 20(1), 138–142. https://doi.org/10.1002/adma.200701853

Li, J., Leung, C. W. T., Wong, D. S. H., Xu, J., Li, R., Zhao, Y., Yung, C. Y. Y., Zhao, E., Tang, B. Z., & Bian, L. (2019). Photocontrolled SiRNA Delivery and Biomarker-Triggered Luminogens of Aggregation-Induced Emission by Up-Conversion NaYF4:Yb3+Tm3+@SiO2 Nanoparticles for Inducing and Monitoring Stem-Cell Differentiation. ACS Applied Materials and Interfaces, 11(25), 22074–22084. https://doi.org/10.1021/acsami.7b00845

Li, L., & Fourkas, J. T. (2007). Multiphoton polymerization. Materials Today, 10(6), 30–37. https://doi.org/10.1016/S1369-7021(07)70130-X

Li, W., Liu, Z., Fontana, F., Ding, Y., Liu, D., Hirvonen, J. T., & Santos, H. A. (2018). Tailoring Porous Silicon for Biomedical Applications: From Drug Delivery to Cancer Immunotherapy. Advanced Materials, 30(24). https://doi.org/10.1002/adma.201703740

Li, Z. G., Liu, A. Q., Klaseboer, E., Zhang, J. B., & Ohl, C. D. (2013). Single cell membrane poration by bubble-induced microjets in a microfluidic chip. Lab on a Chip, 13(6), 1144–1150. https://doi.org/10.1039/c3lc41252k

Link, J. R., & Sailor, M. J. (2003). Smart dust: Self-assembling, self-orienting photonic crystals of porous Si. Proceedings of the National Academy of Sciences of the United States of America, 100(19), 10607–10610. https://doi.org/10.1073/PNAS.1233824100

Lissandrello, C. A., Santos, J. A., Hsi, P., Welch, M., Mott, V. L., Kim, E. S., Chesin, J., Haroutunian, N. J., Stoddard, A. G., Czarnecki, A., Coppeta, J. R., Freeman, D. K., Flusberg, D. A., Balestrini, J. L., & Tandon, V. (2020). High-throughput continuous-flow microfluidic electroporation of mRNA into primary human T cells for applications in cellular therapy manufacturing. Scientific Reports, 10(1), 18045. https://doi.org/10.1038/s41598-020-73755-0

Liu, F., Yang, Z., Yao, R., Li, H., Cheng, J., & Guo, M. (2022). Bulk Electroporation for Intracellular Delivery Directly Driven by Mechanical Stimulus. ACS Nano, 16(11), 19363–19372. https://doi.org/10.1021/acsnano.2c08945

Liu, J., Fraire, J. C., De Smedt, S. C., Xiong, R., & Braeckmans, K. (2020). Intracellular Labeling with Extrinsic Probes: Delivery Strategies and Applications. Small, 16(22), 2000146. https://doi.org/10.1002/smll.202000146

Liu, J., Li, C., Brans, T., Harizaj, A., Van de Steene, S., De Beer, T., De Smedt, S., Szunerits, S., Boukherroub, R., Xiong, R., & Braeckmans, K. (2020). Surface functionalization with polyethylene glycol and polyethyleneimine improves the performance of graphene-based materials for safe and efficient intracellular delivery by laser-induced photoporation. International Journal of Molecular Sciences, 21(4), 1540. https://doi.org/10.3390/ijms21041540

Liu, J., Xiong, R., Brans, T., Lippens, S., Parthoens, E., Zanacchi, F. C., Magrassi, R., Singh, S. K., Kurungot, S., Szunerits, S., Bové, H., Ameloot, M., Fraire, J. C., Teirlinck, E., Samal, S. K., Rycke, R. De, Houthaeve, G., De Smedt, S. C., Boukherroub, R., & Braeckmans, K. (2018). Repeated photoporation with graphene quantum dots enables homogeneous labeling of live cells with extrinsic markers for fluorescence microscopy. Light: Science and Applications, 7(1), 47. https://doi.org/10.1038/s41377-018-0048-3

Liu, Y., Yan, J., & Prausnitz, M. R. (2012). Can Ultrasound Enable Efficient Intracellular Uptake of Molecules? A Retrospective Literature Review and Analysis. Ultrasound in Medicine and Biology, 38(5), 876–888. https://doi.org/10.1016/j.ultrasmedbio.2012.01.006

Liu, Y., Yan, J., Santangelo, P. J., & Prausnitz, M. R. (2016). DNA uptake, intracellular trafficking and gene transfection after ultrasound exposure. Journal of Controlled Release, 234, 1–9. https://doi.org/10.1016/j.jconrel.2016.05.013

Longati, P., Jia, X., Eimer, J., Wagman, A., Witt, M. R., Rehnmark, S., Verbeke, C., Toftgard, R., Lohr, M., & Heuchel, R. L. (2013). 3D pancreatic carcinoma spheroids induce a matrix-rich, chemoresistant phenotype offering a better model for drug testing. BMC Biophysics, 13(95). https://doi.org/10.1186/2046-1682-4-13

Loni, A. (2014). Porous silicon formation by anodization. In L. Canham (Ed.), Handbook of Porous Silicon (pp. 11–23). Springer Reference. https://doi.org/10.1007/978-3-319-05744-6

Lotze, M. T., & Thomson, A. W. (2005). Measuring Immunity: Basic Biology and Clinical Assessment. Elsevier Ltd. https://doi.org/10.1016/B978-0-12-455900-4.X5260-X

Löwen, H., & Madden, P. A. (1992). A microscopic mechanism for shock-wave generation in pulsed-laser-heated colloidal suspensions. The Journal of Chemical Physics, 97(11), 8760–8766. https://doi.org/10.1063/1.463345

Lu, F., Wu, S. H., Hung, Y., & Mou, C. Y. (2009). Size effect on cell uptake in well-suspended, uniform mesoporous silica nanoparticles. Small, 5(12), 1408–1413. https://doi.org/10.1002/smll.200900005

Luecke, I. W., Lin, G., Santarriaga, S., Scaglione, K. M., & Ebert, A. D. (2023). Viral vector gene delivery of the novel chaperone protein SRCP1 to modify insoluble protein in in vitro and in vivo models of ALS. Gene Therapy, 30(6), 528–533. https://doi.org/10.1038/s41434-021-00276-4

Lukianova-Hleb, E. Y., Samaniego, A. P., Wen, J., Metelitsa, L. S., Chang, C. C., & Lapotko, D. O. (2011). Selective gene transfection of individual cells in vitro with plasmonic nanobubbles. Journal of Controlled Release, 152(2), 286–293. https://doi.org/10.1016/j.jconrel.2011.02.006

Lv, J., Chang, H., Wang, Y., Wang, M., Xiao, J., Zhang, Q., & Cheng, Y. (2015). Fluorination on polyethylenimine allows efficient 2D and 3D cell culture gene delivery. Journal of Materials Chemistry B, 3(4), 642–650. https://doi.org/10.1039/c4tb01447b

Lynch, I., Salvati, A., & Dawson, K. A. (2009). What does the cell see? Nature Nanotechnology, 4(9), 547. https://doi.org/10.1038/nnano.2009.248

MacKey, M. A., Ali, M. R. K., Austin, L. A., Near, R. D., & El-Sayed, M. A. (2014). The most effective gold nanorod size for plasmonic photothermal therapy: Theory and in vitro experiments. Journal of Physical Chemistry B, 118(5), 1319–1326. https://doi.org/10.1021/jp409298f

Maginnis, M. S. (2018). Virus–Receptor Interactions: The Key to Cellular Invasion. Journal of Molecular Biology, 430(17), 2590–2611. https://doi.org/10.1016/j.jmb.2018.06.024

Magrez, A., Kasas, S., Salicio, V., Pasquier, N., Seo, J. W., Celio, M., Catsicas, S., Schwaller, B., & Forró, L. (2006). Cellular toxicity of carbon-based nanomaterials. Nano Letters, 6(6), 1121–1125. https://doi.org/10.1021/nl060162e

Mahmoudi, M., Sant, S., Wang, B., Laurent, S., & Sen, T. (2011). Superparamagnetic iron oxide nanoparticles (SPIONs): Development, surface modification and applications in chemotherapy. Advanced Drug Delivery Reviews, 63(1–2), 24–46. https://doi.org/10.1016/j.addr.2010.05.006

Malvern Panalytical. (2017). Polydispersity – what does it mean for DLS and chromatography? https://www.materials-talks.com/polydispersity-what-does-it-mean-for-dls-and-chromatography/

Manfrin, A., Tabata, Y., Paquet, E. R., Vuaridel, A. R., Rivest, F. R., Naef, F., & Lutolf, M. P. (2019). Engineered signaling centers for the spatially controlled patterning of human pluripotent stem cells. Nature Methods, 16, 640–648. https://doi.org/10.1038/s41592-019-0455-2

Manshian, B. B., Jiménez, J., Himmelreich, U., & Soenen, S. J. (2017). Personalized medicine and follow-up of therapeutic delivery through exploitation of quantum dot toxicity. Biomaterials, 127, 1–12. https://doi.org/10.1016/j.biomaterials.2017.02.039

Marchington, R. F., Arita, Y., Tsampoula, X., Gunn-Moore, F. J., & Dholakia, K. (2010). High throughput photoporation of mammalian cells using microfluidic cell delivery. Biomedical Optics and 3D Imaging, 1–2. https://doi.org/10.1364/biomed.2010.btud92

Mariani, S., Pino, L., Strambini, L. M., Tedeschi, L., & Barillaro, G. (2016). 10 000-Fold Improvement in Protein Detection Using Nanostructured Porous Silicon Interferometric Aptasensors. ACS Sensors, 1(12), 1471–1479. https://doi.org/10.1021/acssensors.6b00634

Mariani, S., Robbiano, V., Strambini, L. M., Debrassi, A., Egri, G., Dähne, L., & Barillaro, G. (2018). Layer-by-layer biofunctionalization of nanostructured porous silicon for high-sensitivity and high-selectivity label-free affinity biosensing. Nature Communications, 9(1), 5256. https://doi.org/10.1038/s41467-018-07723-8

Mashel, T. V., Tarakanchikova, Y. V., Muslimov, A. R., Zyuzin, M. V., Timin, A. S., Lepik, K. V., & Fehse, B. (2020). Overcoming the delivery problem for therapeutic genome editing: Current status and perspective of non-viral methods. Biomaterials, 258, 120282. https://doi.org/10.1016/j.biomaterials.2020.120282

Mason, T., & Peters, D. (2002). Practical sonochemistry: Power ultrasound uses and applications. Woodhead Publishing.

Mayne, A. H., Bayliss, S. C., Barr, P., Tobin, M., & Buckberry, L. D. (2000). Biologically Interfaced Porous Silicon Devices. Physica Status Solidi (a), 182(1), 12. https://doi.org/10.1002/1521-396X(200011)182:1<505::AID-PSSA505>3.0.CO;2

McIlwain, D. R., Berger, T., & Mak, T. W. (2013). Caspase functions in cell death and disease. Cold Spring Harbor Perspectives in Biology, 5(4), 1–28. https://doi.org/10.1101/cshperspect.a008656

McNeil, P. L., & Kirchhausen, T. (2005). An emergency response team for membrane repair. Nature Reviews Molecular Cell Biology, 6, 499–505. https://doi.org/10.1038/nrm1665

Medrzycka, K. B. (1991). The effect of particle concentration on zeta potential in extremely dilute solutions. Colloid & Polymer Science, 269(1), 85–90. https://doi.org/10.1007/BF00654663

Meng, L., Cai, F., Jiang, P., Deng, Z., Li, F., Niu, L., Chen, Y., Wu, J., & Zheng, H. (2014). On-chip targeted single cell sonoporation with microbubble destruction excited by surface acoustic waves. Applied Physics Letters, 104(7), 073701. https://doi.org/10.1063/1.4865770

Mengstie, M. A. (2022). Viral Vectors for the in Vivo Delivery of CRISPR Components: Advances and Challenges. Frontiers in Bioengineering and Biotechnology, 10, 895713. https://doi.org/10.3389/fbioe.2022.895713

Merck. (2023a). Cultrex® 3-D Spheroid Fluorometric Proliferation/Viability Assay Protocol. https://www.sigmaaldrich.com/GB/en/technical-documents/protocol/cell-culture-and-cell-culture-analysis/3d-cell-culture/3d-spheroid-fluorometric-proliferation-viability-assay

Merck. (2023b). IR spectrum table & chart. https://www.sigmaaldrich.com/GB/en/technical-documents/technical-article/analytical-chemistry/photometry-and-reflectometry/ir-spectrum-table

Meredith, J. E., Fazeli, B., & Schwartz, M. A. (1993). The Extracellular Matrix as a Cell Survival Factor. Molecular Biology of the Cell, 4(9), 953–961. https://doi.org/10.1091/mbc.4.9.953

Messina, G. C., Dipalo, M., La Rocca, R., Zilio, P., Caprettini, V., Proietti Zaccaria, R., Toma, A., Tantussi, F., Berdondini, L., & De Angelis, F. (2015). Spatially, Temporally, and Quantitatively Controlled Delivery of Broad Range of Molecules into Selected Cells through Plasmonic Nanotubes. Advanced Materials, 27(44), 7145–7149. https://doi.org/10.1002/adma.201503252

Mignone, F., Gissi, C., Liuni, S., & Pesole, G. (2002). Untranslated regions of mRNAs. Genome Biology, 3(3), 1–10. https://doi.org/10.1186/gb-2002-3-3-reviews0004

Minai, L., Yeheskely-Hayon, D., & Yelin, D. (2013). High levels of reactive oxygen species in gold nanoparticle-targeted cancer cells following femtosecond pulse irradiation. Scientific Reports, 3, 1–7. https://doi.org/10.1038/srep02146

Mintzer, M. A., & Simanek, E. E. (2009). Nonviral vectors for gene delivery. Chemical Reviews, 109(2), 259–302. https://doi.org/10.1021/cr800409e

Miyake, K., McNeil, P. L., Suzuki, K., Tsunoda, R., & Sugai, N. (2001). An actin barrier to resealing. Journal of Cell Science, 114, 3487–3494.

Moe, A. M., Golding, A. E., & Bement, W. M. (2015). Cell healing: Calcium, repair and regeneration. Seminars in Cell and Developmental Biology, 45, 18–23. https://doi.org/10.1016/j.semcdb.2015.09.026

Mohan, L., Kar, S., Nagai, M., & Santra, T. S. (2021). Electrochemical fabrication of TiO2 micro-flowers for an efficient intracellular delivery using nanosecond light pulse. Materials Chemistry and Physics, 267, 124604. https://doi.org/10.1016/j.matchemphys.2021.124604

Mohan, L., Kar, S., Ren Hattori, Ishii-Teshima, M., Bera, P., Roy, S., Santra, T. S., Shibata, T., & Nagai, M. (2021). Can titanium oxide nanotubes facilitate intracellular delivery by laser-assisted photoporation? Applied Surface Science, 543, 148815. https://doi.org/10.1016/j.apsusc.2020.148815

Mohanty, S. K., Sharma, M., & Gupta, P. K. (2003). Laser-assisted microinjection into targeted animal cells. Biotechnology Letters, 25(11), 895–899. https://doi.org/10.1023/a:1024038609045

Moretta, R., De Stefano, L., Terracciano, M., & Rea, I. (2021). Porous silicon optical devices: Recent advances in biosensing applications. Sensors, 21(4), 1–26. https://doi.org/10.3390/s21041336

Mthunzi, P., Dholakia, K., & Gunn-Moore, F. (2010). Phototransfection of mammalian cells using femtosecond laser pulses: optimization and applicability to stem cell differentiation. Journal of Biomedical Optics, 15(4), 041507. https://doi.org/10.1117/1.3430733

Murphy, M. P., Bayir, H., Belousov, V., Chang, C. J., Davies, K. J. A., Davies, M. J., Dick, T. P., Finkel, T., Forman, H. J., Janssen-Heininger, Y., Gems, D., Kagan, V. E., Kalyanaraman, B., Larsson, N. G., Milne, G. L., Nyström, T., Poulsen, H. E., Radi, R., Van Remmen, H., … Halliwell, B. (2022). Guidelines for measuring reactive oxygen species and oxidative damage in cells and in vivo. Nature Metabolism, 4(6), 651–662. https://doi.org/10.1038/s42255-022-00591-z

Muthaiyan Shanmugam, M. (2016). Improved Methods of Microinjection in Caenorhabditis elegans: Automation and Microfluidic Systems. JSM Biotechnology & Biomedical Engineering, 3(5), 1072. https://doi.org/10.47739/2333-7117/1072

Myat, Y. Y., Sahatsapan, N., Rojanarata, T., Ngawhirunpat, T., Opanasopit, P., Pornpitchanarong, C., & Patrojanasophon, P. (2024). Antibody-decorated chitosan-iodoacetamide-coated nanocarriers for the potential delivery of doxorubicin to breast cancer cells. International Journal of Biological Macromolecules, 258, 128797. https://doi.org/10.1016/j.ijbiomac.2023.128797

Nalluri, S. K. M., Voskuhl, J., Bultema, J. B., Boekema, E. J., & Ravoo, B. J. (2011). Light-responsive capture and release of DNA in a ternary supramolecular complex. Angewandte Chemie, 50(41), 9747–9751. https://doi.org/10.1002/anie.201103707

Nation, J. L. (1983). A new method using hexamethyldisilazane for preparation of soft insect tissues for scanning electron microscopy. Stain Technology, 58(6), 347–351. https://doi.org/10.3109/10520298309066811

Nicolson, G. L. (2014). The Fluid - Mosaic Model of Membrane Structure: Still relevant to understanding the structure, function and dynamics of biological membranes after more than 40 years. Biochimica et Biophysica Acta - Biomembranes, 1838(6), 1451–1466. https://doi.org/10.1016/j.bbamem.2013.10.019

Ogata, Y., Niki, H., Sakka, T., & Iwasaki, M. (1995). Oxidation of Porous Silicon under Water Vapor Environment. Journal of the Electrochemical Society, 142(5), 1595. https://doi.org/10.1149/1.2048619

Oh, S., & Kessler, J. A. (2018). Design, Assembly, Production, and Transfection of Synthetic Modified mRNA. Methods, 133, 29–43. https://doi.org/10.1016/j.ymeth.2017.10.008

Pack, D. W., Hoffman, A. S., Pun, S., & Stayton, P. S. (2005). Design and development of polymers for gene delivery. Nature Reviews Drug Discovery, 4(7), 581–593. https://doi.org/10.1038/nrd1775

Palumbo, G., Caruso, M., Crescenzi, E., Tecce, M. F., Roberti, G., & Colasanti, A. (1996). Targeted gene transfer in eucaryotic cells by dye-assisted laser optoporation. Journal of Photochemistry and Photobiology B: Biology, 36(1), 46. https://doi.org/10.1016/s1011-1344(96)07335-6

Pan, Y., Neuss, S., Leifert, A., Fischler, M., Wen, F., Simon, U., Schmid, G., Brandau, W., & Jahnen-Dechent, W. (2007). Size-dependent cytotoxicity of gold nanoparticles. Small, 3(11), 1941–1949. https://doi.org/10.1002/smll.200700378

Panchal, J., Kotarek, J., Marszal, E., & Topp, E. M. (2014). Analyzing subvisible particles in protein drug products: A comparison of Dynamic Light Scattering (DLS) and Resonant Mass Measurement (RMM). AAPS Journal, 16(3), 440–451. https://doi.org/10.1208/S12248-014-9579-6

Pap, A. E., Kordás, K., George, T. F., & Leppävuori, S. (2004). Thermal oxidation of porous silicon: Study on reaction kinetics. Journal of Physical Chemistry B, 108(34), 12744–12747. https://doi.org/10.1021/jp049323y

Paris, J. L., Coelho, F., Teixeira, A., Diéguez, L., Silva, B. F. B., & Abalde-Cela, S. (2020). In vitro evaluation of lipopolyplexes for gene transfection: Comparing 2D, 3D and microdroplet-enabled cell culture. Molecules, 25(14), 3277. https://doi.org/10.3390/molecules25143277

Park, J. H., Gu, L., Von Maltzahn, G., Ruoslahti, E., Bhatia, S. N., & Sailor, M. J. (2009). Biodegradable luminescent porous silicon nanoparticles for in vivo applications. Nature Materials, 8(4), 331–336. https://doi.org/10.1038/nmat2398

Park, J. H., Park, J. S., & Choi, J. S. (2014). Basic amino acid-conjugated polyamidoamine dendrimers with enhanced gene transfection efficiency. Macromolecular Research, 22(5), 500–508. https://doi.org/10.1007/s13233-014-2073-2

Pascolo, S. (2021). Synthetic messenger rna-based vaccines: From scorn to hype. Viruses, 13(2), 270. https://doi.org/10.3390/v13020270

Patskovsky, S., Qi, M., & Meunier, M. (2020). Single point single-cell nanoparticle mediated pulsed laser optoporation. Analyst, 145(2), 523–529. https://doi.org/10.1039/c9an01869g

Piñero, J., López-Baena, M., Ortiz, T., & Cortés, F. (1997). Apoptotic and necrotic cell death are both induced by electroporation in HL60 human promyeloid leukaemia cells. Apoptosis, 2(3), 330–336. https://doi.org/10.1023/a:1026497306006

Ping Gordon Xu, Z. (2022). Strategy for Cytoplasmic Delivery Using Inorganic Particles. Pharmaceutical Research, 39(6), 1035–1045. https://doi.org/10.1007/s11095-022-03178-1

Pirozzi, N. M., Hoogenboom, J. P., & Giepmans, B. N. G. (2018). ColorEM: analytical electron microscopy for element-guided identification and imaging of the building blocks of life. Histochemistry and Cell Biology, 150(5), 509–520. https://doi.org/10.1007/S00418-018-1707-4

Potez, S., Luginbühl, M., Monastyrskaya, K., Hostettler, A., Draeger, A., & Babiychuk, E. B. (2011). Tailored protection against plasmalemmal injury by annexins with different Ca2+ sensitivities. Journal of Biological Chemistry, 286(20), 17982–17991. https://doi.org/10.1074/jbc.M110.187625

Prabhakar, D., Kumari, V., & Islam, S. S. (2012). Nanoporous silicon based electrochemical immunosensor. Science of Advanced Materials, 4(1), 121–125. https://doi.org/10.1166/sam.2012.1260

Praveen, B. B., Stevenson, D. J., Antkowiak, M., Dholakia, K., & Gunn-Moore, F. J. (2011). Enhancement and optimization of plasmid expression in femtosecond optical transfection. Journal of Biophotonics, 4(4), 229–235. https://doi.org/10.1002/jbio.201000105

Promega. (2023). CellTiter-Glo® 2.0 Cell Viability Assay | ATP Assay | Promega. https://www.promega.co.uk/products/cell-health-assays/cell-viability-and-cytotoxicity-assays/celltiter_glo-2_0-assay/?catNum=G9241#protocols

Puhl, D. L., D'Amato, A. R., & Gilbert, R. J. (2019). Challenges of gene delivery to the central nervous system and the growing use of biomaterial vectors. Brain Research Bulletin, 150, 216–230. https://doi.org/10.1016/j.brainresbull.2019.05.024

Qin, Z., Joo, J., Gu, L., & Sailor, M. J. (2014). Size control of porous silicon nanoparticles by electrochemical perforation etching. Particle and Particle Systems Characterization, 31(2), 252–256. https://doi.org/10.1002/ppsc.201300244

Quinto-Su, P. A., & Venugopalan, V. (2007). Mechanisms of Laser Cellular Microsurgery. Methods in Cell Biology, 82, 111–151. https://doi.org/10.1016/S0091-679X(06)82004-2

Raes, L., Pille, M., Harizaj, A., Goetgeluk, G., Van Hoeck, J., Stremersch, S., Fraire, J. C., Brans, T., de Jong, O. G., Maas-Bakker, R., Mastrobattista, E., Vader, P., De Smedt, S. C., Vandekerckhove, B., Raemdonck, K., & Braeckmans, K. (2021). Cas9 RNP transfection by vapor nanobubble photoporation for ex vivo cell engineering. Molecular Therapy - Nucleic Acids, 25, 696–707. https://doi.org/10.1016/j.omtn.2021.08.014

Raes, L., Stremersch, S., Fraire, J. C., Brans, T., Goetgeluk, G., De Munter, S., Van Hoecke, L., Verbeke, R., Van Hoeck, J., Xiong, R., Saelens, X., Vandekerckhove, B., De Smedt, S., Raemdonck, K., & Braeckmans, K. (2020). Intracellular Delivery of mRNA in Adherent and Suspension Cells by Vapor Nanobubble Photoporation. Nano-Micro Letters, 12(1), 1–17. https://doi.org/10.1007/s40820-020-00523-0

Raes, L., Van Hecke, C., Michiels, J., Stremersch, S., Fraire, J. C., Brans, T., Xiong, R., De Smedt, S., Vandekerckhove, L., Raemdonck, K., & Braeckmans, K. (2019). Gold nanoparticle-mediated photoporation enables delivery of macromolecules over a wide range of molecular weights in human CD4+ T cells. Crystals, 9(8), 1–16. https://doi.org/10.3390/cryst9080411

Rahim, M. K. A., Fukaminato, T., Kamei, T., & Tamaoki, N. (2011). Dynamic photocontrol of the gliding motility of a microtubule driven by kinesin on a photoisomerizable monolayer surface. Langmuir, 27(17), 10347–10350. https://doi.org/10.1021/la2024499

Rahmanzadeh, R., Rudnitzki, F., & Hüttmann, G. (2019). Two ways to inactivate the Ki-67 protein—Fragmentation by nanoparticles, crosslinking with fluorescent dyes. Journal of Biophotonics, 12(9), 1–7. https://doi.org/10.1002/jbio.201800460

Rau, K. R., Quinto-Su, P. A., Hellman, A. N., & Venugopalan, V. (2006). Pulsed laser microbeam-induced cell lysis: Time-resolved imaging and analysis of hydrodynamic effects. Biophysical Journal, 91(1), 317–329. https://doi.org/10.1529/biophysj.105.079921

Raveux, A., Vandormael-Pournin, S., & Cohen-Tannoudji, M. (2017). Optimization of the production of knock-in alleles by CRISPR/Cas9 microinjection into the mouse zygote. Scientific Reports, 7(1), 42661. https://doi.org/10.1038/srep42661

Redza-Dutordoir, M., & Averill-Bates, D. A. (2016). Activation of apoptosis signalling pathways by reactive oxygen species. Biochimica et Biophysica Acta - Molecular Cell Research, 1863(12), 2977–2992. https://doi.org/10.1016/j.bbamcr.2016.09.012

Rest, M. van Der, Cole, W. G., & Glorieux, F. H. (1977). Human collagen “fingerprints” produced by clostridopeptidase A digestion and high-pressure liquid chromatography. Biochemical Journal, 161(3), 527–534. https://doi.org/10.1042/bj1610527

Rich, J., Tian, Z., & Huang, T. J. (2022). Sonoporation: Past, Present, and Future. Advanced Materials Technologies, 7(1), 2100885. https://doi.org/10.1002/admt.202100885

Riss, Terry. L., Martha, A. O., Richard, A. M., Kevin, K., & Andrew, L. N. (2021). Apoptosis marker assays for HTS.

Romshin, A. M., Zeeb, V., Glushkov, E., Radenovic, A., Sinogeikin, A. G., & Vlasov, I. I. (2023). Nanoscale thermal control of a single living cell enabled by diamond heater-thermometer. Scientific Reports, 13(1), 8546. https://doi.org/10.1038/s41598-023-35141-4

Romshin, A. M., Zeeb, V., Martyanov, A. K., Kudryavtsev, O. S., Pasternak, D. G., Sedov, V. S., Ralchenko, V. G., Sinogeykin, A. G., & Vlasov, I. I. (2021). A new approach to precise mapping of local temperature fields in submicrometer aqueous volumes. Scientific Reports, 11(1), 14228. https://doi.org/10.1038/s41598-021-93374-7

Rudiuk, S., Saito, H., Hara, T., Inoue, T., Yoshikawa, K., & Baigl, D. (2011). Light-regulated mRNA condensation by a photosensitive surfactant works as a series photoswitch of translation activity in the presence of small RNAs. Biomacromolecules, 12(11), 3945–3951. https://doi.org/10.1021/bm200962s

Ruzgys, P., Novickij, V., Novickij, J., & Šatkauskas, S. (2019). Influence of the electrode material on ROS generation and electroporation efficiency in low and high frequency nanosecond pulse range. Bioelectrochemistry, 127, 87–93. https://doi.org/10.1016/j.bioelechem.2019.02.002

Rwei, A. Y., Wang, W., & Kohane, D. S. (2015). Photoresponsive nanoparticles for drug delivery. Nano Today, 10(4), 451–467. https://doi.org/10.1016/j.nantod.2015.06.004

Sacconi, L., O'Connor, R. P., Jasaitis, A., Masi, A., Buffelli, M., & Pavone, F. S. (2007). In vivo multiphoton nanosurgery on cortical neurons. Journal of Biomedical Optics, 12(5), 050502. https://doi.org/10.1117/1.2798723

Sahay, G., Querbes, W., Alabi, C., Eltoukhy, A., Sarkar, S., Zurenko, C., Karagiannis, E., Love, K., Chen, D., Zoncu, R., Buganim, Y., Schroeder, A., Langer, R., & Anderson, D. G. (2013). Efficiency of siRNA delivery by lipid nanoparticles is limited by endocytic recycling. Nature Biotechnology, 31(7), 653–658. https://doi.org/10.1038/nbt.2614

Sailor, M. J. (2014). Chemical reactivity and surface chemistry of porous silicon. In L. Canham (Ed.), Handbook of Porous Silicon (pp. 355–381). https://doi.org/10.1007/978-3-319-05744-6

Sailor, M. J., & Wu, E. C. (2009). Photoluminescence-based sensing with porous silicon films, microparticles, and nanoparticles. Advanced Functional Materials, 19(20), 3195–3208. https://doi.org/10.1002/adfm.200900535

Saklayen, N., Kalies, S., Madrid, M., Nuzzo, V., Huber, M., Shen, W., Sinanan-Singh, J., Heinemann, D., Heisterkamp, A., & Mazur, E. (2017). Analysis of poration-induced changes in cells from laser-activated plasmonic substrates. Biomedical Optics Express, 8(10), 4756. https://doi.org/10.1364/boe.8.004756

Sankin, G. N., Yuan, F., & Zhong, P. (2010). Pulsating tandem microbubble for localized and directional single-cell membrane poration. Physical Review Letters, 105(7). https://doi.org/10.1103/PhysRevLett.105.078101

Santos, H. A., Riikonen, J., Salonen, J., Mäkilä, E., Heikkilä, T., Laaksonen, T., Peltonen, L., Lehto, V. P., & Hirvonen, J. (2010). In vitro cytotoxicity of porous silicon microparticles: Effect of the particle concentration, surface chemistry and size. Acta Biomaterialia, 6(7), 2721–2731. https://doi.org/10.1016/j.actbio.2009.12.043

Santra, T. S., Chang, H. Y., Wang, P. C., & Tseng, F. G. (2014). Impact of pulse duration on localized single-cell nano-electroporation. Analyst, 139(23), 6249–6258. https://doi.org/10.1039/c4an01050g

Santra, T. S., Kar, S., Chen, T. C., Chen, C. W., Borana, J., Lee, M. C., & Tseng, F. G. (2020). Near-infrared nanosecond-pulsed laser-activated highly efficient intracellular delivery mediated by nano-corrugated mushroom-shaped gold-coated polystyrene nanoparticles. Nanoscale, 12(22), 12057–12067. https://doi.org/10.1039/d0nr01792b

Sawant, R. R., & Torchilin, V. P. (2012). Challenges in development of targeted liposomal therapeutics. AAPS Journal, 14(2), 303–315. https://doi.org/10.1208/s12248-012-9330-0

Schaeublin, N. M., Braydich-Stolle, L. K., Schrand, A. M., Miller, J. M., Hutchison, J., Schlager, J. J., & Hussain, S. M. (2011). Surface charge of gold nanoparticles mediates mechanism of toxicity. Nanoscale, 3(2), 410–420. https://doi.org/10.1039/c0nr00478b

Schaffer, D. V., Fidelman, N. A., Dan, N., & Lauffenburger, D. A. (2000). Vector unpacking as a potential barrier for receptor-mediated polyplex gene delivery. Biotechnology and Bioengineering, 67(5), 598–606. https://doi.org/10.1002/(SICI)1097-0290(20000305)67:5<598::AID-BIT10>3.0.CO;2-G

Schmiderer, L., Subramaniam, A., Žemaitis, K., Bäckström, A., Yudovich, D., Soboleva, S., Galeev, R., Prinz, C. N., Larsson, J., Hjort, M., & Weitz, D. A. (2020). Efficient and nontoxic biomolecule delivery to primary human hematopoietic stem cells using nanostraws. Proceedings of the National Academy of Sciences, 117(35), 21267–21273. https://doi.org/10.1073/pnas.2001367117/-/DCSupplemental

Schneckenburger, H., Hendinger, A., Sailer, R., Strauss, W. S. L., & Schmitt, M. (2002). Laser-assisted optoporation of single cells. Journal of Biomedical Optics, 7(3), 410–416. https://doi.org/10.1117/1.1485758

Schomaker, M., Heinemann, D., Kalies, S., Willenbrock, S., Wagner, S., Nolte, I., Ripken, T., Escobar, H. M., Meyer, H., & Heisterkamp, A. (2015). Characterization of nanoparticle mediated laser transfection by femtosecond laser pulses for applications in molecular medicine. Journal of Nanobiotechnology, 13(1), 1–15. https://doi.org/10.1186/s12951-014-0057-1

Secret, E., Maynadier, M., Audrey, G., Gary-Bobo, M., Chaix, A., Belamie, E., Maillard, P., Sailor, M. J., Garcia, M., Durand, J. O., & Cunin, F. (2013). Anionic porphyrin-grafted porous silicon nanoparticles for photodynamic therapy. Chemical Communications, 49(39), 4202–4204. https://doi.org/10.1039/c3cc38837a

Secret, E., Maynadier, M., Gallud, A., Chaix, A., Bouffard, E., Gary-Bobo, M., Marcotte, N., Mongin, O., El Cheikh, K., Hugues, V., Auffan, M., Frochot, C., Morère, A., Maillard, P., Blanchard-Desce, M., Sailor, M. J., Garcia, M., Durand, J. O., & Cunin, F. (2014). Two-photon excitation of porphyrin-functionalized porous silicon nanoparticles for photodynamic therapy. Advanced Materials, 26(45), 7643–7648. https://doi.org/10.1002/adma.201403415

Sengupta, A., Kelly, S. C., Dwivedi, N., Thadhani, N., & Prausnitz, M. R. (2014). Efficient intracellular delivery of molecules with high cell viability using nanosecond-pulsed laser-activated carbon nanoparticles. ACS Nano, 8(3), 2889–2899. https://doi.org/10.1021/nn500100x

Seo, H., & Lee, H. (2022). Spatiotemporal control of signal-driven enzymatic reaction in artificial cell-like polymersomes. Nature Communications, 13(1), 5179. https://doi.org/10.1038/s41467-022-32889-7

Shahbazi, M. A., Herranz, B., & Santos, H. A. (2012). Nanostructured porous Si-based nanoparticles for targeted drug delivery. Biomatter, 2(4), 296–312. https://doi.org/10.4161/biom.22347

Shalek, A. K., Robinson, J. T., Karp, E. S., Lee, J. S., Ahn, D. R., Yoon, M. H., Sutton, A., Jorgolli, M., Gertner, R. S., Gujral, T. S., MacBeath, G., Yang, E. G., & Park, H. (2010). Vertical silicon nanowires as a universal platform for delivering biomolecules into living cells. Proceedings of the National Academy of Sciences of the United States of America, 107, 1870–1875. https://doi.org/10.1073/pnas.0909350107

Sheikh, A. A., Asema, S. U. K., Asif, M., & Patel, S. (2019). Effect of Temperature and Electrolytic Concentration on Density and Viscosity of Ethanol-Water Mixed Solvent Systems. International Journal of Scientific Research in Science and Technology, 6(6), 01–05. https://doi.org/10.32628/ijsrst196525

Shen, S., Wang, S., Zheng, R., Zhu, X., Jiang, X., Fu, D., & Yang, W. (2015). Magnetic nanoparticle clusters for photothermal therapy with near-infrared irradiation. Biomaterials, 39, 67–74. https://doi.org/10.1016/j.biomaterials.2014.10.064

Shen, Y., Shuhendler, A. J., Ye, D., Xu, J. J., & Chen, H. Y. (2016). Two-photon excitation nanoparticles for photodynamic therapy. Chemical Society Reviews, 45(24), 6725–6741. https://doi.org/10.1039/c6cs00442c

Shi, J., Ma, Y., Zhu, J., Chen, Y., Sun, Y., Yao, Y., Yang, Z., & Xie, J. (2018). A review on electroporation-based intracellular delivery. Molecules, 23(11), 3044. https://doi.org/10.3390/molecules23113044

Shim, M. K., Yoon, H. Y., Lee, S., Jo, M. K., Park, J., Kim, J. H., Jeong, S. Y., Kwon, I. C., & Kim, K. (2017). Caspase-3/-7-Specific Metabolic Precursor for Bioorthogonal Tracking of Tumor Apoptosis. Scientific Reports, 7(1), 1–15. https://doi.org/10.1038/s41598-017-16653-2

Shinde, A., Kar, S., Nagai, M., Tseng, F. G., & Santra, T. S. (2021). Light-Induced cellular delivery and analysis. In T. S. Santra & F. G. Tseng (Eds.), Handbook of Single-Cell Technologies (pp. 3–29). Springer Singapore. https://doi.org/10.1007/978-981-10-8953-4

Shinde, P., Kar, S., Loganathan, M., Chang, H. Y., Tseng, F. G., Nagai, M., & Santra, T. S. (2020). Infrared Pulse Laser-Activated Highly Efficient Intracellular Delivery Using Titanium Microdish Device. ACS Biomaterials Science and Engineering, 6(10), 5645–5652. https://doi.org/10.1021/acsbiomaterials.0c00785

Shokouhi, A. R., Aslanoglou, S., Nisbet, D., Voelcker, N. H., & Elnathan, R. (2020). Vertically configured nanostructure-mediated electroporation: A promising route for intracellular regulations and interrogations. Materials Horizons, 7(11), 2810–2831. https://doi.org/10.1039/d0mh01016b

Shull, G., Haffner, C., Huttner, W. B., Kodandaramaiah, S. B., & Taverna, E. (2019). Robotic platform for microinjection into single cells in brain tissue. EMBO Reports, 20(10), e47880. https://doi.org/10.15252/embr.201947880

Simunovic, M., Metzger, J. J., Etoc, F., Yoney, A., Ruzo, A., Martyn, I., Croft, G., You, D. S., Brivanlou, A. H., & Siggia, E. D. (2019). A 3D model of a human epiblast reveals BMP4-driven symmetry breaking. Nature Cell Biology, 21(7), 900–910. https://doi.org/10.1038/s41556-019-0349-7

Smith, B. N., Burton, L. J., Henderson, V., Randle, D. D., Morton, D. J., Smith, B. A., Taliaferro-Smith, L., Nagappan, P., Yates, C., Zayzafoon, M., Chung, L. W. K., & Odero-Marah, V. A. (2014). Snail promotes epithelial mesenchymal transition in breast cancer cells in part via activation of nuclear ERK2. PLoS ONE, 9(8), e104987. https://doi.org/10.1371/journal.pone.0104987

Sohaebuddin, S. K., Thevenot, P. T., Baker, D., Eaton, J. W., & Tang, L. (2010). Nanomaterial cytotoxicity is composition, size, and cell type dependent. Particle and Fibre Toxicology, 7, 1–17. http://www.particleandfibretoxicology.com/content/7/1/22

Soenen, S. J., Manshian, B., Montenegro, J. M., Amin, F., Meermann, B., Thiron, T., Cornelissen, M., Vanhaecke, F., Doak, S., Parak, W. J., De Smedt, S., & Braeckmans, K. (2012). Cytotoxic effects of gold nanoparticles: A multiparametric study. ACS Nano, 6(7), 5767–5783. https://doi.org/10.1021/nn301714n

Soman, P., Zhang, W., Umeda, A., Zhang, Z. J., & Chen, S. (2011). Femtosecond laser-assisted optoporation for drug and gene delivery into single mammalian cells. Journal of Biomedical Nanotechnology, 7(3), 334–341. https://doi.org/10.1166/jbn.2011.1295

Søndergaard, J. N., Geng, K., Sommerauer, C., Atanasoai, I., Yin, X., & Kutter, C. (2020). Successful delivery of large-size CRISPR/Cas9 vectors in hard-to-transfect human cells using small plasmids. Communications Biology, 3(1), 319. https://doi.org/10.1038/s42003-020-1045-7

Spiteri, C., Caprettini, V., & Chiappini, C. (2020). Biomaterials-based approaches to model embryogenesis. Biomaterials Science, 8(24), 6992–7013. https://doi.org/10.1039/d0bm01485k

Stanley, P. E. (1989). A review of bioluminescent ATP techniques in rapid microbiology. Journal of Bioluminescence and Chemiluminescence, 4(1), 375–380. https://doi.org/10.1002/BIO.1170040151

Stevenson, D., Agate, B., Tsampoula, X., Fischer, P., A Brown, C. T., Sibbett, W., Riches, A., Gunn-Moore, F., Dholakia, K., Lake, T. K., Morris, J. E., Carruthers, A. E., Bryant, P. E., & Riches, A. C. (2006). Femtosecond optical transfection of cells: viability and efficiency. Optics Express, 14(16), 7125–7133. https://doi.org/10.1364/OE.14.007125

Stevenson, D. J., Gunn-Moore, F. J., Campbell, P., & Dholakia, K. (2010). Single cell optical transfection. Journal of the Royal Society Interface, 7(47), 863–871. https://doi.org/10.1098/rsif.2009.0463

Stewart, M. P., Langer, R., & Jensen, K. F. (2018). Intracellular delivery by membrane disruption: Mechanisms, strategies, and concepts. Chemical Reviews, 118(16), 7409–7531. https://doi.org/10.1021/acs.chemrev.7b00678

Stojanovic, V., Cunin, F., Durand, J. O., Garcia, M., & Gary-Bobo, M. (2016). Potential of porous silicon nanoparticles as an emerging platform for cancer theranostics. Journal of Materials Chemistry B, 4(44), 7050–7059. https://doi.org/10.1039/c6tb01829g

Stracke, F., Rieman, I., & König, K. (2005). Optical nanoinjection of macromolecules into vital cells. Journal of Photochemistry and Photobiology B: Biology, 81(3), 136–142. https://doi.org/10.1016/j.jphotobiol.2005.07.006

Stratech. (2023). EZ CapTM Cy5 EGFP mRNA (5-moUTP). https://www.stratech.co.uk/products/R1011-APE/

Sypabekova, M., Hagemann, A., Rho, D., & Kim, S. (2023). Review: 3-Aminopropyltriethoxysilane (APTES) Deposition Methods on Oxide Surfaces in Solution and Vapor Phases for Biosensing Applications. Biosensors, 13(1), 1–25. https://doi.org/10.3390/bios13010036

Szili, E. J., Jane, A., Low, S. P., Sweetman, M., MacArdle, P., Kumar, S., Smart, R. S. C., & Voelcker, N. H. (2011). Interferometric porous silicon transducers using an enzymatically amplified optical signal. Sensors and Actuators, B: Chemical, 160(1), 341–348. https://doi.org/10.1016/j.snb.2011.07.059

Talone, B., Bazzarelli, M., Schirato, A., Dello Vicario, F., Viola, D., Jacchetti, E., Bregonzio, M., Raimondi, M. T., Cerullo, G., & Polli, D. (2021). Phototoxicity induced in living HeLa cells by focused femtosecond laser pulses: a data-driven approach. Biomedical Optics Express, 12(12), 7886. https://doi.org/10.1364/boe.441225

Tanaka, T., Mangala, L. S., Vivas-Mejia, P. E., Nieves-Alicea, R., Mann, A. P., Mora, E., Han, H. D., Shahzad, M. M. K., Liu, X., Bhavane, R., Gu, J., Fakhoury, J. R., Chiappini, C., Lu, C., Matsuo, K., Godin, B., Stone, R. L., Nick, A. M., Lopez-Berestein, G., … Ferrari, M. (2010). Sustained small interfering

RNA delivery by mesoporous silicon particles. Cancer Research, 70, 3687–3696. https://doi.org/10.1158/0008-5472.CAN-09-3931

Tang, D., Kang, R., Berghe, T. Vanden, Vandenabeele, P., & Kroemer, G. (2019). The molecular machinery of regulated cell death. Cell Research, 29(5), 347–364. https://doi.org/10.1038/s41422-019-0164-5

Tantra, R., Schulze, P., & Quincey, P. (2010). Effect of nanoparticle concentration on zeta-potential measurement results and reproducibility. Particuology, 8(3), 279–285. https://doi.org/10.1016/j.partic.2010.01.003

Taverna, E., Haffner, C., Pepperkok, R., & Huttner, W. B. (2012). A new approach to manipulate the fate of single neural stem cells in tissue. Nature Neuroscience, 15(2), 329–337. https://doi.org/10.1038/nn.3008

Tay, A., & Melosh, N. (2019). Transfection with Nanostructure Electro-Injection is Minimally Perturbative. Advanced Therapeutics, 2(12), 1900133. https://doi.org/10.1002/adtp.201900133

Tchoryk, A., Taresco, V., Argent, R. H., Ashford, M., Gellert, P. R., Stolnik, S., Grabowska, A., & Garnett, M. C. (2019). Penetration and uptake of nanoparticles in 3D tumor spheroids. Bioconjugate Chemistry, 30(5), 1371–1384. https://doi.org/10.1021/acs.bioconjchem.9b00136

Terracciano, M., De Stefano, L., Borbone, N., Politi, J., Oliviero, G., Nici, F., Casalino, M., Piccialli, G., Dardano, P., Varra, M., & Rea, I. (2016). Solid phase synthesis of a thrombin binding aptamer on macroporous silica for label free optical quantification of thrombin. RSC Advances, 6(90), 86762–86769. https://doi.org/10.1039/c6ra18401d

Thomas, C. E., Ehrhardt, A., & Kay, M. A. (2003). Progress and problems with the use of viral vectors for gene therapy. Nature Reviews Genetics, 4(5), 346–358. https://doi.org/10.1038/nrg1066

Tieu, T., Alba, M., Elnathan, R., Cifuentes-Rius, A., & Voelcker, N. H. (2019). Advances in Porous Silicon–Based Nanomaterials for Diagnostic and Therapeutic Applications. Advanced Therapeutics, 2(1), 1800095. https://doi.org/10.1002/adtp.201800095

Tieu, T., Wojnilowicz, M., Huda, P., Thurecht, K. J., Thissen, H., Voelcker, N. H., & Cifuentes-Rius, A. (2021). Nanobody-displaying porous silicon nanoparticles for the co-delivery of siRNA and doxorubicin. Biomaterials Science, 9(1), 133–147. https://doi.org/10.1039/d0bm01335h

Timmins, N. E., & Nielsen, L. K. (2007). Generation of multicellular tumor spheroids by the hanging-drop method. Tissue Engineering, 140, 141–151. https://doi.org/10.1007/978-1-59745-443-8_8

Tinsley-Bown, A. M., Canham, L. T., Hollings, M., Anderson, M. H., Reeves, C. L., Cox, T. I., Nicklin, S., Squirrell, D. J., Perkins, E., Hutchinson, A., Sailor, M. J., & Wun, A. (2000). Tuning the pore size and surface chemistry of porous silicon for immunoassays. Physica Status Solidi (A) Applied Research, 182(1), 547–553. https://doi.org/10.1002/1521-396X(200011)182:1<547::AID-PSSA547>3.0.CO;2-C

Tirlapur, U. K., König, K., Peuckert, C., Krieg, R., & Halbhuber, K. (2001). Femtosecond near-infrared laser pulses elicit generation of reactive oxygen species in mammalian cells leading to apoptosis-like death. Experimental Cell Research, 263(1), 88–97. https://doi.org/10.1006/excr.2000.5082

Tirlapur, U. K., König, K., Peuckert, C., Krieg, R., & Halbhuber, K. (2001). Femtosecond near-infrared laser pulses elicit generation of reactive oxygen species in mammalian cells leading to apoptosis-like death. Experimental Cell Research, 263(1), 88–97. https://doi.org/10.1006/excr.2000.5082

Torres, M. L., Gunn-Moore, F., & Dholakia, K. (2010). Transient transfection of mammalian cells using a violet diode laser. Journal of Biomedical Optics, 15, 041506–041506. https://doi.org/10.1117/1.3430730

Torres-Mapa, M. L., Antkowiak, M., Cizmarova, H., Ferrier, D. E. K., Dholakia, K., & Gunn-Moore, F. J. (2011). Integrated holographic system for all-optical manipulation of developing embryos. Biomedical Optical Express, 2(6), 1564–1575. https://doi.org/10.1364/boe.2.001564

Tsampoula, X., Garćs-Chávez, V., Comrie, M., Stevenson, D. J., Agate, B., Brown, C. T. A., Gunn-Moore, F., & Dholakia, K. (2007). Femtosecond cellular transfection using a nondiffracting light beam. Applied Physics Letters, 91(5). https://doi.org/10.1063/1.2766835

Tsoli, M., Kuhn, H., Brandau, W., Esche, H., & Schmid, G. (2005). Cellular uptake and toxicity of Au55 clusters. Small, 1(8–9), 841–844. https://doi.org/10.1002/smll.200500104

Tsong, T. Y. (1991). Electroporation of cell membranes. Biophysical Journal, 60(2), 297–306. https://doi.org/10.1016/S0006-3495(91)82054-9

Tsukakoshi, M., Kurata, S., Nomiya, Y., Ikawa, Y., & Kasuya, T. (1984). A Novel Method of DNA Transfection by Laser Microbeam Cell Surgery. Appl. Phys. B, 35(3), 135–140. https://doi.org/10.1007/bf00697702

Uchida, M., Li, X. W., Mertens, P., & Alpar, H. O. (2009). Transfection by particle bombardment: Delivery of plasmid DNA into mammalian cells using gene gun. Biochimica et Biophysica Acta, 1790(8), 754–764. https://doi.org/10.1016/j.bbagen.2009.05.013

Uchugonova, A., Isemann, A., Gorjup, E., Tempea, G., Bückle, R., Watanabe, W., & König, K. (2008). Optical knock out of stem cells with extremely ultrashort femtosecond laser pulses. Journal of Biophotonics, 1(6), 463–469. https://doi.org/10.1002/jbio.200810047

Urich, E., Patsch, C., Aigner, S., Graf, M., Iacone, R., & Freskgård, P. O. (2013). Multicellular self-assembled spheroidal model of the blood brain barrier. Scientific Reports, 3(1), 1500. https://doi.org/10.1038/srep01500

Van Hoecke, L., Raes, L., Stremersch, S., Brans, T., Fraire, J. C., Roelandt, R., Declercq, W., Vandenabeele, P., Raemdonck, K., Braeckmans, K., & Saelens, X. (2019). Delivery of mixed-lineage kinase domain-like protein by vapor nanobubble photoporation induces necroptotic-like cell death in tumor cells. International Journal of Molecular Sciences, 20(17), 4254. https://doi.org/10.3390/ijms20174254

Van Hoecke, L., Van Lint, S., Roose, K., Van Parys, A., Vandenabeele, P., Grooten, J., Tavernier, J., De Koker, S., & Saelens, X. (2018). Treatment with mRNA coding for the necroptosis mediator MLKL induces antitumor immunity directed against neo-epitopes. Nature Communications, 9(1), 3417. https://doi.org/10.1038/s41467-018-05979-8

Vandersarl, J. J., Xu, A. M., & Melosh, N. A. (2012). Nanostraws for direct fluidic intracellular access. Nano Letters, 12(8), 3881–3886. https://doi.org/10.1021/nl204051v

Vanzha, E., Pylaev, T., Prilepskii, A., Golubev, A., Khlebtsov, B., Bogatyrev, V., & Khlebtsov, N. (2017). Cell culture surfaces with immobilized gold nanostars: a new approach for laser-induced plasmonic cell optoporation. Saratov Fall Meeting 2016: Optical Technologies in Biophysics and Medicine XVIII., 10336. https://doi.org/10.1117/12.2269948

Viigipuu, K., & Pasi, K. (2004). Microinjection of living adherent cells. Alternatives to Laboratory Animals, 32(4), 417–423. https://doi.org/10.1177/026119290403200414

Vinci, M., Gowan, S., Boxall, F., Patterson, L., Zimmermann, M., Court, W., Lomas, C., Mendiola, M., Hardisson, D., & Eccles, S. A. (2012). Advances in establishment and analysis of three-dimensional tumor spheroid-based functional assays for target validation and drug evaluation. BMC Biology, 10, 29. https://doi.org/10.1186/1741-7007-10-29

Vogel, A., Noack, J., Hüttman, G., & Paltauf, G. (2005). Mechanisms of femtosecond laser nanosurgery of cells and tissues. Applied Physics B: Lasers and Optics, 81(8), 1015–1047. https://doi.org/10.1007/s00340-005-2036-6

von Kockritz-Blickwede, M., Chow, O. A., & Nizet, V. (2009). Fetal calf serum contain heat-stable nucleases that degrade neutrophil extracellular traps. Blood, 114(25), 5245–5246. https://doi.org/10.1182/blood-2009-08-240713

Von Maltzahn, G., Park, J. H., Agrawal, A., Bandaru, N. K., Das, S. K., Sailor, M. J., & Bhatia, S. N. (2009). Computationally guided photothermal tumor therapy using long-circulating gold nanorod antennas. Cancer Research, 69(9), 3892–3900. https://doi.org/10.1158/0008-5472.CAN-08-4242

Walczyk, D., Bombelli, F. B., Monopoli, M. P., Lynch, I., & Dawson, K. A. (2010). What the cell “sees” in bionanoscience. Journal of the American Chemical Society, 132(16), 5761–5768. https://doi.org/10.1021/ja910675v

Waleed, M., Hwang, S.-U., Kim, J.-D., Shabbir, I., Shin, S.-M., & Lee, Y.-G. (2013). Single-cell optoporation and transfection using femtosecond laser and optical tweezers. Biomedical Optics Express, 4(9), 1533–1547. https://doi.org/10.1364/boe.4.001533

Wan, Y., Apostolou, S., Dronov, R., Kuss, B., & Voelcker, N. H. (2014). Cancer-targeting siRNA delivery from porous silicon nanoparticles. Nanomedicine, 9(15), 2309–2321. https://doi.org/10.2217/nnm.14.12

Wang, B. G., König, K., & Halbhuber, K. J. (2010). Two-photon microscopy of deep intravital tissues and its merits in clinical research. Journal of Microscopy, 238(1), 1–20. https://doi.org/10.1111/j.1365-2818.2009.03330.x

Wang, F., Wang, D., Wang, T., Jin, Y., Ling, B., Li, Q., & Li, J. (2021). A simple approach to prepare fluorescent molecularly imprinted nanoparticles. RSC Advances, 11(13), 7732–7737. https://doi.org/10.1039/D0RA10618F

Wang, H., Ding, S., Zhang, Z., Wang, L., & You, Y. (2019). Cationic micelle: A promising nanocarrier for gene delivery with high transfection efficiency. Journal of Gene Medicine, 21(7), e3101. https://doi.org/10.1002/jgm.3101

Wang, H. Y., & Lu, C. (2006). Electroporation of mammalian cells in a microfluidic channel with geometric variation. Analytical Chemistry, 78(14), 5158–5164. https://doi.org/10.1021/ac060733n

Wang, J., Harizaj, A., Wu, Y., Jiang, X., Brans, T., Fraire, J. C., Mejía Morales, J., De Smedt, S. C., Tang, Z., Xiong, R., & Braeckmans, K. (2021). Black phosphorus mediated photoporation: A broad absorption nanoplatform for intracellular delivery of macromolecules. Nanoscale, 13(40), 17049–17056. https://doi.org/10.1039/d1nr05461a

Wang, J., Xie, L., Wang, T., Wu, F., Meng, J., Liu, J., & Xu, H. (2017). Visible light-switched cytosol release of siRNA by amphiphilic fullerene derivative to enhance RNAi efficacy in vitro and in vivo. Acta Biomaterialia, 59, 158–169. https://doi.org/10.1016/j.actbio.2017.05.031

Wang, L., Wei, X., Liu, H., & Fan, Y. (2023). Nanomaterial-mediated photoporation for intracellular delivery. Acta Biomaterialia, 157, 24–48. https://doi.org/10.1016/j.actbio.2022.12.050

Wang, L., Wu, J., Hu, Y., Hu, C., Pan, Y., Yu, Q., & Chen, H. (2018). Using porous magnetic iron oxide nanomaterials as a facile photoporation nanoplatform for macromolecular delivery. Journal of Materials Chemistry B, 6(27), 4427–4436. https://doi.org/10.1039/c8tb01026a

Wang, W., Sun, Y., Zhang, M., Anderson, R., Langille, L., & Chan, W. (2008). A system for high-speed microinjection of adherent cells. Review of Scientific Instruments, 79(10), 104302. https://doi.org/10.1063/1.3006000

Wang, Y., Bruggeman, K. F., Franks, S., Gautam, V., Hodgetts, S. I., Harvey, A. R., Williams, R. J., & Nisbet, D. R. (2021). Is Viral Vector Gene Delivery More Effective Using Biomaterials? Advanced Healthcare Materials, 10(1), 2001238. https://doi.org/10.1002/adhm.202001238

Wang, Y., Song, H., Yu, M., Xu, C., Liu, Y., Tang, J., Yang, Y., & Yu, C. (2018). Room temperature synthesis of dendritic mesoporous silica nanoparticles with small sizes and enhanced mRNA delivery performance. Journal of Materials Chemistry B, 6(24), 4089–4095. https://doi.org/10.1039/c8tb00544c

Wang, Yuan., Wang, Z., Xie, K., Zhao, X., Jiang, X., Chen, B., Han, Y., Lu, Y., Huang, L., Zhang, W., Yang, Y., & Shi, P. (2020). High-Efficiency Cellular Reprogramming by Nanoscale Puncturing. Nano Letters, 20(7), 5473–5481. https://doi.org/10.1021/acs.nanolett.0c01979

Wareing, N., Szymanski, K., Akkaraju, G. R., Loni, A., Canham, L. T., Gonzalez-Rodriguez, R., & Coffer, J. L. (2017). In Vitro Gene Delivery with Large Porous Silicon Nanoparticles Fabricated Using Cost-Effective, Metal-Assisted Chemical Etching. Small, 13(3), 1602739. https://doi.org/10.1002/smll.201602739

Warmflash, A., Sorre, B., Etoc, F., Siggia, E. D., & Brivanlou, A. H. (2014). A method to recapitualte early embryonic spatial patterning in human embryonic stem cells. Nature Methods, 11, 847–854. https://doi.org/10.1038/nmeth.3016.A

Wayteck, L., Xiong, R., Braeckmans, K., De Smedt, S. C., & Raemdonck, K. (2017). Comparing photoporation and nucleofection for delivery of small interfering RNA to cytotoxic T cells. Journal of Controlled Release, 267, 154–162. https://doi.org/10.1016/j.jconrel.2017.08.002

Weaver, J. C., Smith, K. C., Esser, A. T., Son, R. S., & Gowrishankar, T. R. (2012). A brief overview of electroporation pulse strength-duration space: A region where additional intracellular effects are expected. Bioelectrochemistry, 87, 236–243. https://doi.org/10.1016/j.bioelechem.2012.02.007

Wen, R., Zhang, A. H., Liu, D., Feng, J., Yang, J., Xia, D., Wang, J., Li, C., Zhang, T., Hu, N., Hang, T., He, G., & Xie, X. (2019). Intracellular Delivery and Sensing System Based on Electroplated Conductive Nanostraw Arrays. ACS Applied Materials and Interfaces, 11, 43936–43948. https://doi.org/10.1021/acsami.9b15619

Wilson, A. M., Mazzaferri, J., Bergeron, É., Patskovsky, S., Marcoux-Valiquette, P., Costantino, S., Sapieha, P., & Meunier, M. (2018). In Vivo Laser-Mediated Retinal Ganglion Cell Optoporation Using KV1.1 Conjugated Gold Nanoparticles. Nano Letters, 18(11), 6981–6988. https://doi.org/10.1021/ACS.NANOLETT.8B02896

Wu, T. H., Teslaa, T., Kalim, S., French, C. T., Moghadam, S., Wall, R., Miller, J. F., Witte, O. N., Teitell, M. A., & Chiou, P. Y. (2011). Photothermal nanoblade for large cargo delivery into mammalian cells. Analytical Chemistry, 83(4), 1321–1327. https://doi.org/10.1021/ac102532w

Xia, B., Wang, B., Chen, Z., Zhang, Q., & Shi, J. (2016). Near-Infrared Light-Triggered Intracellular Delivery of Anticancer Drugs Using Porous Silicon Nanoparticles Conjugated with IR820 Dyes. Advanced Materials Interfaces, 3(4), 1–11. https://doi.org/10.1002/admi.201500715

Xiao, L., Gu, L., Howell, S. B., & Sailor, M. J. (2011). Porous silicon nanoparticle photosensitizers for singlet oxygen and their phototoxicity against cancer cells. ACS Nano, 5(5), 3651–3659. https://doi.org/10.1021/nn1035262

Xie, X., Xu, A. M., Leal-Ortiz, S., Cao, Y., Garner, C. C., & Melosh, N. A. (2013). Nanostraw-electroporation system for highly efficient intracellular delivery and transfection. ACS Nano, 7(5), 4351–4358. https://doi.org/10.1021/nn400874a

Xie, Y., & Zhao, C. (2017). An optothermally generated surface bubble and its applications. Nanoscale, 9(20), 6622–6631. https://doi.org/10.1039/c7nr01360d

Xiong, R., Drullion, C., Verstraelen, P., Demeester, J., Skirtach, A. G., Abbadie, C., De Vos, W. H., De Smedt, S. C., & Braeckmans, K. (2017). Fast spatial-selective delivery into live cells. Journal of Controlled Release, 266, 198–204. https://doi.org/10.1016/j.jconrel.2017.09.033

Xiong, R., Hua, D., Van Hoeck, J., Berdecka, D., Léger, L., De Munter, S., Fraire, J. C., Raes, L., Harizaj, A., Sauvage, F., Goetgeluk, G., Pille, M., Aalders, J., Belza, J., Van Acker, T., Bolea-Fernandez, E., Si, T., Vanhaecke, F., De Vos, W. H., … Braeckmans, K. (2021). Photothermal nanofibres enable safe engineering of therapeutic cells. Nature Nanotechnology, 16(11), 1281–1291. https://doi.org/10.1038/s41565-021-00976-3

Xiong, R., Raemdonck, K., Peynshaert, K., Lentacker, I., De Cock, I., Demeester, J., De Smedt, S. C., Skirtach, A. G., & Braeckmans, K. (2014). Comparison of gold nanoparticle mediated photoporation: Vapor nanobubbles outperform direct heating for delivering macromolecules in live cells. ACS Nano, 8(6), 6288–6296. https://doi.org/10.1021/nn5017742

Xiong, R., Samal, S. K., Demeester, J., Skirtach, A. G., De Smedt, S. C., & Braeckmans, K. (2016). Laser-assisted photoporation: fundamentals, technological advances and applications. Advances in Physics: X, 1(4), 596–620. https://doi.org/10.1080/23746149.2016.1228476

Xiong, R., Sauvage, F., Fraire, J. C., Huang, C., De Smedt, S. C., & Braeckmans, K. (2023). Photothermal Nanomaterial-Mediated Photoporation. Accounts of Chemical Research, 56(6), 631–643. https://doi.org/10.1021/acs.accounts.2c00770

Yamane, D., Wu, Y. C., Wu, T. H., Toshiyoshi, H., Teitell, M. A., & Chiou, P. Y. (2014). Electrical Impedance Monitoring of Photothermal Porated Mammalian Cells. Journal of Laboratory Automation, 19(1), 50–59. https://doi.org/10.1177/2211068213494390

Yang, Y., Liu, F., Liu, X., & Xing, B. (2013). NIR light controlled photorelease of siRNA and its targeted intracellular delivery based on upconversion nanoparticles. Nanoscale, 5(1), 231–238. https://doi.org/10.1039/c2nr32835f

Yang, Y., Yang, Y. F., Xie, X. Y., Wang, Z. Y., Gong, W., Zhang, H., Li, Y., Yu, F. L., Li, Z. P., & Mei, X. G. (2015). Dual-modified liposomes with a two-photon-sensitive cell penetrating peptide and NGR ligand for siRNA targeting delivery. Biomaterials, 48, 84–96. https://doi.org/10.1016/j.biomaterials.2015.01.030

Yao, C., Rudnitzki, F., He, Y., Zhang, Z., Hüttmann, G., & Rahmanzadeh, R. (2020). Cancer cell-specific protein delivery by optoporation with laser-irradiated gold nanorods. Journal of Biophotonics, 1–10. https://doi.org/10.1002/jbio.202000017

Yoon, J., Ryu, S. W., Lee, S., & Choi, C. (2015). Cytosolic Irradiation of Femtosecond Laser Induces Mitochondria-dependent Apoptosis-like Cell Death via Intrinsic Reactive Oxygen Cascades. Scientific Reports, 5(1), 1–6. https://doi.org/10.1038/srep08231

Young, A. T. L., Moore, R. B., Murray, A. G., Mullen, J. C., & Lakey, J. R. T. (2004). Assessment of Different Transfection Parameters in Efficiency Optimization. Cell Transplantation, 13(2), 179–185. https://doi.org/10.3727/000000004773301861

Yuan, X., Zhang, X., Sun, L., Wei, Y., & Wei, X. (2019). Cellular Toxicity and Immunological Effects of Carbon-based Nanomaterials. Particle and Fibre Toxicology, 16(1), 1–27. https://doi.org/10.1186/s12989-019-0299-z

Yu, L., Liang, D., Chen, C., & Tang, X. (2018). Caged siRNAs with Single cRGD Modification for Photoregulation of Exogenous and Endogenous Gene Expression in Cells and Mice. Biomacromolecules, 19(7), 2526–2534. https://doi.org/10.1021/acs.biomac.8b00159

Ž Knežević, N., Stojanovic, V., Chaix, A., Bouffard, E., El Cheikh, K., Morère, A., Maynadier, M., Lemercier, G., Garcia, M., Gary-Bobo, M., Ruthe, al, Durand, J.-O., & Cunin, F. (2016). Complex-Photosensitized Multifunctionalized Porous Silicon Nanoparticles for Two-Photon Near-Infrared Light Responsive Imaging and Photodynamic Cancer Therapy. Journal of Materials Chemistry B, 4(7), 1–3. https://doi.org/10.1039/C5TB02726Hï

Zeira, E., Manevitch, A., Khatchatouriants, A., Pappo, O., Hyam, E., Darash-Yahana, M., Tavor, E., Honigman, A., Lewis, A., & Galun, E. (2003). Femtosecond infrared laser - An efficient and safe in vivo gene delivery system for prolonged expression. Molecular Therapy, 8(2), 342–350. https://doi.org/10.1016/S1525-0016(03)00184-9

Zhang, D. X., Tieu, T., Esser, L., Wojnilowicz, M., Lee, C. H., Cifuentes-Rius, A., Thissen, H., & Voelcker, N. H. (2022). Differential Surface Engineering Generates Core-Shell Porous Silicon Nanoparticles for Controlled and Targeted Delivery of an Anticancer Drug. ACS Applied Materials and Interfaces, 14(49), 54539–54549. https://doi.org/10.1021/acsami.2c16370

Zhang, S., Nguyen, L. H., Zhou, K., Tu, H. C., Sehgal, A., Nassour, I., Li, L., Gopal, P., Goodman, J., Singal, A. G., Yopp, A., Zhang, Y., Siegwart, D. J., & Zhu, H. (2018). Knockdown of Anillin Actin Binding Protein Blocks Cytokinesis in Hepatocytes and Reduces Liver Tumor Development in Mice Without Affecting Regeneration. Gastroenterology, 154(5), 1421–1434. https://doi.org/10.1053/j.gastro.2017.12.013

Zhang, X. Q., Xu, X., Bertrand, N., Pridgen, E., Swami, A., & Farokhzad, O. C. (2012). Interactions of nanomaterials and biological systems: Implications to personalized nanomedicine. Advanced Drug Delivery Reviews, 64(13), 1363–1384. https://doi.org/10.1016/j.addr.2012.08.005

Zhao, M., Wang, S., Li, Q., Ji, Q., Guo, P., & Liu, X. (2018). Malat1: A long non-coding RNA highly associated with human cancers (review). Oncology Letters, 16(1), 19–26. https://doi.org/10.3892/ol.2018.8613

Zhao, X., Huang, X., Wang, X., Wu, Y., Eisfeld, A. K., Schwind, S., Gallego-Perez, D., Boukany, P. E., Marcucci, G. I., & Lee, L. J. (2015). Nanochannel Electroporation as a Platform for Living Cell Interrogation in Acute Myeloid Leukemia. Advanced Science, 2(12), 1500111. https://doi.org/10.1002/advs.201500111

Zhou, Y., Tang, Z., Shi, C., Shi, S., Qian, Z., & Zhou, S. (2012). Polyethylenimine functionalized magnetic nanoparticles as a potential non-viral vector for gene delivery. Journal of Materials Science: Materials in Medicine, 23(11), 2697–2708. https://doi.org/10.1007/s10856-012-4720-5

Zhou, Y., Yang, K., Cui, J., Ye, J. Y., & Deng, C. X. (2012). Controlled permeation of cell membrane by single bubble acoustic cavitation. Journal of Controlled Release, 157(1), 103–111. https://doi.org/10.1016/j.jconrel.2011.09.068

Zhu, Y., Zhang, X., Zhu, J., Zhao, Q., Li, Y., Li, W., Fan, C., & Huang, Q. (2012). Cytotoxicity of phenol red in toxicity assays for carbon nanoparticles. International Journal of Molecular Sciences, 13(10), 12336–12348. https://doi.org/10.3390/ijms131012336